THE FABRICATION OF NANOMETRIC METAL SULFIDES FROM XANTHATE PRECURSORS

By

ALAN PIQUETTE

Bachelor of Arts
Western State College of Colorado
Gunnison, Colorado
2002

Submitted to the Faculty of the
Graduate College of the
Oklahoma State University
In partial fulfillment of
The requirements for
The Degree of
DOCTOR OF PHILOSOPHY
December, 2007

THE FABRICATION OF NANOMETRIC METAL SULFIDES FROM XANTHATE PRECURSORS

Thesis Approved:

_____Allen Apblett_____

Thesis Advisor

_____Nicholas Materer_____

_____LeGrande Slaughter_____

_____Jim Smay_____

_____A. Gordon Emslie_____

Dean of the Graduate College

ACKNOWLEDGEMENTS

It is with my utmost sincere appreciation that I acknowledge my thesis advisor, Dr. Allen W. Apblett, for his support, guidance, and motivation. He provided a research environment that was both friendly and challenging, which made my years in his group enjoyable and rewarding. His broad range of knowledge was something of which I was happy to take advantage. His dedication to teaching and research is something that will be a positive influence on me for the rest of my scientific career.

I would like to express gratitude to my committee members: Dr. Nicholas Materer, Dr. LeGrande Slaughter, and Dr. Jim Smay, for their assistance, advice, guidance, and support throughout the years.

I am deeply grateful to all my colleagues and friends in the chemistry department. I would specifically like to thank Sulaiman Al-Fadul, Mohammed Al-Hazmi, Zeid Al-Othmann, Mohamed Chehbouni, Satish Kuriyavar, and Tarek Trad for showing me the ropes, for their valuable discussions, continuous encouragement, and for all the help they extended during the course of my stay in the Apblett Group. It would not have been the same without you.

I am also thankful to all the faculty and staff at the Department of Chemistry at Oklahoma State University for their help and kindness.

I am deeply indebted to my siblings: Eric, Jeff, Paul, Megan, and Evan for their unwavering love, support, and friendship. Words cannot express how appreciative of my parents I have been throughout my life. Without them, I would be lost. Finally, I humbly thank God, to whom I owe everyting.

TABLE OF CONTENTS

CHAPTER **PAGE**

CHAPTER **PAGE**

CHAPTER **PAGE**

CHAPTER **PAGE**

CHAPTER **PAGE**

CHAPTER **PAGE**

CHAPTER 10

LIST OF FIGURES

FIGURE **PAGE**

CHAPTER 1

CHAPTER 2

FIGURE **PAGE**

CHAPTER 3

FIGURE **PAGE**

CHAPTER 4

FIGURE **PAGE**

CHAPTER 5

FIGURE **PAGE**

CHAPTER 6

FIGURE **PAGE**

CHAPTER 7

FIGURE **PAGE**

FIGURE **PAGE**

CHAPTER 8

FIGURE **PAGE**

CHAPTER 9

FIGURE **PAGE**

CHAPTER 10

LIST OF TABLES

TABLE **PAGE**

CHAPTER 2

CHAPTER 3

TABLE **PAGE**

CHAPTER 5

CHAPTER 7

CHAPTER 8

CHAPTER 10

LIST OF REACTION SCHEMES

SCHEME **PAGE**

CHAPTER 1

CHAPTER 2

SCHEME **PAGE**

CHAPTER 3

CHAPTER 4

CHAPTER 6

SCHEME **PAGE**

CHAPTER 8

CHAPTER 9

CHAPTER 10

CHAPTER 1

INTRODUCTION

INTRODUCTION TO DISSERTATION

Collaboration. Some of the data and results included in this dissertation were obtained from undergraduate collaborators: Jimmy Smith, Kevin Snyder, Anitra Novy, and Yanci Schilling. All four students briefly worked on water purification projects (Chapter 10), and when it is logical to present some of their data to illustrate a certain point or to provide a bigger picture, their work is included. At this point, their results are unpublished, so proper acknowledgments could not be made by straightforward referencing.

Dissertation outline. This dissertation is informally divided into three parts. The focus of the first part (Chapters 2 and 3) is on metal xanthate compounds. What metal xanthate compounds are, how they are made, and how they were classically applied are topics described in Chapter 2. The potential utilization of metal xanthates as single-source precursors to metal sulfide and metal oxide nanomaterials is discussed in Chapter 3.

The bulk of this work (Chapters 4 through 9) makes up part two. In this second part, the emphasis switches to the nanometric metal sulfide and oxide systems that were prepared from the xanthate precursors. Specifically, optical and electrical properties such

as photoluminescence, electrical conductivity, and photovoltaic activity of several different metal sulfide/oxide arrangements are extensively discussed.

Finally, the last part (Chapter 10) describes work on the remediation of several toxic species from water. High surface area zinc sulfide, prepared from a xanthate single precursor, was used to treat water contaminated with pollutants such as arsenic, lead, and hexavalent chromium. The major issues regarding removal of each contaminant are discussed along with the broad picture of using nanotechnology in water purification. The overall theme that runs throughout each of the three parts is that metal xanthate complexes are extraordinarily useful single precursors for the preparation of a wide assortment of II-VI nanomaterials.

MOTIVATION AND SCOPE OF THE RESEARCH

Basic motivation. The overall objective of this research project was to investigate the usefulness of a family of compounds, known as xanthates, as single-source precursors to metal sulfides. The value of single precursors for applications in preparing semiconducting nanoparticles is well known.[1-3] Obstacles such as high reaction temperatures, precursor instability, and difficult synthetic procedures have somewhat limited the single precursor field to a relatively small number of useful complexes. For this reason, researches are striving to find new metallo-organic compounds that will prove to be effective precursors for nanomaterial fabrication.

Importance of nanometric metal chalcogenides. An increased understanding of the basic properties and possible applications of various nanomaterials has stimulated a

tremendous interest in performing research on said materials. For instance, cadmium selenide and cadmium sulfide are two of the most commonly synthesized semiconducting nanoparticulate systems.[4-9] Early on, both cadmium selenide and cadmium sulfide found success in photovoltaic devices.[10-13] Other potential applications for CdS and CdSe have been discovered, such as light emission[14,15] and sensing.[16,17] By manipulating the size, it is possible to control the luminescence properties of CdSe to such an extent, that emission of essentially any wavelength in the visible spectrum is possible. Other metal chalcogenides have also garnered attention to see if similar success could be achieved. In general, sulfides/selenides smaller than about 10 nm have potential applications in light emitting diodes, photovoltaic cells, or luminescent materials, while larger sulfides in the range of 10-500 nm can be used in photonic crystals, infrared windows, or with the proper dopant scheme, in luminescent materials and resonance light scattering probes.[18-21]

Nanoparticles of semiconducting materials with dimensions in the range of roughly 1-20 nm have distinctive properties.[22-25] These distinctive optical, electronic, catalytic, and magnetic properties are a result of large surface-to-volume ratios and reduced sizes.[14] When the diameter of a particle nears the exciton Bohr radius, the charge carriers become confined with no degrees of freedom.[26-29] This important exciton Bohr radius depends on the material, but often ranges from a few nanometers to a few tens of nanometers.[30] Due to the geometrical limitations, electrons feel the particle boundaries and adjust their energy accordingly. The energy adjustment process is known as the quantum confinement effect or quantum size effect, and this phenomenon causes the continuous bands of the solid to separate into discrete (or quantized) levels and the "band"gap to increase (refer to Figure 1.1).[1,22,31] Since the degree of band separation

depends on particle size, the bandgap and properties that depend on the bandgap can be tuned. This tunability is at the core of most semiconducting nanoparticle research.

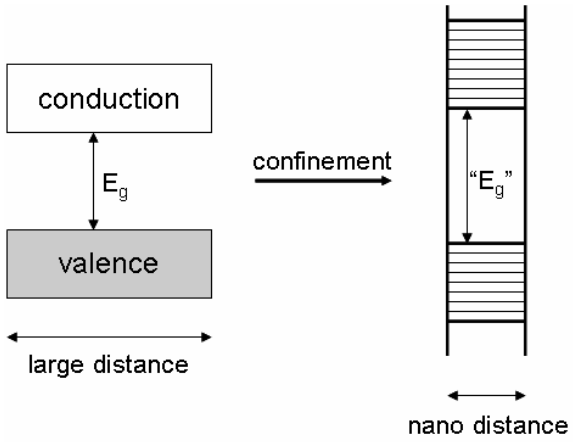

Figure 1.1: A one dimensional spatial electronic diagram for a bulk semiconductor (left) and the same semiconductor after quantum confinement (right).

Beyond the unique tunable properties of these so-called quantum dots, there is a driving force in technology to further miniaturize optical and electrical devices.[32,33] Current optical lithographic methods do not have the resolution necessary to sculpt features in the quantum confinement region (1-20 nm).[34] Nanoimprint lithography demonstrates better resolution than optical lithography, but there are still practical constraints associated with the technology.[35] As an alternative to lithographic fabrication schemes, there is a continuing effort within the scientific community to prepare devices and device material from chemical methods. There are a number of chemical approaches (sometimes called "bottom-up" approaches) used today to fabricate nanomaterials.

Various routes to semiconductor nanoparticles. The colloidal route to semiconductor nanoparticles is accomplished by performing a precipitation reaction in solution. The solution must be as homogenous as possible and stabilizers must be added. If chemical

stabilizers are not added the nanoparticles will aggregate together or simply keep growing beyond the desired size range.[25,31,36,37] Tri-*n*-octylphosphine oxide was the stabilizing agent of choice for years and is still presently used.[38-42] Alternative stabilizers are sought for many reasons. One such reason is that residual tri-*n*-octylphosphine oxide diminishes optical clarity and quenches photoluminescence.[2,43,44] The particle growth mechanism inherent with the colloidal approach is partially governed by phenomena known as nucleation, growth, and Ostwald ripening.[45] In this process, the nuclei (or seeds) are made to grow in unison into larger particles. Small crystals, which are not stable, dissolve and then recrystallize onto larger, more stable particles. For this technique to be successful, the nanoparticles need to have low solubility, which can be accomplished by carefully choosing the proper solvent, pH, and stabilizing agent. Monodispersed particles are realized if nucleation is fast and the growth is slow.[1] The colloid method is fairly effective, but several important materials such as InP, GaAs, and CdSe cannot be easily prepared by this route.

The sol-gel route is generally described as a chemical route for the preparation of glasses and ceramics. Ordinarily, it involves hydrolysis and condensation of a metal–organic precursor in an appropriate solvent, with or without the use of a catalyst. As the hydrolysis and condensation reactions proceed, the viscosity of the solution increases and a gel is formed. Upon precipitating the gel, uniform particles can be obtained. For example, CdS-doped glasses can be prepared via a sol-gel route. Cadmium is introduced into the system as $Cd(NO_3)_2$ before the gel is prepared. As the gel forms, Cd^{2+} ions are trapped in place. The cadmium-doped sodium borosilicate is then heated in the presence of oxygen which converts the all the cadmium species to CdO. Cadmium oxide is then

converted to the sulfide through a sulfidation process; normally H_2S is allowed to react for an extended period of time.[46] Other semiconductor nanoparticles have been prepared in an analogous way, such as CdTe[47] and PbS.[48]

The reverse-micelle, or microemulsion, synthetic approach involves a water-in-oil microemulsion. A water-soluble metal salt is introduced into the aqueous phase of the emulsion where it is contained inside the tiny droplets. For a desired binary product, two different emulsions must be prepared. Combining the two microemulsions will lead to the formation of particles which are entirely enclosed within the aqueous-phase droplets. Thus, the size of the micelle is an important factor in determining particle diameter.[49]

Ultrasound technology is also an important tool in a growing number of research fields.[50] Sonochemical methods provide a unique mechanism, which involves extremely high local temperatures and pressures and very rapid heating and cooling rates. Acoustic cavitation, which is the formation, growth, and implosive collapse of bubbles in liquids, is the driving force of the technique. When solutions are exposed to strong ultrasound irradiation, bubbles collapse by acoustic fields in the solution. High-temperature and high-pressure fields are generated at the centers of the bubbles.[51] The local environment in these hotspots has been measured experimentally, and transient temperatures are on the order of 5000 K while pressures of greater than 1800 atm occur. These rigorous conditions are very short lived (nanoseconds). Due to this phenomenon, nanoparticles produced are stabilized by the rapid cooling rates, which can exceed 10^{10} K/s.[52]

Spray pyrolysis is a rapid and relatively simple technique that is used for the synthesis of nanoparticles at high production rates. There are two main routes for the preparation of ultra fine particles by aerosol processes. The first involves gas-to-particle

conversion, which is considered a build-up method, while the second involves liquid-to-solid particle conversion, a break-down method. In gas-to-particle conversion, particles are formed by cooling a supersaturated vapor.[53] Liquid-to-particle conversion is more common. Under precisely controlled conditions, a solution of aerosol is sprayed into a reactor where it is evaporated. Evaporation causes precipitation, which is followed by thermolysis at elevated temperatures. When successful, the spray method yields uniformly sized nanoparticles. Often, in spray pyrolysis, unless experimental conditions are thoroughly optimized, the products are dense macroporous agglomerates.[54]

Many other synthetic routes, both physical and chemical, are available to those who wish to produce nanometric semiconducting materials. Metal chalcogenides have been generated by microwave-assisted syntheses,[55,56] photochemical syntheses,[57] γ-irradiation techniques,[58] electrochemical templating,[59] molecular beam epitaxy,[60] and pulsed laser deposition among others.[61] Each of these techniques has advantages and disadvantages, and depending on the desired product, one method is better than the others. There is one synthetic approach, however, that is probably the most versatile for preparation of metal sulfide and metal oxide nanoparticles. It is the precursor route, and this synthetic tool is the basis for the research that went into this project.

Not all precursor routes are equal. The anaerobic precursor approach was largely pioneered by Bawendi and colleagues,[2,3] and their work is some of the most regularly cited work in the field of metal chalcogenide nanoparticle synthesis. Two examples of this dual precursor route will be presented to illustrate the process; the synthesis of CdSe and that of ZnS. For cadmium selenide preparation, dimethylcadmium ($Cd(CH_3)_2$) dissolved in tri-*n*-octylphosphine oxide (TOPO) and the chalcogen source, tri-*n*-

octylphosphine selenide also dissolved in TOPO are injected into hot TOPO. The rapid introduction of tri-*n*-octylphosphine selenide leads to supersaturation followed by nucleation. The CdSe particles slowly grow, and they are passivated by the phosphine oxide solvent. As for zinc sulfide, a similar pathway is involved. Dimethyl zinc and tri-*n*-octylphophine sulfide are individually dissolved in TOPO and then mutually injected into hot tri-n-octylphosphine oxide. Similar to the precipitation/colloidal route, the nucleation step should be separate from and faster than particle growth. Varying the time and temperature of the reaction governs the particle size. High quality particles can be attained from the anaerobic dual precursor method. The particle size can be tuned, the particles are monodisperse, and they have a low density of defects. The obvious downside is that toxic starting materials and solvents are required. Another difficulty is that the metal-alkyls are pyrophoric, and can only be used in controlled environments.

In the mid 1990s, O'Brien and coworkers developed a single-source precursor that eliminated the problem of dealing with air-sensitive organometallic starting materials.[38,62-64] They effectively synthesized a number of semiconducting nanoparticles from carbamate-based metallo-organic compounds. A general formula for their precursors is $(RR'NCE2)_2M$ where M denotes a divalent metal, E = S or Se, and R/R' represent typical alkyl groups. To get MS or MSe particles, the desired precursor was dissolved in tri-*n*-octylphosphine oxide and pyrolyzed at 200 °C to 300 °C. Scheme 1.1 summarizes the synthesis of the carbamate precursors and Scheme 1.2 demonstrates the conversion from precursor to nanoparticle.

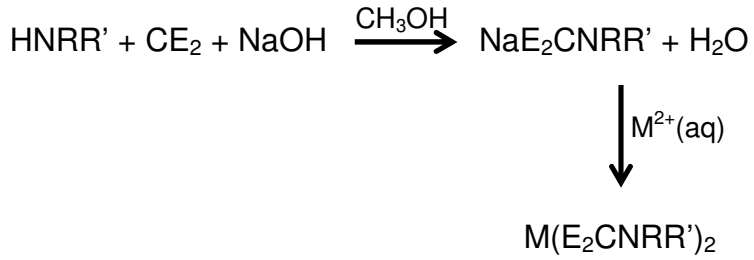

M = Cd, Zn
E = S, Se
R,R' = alkyl group

Scheme 1.1: Schematic reaction for the preparation of carbamate-based single precursors.

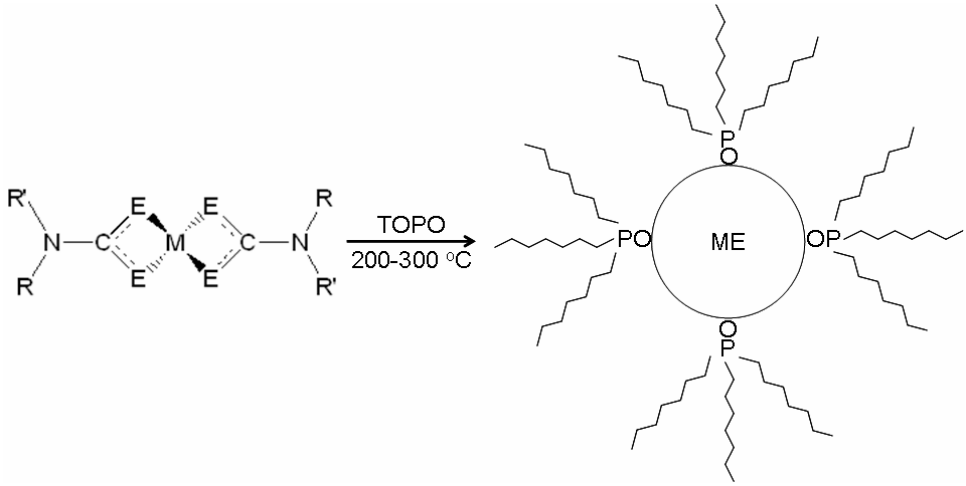

Scheme 1.2: Dithio/diseleno carbamate precursor route to metal sulfide/selenide nanoparticles. Refer to Scheme 1.1 for the definitions of M, E, R, and R'.

The carbamate single-source precursor method eliminated problems related to stoichiometry and air sensitivity, which were concerns when using the dual source anaerobic synthesis. If there is a negative to this approach, it is that the toxic tri-*n*-octylphospine oxide or some similar capping agent is required for the solvent. The necessity for such a harsh solvent comes from the fact that metal dithio- and

diselenocarbamates are quite insoluble in most standard solvents. Chapters 4 and 7 of this thesis contain information about work that is related to this issue for xanthate precursors. Ultimately, it would be ideal if a single molecule precursor was developed that did not require decomposition temperatures greater than 200 °C.

SUMMARY OF RESULTS

Part one. The synthesis of different metal xanthate compounds is easily accomplished. A wide variety of metal centers and alkyl substituents can be readily incorporated into a xanthate species. The simple fact that a transition or p-block metal xanthates will cleanly decompose to the corresponding metal sulfide at only 115 °C to 160 °C is the crux of this dissertation and the driving force of the research that went into it. The decomposition route from xanthate to sulfide is complicated. While metal identity does not appear to affect the reaction pathway to a large extent, alkyl substituents play a more significant role. The thermolysis byproducts detected suggest that as the number of carbons on the parent xanthate increases, the complexity of the decomposition also increases. There are competing reactions such as radical formation and cis-elimination. The alkyl group governs some of the resultant sulfide properties such as surface area. As the number of carbons and branching increases, the specific surface area decreases. Despite the complex nature of the decomposition process, xanthates are incredibly versatile precursors to nanocrystalline sulfide and oxide materials.

Part two. Highly luminescent ZnS nanoparticles were generated by means of the low temperature (60 °C) thermal decomposition of zinc ethylxanthate in dimethyl sulfoxide.

A high degree of size tunability (ca. 2 – 125 nm.) was achieved by varying the reaction time and the precursor concentration. The decomposition of the precursor in dimethyl sulfoxide follows a first-order pathway and particle growth follows the mechanism suggested by La Mer.[45] Zinc and cadmium sulfide particles can be prepared by solid-state, solvothermal, or sol-gel pyrolysis techniques. Intense, broad photoemission is achieved especially from ZnS-SiO_2, CdS-SiO_2, and ZnS-polystyrene nanocomposites.

Electrically conductive mirror films and polymer nanocomposites were easily prepared from the single precursor, nickel(II) ethylxanthate. Neat NiS powders and thin films can have resistivities as low as 10^{-1} to 10^{1} Ωcm. Both the NiS-polystyrene and the NiS-polyvinyl nanocomposites were prepared, and the electrical properties can be tuned based on the concentration of Ni-S units present in the plastic. With a resistivity range of 10^{1} to 10^{8} Ωcm, the polymer composites appear to be useful for many applications, such as electrodes, anti-static packing material, and electromagnetic interference-reducing media.

Ternary metal sulfides such as $CuInS_2$, $CuGaS_2$, and $CuIn_xGa_{1-x}S_2$ were grown from mixed-metal xanthate precursors at low temperature. By tailoring the alkyl substituent on the xanthate precursor, multiple synthetic routes are available to prepare $CuInS_2$. $CuInS_2$-polystyrene composites were tested for photovoltaic activity, and different light sources influenced the film conductivity. Preliminary experiments reveal that other ternary systems such as mercury cadmium sulfide and nickel cadmium sulfide are also accessible from mixed-metal xanthate precursors.

Part three. High surface area ZnS was determined to be a versatile material for the removal of pollutants from water. The nanocrystals can remove lead with an uptake capacity of 2126 mg/g, and the equilibrium allows removal to less than 2 ppb.

At a lower pH range (< 5) ZnS nanopowder can quantitatively reduce hexavalent chromium to the less toxic trivalent species. The reduction capacity is greater than 1400 mg/g. At neutral or basic pH, the reduction does not occur as easily. In fact, at pH 7-8 the reduction capacity is only about 10 mg/g.

It was also established that high surface area ZnS was effective at remediating both arsenate and arsenite from water. To avoid letting the ZnS nanocrystals escape into the same water that needs to be cleaned or from clogging the filter apparatus, they were immobilized in various matrices. The best matrix proved to be a polyvinyl substrate.

Other extractants such as CoS and iron(III) fumarate performed exceedingly well at removing arsenic from aqueous systems. An uptake capacity of 150 mg/g places iron(III) fumarate on a very short list of substances that can adsorb over 100 mg/g arsenic. All these extractants seem to be promising materials for future purification efforts.

CHAPTER 2

SYNTHESIS, CHARACTERIZATION AND APPLICATIONS OF METAL XANTHATE COMPOUNDS

An extensive array of Group I and transition metal xanthates were prepared. Comparisons within the two classifications were made regarding structure and thermal stability. For example, trends in the xanthate's infrared, Raman, and ultraviolet spectra were examined. Powder X-ray diffraction was used to compare and contrast the various crystal structures of the metal xanthate complexes. The chemical stability under conditions of elevated temperature for the various xanthic acid derivatives was monitored with thermal gravimetric analysis. The decomposition of the alkali metal xanthates was determined to be much more complicated than the corresponding transition metal compounds. Finally, by varying the substituents on the metal xanthate compounds, a protocol was established that made it possible to tailor the solubility properties for this versatile class of complexes.

INTRODUCTION

The chemistry of xanthates is dominated by the $-OCS_2^-$ functional group, since they are derivatives of the parent acid, xanthic acid, shown on the left in Figure 2.1. It is common practice to also refer to the mono esters of xanthic acid by the same name so that Figure 2.1 represents a more generic form of xanthic acid where R denotes a hydrogen, alkyl or aryl group.[1] Xanthic acid is also commonly refered to as dithiocarbonic acid (or in the general case, alkyl dithiocarbonic acid).

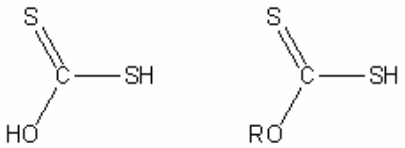

Figure 2.1: Specific and general structures of xanthic acid.

Xanthic acids can be further derivatized by replacement of the thiol proton with an R-group or metal. There are several common practices used for naming xanthic acid derivatives. Throughout this document, the nomenclature system that is used is: the metal or R-group attached to the sulfur is named first followed by the name of the R-group attached through the oxygen of the $-OCS_2^-$ functionality, and finally the root, xanthate. For example, consider the two compounds shown in Figure 2.2. In example (A), there is a methyl group connected to the sulfur and an ethyl group connected to the oxygen. Therefore, the name of compound (A) is *methyl ethylxanthate*. For structure (B), a potassium ion is associated with the sulfur and an ethyl group is attached through the oxygen. The name for (B) is *potassium ethylxanthate*.

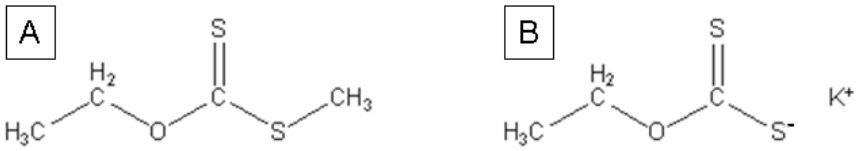

Figure 2.2: The structures of (A) methyl ethylxanthate and (B) potassium ethylxanthate.

In 1822, the first xanthates were synthesized,[2,3] but very little information was developed or provided about such compounds for nearly a century when the mining industry discovered their usefulness as mineral collectors in the 1920s.[4,5] Since that time there has been a constant incentive to acquire as much detail about these compounds as possible. After all these years, the mining and mineral industry still uses xanthate compounds for collection and flotation purposes,[6-9] but there are other applications for these dithiocarbonate species. In fact, xanthic acid derivatives have earned quite a deal of attention for use in various analytical processes. The presence of carbon disulfide in soils or other media can be accurately determined with copper xanthate.[10,11] Xanthates have also been used to detect, separate, and quantitate alcohols.[12-14] Another important category of xanthate-based compounds are cellulose xanthates. While these compounds have been studied from various angles, their role in the fabrication of rayon is of primary importance.[15-17]

The most recent uses discovered for xanthates are their role in nanotechnology and colloid chemistry. Their function as capping agents for nanoparticles has been reported.[18] As stabilizing agents, xanthates are counterparts to thiols, amines, and carboxylates but differ from them in terms of stability. The relative instability introduces new properties to the capping agent repertoire, which opens up new possibilities.[19] Finally, metal xanthates have proven to be versatile precursors for metal sulfide

nanomaterials. High quality CdS,[20] ZnS,[21] and Bi_2S_3[22] nanostructures have all been prepared from dithiocarbonate starting materials. The preparation of metal sulfide nanostructures and nanocomposites are the focus of the remaining chapters of this thesis. However, this chapter focuses on the preparation of the xanthate precursors along with basic characterization of these useful compounds.

EXPERIMENTAL

Materials. Reagent grade lithium hydroxide (LiOH), sodium hydroxide (NaOH), potassium hydroxide (KOH), rubidium hydroxide (RbOH), cesium hydroxide (CsOH), silver nitrate ($AgNO_3$), cadmium chloride 2½ hydrate ($CdCl_2 \cdot 2½H_2O$), cobalt(II) chloride hexahydrate ($CoCl_2 \cdot 6H_2O$), copper(II) chloride dihydrate ($CuCl_2 \cdot 2H_2O$), iron(II) sulfate heptahydrate ($FeSO_4 \cdot 7H_2O$), indium(III) chloride ($InCl_3$), nickel(II) sulfate hexahydrate ($NiSO_4 \cdot 6H_2O$), and zinc sulfate heptahydrate ($ZnSO_4 \cdot 7H_2O$) were obtained commercially and used as received without further purification. A wide variety of organic compounds with alcohol, amine, or carboxylate functional groups were used in this investigation: methanol, ethanol, n-propanol, iso-propanol, n-butanol, sec-butanol, iso-butanol, t-butanol, n-pentanol, n-hexanol, n-octanol, 2-methoxyethanol, 2-ethoxyethanol, ethylene glycol, glycerine, *d*-glucose, diethylene glycol monomethyl ether, triethylene glycol monomethyl ether, triethanolamine, dimethylethanolamine, 1-dimethylamine-2-propanol, glycolic acid, choline chloride, choline hydroxide, 7-amino-1,3-naphthalene-disulfonic acid, Triton X-100, Brij 35, activated carbon, Amberlite IRA-410 CL ion exchange resin, polyvinyl alcohol, sodium isethionate, butylated hydroxyl toluene, and taurine. Finally, tetramethyl ammonium hydroxide, carbon disulfide, potassium ethylxanthate, potassium

isopropylxanthate, and potassium n-butylxanthate were purchased and used as received. All water used throughout the experiment was deionized to a resistivity of 18.1 MΩcm.

Synthesis of group I ethylxanthates. Group I metal ethylxanthates were prepared by mixing the metal hydroxide, carbon disulfide, and ethanol in a stoichiometric ratio. For instance, NaOH (6.00 g, 150 mmole) was dissolved in water (200 ml) and placed in an ice bath. Ethanol (6.91 g, 150 mmole) and carbon disulfide (11.45 g, 150 mmole) were individually added to the chilled hydroxide solution. The three reagents were allowed to mix until the CS_2 had completely reacted (roughly 24 hours). Water was evaporated with a steady stream of air, and solid sodium ethylxanthate was obtained as orange crystals in a yield of (20.8 g, 96.0 %). The crystals were isolated, sparingly washed with cold water, and stored in a glass bottle at room temperature and remained indefinitely stable. The other salts were obtained in a similar manner, substituting the corresponding metal hydroxide for NaOH. The reaction failed to produce lithium ethylxanthate. The dried and powdered products are yellow solids regardless of the metal used. Scheme 2.1 contains the balanced reaction for the preparation of alkali metal ethylxanthates and Table 2.1 contains specific reaction data for the group I ethylxanthate syntheses.

$$MOH(aq) + CH_3CH_2OH(l) + CS_2(l) \rightarrow MS_2COCH_2CH_3(aq) + H_2O(l)$$

Scheme 2.1: Governing reaction for the preparation of Group I etylxanthates, where M represents Li, Na, K, Rb, and Cs respectively.

Table 2.1: Specific reaction data for the synthesis of group I ethylxanthate complexes.

Target Product	Mass MOH (g)	Mass EtOH (g)	Mass CS_2 (g)	Yield (product, %)	Color	Actual Product ID
$Li[S_2COCH_2CH_3]$	6.016	6.623	10.900	5.195 g 28.36 %	White	Li_2CO_3
$Na[S_2COCH_2CH_3]$	6.010	6.902	11.682	20.78 g 96.02 %	Yellow	$Na[S_2COCH_2CH_3]$
$K[S_2COCH_2CH_3]$	6.008	4.933	8.138	16.79 g 97.80 %	Yellow	$K[S_2COCH_2CH_3]$
$Rb[S_2COCH_2CH_3]$	6.000	2.484	3.780	9.888 g 96.32 %	Yellow Orange	$Rb[S_2COCH_2CH_3]$
$Cs[S_2COCH_2CH_3]$	6.002	1.746	2.700	8.604 g 95.45 %	Yellow Orange	$Cs[S_2COCH_2CH_3]$
$N(CH_3)_4$- $[S_2COCH_2CH_3]$	5.998	3.032	5.008	11.73 g 91.22 %	Yellow	$N(CH_3)_4$- $[S_2COCH_2CH_3]$

Synthesis of various potassium alkylxanthate compounds. To vary the substituent on the xanthate compound, a simple replacement for ethanol in the reaction above is all that is required. An example would be the preparation of potassium n-octylxanthate. Potassium hydroxide (8.42 g, 150 mmole) was dissolved in 200 ml of water and the solution was cooled with an ice bath. To the hydroxide solution, both n-octanol (19.53 g, 150 mmole) and carbon disulfide (11.45 g, 150 mmole) were slowly added. The mixture was stirred until all the CS_2 was consumed. The aqueous potassium n-octylxanthate was dried, purified, and stored until needed. A generalized schematic for the preparation of

any potassium alkylxanthate can be found in Scheme 2.2 and Table 2.2 lists important data relevant to each individual reaction. Some yields were not determined due to various reasons such as the extreme hygroscopic nature of the compound. With only a few exceptions, the synthetic process used produced the desired compounds with yields in the range of 75-100 %.

$$xKOH(aq) + R(OH)_x(l,s) + xCS_2(l) \rightarrow (KS_2CO)_xR(aq) + xH_2O(l)$$

Scheme 2.2: Generalized balanced reaction for the preparation of various potassium alkylxanthate compounds. R can be whichever substituent is desired. NOTE: Often it is preferred that, in a compound with more than one –OH functional group, only one of the hydroxides gets converted into a xanthate. If such a situation arises, using one equivalent of KOH and CS_2 will generate the target product.

Table 2.2: Specific reaction data for the synthesis of potassium alkylxanthate and alkylcarbamate complexes.

Product	Mass KOH (g)	Mass R-OH/ R-NH_2 (g)	Mass CS_2 (g)	Yield (mass) (%)	Color
potassium methylxanthate	10.33	29.12	13.70	25.85 g 96.01 %	yellow
potassium ethylxanthate	6.008	4.933	8.138	16.79 g 97.80 %	yellow
potassium n-propylxanthate	5.002	5.358	6.784	14.64 g 94.23 %	yellow
potassium iso-propylxanthate	NA, commercial product used				yellow
potassium n-butylxanthate	NA, commercial product used				yellow
potassium iso-butylxanthate	4.968	6.563	6.737	15.87 g 95.18 %	yellow
potassium sec-butylxanthate	5.013	6.630	6.911	13.48 g 80.12 %	yellow
potassium t-butylxanthate	5.000	6.609	6.903	12.79 g 76.21 %	yellow
potassium n-pentylxanthate	5.01	7.89	6.80	16.8 g 92.9 %	yellow
potassium n-hexylxanthate	5.02	9.14	6.85	17.04 g 88.01 %	yellow

Product	Mass KOH (g)	Mass R-OH/ $R-NH_2$ (g)	Mass CS_2 (g)	Yield (mass) (%)	Color
potassium n-octylxanthate	18.079	42.058	24.448	67.06 g 85.14 %	yellow
potassium methoxyethylxanthate	3.600	4.880	5.498	11.23 g 92.00 %	yellow
potassium ethoxyethylxanthate	2.50	4.02	3.41	8.34 g 91.5%	yellow
potassium 2-methylthioethylxanthate	9.015	14.907	12.228	29.72 g 89.63 %	yellow
potassium 2-hydroxyethylxanthate	5.39	2.98	7.30	15.9 g 94.1 %	yellow
potassium 1,3-dihydroxyisopropylxanthate	2.49	4.09	3.42	8.26 g 90.2 %	yellow
potassium (*d*-glucose)xanthate	18.006	28.946	28.008	NA	brown
potassium 2-(2-methoxyethoxy)ethylxanthate	17.99	38.52	24.99	66.88 g 89.00 %	yellow
potassium 2-(2-(2-methoxyethoxy)ethoxy)ethylxanthate	18.02	52.69	24.50	79.13 g 88.49 %	yellow
potassium 2-bis(hydroxyethyl)amino ethylxanthate	14.99	39.84	20.28	NA	yellow
potassium 2-(dimethylamino) ethylxanthate	3.67	5.83	4.98	NA	light brown
potassium 2-dimethylamino isopropylxanthate	5.01	11.93	6.78	NA	light brown
potassium carboxymethylxanthate	9.88	6.70	6.71	18.2 g 90.3 %	yellow
potassium 2-sulfoethyl carbamodithioate	30.02	33.53	18.70	NA	yellow
potassium BHTxanthate	3.02	11.86	4.10	1.44 g 8.00 %	brown
potassium choline xanthate	4.99	10.80	6.78	NA	yellow
potassium 6,8-disulfonaphthalen-2-yl carbamodithioate	3.33	20.26	4.52	NA	yellow

Synthesis of transition metal ethylxanthates. Transition metal ethylxanthate complexes are not water-soluble. A simple precipitation reaction between an aqueous transition metal salt and a solution of potassium ethylxanthate yields the transition metal complex in a nearly quantitative fashion. As an example, zinc ethylxanthate was generated by reacting an aqueous solution of zinc sulfate and potassium ethylxanthate in a stoichiometric fashion as described in the literature.[1] Typically, $ZnSO_4 \bullet 7H_2O$ (5.760 g, 20.0 mmol) was dissolved in water (150 mL) and $KS_2COCH_2CH_3$ (6.422 g, 40.0 mmol) was dissolved in a similar amount of water. The potassium ethylxanthate solution was slowly poured into the zinc sulfate solution immediately generating the white zinc ethylxanthate, $Zn(S_2COCH_2CH_3)_2$, precipitate in nearly quantitative yield (6.017 g, 97.6%). The solid was collected by vacuum filtration and washed thoroughly with water. The zinc ethylxanthate was stored in a sealed glass bottle away from light and remained stable for several months. Carbon and hydrogen elemental analysis (Found: C, 23.3; H, 3.2. $C_6H_{10}O_2S_4Zn$ requires C, 23.4; H, 3.3 %). Scheme 2.3 is a series of reactions that illustrate how various transition metal ethylxanthates could be prepared.

$$M^+(aq) + KS_2COCH_2CH_3(aq) \rightarrow MS_2COCH_2CH_3(s) + K^+(aq)$$

$$M^{2+}(aq) + 2KS_2COCH_2CH_3(aq) \rightarrow M(S_2COCH_2CH_3)_2(s) + 2K^+(aq)$$

$$M^{3+}(aq) + 3KS_2COCH_2CH_3(aq) \rightarrow M(S_2COCH_2CH_3)_3(s) + 3K^+(aq)$$

Scheme 2.3: The synthesis of mono-, di-, and tri-valent transition metal ethylxanthate complexes.

Most transition metal alkylxanthates are insoluble in water, and they can be prepared in an analogous way to the ethyl complexes discussed above. However, if the

R-group on the xanthate ligand is hydrophilic enough, the resulting product from the reaction of an aqueous metal salt and the potassium alkylxanthate of choice will not result in the formation of a solid. In such cases, isolating the transition metal xanthate is complicated. Table 2.3 contains information about specific reactions between aqueous transition metal salts and various alkylxanthates. Those not in the table are reported elsewhere in this thesis or were not determined. For instance, the yields of the transition metal xanthates that are particularly soluble in water are not precisely known due to the difficulty of isolating them.

Table 2.3: Specific reaction data for the synthesis of selected transition metal alkylxanthates.

Product	**Mass and ID metal salt**	**Mass Metal alkyxanthate**	**Color**	**Yield (%) ± 1.0 %**
cadmium ethylxanthate	6.865 g $CdCl_2 \cdot 2½H_2O$	9.625 g	pale yellow	95.3
cobalt ethylxanthate	5.000 g $CoCl_2 \cdot 6H_2O$	6.737 g	dark green	88.8
copper ethylxanthate	5.111 g $CuCl_2 \cdot 2H_2O$	9.618 g	yellow orange	98.0
iron(II) ethylxanthate	8.681 g $FeSO_4 \cdot 7H_2O$	10.01 g	brown	87.0
indium(III) ethylxanthate	2.044 g $InCl_3$	4.420 g	white	92.1
mercury(II) ethylxanthate	5.011 g $Hg(NO_3)_2$	4.949 g	dirty white	NA
nickel(II) ethylxanthate	11.885 g $NiCl_2 \cdot 6H_2O$	16.04 g	reddish brown	98.8
silver(I) ethylxanthate	5.297 g $AgNO_3$	4.998 g	yellow orange	97.0
zinc methylxanthate	2.876 g $ZnSO_4 \cdot 7H_2O$	2.926 g	white	99.1
zinc ethylxanthate	5.760 g $ZnSO_4 \cdot 7H_2O$	6.017 g	white	97.6
zinc n-propylxanthate	2.875 g $ZnSO_4 \cdot 7H_2O$	3.486 g	white	98.3

Product	Mass and ID of metal salt	Mass potassium alkyxanthate	Color	Yield (%) ± 1.0 %
zinc iso-propylxanthate	2.876 g $ZnSO_4 \cdot 7H_2O$	3.485 g	white	98.8
zinc n-butylxanthate	2.881 g $ZnSO_4 \cdot 7H_2O$	3.774 g	white	97.6
zinc iso-butylxanthate	2.851 g $ZnSO_4 \cdot 7H_2O$	3.769 g	white	97.1
zinc sec-butylxanthate	2.876 g $ZnSO_4 \cdot 7H_2O$	3.759 g	white	88.3
zinc t-butylxanthate	2.879 g $ZnSO_4 \cdot 7H_2O$	3.761 g	white	93.2
zinc n-pentylxanthate	5.006 g $ZnSO_4 \cdot 7H_2O$	7.046 g	white	98.0
zinc n-hexylxanthate	5.000 g $ZnSO_4 \cdot 7H_2O$	7.526 g	white	85.1
zinc n-octylxanthate	2.879 g $ZnSO_4 \cdot 7H_2O$	4.895 g	white	95.2
zinc benzylxanthate	2.875 g $ZnSO_4 \cdot 7H_2O$	4.446 g	white	91.3

Characterization. The UV adsorption spectra of the xanthate compounds were measured with a Perkin-Elmer Lamda EZ201 spectrometer. Spectra were measured at 200 nm/min over various wavelength ranges in a quartz cuvette.

For infrared spectroscopic measurements, approximately 10 mg of the samples were mixed with roughly 100 mg FTIR-grade potassium bromide and the blend was finely ground. Spectra in the 4000-400 cm^{-1} region were collected by diffuse reflectance of the ground powder with a Nicolet Magna-IR 750 spectrometer. Normally, 128 scans were recorded and averaged for each sample (4.0 cm^{-1} resolution) and the background was automatically subtracted.

Raman spectroscopy was also used to characterize some of the xanthate compounds. A Nicolet NXR 9610 Raman Spectrometer was used for the analysis and a

neat pressed pellet was used for each measurement. Typically, 32 scans were averaged in the 4500-50 cm^{-1} range at a resolution of 4.0 cm^{-1}.

Powder X-ray diffraction (XRD) measurements were obtained on a Bruker AXS D8 Advance diffractometer using Cu Kα radiation with an acceleration voltage of 40 kV and current flux of 30 mA. The diffractograms were recorded for a 2θ range of 5-70° with a step size of 0.02° and a counting time of 18 seconds per step. All the XRD patterns were collected at ambient temperature, and the phases were identified using the ICDD database.[23] The peaks were profiled with a Pearson 7 model using Topas P version 1.01 software.[24] The profiles of the standard and the sample were put into the Win-Crysize program version 3.05, which uses the Warren-Averbach evaluation method to determine crystallite size.[25,26]

Thermogravimetric analysis (TGA) was performed on the complexes at a rate of 2.0°/min from room temperature to 600 °C using a Seiko Instruments Exstar 6200. None of the xanthates melt congruently, but a well behaved decomposition curve was observed for most of them.

RESULTS AND DISCUSSION

Structure and thermal stability of alkali metal ethylxanthates. The ethylxanthate salts for lithium, sodium, potassium, rubidium, and cesium were prepared according to Scheme 2.1. All the compounds were successfully synthesized except for the lithium salt. Instead of making lithium ethylxanthate ($LiS_2COCH_2CH_3$), the reaction of LiOH, CS_2, and ethanol produces phase-pure Li_2CO_3 (Refer to Figure 2.3). The lithium carbonate is in the monoclininc phase and matches the crystal structure for Zabuyelite.

There is very little in the literature relevant to lithium ethylxanthate. It can be prepared in a less coordinating solvent than water.[27] Presumably, the nucleophilic oxygen in a water molecule catalyzes the decomposition. Additionally, the ionic radius of Li^+ is much too small to stabilize the large ethylxanthate anion. The powder X-ray diffraction patterns for the effectively formed ethylxanthates can be seen in Figure 2.4. The sodium and

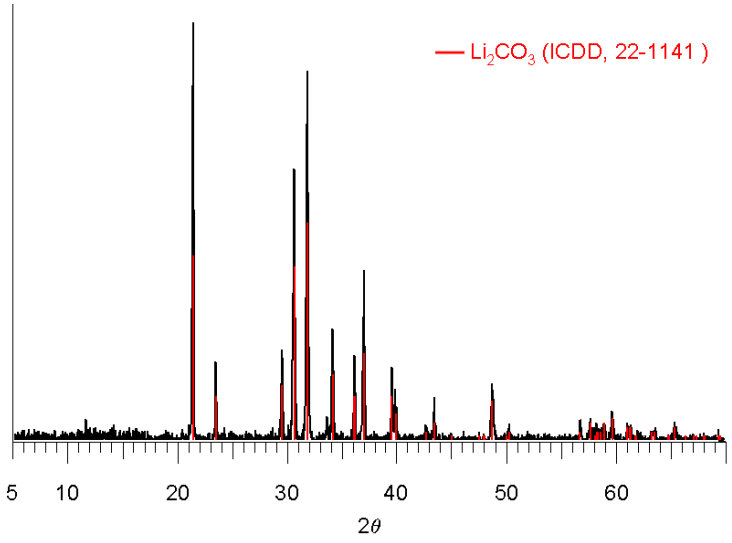

Figure 2.3: Powder X-ray diffraction pattern of the product formed from the reaction of LiOH, CS_2, and ethanol. The pattern matches monoclinic Li_2CO_3.

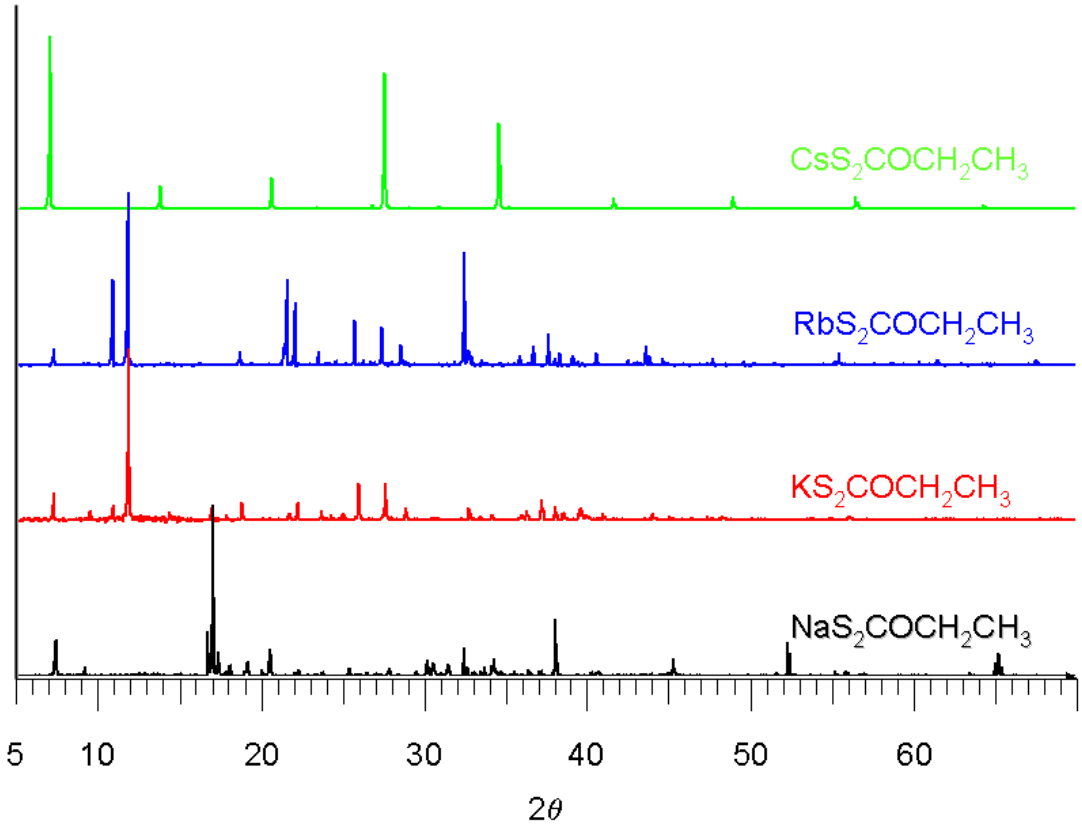

Figure 2.4: X-ray diffraction patterns for sodium, potassium, rubidium, and cesium ethylxanthate.

potassium ethylxanthate structures match known phases: sodium ethylxanthate, ICDD 08-0504 and potassium ethylxanthate, ICDD 09-0700, respectively. There were no known patterns present in the International Centre for Diffraction Data database for either rubidium or cesium ethylxanthate. It is clear from the individual reflection patterns that all four compounds are highly crystalline and it appears that rubidium and potassium ethylxanthate are isostructural. The relative heights of the reflections in the Rb and K patterns are not identical, but the peak placements are superimposable. It had been proposed long ago that potassium ethylxanthate and rubidium ethylxanthate possessed similar crystal structures,[28] and this result validates that claim.

The ultraviolet-visible absorption spectra were collected for $NaS_2COCH_2CH_3$, $KS_2COCH_2CH_3$, $RbS_2COCH_2CH_3$, and $CsS_2COCH_2CH_3$ to explore the influence of the cation on electronic structure (Figure 2.5). There is very little variation from one spectrum to the next. The data were normalized according the intensity of the peak at 300 nm. There was no red or blue shift in that peak position regardless of the cation. However, the signals at 206 and 225 nm grew as the size of the cation increased. The growth in peak intensity at the lower wavelengths is slightly misleading. It appears that

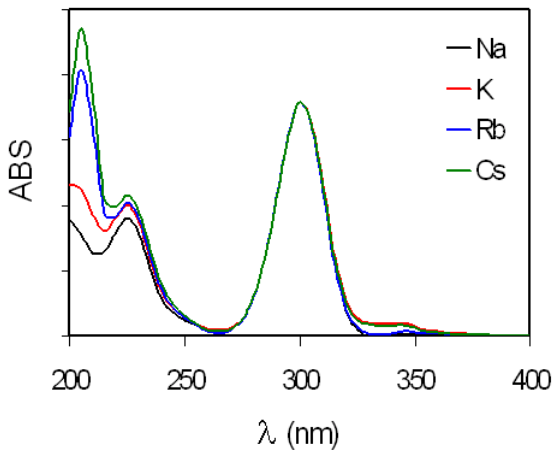

Figure 2.5: Absorption spectra for 4×10^{-5} M sodium, potassium, rubidium, and cesium ethylxanthate. The signals were normalized to the 300 nm peak in the potassium xanthate spectrum.

there is a slight, but constant, drift in the spectrometer. For example, the data shown in Figure 2.5 correspond to measuring the xanthates from smallest cation to largest. If identical solutions are made and measured the next day, and the measurement order is reversed (largest to smallest), the growth phenomenon is greatly diminished. This suggests that the transitions in the range of 200-400 nm are due predominantly to the ligand. A previous study on the ultraviolet absorption of various potassium alkylxanthate compounds claimed that the organic substituent connected to the xanthate played no

appreciable role in the electronic transitions in the region of interest.[29] The $-OCS_2^-$ functional group appears to be responsible for the signals at 206, 225, and 300 nm since neither alkyl group or metal ion influences the peak profiles. The signals at higher energy are likely due to the OCS group while the signal at lower energy arises from the SCS.

Potassium and sodium ethylxanthate have been thoroughly studied using infrared spectroscopy.[30-35] As with other characterization techniques, much less, if any, has been done with rubidium and cesium ethylxanthate. The infrared spectra of the four alkali xanthates are presented in Figure 2.6. As expected, there is little distinction from one spectrum relative to the others since the metal-sulfur stretches occur at lower energy. For this reason, Raman spectroscopy is better suited to examine the subtle differences of the ethylxanthates. The M-S region of interest is roughly around 300-400 cm^{-1}. The Raman spectra were collected for each ethylxanthate, and like the IR results, there was no significant difference for wavenumbers greater than 400 cm^{-1}. Figure 2.7 shows how the metal-sulfide motions vary with metal ion. While the difference is not completely obvious, there is a trend for both peaks. There is a small shift to lower energy as cation mass/size increases. This trend makes sense from both mass and size considerations. While there are more definite and straightforward ways of distinguishing the potassium salt from the sodium salt, for instance, Raman spectroscopy could be used to identify one ethylxanthate from the other in a quick, non-destructive way.

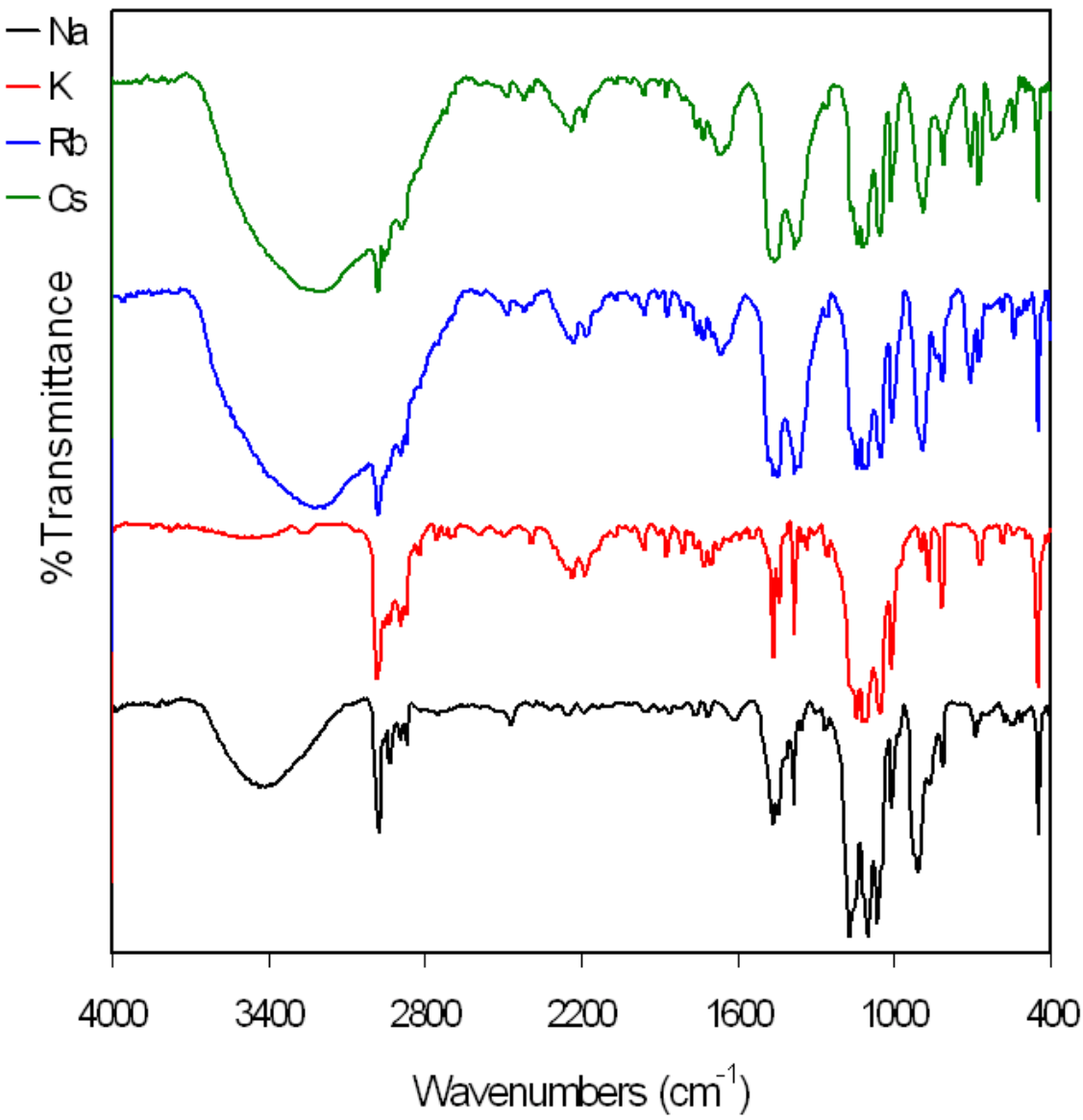

Figure 2.6: Infrared spectra of cesium, rubidium, potassium, and sodium ethylxanthate.

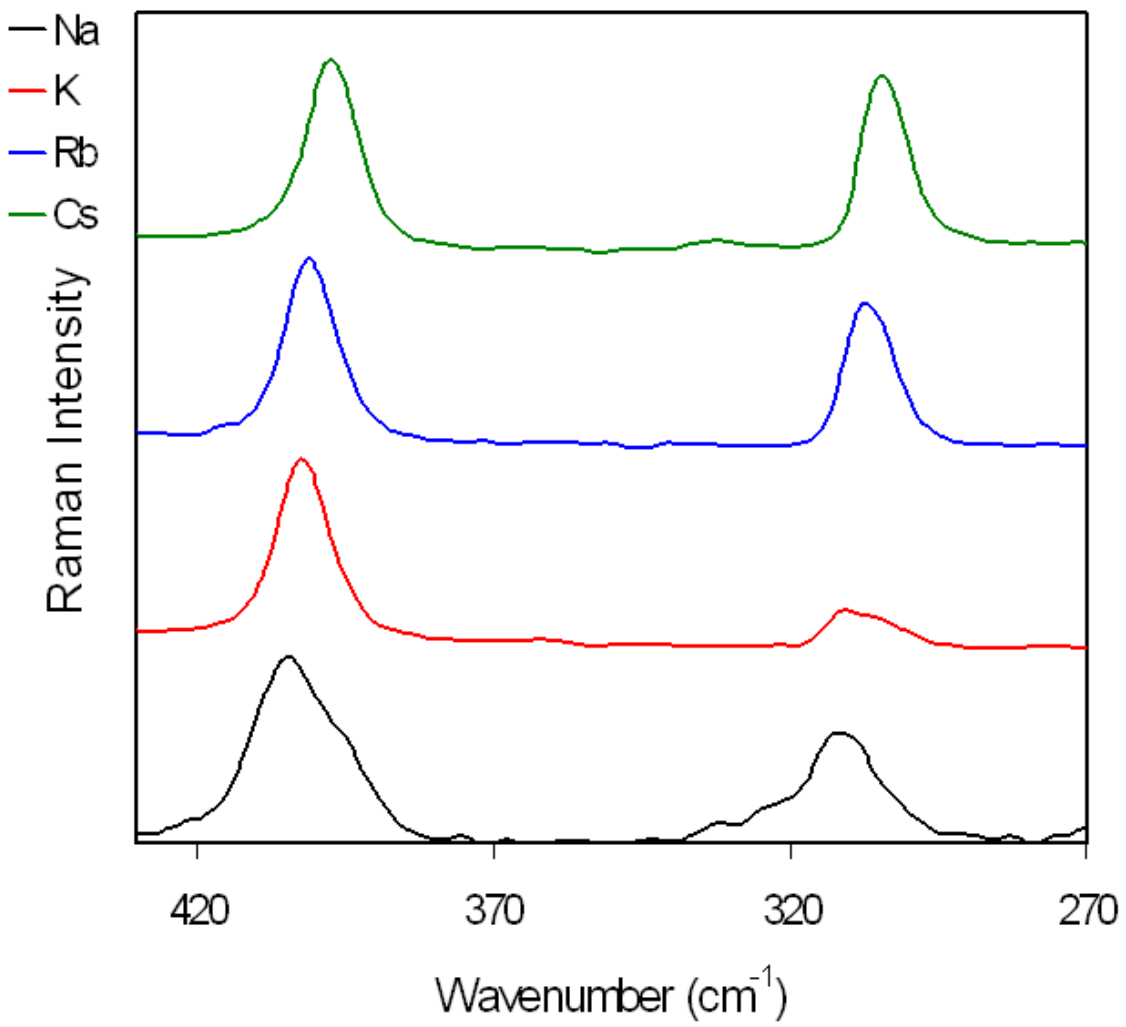

Figure 2.7: Raman spectra for cesium, rubidium, potassium, and sodium ethylxanthate for a narrow range of energy (430-275 cm^{-1}).

Thermal stability was monitored by thermal gravimetric analysis in air. The thermal gravimetric analysis traces can be seen in Figure 2.8. The decomposition patterns are similar for each ethylxanthate complex. As one would expect, the overall percentage of mass loss for the heavier xanthates was less than for the lighter species except for the fact that the sodium and potassium decomposition product masses were reversed. The degradation of sodium ethylxanthate clearly follows a different pathway

than the other three. There are two obvious steps in the sodium xanthate decomposition while just one for the others. The eventual decomposition products for each salt were examined by a combination of the mass values yielded from the thermal studies, spectroscopy, and X-ray powder diffraction. In all four cases, there is a mixture of solid decomposition products such as metal di- and trithiocarbonates, sulfides, and sulfates. The mixture is complicated for all four compounds. There was a study done previously that describes what happens when sodium ethylxanthate is thermally decomposed in a nitrogen environment,[36] and a comparison of the two suggests that the presence of oxygen has a tremendous influence on the elimination and eventual products. Table 2.4 contains information about the decomposition of each of the four Group I ethylxanthate salts.

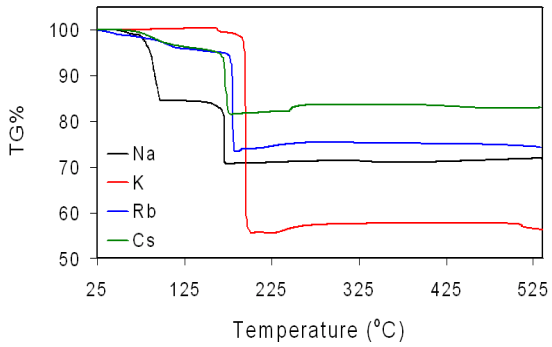

Figure 2.8: Thermal analysis traces for sodium, potassium, rubidium, and cesium ethylxanthate.

Table 2.4: Thermal stability and decomposition products for sodium, potassium, rubidium, and cesium ethylxanthate.

	Major Decomposition Step Temperature(s) (°C)	Decomposition Step Percentage Mass Loss
$NaS_2COCH_2CH_3$	97, 169	14.4, 13.4
$KS_2COCH_2CH_3$	195	44.3
$RbS_2COCH_2CH_3$	180	26.6
$CsS_2COCH_2CH_3$	170	18.4

Structure and thermal stability of transition metal ethylxanthates. As described in the experimental portion of this chapter, a simple precipitation reaction between certain aqueous transition metals and aqueous potassium ethylxanthate will result in the quantitative formation of the transition metal ethylxanthate complex. The reaction will not work for all transition metals; however it does for a significant number of them. Some basic information about Co(II), Ni(II), Cu(II), Fe(II), Zn(II), Ag(I), Cd(II), In(III), and Hg(II) will be presented. The crystal structures for nickel(II) ethylxanthate,[37] zinc ethylxanthate,[38] mercury(II) ethylxanthate,[39] and cadmium ethylxanthate[40] have been published. The structures for Fe(III) ethylxanthate[41] and Co(III) ethylxanthate[42] have also been reported, but a simple literature search for the divalent versions was unsuccessful. So far there has not been a thorough comparison of the structures for the divalent ethylxanthate compounds. Figure 2.9 contains the powder X-ray diffraction patterns for numerous metal(II) ethylxanthate salts. All of the complexes show a high degree of crystallinity. Interestingly, each compound has a distinct diffraction pattern,

which means that no two ethylxanthates are formally isostructural. This is unusual for a family of related divalent 3*d* metal salts. The crystal structure database did not have entries for the relevant substances.

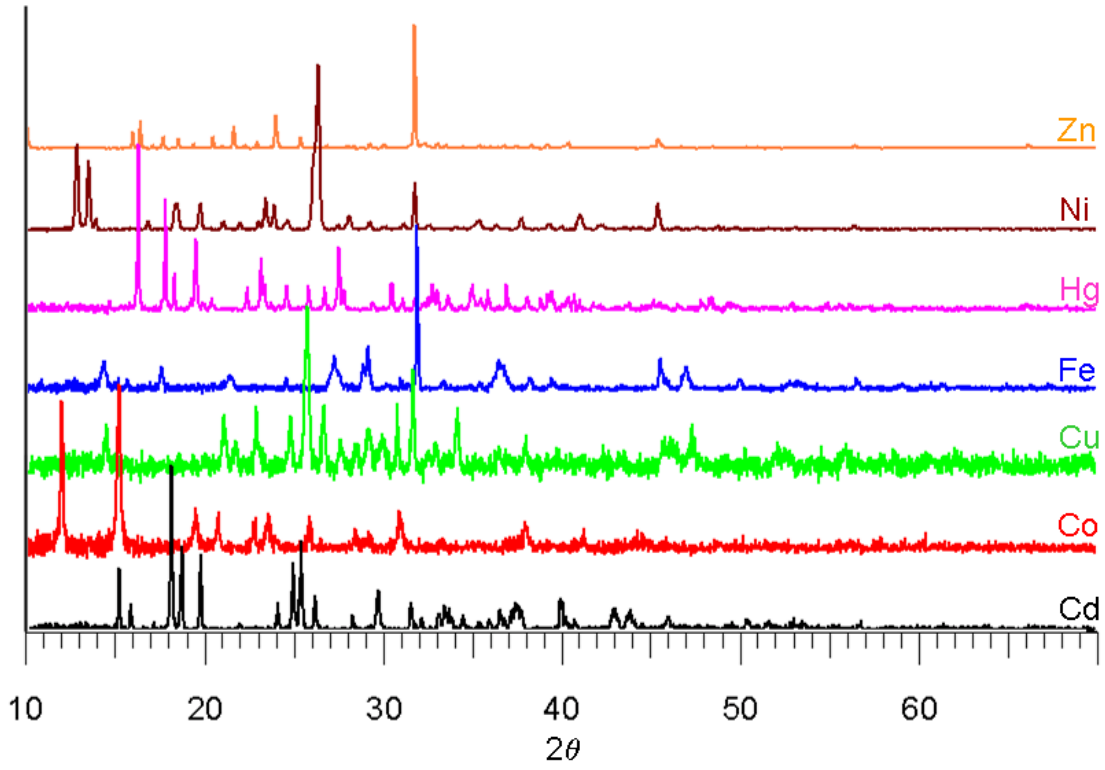

Figure 2.9: X-ray powder diffraction patterns for several metal(II) ethylxanthate complexes.

Since there were no database entries to positively identify the synthesized compounds, other characterization techniques were employed. Xanthic acid derivatives have very distinct infrared spectra. Therefore, the product of each reaction between a given water-soluble metal salt and potassium ethylxanthate was tested via infrared spectroscopy. A few representative infrared spectra are shown in Figure 2.10. The peak identification for transition metal ethylxanthates has been established.[34,35,43,44] The spectra shown in Figure 2.8 match those from the literature. The divalent cadmium and

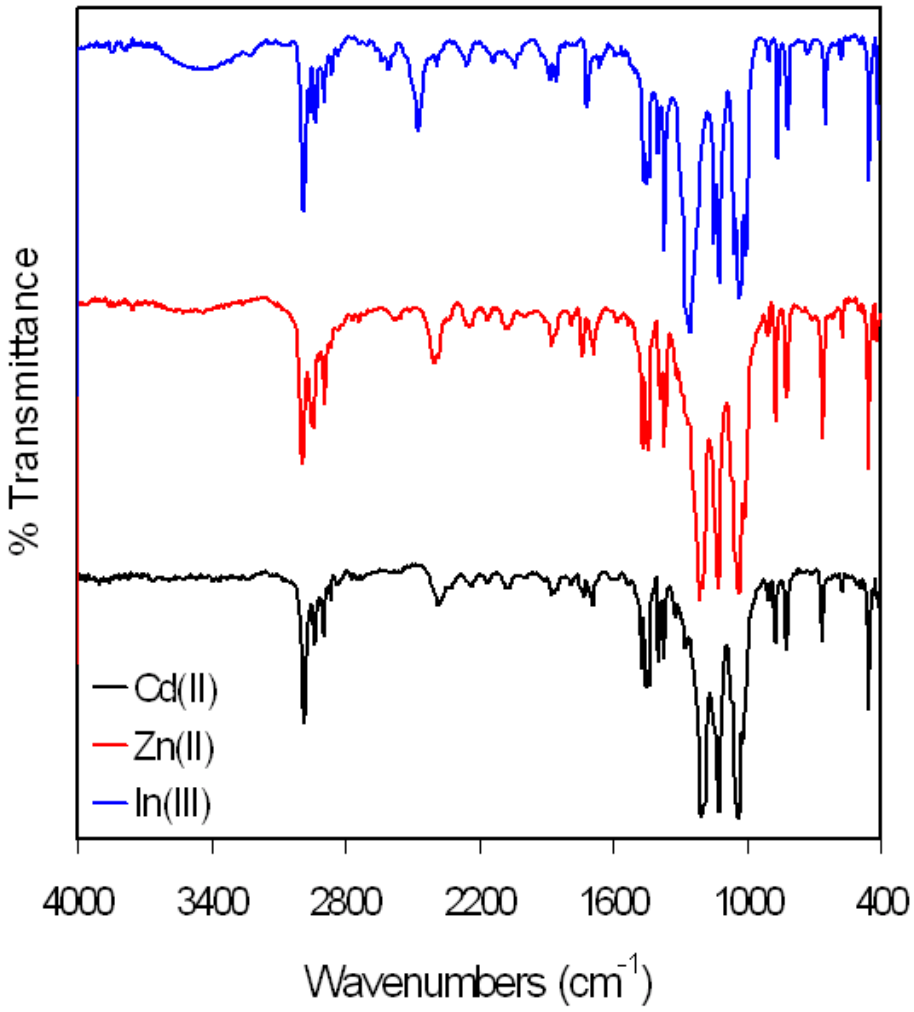

Figure 2.10: Infrared spectra for two transition metal ethylxanthates, $Cd(S_2COCH_2CH_3)_2$ and $Zn(S_2COCH_2CH_3)_2$, and a trivalent p-block metal ethylxanthate, $In(S_2COCH_2CH_3)_3$.

zinc ethylxanthate profiles are nearly identical, while the trivalent indium ethylxanthate spectrum contains some subtle distinctions. The biggest difference is that the peak at 1205 cm^{-1} in the cadmium and zinc xanthate spectra moves to 1250 cm^{-1} for the indium(III) complex. Raman spectroscopy is very useful for measuring metal-sulfur linkages. Raman spectra were measured for the all the transition metal ethylxanthates

(that did not burn during measurement). More infrared and Raman spectroscopy data will be given throughout this document where appropriate.

The thermal stability of each transition metal ethylxanthate was observed using thermalgravimetric analysis. Unlike the Group I metal complexes where multiple solid species are formed from the thermal treatment, the decomposition for the d- and p-block ethylxanthate compounds proceeds in a much cleaner manner. While the thermal decomposition will be discussed in more detail in later chapters, the thermal gravimetric analysis traces for a characteristic sample is included in Figure 2.11. Invariably, the solid product formed from the initial thermal elimination is a metal sulfide. If the ethylxanthate is burned in air, the metal sulfide will oxidize at high temperature to the sulfate or oxide. Eventually, even the sulfate compounds will convert to the oxide if high enough temperatures are reached.

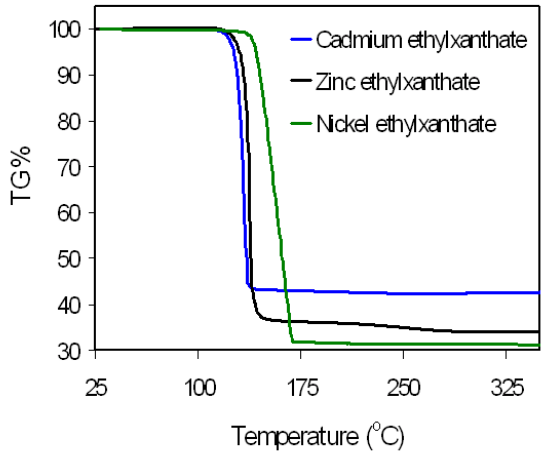

Figure 2.11: Thermalgravimetric analysis traces for cadmium ethylxanthate, zinc ethylxanthate, and nickel(II) ethylxanthate.

The decomposition from ethylxanthate to sulfide occurs in one rapid step. The thermal decomposition initiation temperatures for cadmium, zinc, and nickel(II)

ethylxanthate are 132 °C, 137 °C, and 151 °C, respectively. All of the d- and p-block ethylxanthate compounds that were made have an elimination temperature in the range from 115 °C to 160 °C.

Tailoring the xanthate substituent for specific purposes. Transition metal ethylxanthates have limited solubility in standard solvents such as water, alcohols, acetone, toluene, hexanes, etc. Furthermore, the xanthate ligand will decompose if the solvent pH strays too far from neutrality. Table 2.5 contains solubility information related to several ethylxanthate compounds. With the lone exception of nickel(II) ethylxanthate, the solubility options are poor and very limited.

Table 2.5: Solubiliy of three ethylxanthate salts.

	$Ni(S_2COCH_2CH_3)_2$	$Zn(S_2COCH_2CH_3)_2$	$Cd(S_2COCH_2CH_3)_2$
Water	Insoluble	Insoluble	Insoluble
Methanol	Sparingly Soluble	Sparingly Soluble	Sparingly Soluble
Ethanol	Slightly Soluble	Slightly Soluble	Sparingly Soluble
Toluene	Soluble	Sparingly Soluble	Insoluble
Hexanes	Slightly Soluble	Insoluble	Insoluble
Acetone	Soluble	Slightly Soluble	Insoluble
Methylene chloride	Soluble	Insoluble	Insoluble
Dimethyl sulfoxide	Soluble	Soluble	Soluble

To change the solubility properties of a xanthate compound, all one needs to do is tailor the substituent. For example, to improve solubility in an organic solvent such as hexanes, the alkyl chain was lengthened. To improve solubility in water, a hydrophilic group, such as a hydroxyl was added to the xanthate. A series of different R-group substituted xanthates were made for both zinc and cadmium. Table 2.6 shows the substituents that were expected to improve solubility in non-polar or weakly polar aprotic solvents, such as hexanes, toluene, and methylene chloride. Table 2.7 lists the substituents that were thought to enhance solubility in water or other protic solvents.

Table 2.6: Substituent effect on solubility for aprotic solvents.

Parent Compound of Substituent	**Solubility (Relative to R = ethyl)**
n-Propanol	Similar
iso-Propanol	Similar
n-Butanol	Slightly Improved
iso-Butanol	Similar
sec-Butanol	Similar
t-Butanol	Similar
n-pentanol	Improved
n-hexanol	Improved
n-octanoal	Improved
Benzyl alcohol	Improved
Butylated hydroxyl toluene	Slightly improved

Table 2.7: Substituent effect on solubility for protic solvents.

Parent Compound of Substituent	Solubility (Relative to R = ethyl)
Methoxyethanol	Slightly Improved
Ethoxyethanol	Slightly Improved
Ethylene glycol	Improved
Glycerine	Improved
d-Glucose	Improved
Diethylene glycol monomethyl ether	Slightly Improved
Triethylene glycol monomethyl ether	Slightly Improved
Triethanoloamine	Improved
Dimethylethanolamine	Improved
Glycolic acid	Improved
Choline Chloride	Slightly Improved
Triton X-100	Improved
Brij 35	Improved
Isethionic acid	Improved
Taurine	Improved

We were successfully able to tune solubility based on the alkyl attachment (R-group) on the $(R\text{-}OCS_2)_2M$ complexes. There were a few surprises with regards to this solubility experiment. While it is true that incorporating a hydrophilic functionality into

the xanthate improves water-solubility, increasing steric bulk has a similar effect. For example, the transition metal t-butylxanthates or butylated hydroxyl toluene xanthates have a respectable solubility in water. Since there are no polar groups on either of those xanthates, the water solubility must have been caused by an alternative driving force. It seems likely that the bulkiness prevents the metal xanthate from polymerizing, whereas a smaller group with no hydrophilic character cannot stop the polymerization process. Some of the substituents that were predicted to enhance water-solubility turned out not to to improve solubility in water, but did enhance solubility in polar aprotic organic solvents such as acetone and methylene chloride. Xanthates with two or more ether linkages displayed marked improvement in acetone and methylene chloride solubility. Having the capacity to tune the solubility of d-block and p-block metal xanthates is a powerful tool, and opens up the possibilities for various applications. Some of these applications will be discussed in the succeeding chapters. A final note of interest is that the R-group plays very little role in determining the decomposition temperature for metal xanthates.

CONCLUSIONS

The synthesis of s-block, p-block, and d-block metal xanthate complexes is easily accomplished. A wide variety of metal centers and alkyl substituents can be readily incorporated into a xanthate species. The simple fact that a transition or p-block metal xanthate will cleanly decompose to the corresponding metal sulfide at only 115 °C to 160 °C is the crux of this dissertation and the driving force of the research that went into it. The following chapters will relate how this low temperature decomposition from xanthate to sulfide was exploited to generate a number of useful materials.

REFERENCES

[1] Rao, S. R. *Xanthates and Related Compounds*, 1971.

[2] Zeise, W. C. *Journal of Chemical Physics* **1822**, *35*, 173.

[3] Zeise, W. C. *Journal of Chemical Physics* **1822**, *36*, 1.

[4] Keller, C. H. US, 1925.

[5] Taggart, A. F. **1951**.

[6] Vanthuyne, M.; Maes, A. *Science of the Total Environment* **2002**, *290*, 69-80.

[7] Szymula, M.; Koziol, A. E.; Szczypa, J. *International Journal of Mineral Processing* **1996**, *46*, 123-135.

[8] Moskalyk, R. R.; Alfantazi, A. M. *Mineral Processing and Extractive Metallurgy Review* **2002**, *23*, 141-180.

[9] Marabini, A. M.; Ciriachi, M.; Plescia, P.; Barbaro, M. *Minerals Engineering* **2007**, *20*, 1014-1025.

[10] Higgins, J. C.; Pollard, A. G. *Journal of the Society of Chemical Industry, London* **1937**, *56*, 122-7T.

[11] Idel'son, E. M. *Zavodskaya Laboratoriya* **1960**, *26*, 947-8.

[12] Spanyer, J. W.; Phillips, J. P. *Anal. Chem.* **1956**, *28*, 253.

[13] Dechsuwan, P.; Vaneesorn, Y. *Journal of the Science Faculty of Chiang Mai University* **1997**, *24*, 8-13.

[14] Shupe, I. S. *Journal of the Association of Official Agricultural Chemists* **1942**, *25*, 495-8.

[15] Parekh, I. H.; Moulik, S. K. R.; (India). Application: US
US, 1994, p 7 pp.

[16] Belokonev, S. V.; Glichev, G. T.; Serkov, A. T. *Khimicheskie Volokna* **1976**, 40.

[17] Yamada, M.; Ohshima, K.; (Kurashiki Boseki Kabushiki Kaisha, Japan). Application: WO
WO, 2007, p 23pp.

[18] Efrima, S.; Pradhan, N. *Comptes Rendus Chimie* **2003**, *6*, 1035-1045.

[19] Tzhayik, O.; Sawant, P.; Efrima, S.; Kovalev, E.; Klug, J. T. *Langmuir* **2002**, *18*, 3364-3369.

[20] Pradhan, N.; Katz, B.; Efrima, S. *Journal of Physical Chemistry B* **2003**, *107*, 13843-13854.

[21] Li, Y.; Li, X.; Yang, C.; Li, Y. *Journal of Physical Chemistry B* **2004**, *108*, 16002-16011.

[22] Koh, Y. W.; Lai, C. S.; Du, A. Y.; Tiekink, E. R. T.; Loh, K. P. *Chemistry of Materials* **2003**, *15*, 4544-4554.

[23] Brusetti, R.; Coey, J. M. D.; Czjzek, G.; Fink, J.; Gompf, F.; Schmidt, H. *Journal of Physics F: Metal Physics* **1980**, *10*, 33-51.

[24] Topas 1.0.1 ed.; Bruker AXS, GmbH: 1998.

[25] Warren, B. E.; Averbach, B. L. *Journal of Applied Physics* **1950**, *21*, 595-8.

[26] Warren, B. E. *Prog. Metal Phys. (Bruce Chalmers and R. King, editors. Pergamon Press)* **1959**, *8*, 147-202.

[27] Wilczewski, T. *Journal of Organometallic Chemistry* **1986**, *306*, 125-32.

[28] Mazzi, F.; Tadini, C. *Zeitschrift fuer Kristallographie, Kristallgeometrie, Kristallphysik, Kristallchemie* **1963**, *118*, 378-92.

[29] Zahradnik, R. *Zeitschrift fuer Physikalische Chemie (Leipzig)* **1960**, *213*, 318-37.

[30] Coleman, R. E.; Powell, H. E.; Cochran, A. A. *Transactions of the American Institute of Mining, Metallurgical and Petroleum Engineers* **1967**, *238*, 408-12.

[31] Wilfong, R. L.; Maust, E. E., Jr. □Infrared spectra of compounds of importance in lead sulfide flotation,□ College Park Metall. Res. Cent.,Bur. Mines,College Park,MD,USA., 1974.

[32] Noskov, A. M.; Kirbitova, N. V.; Eliseev, N. I. *Izvestiya Vysshikh Uchebnykh Zavedenii, Gornyi Zhurnal* **1974**, *17*, 144-7.

[33] Sobue, H.; Ogura, K.; Kamio, K.; Kubota, T. *Kami Pa Gikyoshi* **1969**, *23*, 523-7.

[34] Shankaranarayana, M. L.; Patel, C. C. *Canadian Journal of Chemistry* **1961**, *39*, 1633-7.

[35] Shankaranarayana, M. L.; Patel, C. C. *Spectrochimica Acta* **1965**, *21*, 95-103.

[36] Dunn, J. G.; Chamberlain, A. C.; Fisher, N. G.; Avraamides, J. *Journal of Thermal Analysis* **1997**, *49*, 1399-1408.

[37] Franzini, M. *Min. Crist. C.N.R. Ist. Min. (Univ. Pisa, Italy). Z. Krist.* **1963**, *118*, 393-403.

[38] Ikeda, T.; Hagihara, H. *Acta Crystallographica* **1966**, *21*, 919-27.

[39] Watanabe, Y. *Acta Crystallographica, Section B: Structural Crystallography and Crystal Chemistry* **1977**, *B33*, 3566-8.

[40] Iimura, Y.; Ito, T.; Hagihara, H. *Acta Crystallographica, Section B: Structural Crystallography and Crystal Chemistry* **1972**, *28*, 2271-9.

[41] Watanabe, Y.; Yamahata, K. *Scientific Papers of the Institute of Physical and Chemical Research (Japan)* **1970**, *64*, 71-3.

[42] Merlino, S. *Acta Crystallographica, Section B: Structural Crystallography and Crystal Chemistry* **1969**, *25*, 2270-6.

[43] Little, L. H.; Poling, G. W.; Leja, J. *Canadian Journal of Chemistry* **1961**, *39*, 745-54.

[44] Watt, G. W.; McCormick, B. J. *Spectrochimica Acta* **1965**, *21*, 753-61.

CHAPTER 3

SINGLE PRECURSOR ROUTE TO SULFIDES: INFLUENCE OF THE METAL AND R-GROUP IN THE DECOMPOSITION OF ALKYLXANTHATES

The low-temperature decomposition products of various metal alkylxanthates were studied to determine what influence, if any, different metals or R-groups had on the thermal breakdown. The metal ions chosen to examine were Fe^{2+}, Zn^{2+}, Ni^{2+}, Cd^{2+}, and In^{3+}. The R-groups selected were methyl, ethyl, n-propyl, iso-propyl, n-butyl, iso-butyl, sec-butyl, t-butyl, n-pentyl, n-hexyl, and n-octyl. A pyrolysis temperature of 150 °C is sufficient to cause each of the metal xanthates to, at least partially, decompose to the sulfide. The R-group study was performed with Zn^{2+} as the metal center. Nanocrystalline ZnS in the cubic phase is formed regardless of which alkylxanthate is pyrolyzed. The specific surface area, crystallite size, ceramic yield, and luminescence spectrum of the zinc sulfide prepared from each xanthate was obtained while the other decomposition products were identified by gas chromatography/mass spectrometry. A trend in the surface area of ZnS versus R-group suggests that, with the exception of methyl, the bulkier the alkyl group, the lower the specific area.

INTRODUCTION

Some of the earliest work completed on the quantitative decomposition and dissociation of xanthic acid derivatives was performed in the early 20th century.[1,2] The work was done on alkali methal xanthates in solution. It was shown that the rate of decomposition in solution increases with the polar and/or coordinating character of the solvent. In this chapter, however, the solid-state decomposition of xanthates is considered. Herbert was the first to describe thermal decomposition of solid-state potassium xanthate salts.[3] At that time, no mechanism was suggested due to the complicated mixture of decomposition products. Everything from alcohols, dixanthogens, elemental sulfur, and dialkyl xanthates to thiols, alkyl sulfides, and metal sulfides were reported. A more recent study only added to the complexity of the decomposition of potassium ethylxanthates. Gas chromatographic analysis showed the production of species reported earlier with the additions of alkanes, alkenes, acetylene, carbonyl sulfide, and carbon disulfide.[4] Even as recent as 1994, Hill *et. al.*[5] suggested that no meaningful trend in the solid-state decomposition of metal xanthates could be identified.

The Chugaev reaction has been used in organic chemistry to synthesize alkenes by the pyrolysis of various organic xanthates. In the overall Chugaev reaction, a xanthate (usually an (S)-methyl xanthate) is thermally decomposed into an alkene, carbonyl sulfide, and alkyl thiol.[6] Scheme 3.1 demonstrates a common Chugaev reaction. It has been suggested that metal xanthates decompose via a Chugaev-like elimination. The metal xanthate decomposition supposedly occurs through a concerted shift of three electron pairs.[7,8] A Chugaev-like pathway would explain the detection of alkenes and

thiols, but not dialkylxanthates or other dialkly dithiocarbonate byproducts. Moreover, a strict Chugaev pathway cannot explain the presence of carbon disulfide from the decomposition of metal xanthates, which is a commonly reported byproduct.

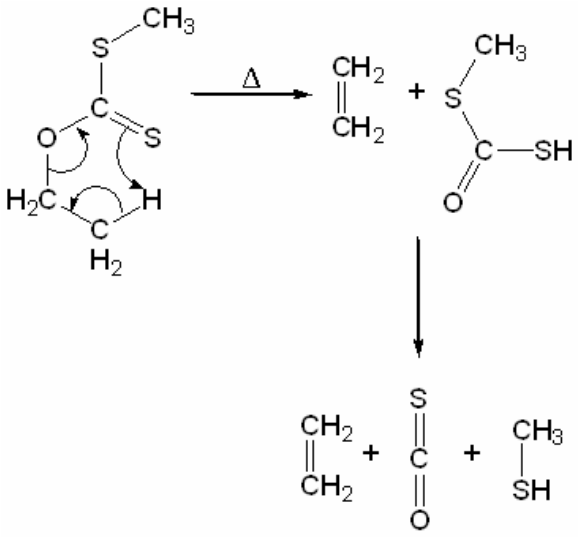

Scheme 3.1: Chugaev elimination pathway for a representative xanthic acid derivative (methyl ethylxanthate).

The complexity surrounding the thermal, solid-state decomposition of metal xanthates does not take away from the fact that they are first-rate single precursors for metal sulfide materials. Everything from bismuth sulfide nanowires,[9] to cadmium sulfide quantum dots,[7,10-12] to CdS/ZnS core/shell systems,[13] to ZnS thin films,[14] to NiS and CoS[15] have been prepared by the low temperature decomposition of certain xanthate compounds. In this chapter, metal sulfides with unique properties are discussed and research designed to shed some light on the xanthate-to-sulfide process is presented.

EXPERIMENTAL

Materials. Reagent grade cadmium nitrate tetrahydrate ($Cd(NO_3)_2 \cdot 4H_2O$, Mallinkrodt), iron(II) sulfate heptahydrate ($FeSO_2 \cdot 7H_2O$, Malllinkrodt), indium(III) chloride ($InCl_3$, Acros), nickel(II) sulfate hexahydrate ($NiSO_4 \cdot 6H_2O$, GFS), zinc sulfate heptahydrate ($ZnSO_4 \cdot 7H_2O$, EM Science), potassium ethylxanthate ($KS_2COCH_2CH_3$, Aldrich), potassium n-butylxanthate ($KS_2COCH_2CH_2CH_2CH_3$, TCI), and potassium isopropylxanthate ($KS_2COCH(CH_3)_2$, TCI) were purchased and used as received without further purification. Carbon disulfide, potassium hydroxide, methanol, ethanol, n-propanol, sec-butanol, iso-butanol, t-butanol, n-pentanol, n-hexanol, and n-octanol were also obtained and used as is. All water used throughout the experiment was deionized and had a resistivity of 18.1 MΩcm.

Synthesis of potassium alkylxanthates. Several potassium alkylxanthates were prepared by mixing potassium hydroxide, carbon disulfide, and a given alcohol in a stoichiometric ratio. For instance, to prepare potassium methylxanthate, KOH (10.33 g, 184 mmole) was dissolved in water (200 ml) and placed in an ice bath. Methanol (5.88 g, 184 mmole) and carbon disulfide (14.01 g, 184 mmole) were individually added to the chilled hydroxide solution. The mixture was allowed to react until the CS_2 was completely consumed (roughly 24-48 hours) – an orange solution is formed for all potassium alkylxanthates. The water was evaporated to yield the solid potassium methylxanthate (25.8 g, 96.0 %). The dried and powdered products for all potassium alkylxanthate salts are yellow to yellow/orange solids regardless of the alkyl group. Scheme 3.1 displays the balanced reaction for the preparation of any potassium

alkylxanthate. Specific information regarding amounts of reactants used and yield for individual reactions can be found in Table 3.1.

$$KOH(aq) + ROH(l) + CS_2(l) \rightarrow KS_2COR(aq) + H_2O(l)$$

Scheme 3.1: Governing reaction for the preparation of various potassium alkylxanthates, where R represents methyl, ethyl, n-propyl, isopropyl, n-butyl, isobutyl, sec-butyl, t-butyl, n-pentyl, n-hexyl, or n-octyl.

Table 3.1: Reaction data for the preparation of several potassium alkylxanthate salts.

Product	Mass KOH (g)	Mass R-OH (g)	Mass CS_2 (g)	Yield (mass) (%)	Color
potassium methylxanthate	10.33	5.88	14.01	25.84 g 96.01 %	yellow
potassium ethylxanthate	NA, commercial product used				yellow
potassium n-propylxanthate	5.002	5.358	6.784	14.64 g 94.23 %	yellow
potassium iso-propylxanthate	NA, commercial product used				yellow
potassium n-butylxanthate	NA, commercial product used				yellow
potassium iso-butylxanthate	4.968	6.563	6.737	15.87 g 95.18 %	yellow
potassium sec-butylxanthate	5.013	6.630	6.911	13.48 g 80.12 %	yellow
potassium t-butylxanthate	5.000	6.609	6.903	12.79 g 76.21 %	yellow
potassium n-pentylxanthate	5.01	7.89	6.80	16.8 g 92.9 %	yellow
potassium n-hexylxanthate	5.02	9.14	6.85	17.04 g 88.01 %	yellow
potassium n-octylxanthate	18.079	42.058	24.448	67.06 g 85.14 %	yellow

Synthesis of transition metal alkylxanthates. Transition metal alkylxanthate complexes are not particularly soluble in water. A one-step precipitation reaction between an aqueous transition metal salt and a solution of any potassium alkylxanthate yields the transition metal complex in a quantitative fashion. As an example, indium(III) ethylxanthate was generated by reacting an aqueous solution of indium(III) chloride and potassium ethylxanthate in a stoichiometric fashion as described in the literature.[16] Typically, $InCl_3$ (2.044 g, 9.24 mmol) was dissolved in water (150 mL) and $KS_2COCH_2CH_3$ (4.440 g, 27.7 mmol) was dissolved in a similar amount of water. The potassium ethylxanthate solution was slowly poured into the indium(III) chloride solution immediately generating the white indium(III) ethylxanthate, $In(S_2COCH_2CH_3)_3$, precipitate in nearly quantitative yield. The solid was collected by vacuum filtration and washed thoroughly with water. The yield after drying was (4.07 g, 92.1 %). Scheme 3.2 shows two generic reactions that illustrate how various divalent and trivalent metal alkylxanthates could be prepared while Table 3.2 lists actual reaction conditions and yield information.

$$M^{2+}(aq) + 2KS_2COR(aq) \rightarrow M(S_2COR)_2(s) + 2K^+(aq)$$

$$M^{3+}(aq) + 3KS_2COR(aq) \rightarrow M(S_2COR)_3(s) + 3K^+(aq)$$

Scheme 3.2: Synthesis of di- and tri-valent d-block and p-block metal alkylxanthate complexes.

Table 3.2: Reaction data for the preparation of certain transition metal alkylxanthates.

Product	Mass and ID of metal salt	Mass potassium alkyxanthate	Color	Yield (%) ± 1.0 %
cadmium ethylxanthate	6.865 g $CdCl_2 \cdot 2½H_2O$	9.625 g	pale yellow	95.3
iron(II) ethylxanthate	8.681 g $FeSO_4 \cdot 7H_2O$	10.01 g	brown	87.0
indium(III) ethylxanthate	2.044 g $InCl_3$	4.440 g	white	92.1
nickel(II) ethylxanthate	11.885 g $NiCl_2 \cdot 6H_2O$	16.04 g	reddish brown	98.8
zinc methylxanthate	2.876 g $ZnSO_4 \cdot 7H_2O$	2.926 g	white	99.1
zinc ethylxanthate	5.760 g $ZnSO_4 \cdot 7H_2O$	6.449 g	white	97.6
zinc n-propylxanthate	2.875 g $ZnSO_4 \cdot 7H_2O$	3.486 g	white	98.3
zinc iso-propylxanthate	2.876 g $ZnSO_4 \cdot 7H_2O$	3.485 g	white	98.8
zinc n-butylxanthate	2.881 g $ZnSO_4 \cdot 7H_2O$	3.774 g	white	97.6
zinc iso-butylxanthate	2.851 g $ZnSO_4 \cdot 7H_2O$	3.769 g	white	97.1
zinc sec-butylxanthate	2.876 g $ZnSO_4 \cdot 7H_2O$	3.759 g	white	88.3
zinc t-butylxanthate	2.879 g $ZnSO_4 \cdot 7H_2O$	3.761 g	white	93.2
zinc n-pentylxanthate	5.006 g $ZnSO_4 \cdot 7H_2O$	7.046 g	white	98.0
zinc n-hexylxanthate	5.000 g $ZnSO_4 \cdot 7H_2O$	7.526 g	white	85.1
zinc n-octylxanthate	2.879 g $ZnSO_4 \cdot 7H_2O$	4.895 g	white	95.2

Characterization. Powder X-ray diffraction (XRD) measurements were obtained on a Bruker AXS D8 Advance diffractometer using Cu Kα radiation with an acceleration voltage of 40 kV and current flux of 30 mA. The diffractograms were recorded for a 2θ range of 17-70° with a step size of 0.02° and a counting time of 18 seconds per step. All

the XRD patterns where collected at ambient temperature, and the phases were identified using the ICDD database.[17] The peaks were profiled with a Pearson 7 model using Topas P version 1.01 software.[18] The profiles of the standard and the sample were put into the Win-Crysize program version 3.05, which uses the Warren-Averbach evaluation method to determine crystallite size.[19,20]

Thermogravimetric analysis (TGA) was performed on the complexes with a heating rate of 2.0°/min from room temperature to 600 °C using a Seiko Instruments Exstar 6200. None of the xanthates melt congruently, but a well behaved decomposition curve was observed for each of the xanthate salts.

GC/MS was performed on a Hewlett Packard G1800A instrument equipped with 30 m x 0.25 mm HP5 column. The helium flow rate was 1.0 ml/min and the injection port was set at 250 °C.

The specific surface areas were obtained with a conventional Brunauer-Emmett-Teller (BET) multilayer nitrogen adsorption method using a Quantachrome Nova 1200 instrument.

RESULTS AND DISCUSSION

Metal influence: thermogravimetric analysis and decomposition products. Thermogravimetric analyses were performed on each of the ethylxanthate salts of Fe^{2+}, Zn^{2+}, Ni^{2+}, Cd^{2+}, and In^{3+}. The thermal analysis curve from one metal ethylxanthate varies slightly from the others (Figure 3.1) with respect to onset temperature. Iron(II)

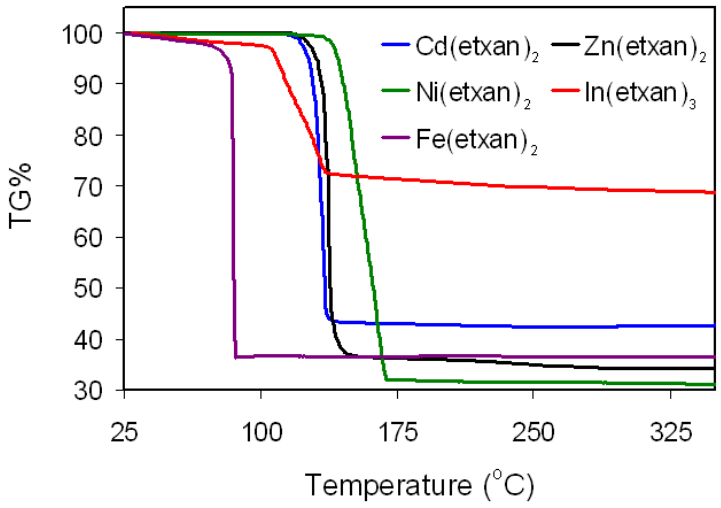

Figure 3.1: Thermogravimetric analysis traces for five different metal ethylxanthates.

ethylxanthate is an exception and will be discussed shortly. The remaining four compounds display decomposition in the region from 120 °C to 150 °C.

At 150 °C many of the decomposition products are gases or have a vapor pressure such that a headspace experiment is useful in determining the identity of those products. Each metal ethylxanthate was individually heated in a sealed tube at 150 °C, and the tube was then cooled to room temperature before a sample of the headspace vapor was analyzed. The byproducts from the decomposition were invariably carbonyl sulfide, carbon disulfide, diethyl sulfide, diethyl disulfide, diethylxanthate, and (S,S)-diethyldithiocarbonate, which suggests that the identity of the metal is not of great consequence with regard to the off-gas byproducts. A further discussion of the gaseous products will be presented in the next section of this chapter.

The solid product generated from the thermal elimination is more the focus of this entire study. With the exception of iron(II), each of the other metal ethylxanthate

complexes decomposed to their resultant metal sulfide. This was proven by powder X-ray diffraction (Figure 3.2). The solid formed when $Fe(S_2COCH_2CH_3)_2$ was heated to 150 °C was FeO(OH) in a mixture of goethite and lepidocrocite phases. Iron oxyhydroxide is a useful substance, and it has been shown to be a promising material for water purification,[21-23] but the metal sulfides prepared from the thermal treatment are the materials of interest in this investigation. One obvious feature of each of the sulfide X-ray diffraction patterns is the breadth of the peaks. The broad peaks indicate a very small grain size, which means the sulfides formed from the xanthates are nanocrystalline materials. The fact that these sulfides are nanocrystalline opens up new possibilities for their use. Table 3.3 contains data about each metal sulfide generated from the low temperature decomposition of the parent precursor. Specifically, product identity, crystallite size, specific surface area, and ceramic yield are presented.

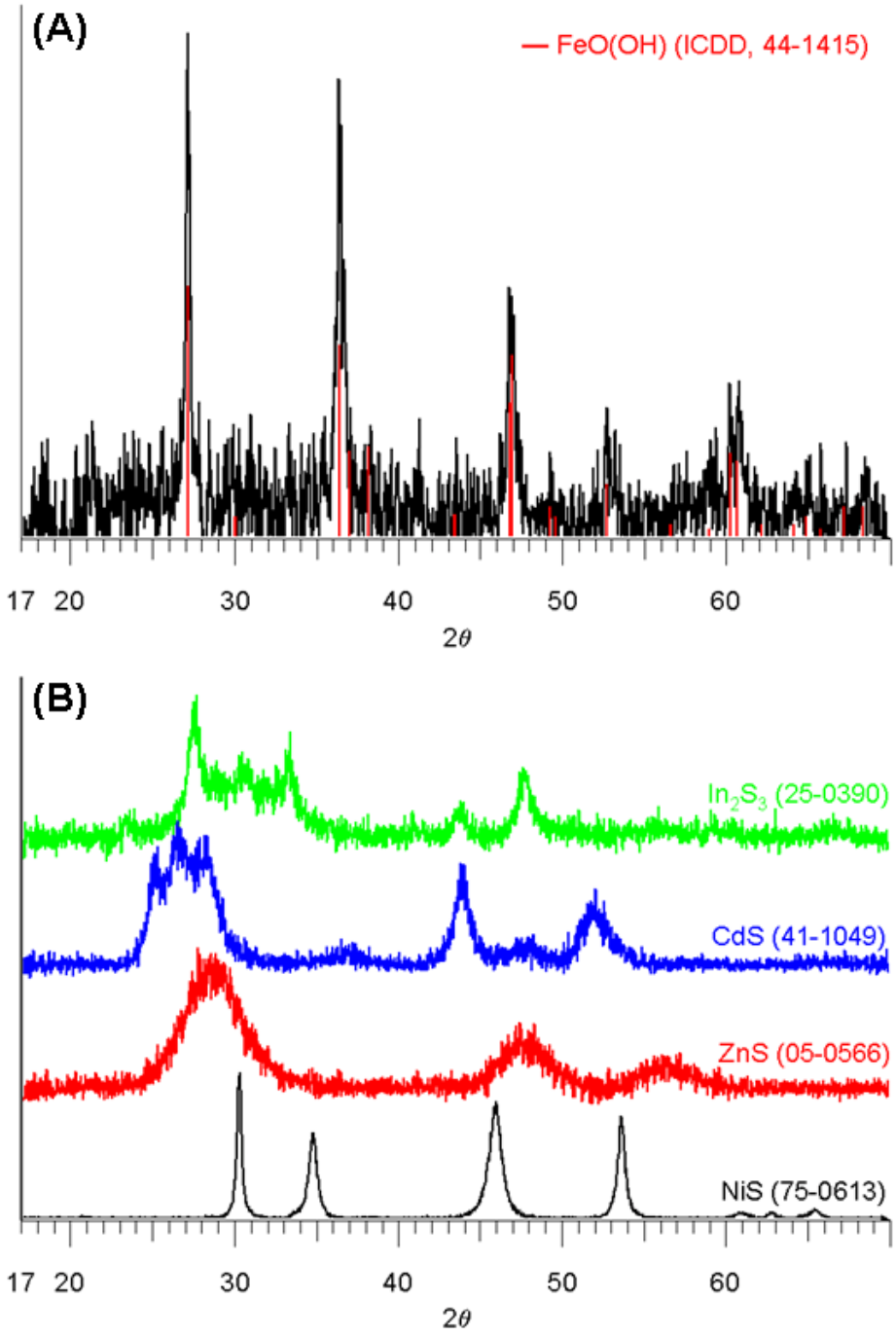

Figure 3.2: Pyrolysis (150 °C) products for (A) iron(II) ethylxanthate and (B) In(III), Cd(II), Zn(II), and Ni(II) ethylxanthate. The peak patterns match the species indicated. At lower temperatures, the In(III) ethylxanthate product is too amorphous. Thus, the In_2S_3 diffractogram was attained at 300 °C.

Table 3.3: Product identity, ceramic yield, specific surface area, and crystallite size for the 150 °C treatment of iron(II), nickel(II), zinc, cadmium, and indium(III) ethylxanthate.

	Decomposition Product (ID, ICDD number)	Crystallite Size (nm)	Surface Area (m^2/g)	Ceramic Yield (%) Theoretical (%)
$Fe(S_2COCH_2CH_3)_2$	FeO(OH) (44-1415)	6.4	38	30.1 (29.8)
$Ni(S_2COCH_2CH_3)_2$	NiS (75-0613)	8.3	2	28.3 (30.1)
$Zn(S_2COCH_2CH_3)_2$	ZnS (05-0566)	1.6	320	38.1 (31.7)
$Cd(S_2COCH_2CH_3)_2$	CdS (41-1049)	2.8	138	39.9 (40.7)
$In(S_2COCH_2CH_3)_3$	In_2S_3 (25-0390)	NA	93	28.0 (34.1)

Nickel sulfide notwithstanding, the surface areas of the synthesized metal sulfides are quite large. In fact, the value for ZnS is the highest reported value for that compound of which we are aware. Several useful applications will be discussed in later chapters that rely on the ultrahigh surface areas of CdS and ZnS. At this point it is not clear why zinc ethylxantate produces the sulfide with the highest surface area. The decomposition products and pathway are similar from one metal salt to the next. [In chapter 8, the reason why NiS has such a low surface area compared to the others is presented]. The surface area for ZnS, CdS, NiS, and In_2S_3 was further probed by monitoring the effect of decomposition temperature on the parent ethylxanthate. Figures 3.3, 3.4, 3.5, and 3.6 illustrate the results obtained from the surface area versus reaction temperature

experiment for nickel(II) ethylxanthate, cadmium ethylxanthate, indium(III) ethylxanthate, and zinc ethylxanthate respectively. In each case, the clear trend is that metal sulfide surface area decreases with increasing temperature. This trend is not a surprise since at higher temperatures the sulfides are sintered, and the fusing process removes exposed surface. It is important to keep in mind that for each metal system the sulfide begins to oxidize to the sulfate and/or oxide at around 450-500 °C. Therefore, some of the data in the following figures corresponds to surface area for the metal oxide. The sulfide regions are appropriately marked. Table 3.4 sums up the results for the solid-state decomposition products of nickel(II), indium(III), cadmium, and zinc ethylxanthate for a wide range of reaction temperatures.

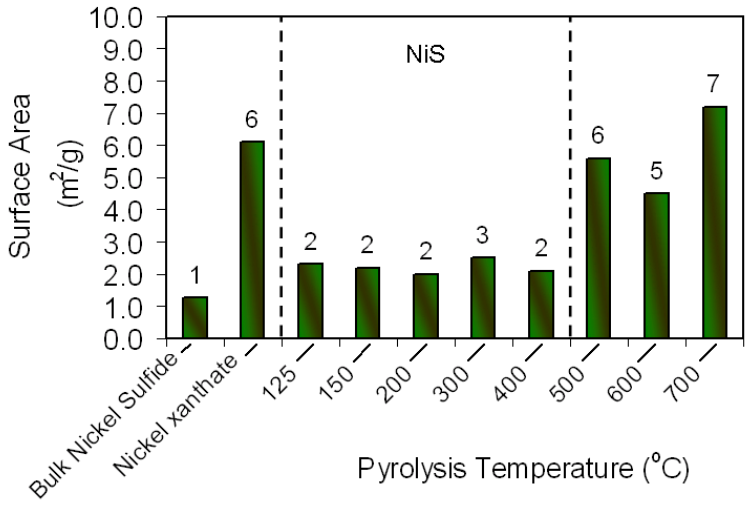

Figure 3.3: Influence of decomposition temperature on the surface area of the solid product formed from $Ni(S_2COCH_2CH_3)_2$. The NiS region is marked.

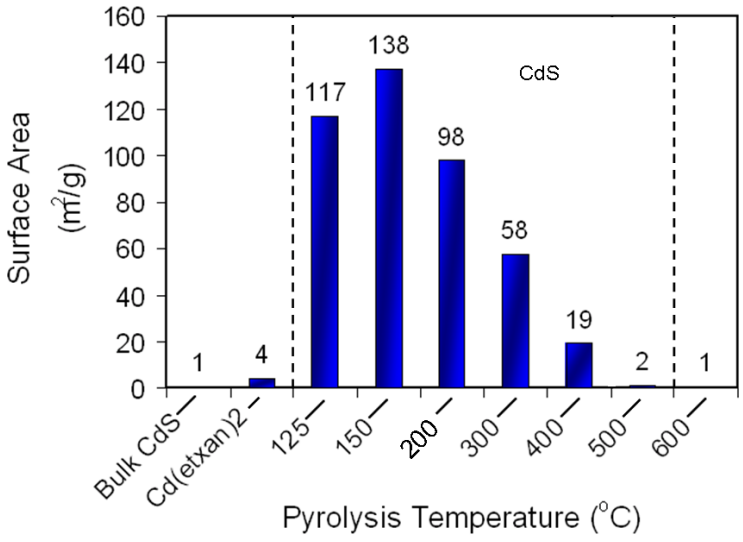

Figure 3.4: Influence of decomposition temperature on the surface area of the solid product formed from $Cd(S_2COCH_2CH_3)_2$. The CdS region is marked.

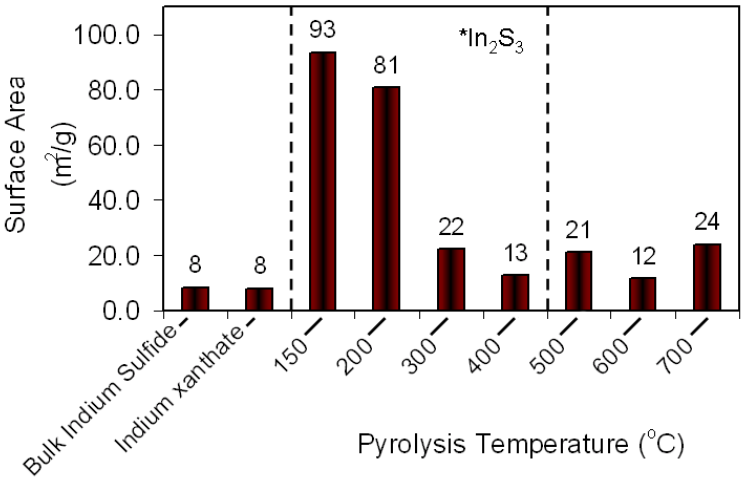

Figure 3.5: Influence of decomposition temperature on the surface area of the solid product formed from $In(S_2COCH_2CH_3)_3$. The In_2S_3 region is marked (*there is some In_2O_3 present at 300 °C and 400 °C, but the major product is the sulfide).

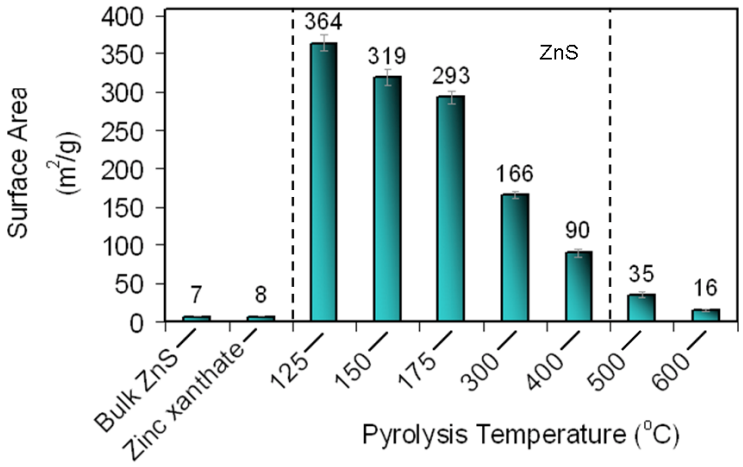

Figure 3.6: Influence of decomposition temperature on the surface area of the solid product formed from $Zn(S_2COCH_2CH_3)_2$. The ZnS region is marked.

Table 3.4: Summary of results for the solid-state decomposition products of four ethylxanthate salts.

	Temperature (°C)	Product ID	Crystallite Size (nm)	Surface Area (m^2/g)	Ceramic Yield (%)
NiXan	125	NiS	6.9	2	28.3
	150	NiS	8.3	2	28.3
	200	NiS	13.5	2	26.1
	300	NiS	15.7	3	26.3
	400	$Ni_{17}S_{18}$	18.1	2	25.8
	500	NiO, $NiSO_4$, $Ni_{17}S_{18}$	NA	6	26.8
	600	NiO, $NiSO_4$	NA	5	24.1
	700	NiO	20.2	7	21.0
CdXan	125	CdS	2.7	117	44.8
	150	CdS	2.8	138	39.9
	200	CdS	3.3	98	39.5
	300	CdS	3.8	58	39.0
	400	CdS	4.4	19	39.8
	500	CdS	60.9	2	39.2
	600	CdS, $Cd_3O_2SO_4/CdSO_4{\cdot}2CdO$	NA	1	39.2
	700	CdS, $Cd_3O_2SO_4/CdSO_4{\cdot}2CdO$	NA	1	40.2
InXan	150	Amorphous	NA	93	28.0
	200	Amorphous	NA	81	29.5
	300	In_2S_3	NA	22	22.5
	400	In_2S_3, In_2O_3	NA	13	36.0
	500	In_2O_3	8.6	21	32.0
	600	In_2O_3	11.8	12	31.3
	700	In_2O_3	15.0	24	30.5
ZnXan	125	ZnS	1.5	368	38.7
	150	ZnS	1.6	319	38.1
	175	ZnS	1.7	293	36.8
	300	ZnS	1.9	166	34.0
	400	ZnS	2.1	85	34.1
	500	ZnS, ZnO	NA	35	30.0
	600	ZnO	14.7	16	29.3
	700	ZnO	21.2	20	27.0

Alkyl group influence: thermogravimetric analysis and decomposition products. Zinc alkylxanthate salts were synthesized with eleven different R-groups: methyl, ethyl, n-propyl, iso-propyl, n-butyl, iso-butyl, sec-butyl, t-butyl, n-pentyl, n-hexyl, and n-octyl. In order to understand what impact size and shape of the alkyl chain had on the thermal decomposition, each zinc salt was investigated with a thermogravimetric analyzer. The traces obtained from the thermal analysis experiment for the n-alkylxanthates are displayed in Figure 3.7. Suprisingly, the length of the alkyl group had very little impact

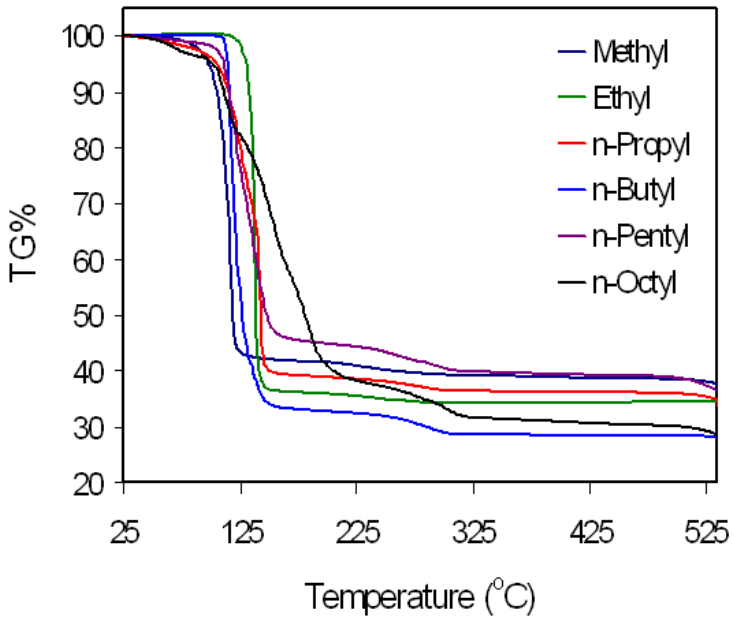

Figure 3.7: Thermogravimetric analysis traces for a series of zinc n-alkylxanthates.

on the decomposition profile. Based on the minimum values of the first derivative for each curve in Figure 3.7, the temperature of the major decomposition step varied only from 119 °C to 160 °C. Refer to Figure 3.8 for a plot of first derivative minima versus carbon chain length. There is an apparent trend between elimination temperature and

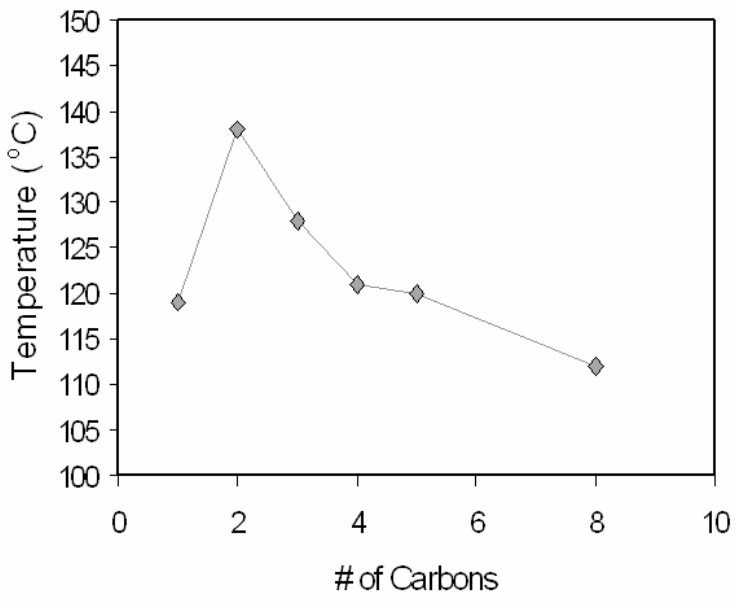

Figure 3.8: Zinc alkylxanthate onset decomposition temperature versus straight-chain carbon length.

chain length, with the exception of methyl. As the R-group lengthens, the onset decomposition temperature is reduced, which fits the ionic model. Four-coordinate zinc is relatively small and cannot stabilize large anions. As the chain length increases, the anion gets bigger making it harder and harder for the small Zn^{2+} to stabilize increasingly large xanthates. Since 150 °C was determined a sufficient temperature to decompose each straight-chain zinc alkylxanthate, each of the xanthates was pyrolyzed in a sealed tube at that temperature. A headspace analysis of the decomposition products for each n-alkylxanthate using GC-MS (a gas chromatograph coupled to a mass spectrometer detector) was carried out to identify the species formed due to the thermal breakdown. Table 3.5 contains the data from the headspace analysis. In all cases there are multiple gases formed during the reaction. Carbonyl sulfide and carbon disulfide are present for each zinc n-alkylxanthate. The decomposition products from the shorter-chain species

Table 3.5: Headspace identification of zinc n-alkylxanthates pyrolyzed at 150 °C.

R-group	Gas-phase Pyrolysis Products
Methyl	carbonyl sulfide, dimethyl sulfide, dimethyl disulfide, carbon disulfide, dimethylxanthate, (S,S)-dimethyldithiocarbonate
Ethyl	carbonyl sulfide, diethyl sulfide, diethyl disulfide, carbon disulfide, diethylxanthate, (S,S)-diethyldithiocarbonate
n-propyl	carbonyl sulfide, di(n-propyl) sulfide, di(n-propyl) disulfide, carbon disulfide, di(n-propyl)xanthate, di(n-propyl)carbonate, 1,1-dipropoxypropane
n-butyl	carbonyl sulfide, carbon disulfide, di(isopropyl)sulfide, di(n-butyl)sulfide, n-butanol
n-pentyl	carbonyl sulfide, carbon disulfide, 2-pentene, 1-pentanethiol, 2-methyl-1-butene, (E)-5-decene
n-octyl	Carbonyl sulfide, carbon disulfide, n-octanethiol

are analogous with each other, which indicates that their elimination pathways are essentially the same. Based on the relative peak areas of the headspace products from zinc methyl-, ethyl- and n-propylxanthate, a general scheme for the decomposition process can be speculated (Scheme 3.3). The products that do not appear in the reaction scheme, but were detected in the experiment are not as prevalent but can be explained as different radical combinations. For example, it is logical that if in the decomposition of the *O,S*-dialkyl dithiocarbonate, RS• and R• radicals are formed; two RS• species could

combine to form the disulfide before the alkyl radical had a chance to interact with the thio radical to form the monosulfide.

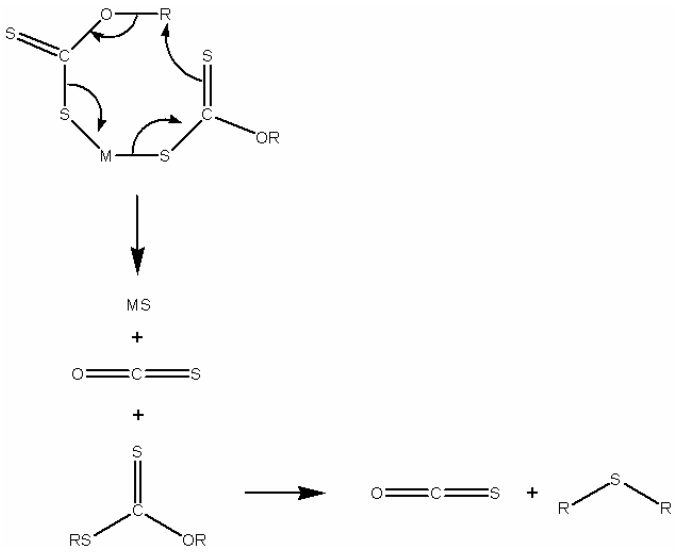

Scheme 3.3: Principal decomposition route for short-chain zinc n-alkylxanthates where R denotes methyl-, ethyl-, or n-propyl.

The fact that various dialkyl dithiocarbonate species are detected – namely the (O,S) and (S,S) dialkyl dithiocarbonates – also suggests a radical pathway since it appears the R-groups are free to bond with either the oxygen or sulfur of the OCS_2 core.

As the chain grows, new trends in the decomposition products arise. For example, the formation of alkenes, thiols, and alcohols did not occur for methyl, ethyl, or propyl, but are significant products for the longer-chained alkyl groups. Thiols and alkenes are well known products of the Chugaev reaction, which was discussed in the introduction section of this chapter. Thus, for larger n-alkylxanthates, it appears there are competing reactions; a modified Chugaev elimination and a radical pathway similar to that shown in Scheme 3.1.

Figure 3.9 demonstrates the thermal decomposition trend corresponding to branched zinc alkylxanthates. From the four examples shown, there looks to be two

groups of two similar thermogravimetric analysis traces. Zinc iso-propylxanthate and zinc iso-butylxanthate exhibit one trend while zinc sec-butylxanthate and zinc t-butylxanthate display the other. The main difference between those two groups of alkyl attachments is that the iso-species connect to the xanthate through a primary carbon whereas the other two groups bind through secondary (sec-butyl) or tertiary (t-butyl) carbons. The headspace decomposition products for the branched xanthates can be seen in Table 3.6. Zinc isopropylxanthate breaks down identically to the shorter n-alkyl counterparts. Also like the straight chain compounds, there seems to be multiple decomposition pathways as the number of carbons in a branched xanthate increases. It should be stated that neither of the sec-butyl or t-butyl xanthates are pure. In fact, they begin to slowly decompose to the sulfide at room temperature. Therefore, the TGA traces are potentially misleading.

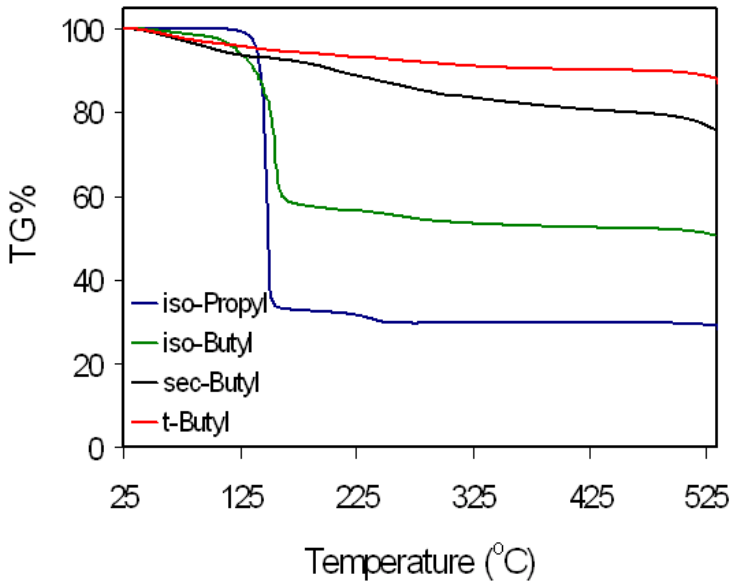

Figure 3.9: Thermogravimetric analysis traces for four branched zinc alkylxanthates.

Table 3.6: Headspace identification of zinc branched alkylxanthates fired to 150 °C.

R-group	Gas-phase Pyrolysis Products
iso-propyl	carbonyl sulfide, carbon disulfide, diisopropyl sulfide, diisopropyl disulfide, diisopropyl xanthate, diisopropyl carbonate
iso-butyl	carbonyl sulfide, carbon disulfide, diisobutyl sulfide
sec-butyl	carbonyl sulfide, carbon disulfide, 1-butene, sec-butanol, di(sec-butyl)ether, di(n-propyl)sulfide
t-butyl	carbonyl sulfide, carbon disulfide

The solid pyrolysis product for each of the 11 zinc alkylxanthates, when heated to 150 °C, was determined to be cubic zinc sulfide. The product identification was accomplished using powder X-ray diffraction. Some representative diffraction patterns

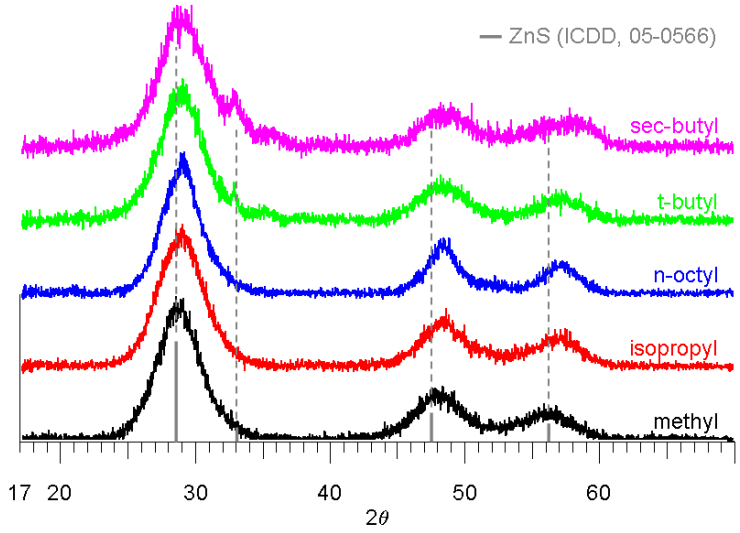

Figure 3.10: X-ray diffraction patterns for the 150 °C pyrolysis product of $Zn(S_2COR)_2$ where R denotes methyl, isopropyl, n-octyl, t-butyl, or sec-butyl. Each precursor generated nanocrystalline ZnS.

are shown in Figure 3.10. In each case the peaks are broad, and the average crystallite size varies from 1.4 nm to 1.9 nm. One of the major reasons that various R-groups were studied was to determine if the alkyl attachment would have some bearing on the surface area of the resultant ZnS. It was hoped that a bulkier R-group would create more porosity during the decomposition, leaving behind ZnS with an even higher surface area than the value reported for the material prepared from the ethylxanthate. Since the thermal analysis suggested that 150 °C was sufficient to convert each alkylxanthate to the sulfide, and X-ray diffraction confirmed the formation of ZnS at that temperature for each of the alkylxanthates, 150 °C was selected as the reaction temperature for a surface area experiment. The results of the surface area study (see Figure 3.11) were interesting and somewhat unexpected. Two key relationships can be extracted from the results. First, with the exception of methyl, ZnS surface area decreases with increasing chain length on

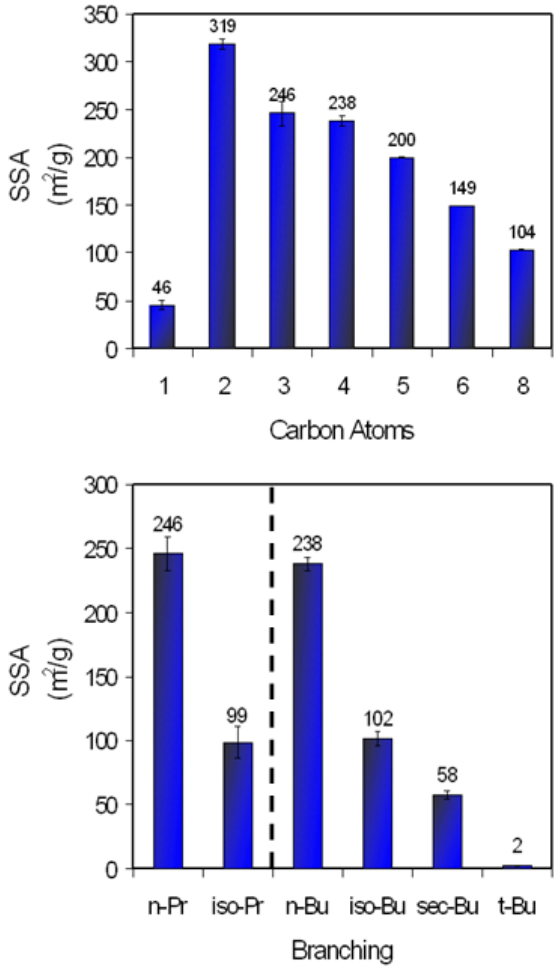

Figure 3.11: Zinc sulfide surface area from eleven different alkylxanthate salts.

the parent zinc n-alklyxanthate. Second, as branching on the parent xanthate increases, surface area of the subsequent ZnS decreases. Additionally, when there is identical branching, the precursor with the larger number of carbons will produce a lower surface area sulfide. In the case of iso-butyl, the xanthate attachment is through a primary carbon and the branching occurs on the beta position. The resultant surface area falls between that from a straight-chain primary group and branched secondary group. Thus, branching at the beta position influences the decomposition, but not to the extent of alpha

branching. Table 3.7 provides a summary of the results for the solid product formation due to the 150 °C thermal breakdown of various zinc alkylxanthate compounds. In the future it would be beneficial to repeat the surface area experiment at the optimum decomposition temperatures for each individual compound. It is possible that some of the trends would change or become more apparent.

Table 3.7: ZnS formation results from an assortment of alkylxanthate salts at 150 °C.

R-group	Product ID	Ceramic Yield (%)	Theoretical Yield (%)	Average Crystallite Size (nm)	Specific Surface Area (m^2/g)
Methyl	ZnS	37.6	34.8	1.7	45
Ethyl	ZnS	38.1	31.7	1.6	319
n-propyl	ZnS	39.5	29.0	1.8	245
iso-propyl	ZnS	33.0	29.0	1.7	96
n-butyl	ZnS	36.1	26.8	1.7	238
iso-butyl	ZnS	31.5	26.8	1.7	102
sec-butyl	ZnS	63.2	26.8	1.4	58
t-butyl	ZnS	44.1	26.8	1.5	2
n-pentyl	ZnS	44.6	24.9	1.7	200
n-hexyl	ZnS	54.6	23.3	1.7	149
n-octyl	ZnS	16.4	20.5	1.9	104

CONCLUSIONS

Numerous transition metal (and p-block metal) sulfides were easily prepared from the low temperature decomposition of alkylxanthate salts. The advantage of using xanthate precursors to the other available materials is that the necessary elimination temperature is substantially lower. For example, an analogous metal dithiocarbamate requires a temperature of nearly 100 °C higher than the dithiocarbonate to produce the same sulfide. Cadmium, zinc, nickel, and indium were chosen as example metals that will work with the xanthate system to generate useful sulfides, but the list of transition and p-block metals that could also be used is extensive. During this study, we were able to successfully synthesize other alkylxanthates and sulfides, such as those from copper, gallium, silver, mercury, lead, cobalt, and bismuth. Mixed metal sulfides such as copper indium sulfide and copper gallium sulfide (discussed extensively in chapter 9) along with mercury cadmium sulfide can be synthesized using the xanthate precursor route.

Not only are sulfides easily attainable, their material properties offer several advantages. Their ultra small crystallite sizes make these sulfides useful additions to the ever growing field of nanotechnology. It is no trivial discovery that nanometric metal sulfides with surface areas on the order of 100 m^2/g can be made entirely in the solid state at temperatures no higher than 150 °C.

The decomposition route from xanthate to sulfide is complicated. While metal identity does not appear to affect the reaction pathway to a large extent (iron being a major exception), alkyl substituents play a more significant role. The alkyl group does not substantially change the energy required to accomplish sulfide formation since 150 °C is sufficient to produce the desired product in each case. The off-gas byproducts

detected do suggest that as the number of carbons on the parent xanthate increases, the complexity of the decomposition likewise increases. There are competing reactions such as radical formation and Chugaev-like elimination. There is also evidence of carbocation involvement since there is alkyl transfer within the same R-group (1-pentene and 2-methyl-1-butene produced from n-pentylxanthate). The alkyl group has a profound influence on some of the resultant sulfide properties such as surface area. As the number of carbons and branching increases, the specific surface area decreases. The precise reason for why such large surface areas arise or why there is such a deviation from one metal to the next is not known; cation size and coordination environment likely play a role. Regardless of the intricate nature of the decomposition process, xanthates are incredibly versatile precursors to nanocrystalline sulfide and oxide materials.

REFERENCES

[1] von Halban, H.; Hecht, W. *Journal of the Chemical Society, Abstracts* **1918**, *114*, 222-3.

[2] von Halban, H.; Hecht, W. *Zeitschrift fuer Elektrochemie und Angewandte Physikalische Chemie* **1918**, *24*, 65-82.

[3] Herbert, A. *Bull. Soc. Chim. France* **1911**, *9*, 523-532.

[4] Tyden, I. *Talanta* **1966**, *13*, 1353-60.

[5] Hill, J. O.; Murray, J. P.; Patil, K. C. *Reviews in Inorganic Chemistry* **1994**, *14*, 363-87.

[6] DePuy, C. H.; King, R. W. *Chemical Reviews (Washington, DC, United States)* **1960**, *60*, 431-57.

[7] Pradhan, N.; Katz, B.; Efrima, S. *Journal of Physical Chemistry B* **2003**, *107*, 13843-13854.

[8] Efrima, S.; Pradhan, N. *Comptes Rendus Chimie* **2003**, *6*, 1035-1045.

[9] Koh, Y. W.; Lai, C. S.; Du, A. Y.; Tiekink, E. R. T.; Loh, K. P. *Chemistry of Materials* **2003**, *15*, 4544-4554.

[10] Barreca, D.; Gasparotto, A.; Maragno, C.; Seraglia, R.; Tondello, E.; Venzo, A.; Krishnan, V.; Bertagnolli, H. *Applied Organometallic Chemistry* **2005**, *19*, 59-67.

[11] Nair, P. S.; Radhakrishnan, T.; Revaprasadu, N.; O'Brien, P. *Materials Science and Technology* **2005**, *21*, 237-242.

[12] Nair, P. S.; Scholes, G. D. *Journal of Materials Chemistry* **2006**, *16*, 467-473.

[13] Pradhan, N.; Efrima, S. *J Am Chem Soc FIELD Full Journal Title:Journal of the American Chemical Society* **2003**, *125*, 2050-1.

[14] Barreca, D.; Gasparotto, A.; Maragno, C.; Tondello, E.; Spalding, T. R. *Surface Science Spectra* **2004**, *9*, 54-61.

[15] Singhal, G. H.; Botto, R. I.; Brown, L. D.; Colle, K. S. *Journal of Solid State Chemistry* **1994**, *109*, 166-71.

[16] Rao, S. R. *Xanthates and Related Compounds*, 1971.

[17] The International Centre for Diffraction Data, Newton Square, PA: (The International Centre for Diffraction Data, Newton Square, PA); File Nos. 05-0566 & 36-1451.

[18] Topas 1.0.1 ed.; Bruker AXS, GmbH: 1998.

[19] Warren, B. E.; Averbach, B. L. *Journal of Applied Physics* **1950**, *21*, 595-8.

[20] Warren, B. E. *Prog. Metal Phys. (Bruce Chalmers and R. King, editors. Pergamon Press)* **1959**, *8*, 147-202.

[21] Guo, X.; Du, Y.; Chen, F.; Park, H.-S.; Xie, Y. *Journal of Colloid and Interface Science* **2007**, *314*, 427-433.

[22] Yuan, C.; Chiang, T.-S. *Chemosphere* **2007**, *67*, 1533-1542.

[23] Zhang, J.; Stanforth, R. *Langmuir FIELD Full Journal Title:Langmuir: the ACS journal of surfaces and colloids* **2005**, *21*, 2895-901.

CHAPTER 4

LOW TEMPERATURE GROWTH OF ZINC SULFIDE NANOPARTICLES FROM ZINC XANTHATE SINGLE SOURCE PRECURSORS

Zinc sulfide nanoparticles were generated by means of the low temperature (60 °C) thermal decomposition of zinc ethylxanthate. When the decomposition of the xanthate precursor is carried out in dimethyl sulfoxide (DMSO), the result is a capping of the zinc sulfide particles with a ZnS-DMSO complex. An increase in particle size with heating time is indicated by dynamic light scattering and ultraviolet adsorption. A high degree of size tunability (ca. 2 – 125 nm.) was achieved by varying the reaction time and the precursor concentration. Infrared spectra recorded for the capped ZnS yielded peaks that are indicative of DMSO complexation. The decomposition of the precursor in DMSO appears to follow a first-order pathway as determined by ^{1}H and ^{13}C NMR spectroscopy. Furthermore, the decomposition pathway appears to be the transfer of an ethyl group from one ethylxanthate ligand to another, suggesting a unique deposition process whereby ZnS first forms as monomer ion-pairs in solution. This might also explain why increasing the precursor concentration does not have a major effect on the particle size, making the process easily scaled upward to produce more nanoparticles. X-ray powder diffraction indicates that the crystallite size of the ZnS is 1.2 – 1.6 nm. Thus, the particles of ZnS consist of much smaller grains. Transmission electron microscopy confirms the particle size obtained by dynamic light scattering.

INTRODUCTION

Nanometric materials have earned a good deal of attention recently, particularly semiconductor nanoparticles, due to electronic properties that change with particle size.[1-4] Sulfides smaller than about 10 nm have potential applications in light emitting diodes, photovoltaic cells, or luminescent materials, while larger sulfide particles in the range of 10-500 nm can be used in IR windows, photonic crystals, or with the proper dopants, in luminescent materials and resonance light scattering probes.[5-8] Numerous synthetic methods for the preparation of nanoscale binary sulfides have been reported in the literature.[9-13]

The large surface areas inherent with nanomaterials typically lead to aggregation, which reduces the surface energy. Therefore, capping agents must be used to stabilize the nanoparticles. The capping technique is well known and includes the use of polymers, micelles, organic ligands, porous materials, etc.[14-16] Dimethyl sulfoxide has been shown to be a promising stabilizing agent for metal sulfide nanoparticles, particularly CdS.[17]

There have been several studies on the use of single-source precursors for the growth of metal sulfide nanomaterials such as thin films[18] and nanowires[19] by chemical vapor deposition or by other means such as colloids in organic solution.[20-21] An advantage of the single-source approach is that it is a one-step synthesis whereas dual source precursors often suffer from premature reactions between the precursors, which can lead to inhomogeneity and stoichiometry control difficulties.[22] While much success has been accomplished with alkyldithiocarbamate single-source precursors,[23-25] the corresponding alkyldithiocarbonate precursors are even more promising due to their

typically lower decomposition temperatures. In this paper, we discuss the preparation of ZnS, which is one of the most important II-VI semiconductors, from the zinc ethylxanthate single source precursor in a DMSO solution. For zinc ethylxanthate, the Zn coordination sphere is comprised solely of sulfur, and the precursor decomposes at low temperatures to give nanometric ZnS.

EXPERIMENTAL

Materials. Reagent grade zinc sulfate heptahydrate (J. T. Baker), O-ethylxanthic acid, potassium salt (Aldrich), and 99.6+% dimethyl sulfoxide (Sigma-Aldrich) were obtained commercially and used as received without further purification. Zinc xanthate was generated by reacting aqueous solutions of zinc sulfate heptahydrate and potassium xanthate in a stoichiometric fashion as described in the literature.[26] Typically, $ZnSO_4 \bullet 7H_2O$ (5.00 g, 17.4 mmol) was dissolved in water (150 mL) and $KS_2COCH_2CH_3$ (5.57 g, 34.8 mmol) was dissolved in a similar amount of water. The potassium ethylxanthate solution was slowly poured into the zinc sulfate solution immediately generating the white zinc xanthate precipitate in a nearly quantitative yield (97.6 %). The solid was collected by vacuum filtration and washed thoroughly with water. The zinc xanthate was stored in a sealed glass bottle away from light and remained stable for several months. Carbon and hydrogen elemental analysis (Found: C, 23.3; H, 3.2. $C_6H_{10}O_2S_4Zn$ requires C, 23.4; H, 3.3 %).

Synthesis of ZnS suspensions in DMSO. ZnS solutions were prepared by dissolving $Zn(S_2COCH_2CH_3)_2$ in DMSO under ambient conditions. Both 0.1% and 1.0% solutions

were made and then filtered through a 0.2 μm nylon syringe filter to remove any impurities. The filtered solutions were placed in reaction flasks (typically 50 mL) and sealed before being placed in a preheated 60 °C oven for fifteen or thirty minute intervals. After each interval an adsorption spectrum was measured as well as determination of particle size by dynamic light scattering. NMR data were also collected at each interval. ^{1}H NMR chemical shifts for zinc ethylxanthate: δ 1.29, 4.35 (CH_3CH_2O-) (refer to Figure 4.6). ^{13}C NMR shifts for zinc ethylxanthate: δ 13.9, 69.7 (CH_3CH_2O-), 225.1 (-OCS_2-).

A powder sample for solid-state characterization was obtained by diluting the ZnS-DMSO suspension by half with toluene. After approximately 24 hours, the DMSO capped ZnS particles fell out of solution and were collected by centrifugation (4300 rpm). The resultant solid material was then washed repeatedly with toluene to remove any non-coordinated DMSO.

Characterization. For infrared spectroscopic measurements, roughly 10 mg of the zinc xanthate or capped zinc sulfide was mixed with approximately 100 mg FTIR-grade potassium bromide and the blend was finely ground. Spectra in the 4000-400 cm^{-1} region were collected by diffuse reflectance of the ground powder with a Nicolet Magna-IR 750 spectrometer. Typically, 128 scans were recorded and averaged for each sample (4.0 cm^{-1} resolution) and the background was automatically subtracted. Prominent IR adsorption signals for zinc xanthate (cm^{-1}): 2990(m), 2941(m), 2888(w), 1467(m, sh), 1442(s), 1383(m, sh), 1364(m), 1210(vs), 1126(vs), 1031(vs), 868(m), 817(m), 657(m), 451(s) (refer to Figure 8A).

Powder X-ray diffraction (XRD) measurements were obtained on a Bruker AXS D8 Advance diffractometer using Cu Kα radiation with an acceleration voltage of 40 kV and current flux of 30 mA. The diffractograms were recorded for a 2θ range of 17-70° with a step size of 0.02° and a counting time of 18 seconds per step. All the XRD patterns where collected at ambient temperature, and the phases were identified using the ICDD database.[27] The peaks were profiled with a Pearson 7 model using Topas P version 1.01 software.[28] The profiles of the standard and the sample were put into the Win-Crysize program version 3.05, which uses the Warren-Averbach evaluation method to determine crystallite size.[29,30]

The UV adsorption spectra of the xanthate and sulfide suspensions were measured with a Perkin-Elmer Lamda EZ201 spectrometer. Spectra were measured at 200 nm/min from 265-700 nm in a quartz cuvette for both the undiluted samples and samples diluted by a factor of 100.

A Horiba Jobin Yvon Fluorolog FL-1039 was used to measure the luminescence spectra of the ZnS-DMSO suspensions and isolated ZnS-DMSO powder. While many different excitation wavelengths were utilized, only spectra recorded for 365 nm excitation will be reported here. Chromaticity coordinates were determined using the 1931 Commission Internationale de l'Eclairage (CIE) color matching functions and corresponding color space map.

Transmission electron micrographs (TEM) were obtained using a JEOL JEM-100CXII electron microscope operated at 80 kV. The solid ZnS-DMSO particles isolated from solution were embedded in a polymer and sectioned before being placed on a carbon-coated copper TEM grid.

Dynamic light scattering (DLS) measurements were performed on the DMSO suspensions with a Malvern HPPS 3001 instrument at each thirty minute heating interval with one measurement performed after only 15 minutes. The reaction flask was allowed to cool to room temperature and 1.5 mL of the suspension was placed in a disposable sample cuvette. Particle size measurements were obtained at 27.0 °C with dispersant viscosity and refractive index values of 1.10 cP and 1.479 respectively.

Thermogravimetric analysis (TGA) was performed on the zinc xanthate complex at a rate of 2.0°/min from room temperature to 1000 °C using a Seiko Instruments Exstar 6200. Zinc xanthate does not melt congruently, but a well behaved decomposition curve was observed with a defined onset temperature, 115 ^{o}C.

GC/MS was performed on a Hewlett Packard G1800A instrument equipped with 30 m x 0.25 mm HP5 column. The helium flow rate was 1.0 ml/min and the injection port was set at 250 °C.

A Hach DR/890 Colorimeter was used to determine the amount of sulfate present on the zinc sulfide nanoparticles. The ZnS-DMSO particles were dissolved in hydrochloric acid and the solution was then brought to neutral before testing for sulfate.

Proton and carbon-13 NMR data were obtained using a 300 MHz Varian Gemini 2000 instrument. For ^{1}H NMR, 32 spectra were recorded per sample and automatically averaged, while for ^{13}C about 5000 spectra were collected. In both cases, the deuterated DMSO solvent was used as the reference point (2.49 ppm for proton and 39.50 ppm for carbon-13). Many liquid NMR spectra were collected with capped ZnS nanoparticles present in the sample, but no line broadening was observed in those cases. Solid state carbon-13 spectra were generated by a Chemagnetics CMX-II 300 MHz spectrometer.

RESULTS AND DISCUSSION

Preparation of ZnS nanoparticles from $Zn(S_2COCH_2CH_3)_2$. Size tunability of the ZnS particles – prepared from the low temperature decomposition of zinc xanthate in dimethyl sulfoxide – can be achieved by controlling the reaction time and temperature as well as the xanthate precursor concentration. Consequently, this method appears to be a versatile approach since it offers a sizeable degree of control for product formation. Figure 4.1 illustrates the effect of reaction time as well as precursor concentration on

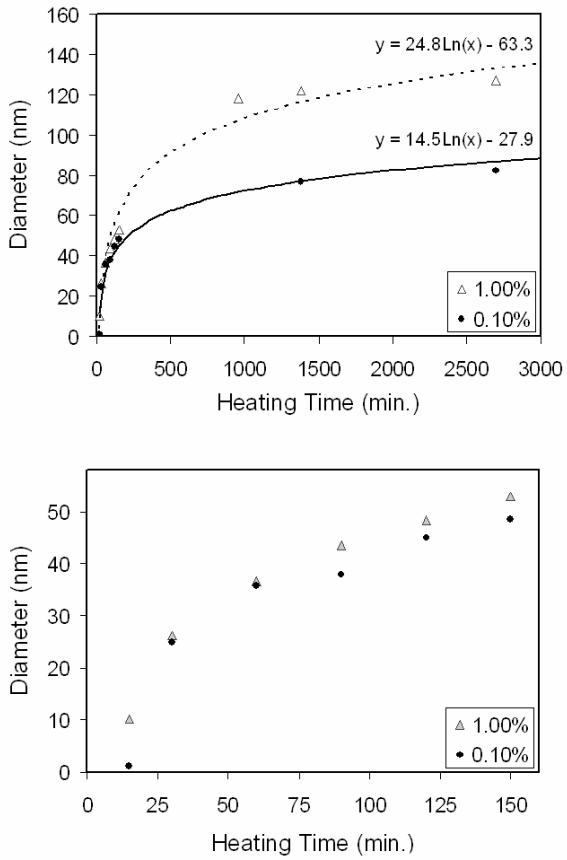

Figure 4.1: Average particle size of DMSO-capped ZnS versus heating time determined by DLS. The lower graph is a rescaled view for shorter heating times. The decomposition temperature used was 60 ^{o}C.

particle size as measured by dynamic light scattering. For both concentrations, the particle size increases with increasing time which seems to suggest that Ostwald ripening applies to both systems. However, proton NMR spectra collected at each time interval indicate that the decomposition is not complete after fifteen minutes, in fact approximately 95% of the ethylxanthate precursor remains, which means that the particle growth is likely due primarily to additional deposition of ZnS from the precursor as opposed to standard ripening. The deposition and growth follow a logarithmic increase – as the ZnS particles get bigger, the rate of diameter expansion slows. This type of particle growth is not uncommon and was first described by La Mer.[31] The zinc ethylxanthate concentration does not have much of an effect on the particle size for heating times greater than 15 minutes. This can be beneficial since a more concentrated solution of nanoparticles is desirable for many applications, and, if a lower concentration is required, this preparative approach will also be suitable. The particle growth levels off at about 110 nm for the 1.0% solution and 85 nm for the 0.1% solution.

In order to confirm that the dynamic light scattering measurements were accurate, TEM images were collected for the sulfide nanoparticles. Figure 4.2 shows a typical TEM image obtained from a ZnS-DMSO suspension. The specific image shown corresponds to a 1.0% starting xanthate concentration heated at 60 °C for 15 minutes. The particles are irregular in shape with diameters that vary from roughly 5 to 10 nm. Even with the shape variation, the average diameter from the micrograph compares well with the diameter measured using DLS (~ 10 nm), which assumes the particles are spherical. This finding leads us to believe that the DLS results are a reliable estimate of the actual particle size.

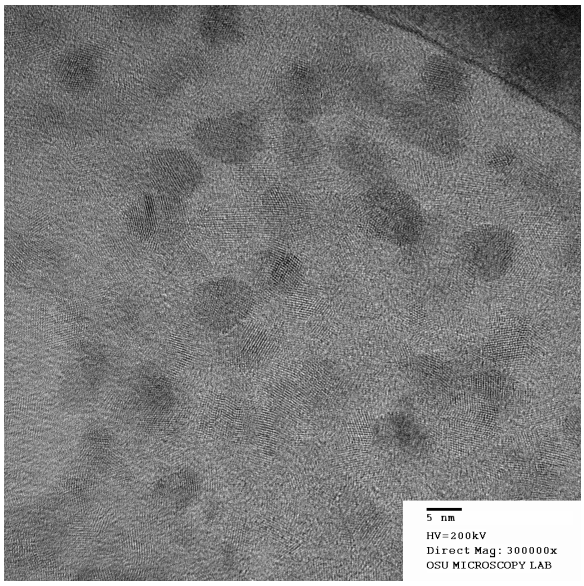

Figure 4.2: TEM image recorded at 200 kV of ZnS-DMSO using $Zn(S_2COCH_2CH_3)_2$ as the single-source precursor. The sample was a 1.0 % xanthate solution heated for 15 minutes.

To verify that ZnS was indeed the species forming in the DMSO suspension, X-ray powder diffraction (XRD) was performed on the isolated powder. The diffractograms shown in Figure 3 suggest that the ZnS is in the cubic (sphaelerite) phase for the particles grown in solution as well as the zinc sulfide generated from pyrolyzing zinc xanthate alone in air at 150 °C. The broad peaks can be ascribed to the small grain size of the particles. Average crystallite sizes were determined for the sulfides using the Warren-Averbach band-broadening method. The ZnS-DMSO particles had a crystallite size of 1.2 nm while the uncapped zinc sulfide size was estimated to be 1.6 nm. As to why the smaller peak at roughly 32.5° (Miller indices of 200) appears for the capped ZnS and not as much for the sample pyrolyzed from the ethylxanthate powder in air, we believe that there is a growth preference that is based on temperature. To explore this possibility an experiment was performed in which the zinc ethylxanthate was

decomposed in the DMSO at 150 °C rather than 60 °C. The 200 peak is no longer present in the diffractogram and the crystallite size is almost identical to that of the other ZnS-DMSO sample, 1.3 nm. The peak disappearance supports the hypothesis that the presence of this X-ray reflection is temperature dependent. The unresolved 200 peak from nanocrystalline ZnS in the cubic phase is common in the literature.[32, 33] It also seems odd that the 200 signal is narrower than the three other peaks. The origin of this anomalous X-ray pattern for nanocrystalline ZnS remains a mystery that is worthy of further investigation.

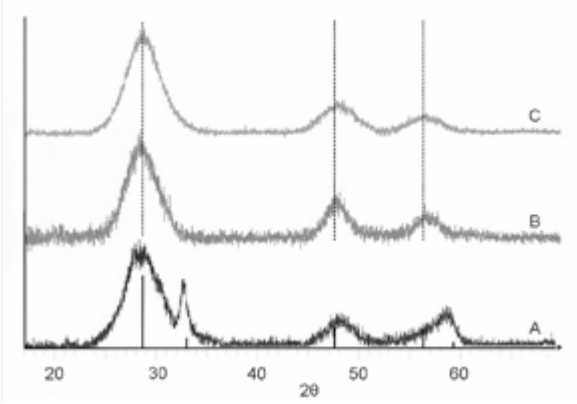

Figure 4.3: Powder X-Ray diffractograms for (A) ZnS-DMSO from the ethylxanthate in DMSO at 60 ^{o}C, (B) ZnS-DMSO from the ethylxanthate in DMSO at 150 ^{o}C, and (C) ZnS from the ethylxanthate fired alone in air at 150 ^{o}C. The vertical lines represent cubic ZnS, ICDD 05-0566.

To monitor the optical properties over time, UV adsorption spectra were recorded at regular intervals. Figure 4.4 details the disappearance of a peak at 370.5 nm and a shift in the band edge with time. The adsorption edge does change with decomposition time, which suggests that the ZnS particles are increasing in size. Band gap estimates calculated for the ZnS particles heated for 60, 90, and 150 minutes based on the UV data and are 3.68, 3.66, and 3.59 eV respectively. The modest change in gap energies is not

unexpected since the particles were 30 nm or bigger, which is slightly larger than the typical quantum dot limit. These band gap values are, however, in the typical zinc sulfide range.[34]

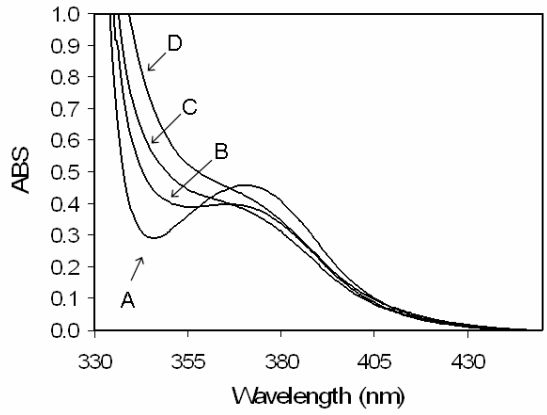

Figure 4.4: UV-Vis adsorption spectra of 0.1% zinc xanthate in DMSO over a 150 minute time period at 60 ^{o}C: (A) No heating, (B) 60 minutes, (C) 90 minutes, and (D) 150 minutes.

The decomposition of $Zn(S_2COCH_2CH_3)_2$. It has been suggested that xanthic acid and its derivatives decompose by way of the Chugaev[35] or Chugaev-like[36] reaction, Scheme 4.1. To see if our system behaved in a similar manner, the decomposition of the xanthate to the sulfide was monitored by thermogravimetric analysis, NMR spectroscopy, and GC-MS. Thermogravimetric analysis was performed on the solid zinc xanthate and the trace can be seen in Figure 4.5. The first derivative of the curve suggests decomposition occurs

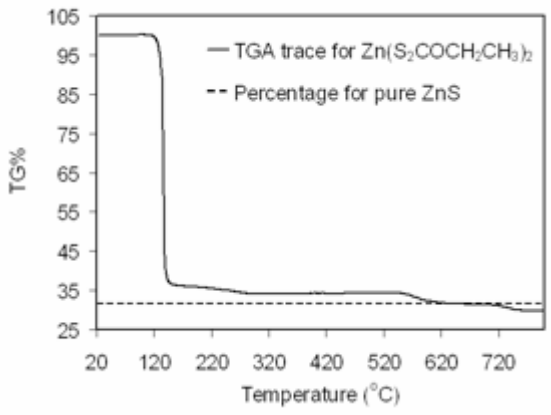

Figure 4.5: Thermogravimetric anaylsis trace of zinc ethylxanthate.

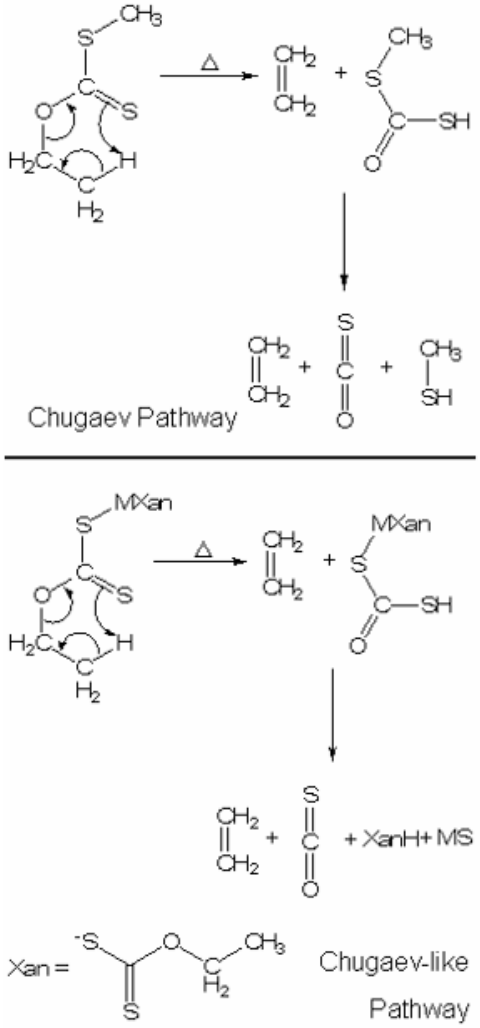

Scheme 4.1: The Chugaev (top) and Chugaev-like (bottom) decomposition pathways.

in a single step. Decomposition begins at a temperature of 115 °C and is virtually completed by 165 °C. The experimental mass loss at 165 ^{o}C is slightly lower than the loss calculated for ZnS formation even though XRD suggests that ZnS is the only compound present. However, the small discrepancy between measured and calculated weight loss can be partially explained by the presence of sulfate and possibly other xanthate decomposition products on the surface of the ZnS nanocrystals. For the ZnS-DMSO particles grown from the 1.0% solution, the amount of sulfate present was determined to be 2.3% by mass. This mass percentage suggests that about three in every one-hundred anions present in or on the ZnS particles are, in reality, sulfate ions.

The identity of the decomposition products were obtained from a headspace experiment using gas chromatography coupled with a mass spectrometer detector. Pure zinc xanthate was pyrolyzed in a sealed tube and the off-gases were measured. Ethylene is not detectable by our instrument, but heavier gases produced by the decomposition could be identified. Carbonyl sulfide was present, but interestingly an *O,S*-diethyldithiocarbonate (diethylxanthate) species was detected as well. Longer chain xanthates were tested and no olefins were detected as byproducts for zinc n-propyl or n-butylxanthate. This finding leads us to believe that the Chugaev mechanism, if present at all, is not the major elimination pathway. Proton and carbon-13 NMR were used to track the decomposition of the precursor in the DMSO suspension over time. Figure 4.6A shows the proton spectrum obtained from the 1.0% zinc xanthate in DMSO with no heating. As expected, the hydrogens from the two identical ethyl groups are the only signal present with the exception of water and DMSO. The spectrum obtained after 120 minutes of heating at 60 ^{o}C is shown in Figure 4.6B. The two signals that correspond to

the xanthate precursor are still present, but two new groups of peaks are also present. There are two new quartets at about 3.43 ppm and what appears to be one triplet at 1.04 ppm. Upon further heating and zooming in on the apparent triplet, it was observed that the signal at 1.04 ppm was actually two separate triplets. The ^{13}C spectra revealed similar results. With no heating, there were three peaks present arising from the ethyl groups (69.7 ppm, 13.9 ppm) and the dithiocarbonate carbon (225.1 ppm). After heating, three new peaks originated that correspond to ethyl groups and a dithiocarbonate carbon in slightly

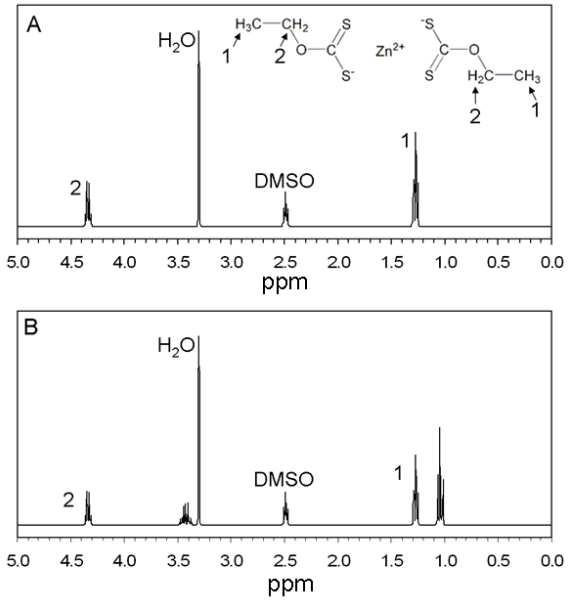

Figure 4.6: Proton NMR spectra of (A) a 1.0% solution of zinc xanthate in DMSO with no heating and (B) a 1.0% solution of zinc xanthate in DMSO heated at 60 ^{o}C for 120 minutes. The baselines in both spectra have been manually smoothed.

different environments than in the xanthate. The slight shift of the product ethyl groups from one another, which was present in the proton spectra is not as evident in the carbon-13 spectra. However that is not unexpected bearing in mind how small the shift in the ^{1}H spectrum is. Thus, it appears that the ethylxanthate decomposes to a species with two

distinct but very similar ethyl groups, which is consistent with the findings from the GC-MS. The elimination pathway for zinc ethylxanthate, by itself or in DMSO, does not appear to be Chugaev or Chugaev-like. Rather, the elimination products (Scheme 4.2) from the decomposition suggest an alkyl transfer from one xanthate ligand to another.

Figure 4.7 shows a plot of the zinc ethylxanthate concentration versus heating time as determined by ^{1}H NMR. It is apparent that with a an excess of DMSO, the elimination

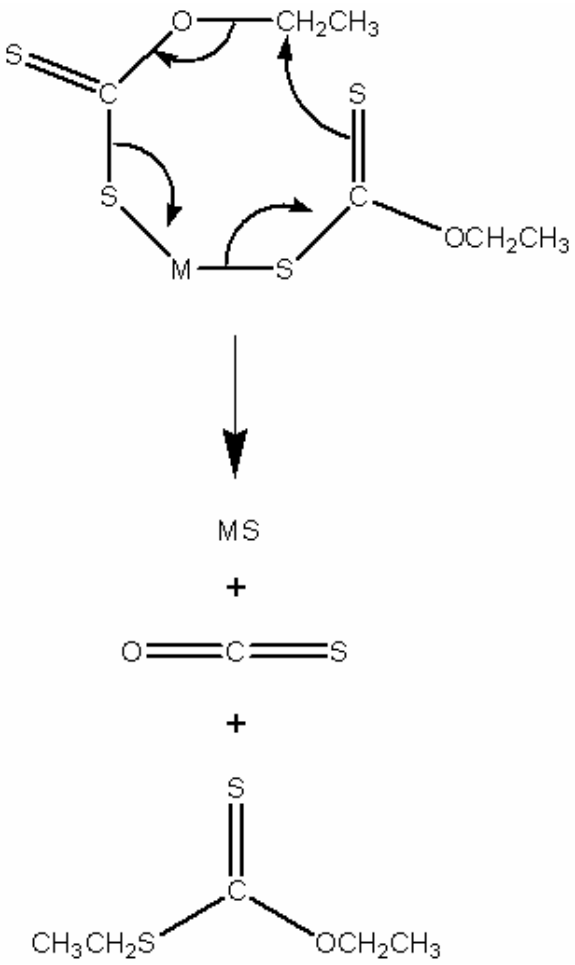

Scheme 4.2: Decomposition reaction for zinc ethylxanthate.

is first order. The rate law can be expressed in terms of zinc ethylxanthate concentration alone since the DMSO concentration is virtually unchanged throughout the experiment. The reaction was found to be first order in zinc ethylxanthate with a rate constant of 4.4×10^{-3} min^{-1} or 7.3×10^{-5} s^{-1} at 60 ^{o}C.

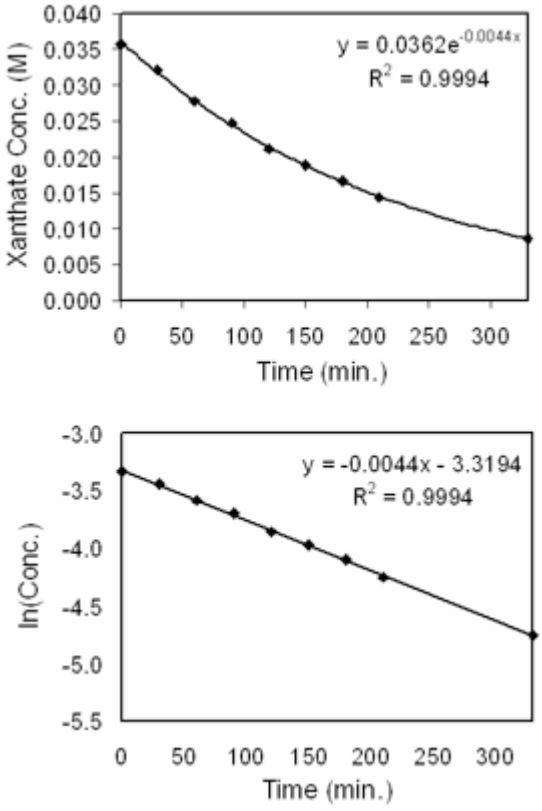

Figure 4.7: Plots of zinc ethylxanthate concentration versus time (top) and the natural log of the xanthate concentration versus time (bottom) for a 1.0% solution in DMSO heated at 60 ^{o}C.

DMSO bonding in the ZnS-DMSO complex. The surface properties of the ZnS prepared from the xanthate in DMSO were examined by IR and NMR spectroscopies. Both IR and NMR are effective tools for determining the nature of the DMSO coordination to the ZnS since pure ZnS shows virtually no adsorption in the typical IR

energy range and obviously has no signal in a proton or ^{13}C NMR spectrum. As has been shown in previous studies with CdS[17,37] the most prominent features in the IR spectrum for the capped ZnS are the S-O stretching bands. Free DMSO in the gas phase has been shown to exhibit a very strong band at 1050 cm^{-1} that is fairly broad while the S-coordinated signal is blue shifted and O-bonded complexes show an opposing Stokes shift.[37] Figure 4.8A is the IR adsorption spectrum for zinc xanthate and Figure 4.8B is that of ZnS-DMSO. The adsorption frequencies for metal xanthate species have been studied and reported,[38-41] and the spectrum shown matches well with the previous studies. Taking into consideration IR research reported for complexes with sulfoxide ligands,[42] peaks in the range of 620 cm^{-1} to 800 cm^{-1} are assigned to symmetric and asymmetric C-S stretching. The peaks associated with the symmetric and asymmetric CH_3 deformation appear at roughly 1300 to 1550 cm^{-1}. The strong peaks at 1120 wavenumbers correspond to the stretching of the S-O bond. The anti-Stoke shift of the S-O bond compared to that of free dimethyl sulfoxide implies that the bond order increased, which can be explained by coordination through the sulfur atom. However, DMSO may not be the species giving rise to the signals at 1120 cm^{-1}, but rather the absorbance could be due to sulfate on the surface of the ZnS particles. Likewise, the signals in the region of 950 to 1050 cm^{-1} can be assigned to many possible species. Free DMSO, O-bonded DMSO, oxidized sulfur species such as sulfites and sulfates, or CH_3 rocking movements are possible. However, since the peak signal does not significantly decrease after excessive toluene washings, it seems unlikely to be free DMSO.

To help further understand the bonding of the DMSO, a sample of the ZnS was made in d_6-DMSO and an IR spectrum was obtained (Figure 4.9A). As expected, since

deuterium is heavier than hydrogen, the CH_3 peaks at just fewer than 3000 cm^{-1} moved to lower frequencies. Additionally, the peak at 953 cm^{-1} significantly shifted to a lower energy suggesting that it was due to CH_3 rocking as opposed to an S-O motion.

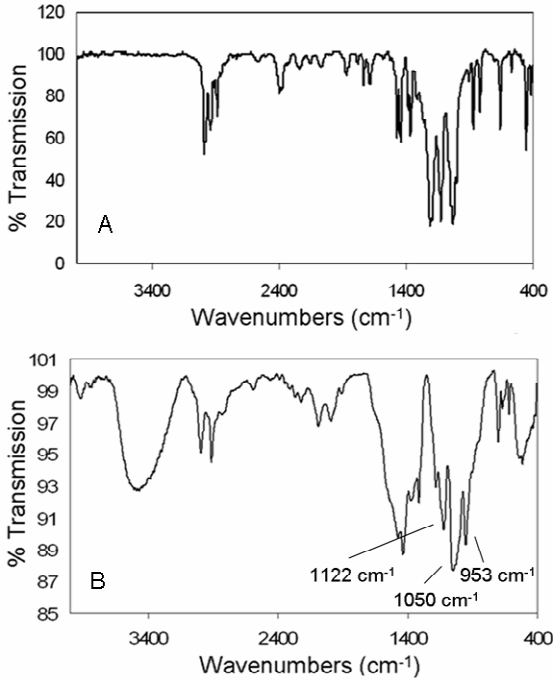

Figure 4.8: Infrared adsorption spectra of (A) zinc ethylxanthate and (B) ZnS-DMSO.

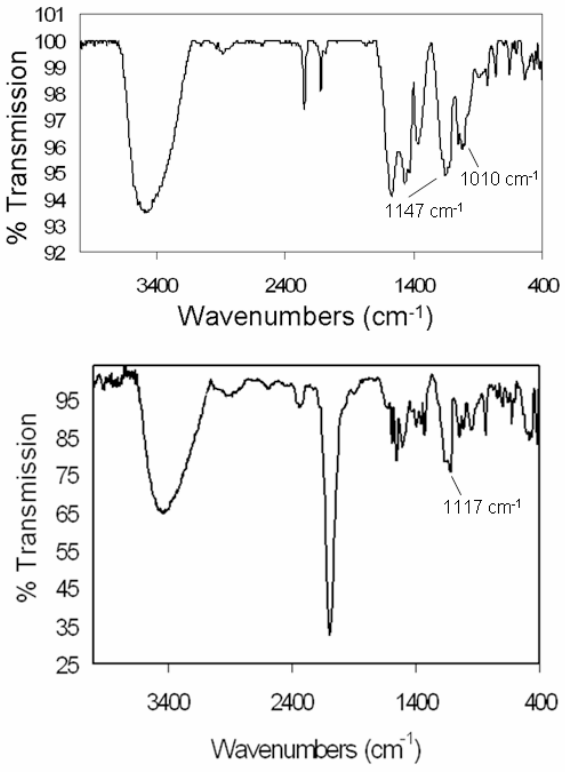

Figure 4.9: Infrared adsorption spectra of (A) ZnS-d_6-DMSO and (B) ZnS-DMSO after washing extensively with water and acetone.

However, strong signals on either side of 1050 cm^{-1} were still present. To distinguish the S-O signals arising from Zn-DMSO from the $ZnSO_4$ bands, the ZnS-DMSO nanoparticles were thoroughly washed with both water and acetone several times. Solid state carbon-13 NMR confirmed that there was no DMSO present after the acetone washings. Figure 4.9B shows the infrared spectrum of the water and acetone washed ZnS-DMSO. The S-O region is clearly different than that of figure 8B, and it is also apparent that a significant amount of that region is due to the presence of sulfate. The solid state NMR results (Figure 4.10) indicated that there was a small amount of carbon-

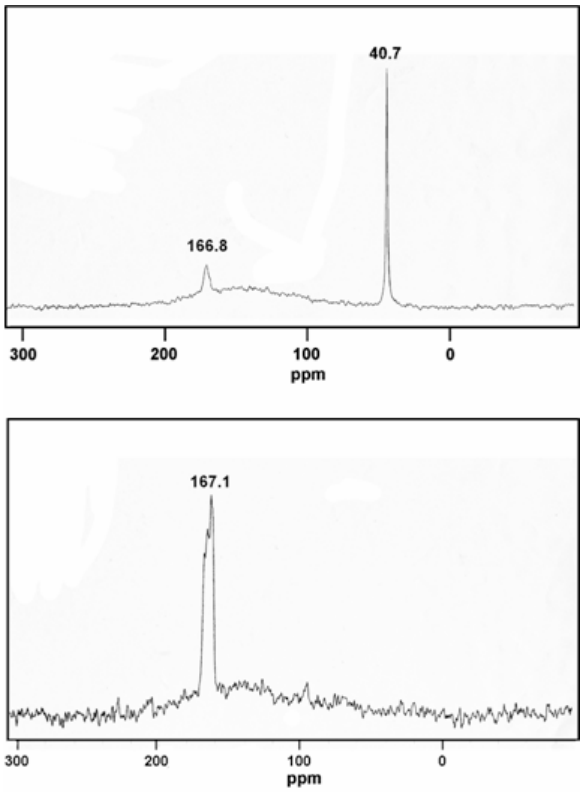

Figure 4.10: ^{13}C solid state NMR spectra for toluene-washed ZnS-DMSO (top) and water/acetone-washed ZnS-DMSO (bottom).

containing ethylxanthate decomposition products present on the particles. For the toluene washed ZnS, the dimethyl sulfoxide peak is present along with a signal at roughly 166.8 ppm. For the water and acetone washed ZnS, the DMSO peak disappears while the signal at 167.1 ppm remains. A likely assignment for the signal at 166.8 ppm is $[CO_xS_{3-x}]^{2-}$ (where x = 1, 2, or 3) since no alkyl peaks are present. Indeed, it has been shown that carbonate on the surface of zinc chalcogenides has a carbon-13 NMR signal at 166.9 ppm.[43] Thus, it can be concluded that the ZnS surface contains carbonate regardless of the washing method. The C-O-C=S linkage in dithiocarbonates usually appears in the 1030 to 1120 cm^{-1} region[37-40] overlapping the sulfoxide and sulfate S-O bands. These dithiocarbonate bands are negligible since sulfate is present on the ZnS nanoparticles in a

much greater amount than the dithiocarbonate and we believe the peaks from 1030 to 1120 cm^{-1} are due primarily to DMSO and sulfate bound to the surface. At this point, it is difficult to make a definite statement about the nature of the DMSO bonding as to whether it is through sulfur, oxygen, or a combination of the two. A subtraction of the water/acetone washed ZnS-DMSO spectrum (Figure 4.9B) from the toluene washed spectrum (Figure 4.8B) should give an estimate of which peaks were lost by the removal of dimethyl sulfoxide. This subtraction result is shown in Figure 4.11, and it seems to indicate that both bonding schemes are present since there are peaks at roughly 1030 cm^{-1} (suggesting bonding through oxygen) and at about 1190 cm^{-1} (suggesting bonding through sulfur).

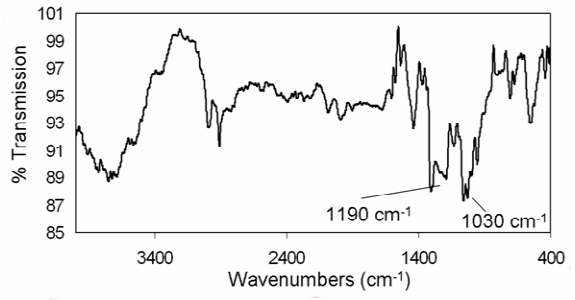

Figure 4.11: Infrared asorption spectrum obtained from the subtraction of the water/acetone washed ZnS-DMSO particles from the toluene washed ZnS-DMSO particles.

Material application: broad luminescence. As mentioned in the introduction, one of the many possible uses of II-VI semiconductor nanoparticle materials is that of light emission. When a long-wave mercury lamp is used as an excitation source, the ZnS-DMSO particles exhibit white-light emission. When a solid sample of ZnS-DMSO is

excited with 365 nm ultraviolet light, the luminescence profile spans the entire visible portion of the spectrum (Figure 4.12). While the quantum efficiency is rather low

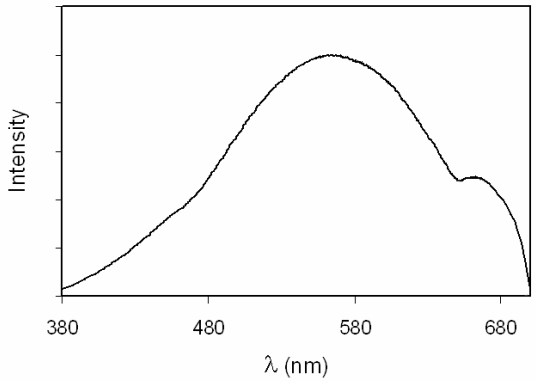

Figure 4.12: Fluorescence spectra of solid ZnS-DMSO nanoparticles when excited with 365 nm radiation.

(<10%), the chromaticity coordinates are (0.38, 0.44) which are within the white-light area of the CIE color space map although slightly biased towards the yellow region. As such, the emission has a very suitable color to fluorescent lighting. These chromaticity coordinates are based solely on 365 nm excitation. The solid used for luminescence measurements was a 1.0% zinc ethylxanthate solution heated for two hours. Smaller particles would likely shift the emission curve toward the blue due to quantum confinement. A worthwhile experiment to do in the future would be to monitor the fluorescence profile and chromaticity coordinates of ZnS-DMSO particles with respect to particle diameter.

CONCLUSIONS

Although xanthates are beginning to be used more and more as precursors for metal sulfides, this appears to be the first report that describes the combination of zinc ethylxanthate and dimethyl sulfoxide to prepare zinc sulfide nanoparticles. Very stable suspensions of ZnS nanoparticles were prepared in the size range of approximately 2 to 125 nm by dissolving zinc ethylxanthate in DMSO and heating to 60 ^{o}C. Interestingly, the concentration of the precursor had little influence on the ultimate particle size, suggesting an atypical growth mechanism as compared to other methods of synthesis of nanometric sulfides. The zinc sulfide produced from the thermal decomposition of the ethylxanthate precursor adopted the cubic crystal phase whether prepared in DMSO or by solid state thermal decomposition. As opposed to standard Ostwald ripening, the increase in particle size with heating time discussed here is due principally to the rate of decomposition of the xanthate precursor. In light of UV adsorption experiments the bandgap of the sulfide nanoparticles depends on their size as expected for such systems.

The decomposition pathway of the zinc ethylxanthate does not follow the Chugaev elimination mechanism, but rather proceeds by an ethyl transfer from one xanthate ligand to the other. The production of carbonyl sulfide from the decomposition renders the process virtually irreversible. The disappearance of the xanthate in DMSO follows a first-order rate law with a rate constant equal to 7.3×10^{-5} s^{-1}. These facts suggest that individual zinc xanthate complexes decompose in solution to produce zinc sulfide monomer ion-pairs that subsequently deposit on the growing particles. If this is the case, it appears to have a strong influence of the nucleation and growth of the

nanoparticles so that a 10-fold increase in precursor concentration has a minimal influence on the particle size.

While it is clear that DMSO attaches to the surface of the ZnS particles when the particles are grown in the DMSO itself, the nature of that attachment is not perfectly clear. The formation of sulfate from the oxidation of the sulfide complicates the bonding picture as well does the xanthate byproducts that are present on the surface after pyrolysis. Regardless, it is plain to see that dimethyl sulfoxide and most likely other similar molecules can be used as stabilizing agents for metal sulfide nanoparticles.

REFERENCES

[1] H. Gleiter, *Prog. Mater. Sci.,* 1989, **33**, 223.

[2] M. A. El-Sayed, *Acc. Chem. Res.,* 2004, **37**, 326.

[3] R. Rossetti, S. Nakahara and L. E. Brus, *J. Chem. Phys.*, 1983, **79**, 1086.

[4] R. Rossetti, J. L. Ellison, J. M. Gibson and L. E. Brus, *J. Chem. Phys.*, 1984, **80**, 4464.

[5] C. Feldmann and C. Metzmacher, *J. Mater. Chem.*, 2001, **11**, 2603.

[6] L. Wang, F. Xu, Y. Zhou, L. Wang and Y. Liu, *Spectrochim. Acta Part A,* 2004, **60**, 2141.

[7] Y. Xia, B. Gates, Y. Yin, and Y. Lu, *Adv. Mater.*, 2000, **12**, 693.

[8] W. Huynh, X. G. Peng and A. P. Alivisatos, *Adv. Mater.*, 1999, **11**, 923.

[9] Y. Ohko, M. Setani, T. Sakata, H. Mori and H. Yoneyama, *Chem. Lett.*, 1999, **(7)**, 663.

[10] C. Lu, N. Wu, F. Wei, X. Zhao, X. Jiao, J. Xu, C. Luo and W. Cao, *Adv. Funct. Mater.*, 2003, **13**, 548.

[11] Q. Li, Y. Ding, M. Shao, J. Wu, G. Yu and Y. Qian, *Mater. Res. Bull.*, 2003, **38**, 539.

[12] W. Zhang, Z. Yang, J. Liu, Y. Qian, W. Yu, Y. Jia, X. Liu, G. Zhou and J. Zhu, *J. Solid State Chem.*, 2001, **161**, 184.

[13] H. J. Yuan, S. S. Xie, D. F. Liu, D. F. Yan, Z. P. Zhou, L. J. Ci, J. X. Wang, Y. Gao, L. Song, L. F. Liu, W. Y. Zhou and G. Wang, *J. Crystal Growth*, 2003, **258**, 225.

[14] S. Wageh, Z. S. Ling and X. Xu-Rong, *J. Crystal Growth*, 2003, **255**, 332.

[15] Calandra, P.; Longo, A.; Liveri, V. T. *J. Phys. Chem. B* **2003**, *107*, 25.

[16] J. Zhang, B. Han, Z. Hou, Z. Liu, J. He and T. Jiang, *Langmuir,* 2003, **19**, 7616.

[17] M. E. Wankhede and S. K. Haram, *Chem. Mater.*, 2003, **15**, 1296.

[18] J. Cheon, D. S. Talaga and J. I. Zink, *J. Am. Chem. Soc.*, 1997, **119**, 163.

[19] Y. W. Koh, C. S. Lai, A. Y. Du, E. R. T. Tiekink and K. P. Loh, *Chem. Mater.*, 2003, **15**, 4544.

[20] S. Efrima and N. Pradham, *C. R. Chimie*, 2003, **6**, 1035.

[21] S. P. Nair, T. Radhakrishnan, N. Revaprasadu, G. A. Kolawole and P. O'Brien, *Polyhedron*, 2003, **22**, 3129.

[22] H. Kukimoto, *J. Cryst. Growth,* 1991, **107**, 637.

[23] M. Lazell, S. J. Nørager, P. O'Brien and N. Revaprasadu, *Materials Science & Engineering C,* 2001, **16**, 129.

[24] M. A. Malik, N. Revaprasadu and P. O'Brien, *Chem. Mater.*, 2001, **13**, 913.

[25] L. V. Zavyalova, A. K. Savin and G. S. Svechnikov, *Displays,* 1997, **18**, 72.

[26] S. R. Rao, in *Xanthate and Related Compounds*; Dekker: New York, 1971.

[27] "Powder Diffraction File (PDF-2)" (The International Centre for Diffraction Data, Newtown Square, PA), File No. 05-0566.

[28] Topas P Version 1.0.1, 1998, Bruker AXS, GmbH.

[29] B. E. Warren and B. L. Averbach, *J. Appl. Phys.*, 1950, **21**, 595.

[30] B. E. Warren, *Prog. Met. Phys.,* 1959, **8**, 147.

[31] Johnson, I.; LaMer, V. K. *Journal of the American Chemical Society* **1947**, *69*, 1184-92.

[32] Y. He, *Mater. Res. Bull.,* 2005, **40**, 629.

[33] P. S. Khiew, S. Radiman, N. M. Huang, M. S. Ahmad and K. Nadarajah, *Mater. Lett.,* 2005, **59**, 989.

[34] R. Zhang, B. Wang, H. Zhang and L. Wei, *Appl. Sur. Sci.,* 2005, ***241***, 435.

[35] C. H. DePuy and R. W. King, *Chem. Rev.,* 1960, **60**, 431.

[36] N. Pradhan, B. Katz and S. Efrima, *J. Phys. Chem. B,* 2003, **107**, 13843.

[37] R. Elbaum, S. Vega and G. Hodes, *Chem. Mater.,* 2001, **13**, 2272.

[38] G. W. Watt and B. J. Mcormick, *Spectrochim. Acta.,* 1965, **21**, 753.

[39] L. H. Little, G. W. Poling and J. Leja, *Can. J. Chem., 1961*, **39**, 745.

[40] M. L. Shankaranarayana and C. C. Patel, *Spectrochim. Acta.,* 1965, **21**, 95.

[41] M. L. Shankaranarayana and C. C. Patel, *Can. J. Chem.,* 1961, **39**, 1633.

[42] F. A. Cotton, R. Francis and W. D. Horrocks, *J. Phys. Chem.,* 1960, **64**, 1534.

[43] A. Bagabas, Ph.D. Thesis, Oklahoma State University, Stillwater, 2005.

CHAPTER 5

BROADBAND LUMINESCENCE FROM HIGH SURFACE AREA ZINC SULFIDE AND ZINC OXIDE

Zinc sulfide with a surface area greater than 350 m^2g^{-1} was prepared from the low temperature thermal decomposition of zinc ethylxanthate. The nanocrystalline ZnS (1.5 nm) exhibits broadband white-light luminescence when excited with ultraviolet or near-ultraviolet radiation. Dopants such as Mn^{2+} and Al^{3+}, which are typically used to enhance ZnS luminescence intensity, surprisingly hinder the emission. Thus, it appears that the photoluminescence mechanism is dependent on surface phenomena. When the zinc ethylxanthate is pyrolyzed at temperatures greater than 500 ^oC, nanocrystalline zinc oxide (13.4 nm) is formed. The zinc oxide also exhibits broadband fluorescence that is red shifted from the zinc sulfide by about 40 nm. Factors influencing the surface area and luminescence of ZnS and ZnO will be discussed. In addition to emission and excitation spectroscopy, powder X-ray diffraction, thermogravimetric analysis, nuclear magnetic resonance spectroscopy, and BET surface area analysis were the primary characterization techniques used in this study.

INTRODUCTION

Increasing importance has been placed on new materials that can emit white light due to their potential uses in various displays and future solid state light sources. Energy demand is one of the main driving forces for the development of pure white-light emitting materials.[1] There are a number of ways to achieve white-light phosphors, each with advantages and disadvantages. For instance, the traditional coatings on fluorescent bulbs have been mixtures of rare-earth containing oxides[2] or doped calcium halophosphates.[3,4] Not only is cost an issue in such mixtures, but problems can arise from stiochiometry control and complicated doping schemes. More recently, mixtures of semiconductor nanocrystals have been used as emitters in light emitting diode (LED) devices.[5,6] While semiconductor nanocrystals have respectable fluorescence efficiencies and molar absorptivities, mixtures of nanocrystals that produce white light often suffer from self absorption, which decreases overall efficiency.[5,7] Coating a blue emitter, such as InGaN, with a broadband yellow phosphor, such as $Y_3Al_5O_{12}$:Ce, is a widely used method for fabricating a white-light LED.[8-11] Organic light emitting diodes (OLEDs)[12,13] and polymer light emitting diodes (PLEDs)[14] are also often used to prepare white emitting materials. However, there is still a need to develop a method to produce a white-light phosphor that is cost-effective, does not require mixtures or elaborate doping schemes, and does not depend on difficult synthetic procedures.

Ultra small CdSe has been shown to emit white light (420-710 nm) without exhibiting the drawback of self absorption.[15] The luminescence mechanism attributed to the "magic-sized" CdSe is dependent on the surface of the nanocrystals.[15-17] Similarly, it has been demonstrated that ZnSe quantum dots can also act as a white-light phosphor.[18]

These CdSe and ZnSe findings are encouraging since they present a way of generating white light that does not rely on the combination of multiple phosphors or dopants, but in both cases organic coordinating agents (e.g. trioctylphosphine oxide) are necessary to stabilize the phosphors.

Typically, nanoscale ZnS gives off blue[19-21] light when exposed to ultraviolet radiation, but with proper size control and dopant composition, other colors can be obtained.[22-24] We present broadband emission from ZnS nanocrystals grown from the low temperature thermal decomposition of the single-source precursor, zinc ethylxanthate. This method does not require organic solvents or coordinating agents, nor does it require an inert environment.

EXPERIMENTAL

Materials. Reagent grade zinc sulfate heptahydrate (J. T. Baker), aluminum nitrate nonahydrate (Alfa Aesar), manganese chloride tetrahydrate (Mallinckrodt), and O-ethylxanthic acid, potassium salt (potassium xanthate) (Aldrich) were obtained commercially and used as received without further purification. Bulk zinc sulfide (Alfa Aesar) in the cubic phase and nanocrystalline zinc sulfide (MC&B) in the hexagonal phase were used for comparison. Zinc ethylxanthate was generated by reacting aqueous solutions of zinc sulfate and potassium xanthate in a stoichiometric fashion as described in the literature.[25] Typically, $ZnSO_4 \bullet 7H_2O$ (5.00 g, 17.4 mmol) was dissolved in water (150 mL) and $KS_2COCH_2CH_3$ (5.57 g, 34.8 mmol) was dissolved in a similar amount of water. The potassium xanthate solution was slowly poured into the zinc sulfate solution immediately generating the white zinc xanthate, $Zn(S_2COCH_2CH_3)_2$, precipitate nearly

quantitatively (97.6 %). The solid was collected by vacuum filtration and washed thoroughly with water. The zinc xanthate was stored in a sealed glass bottle away from light and remained stable for several months. Carbon and hydrogen elemental analysis (Found: C, 23.3; H, 3.2. $C_6H_{10}O_2S_4Zn$ requires C, 23.4; H, 3.3 %).

Synthesis of neat ZnS, doped ZnS, and ZnO. Cubic ZnS was obtained by heating freshly prepared $Zn(S_2COCH_2CH_3)_2$ in air at temperatures ranging from 125-400 °C. Specifically, 2.00 g of zinc ethylxanthate were placed in a ceramic crucible and heated for two hours at the desired temperature. At temperatures above 400 °C, ZnO begins to form. The solid was ground into a fine powder and used as is. Mn^{2+} and Al^{3+} dopants were individually incorporated into the xanthate precursor (from the chloride and nitrate salts respectively) in concentrations of zero to three mole percent.

To obtain nanocrystalline ZnO in the hexagonal phase, $Zn(S_2COCH_2CH_3)_2$ was pyrolyzed in air at 600 °C or higher. Firing the zinc xanthate between roughly 450 and 550 °C yields a mixture of the sulfide and the oxide. Table 5.1 contains the relevant experimental data for the preparation of ZnS and ZnO samples at different temperatures.

Table 5.1: Thermolysis reaction details for zinc ethylxanthate (reaction time = 2 hours).

Precursor	Pyrolysis Temperature (°C)	Precursor Mass (g)	Product Mass (g)	Ceramic Yield	Product ID
zinc ethylxanthate	125	2.004	0.776	38.7	ZnS
	150	2.003	0.763	38.1	ZnS
	175	2.010	0.740	36.8	ZnS
	300	1.998	0.679	34.0	ZnS
	400	2.001	0.682	34.1	ZnS
	500	2.001	0.600	30.0	ZnS, ZnO
	600	2.000	0.586	29.3	ZnO
	700	2.009	0.542	27.0	ZnO

Characterization. A Horiba Jobin Yvon Fluorolog FL-1039 was used to measure the fluorescence emission spectra of the ZnS, doped ZnS, and ZnO solids. Powder samples were used for all measurements. An equal volume of solid was used for each scan. Three different excitation wavelengths (340 nm, 365 nm, and 425 nm) were utilized and the emission spectra were recorded in the ranges of 365-650 nm, 400-700 nm and 450-700 nm respectively.

Powder X-ray diffraction (XRD) measurements were obtained on a Bruker AXS D8 Advance diffractometer using Cu Kα radiation with an acceleration voltage of 40 kV and current flux of 30 mA. The diffractograms were recorded for a 2θ range of 17-70° with a step size of 0.02° and a counting time of 18 seconds per step. All the XRD patterns where collected at ambient temperature, and the phases were identified using the ICDD database.[26] The peaks were profiled with a Pearson 7 model using Topas P version 1.01 software.[27] The profiles of the standard and the sample were put into the Win-Crysize program version 3.05, which uses the Warren-Averbach evaluation method to determine crystallite size.[28,29]

The specific surface areas were obtained with a conventional Brunauer-Emmett-Teller (BET) multilayer nitrogen adsorption method using a Quantachrome Nova 1200 instrument.

Thermogravimetric analysis (TGA) was performed on the zinc xanthate complex at a rate of 2.0°/min from room temperature to 1000 °C using a Seiko Instruments Exstar 6200. Zinc xanthate exhibited a well behaved decomposition curve with a defined onset temperature of about 115 ^{o}C.

GC/MS was performed on a Hewlett Packard G1800A instrument equipped with 30 m x 0.25 mm HP5 column. The helium flow rate was 1.0 ml/min and the injection port was set at 250 °C.

A Hach DR/890 Colorimeter was used to determine the amount of sulfate present on the zinc sulfide nanoparticles. The ZnS particles were dissolved in hydrochloric acid and the solution was then brought to neutrality before testing for sulfate.

For infrared spectroscopic measurements, roughly 30 mg of the 150 °C zinc xanthate firing product (ZnS) was mixed with approximately 100 mg FTIR-grade potassium bromide and the blend was finely ground. Spectra in the 4000-400 cm^{-1} region were collected by diffuse reflectance of the ground powder with a Nicolet Magna-IR 750 spectrometer. Typically, 128 scans were recorded and averaged for each sample (4.0 cm^{-1} resolution) and the background was automatically subtracted. Prominent IR adsorption signals for the xanthate pyrolysis product (cm^{-1}): 2961(s), 2921(s), 2873(s), 1451(s), 1263(vs), 1124(vs), 1039(m, sh), 973(s), 929(m, sh), 767(w), 619(w), 455(m).

Solid state carbon-13 spectra were generated by a Chemagnetics CMX-II 300 MHz spectrometer.

RESULTS AND DISCUSSION

Thermogravimetric anaylsis of $Zn(S_2COCH_2CH_3)_2$ and powder X-ray diffraction patterns of the solid decomposition products. Thermogravimetric analysis was performed on the solid zinc ethylxanthate and the trace can be seen in Figure 5.1. The first derivative of the curve suggests decomposition occurs in a single step. The elimination begins at a temperature of 115 °C and is virtually completed by 165 °C. A

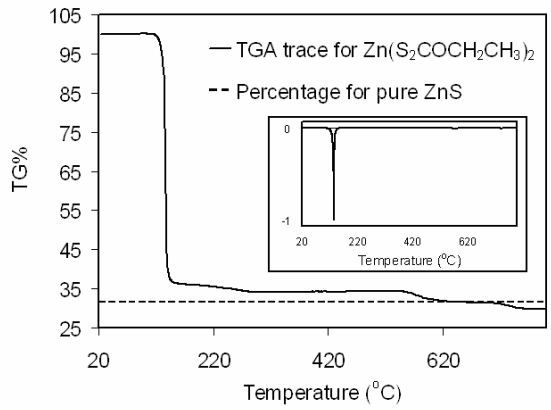

Figure 5.1: Thermogravimetric analysis trace of zinc xanthate. The inset shows the normalized first derivative of the TGA trace.

more detailed account of the decomposition pathway can be found elsewhere in this dissertation. The experimental mass loss at 165 °C is slightly lower than the loss calculated for ZnS formation. However, the small discrepancy between measured and calculated weight loss can be explained by the presence of sulfate and possibly other xanthate decomposition products on the surface. In fact, a colorimetery experiment indicated that sulfate made up over 0.6% of the ZnS mass. This percentage, based on pure ZnS, indicates that roughly one out of every 160 anions present in or on the ZnS particles are, in reality, sulfate ions. Additionally, elemental analysis performed on the firing product of zinc ethylxanthate (pyrolysis temperature of 150 °C) demonstrated the

following percentages: C, 6.0; H, 1.2; S, 30.8 %. Pure zinc sulfide requires a sulfur percentage of 32.9 %.

Since carbonaceous species were present on the xanthate firing product, solid state carbon-13 NMR spectroscopy was used to help determine the carbon environments. Figure 5.2 is the carbon-13 NMR spectrum of the 150 °C ethylxanthate pyrolysis product.

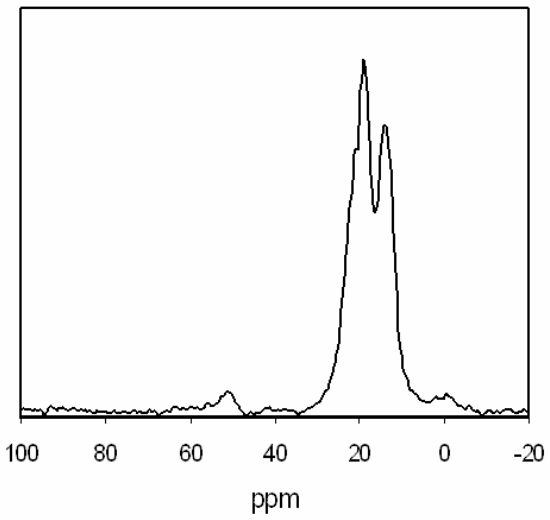

Figure 5.2: Solid state carbon-13 NMR spectrum of the zinc xanthate pyrolysis product. The firing temperature used was 150 °C.

The primary signals found at roughly 14 and18 ppm confirm the presence of carbon-containing species and can most likely be attributed to ethylthio zinc species that were formed during the decomposition process. This assignment is based on calculations performed with ChemNMR[30] software, which indicated that for bis(ethylthio)zinc there should be two carbon-13 signals, one at about 15 ppm and the second at roughly 17 ppm. An ethyl arrangement is consistent with the decomposition pathway (refer to chapter 2) and the molar ratio of hydrogen to carbon, based on the elemental analysis, is 2.4 (ethyl requires 2.5). Thus, it appears likely that ethyl groups generated by the zinc xanthate

decomposition attach to ZnS particles through the sulfur. However, it is doubtful that the only carbon-containing species on the surface of the particles is ethylthio zinc. Diethyl sulfone, diethyl sulfoxide, diethyl sulfide, and diethyl disulfide are also possible decomposition products, and the two former compounds have predicted carbon-13 NMR signals at roughly 45 and 10 ppm. The presence of the sulfone or the sulfoxide would explain the small NMR signal that is found at 46 ppm. A sample of the headspace gases produced by firing zinc xanthate was examined by GC/MS, and the major components detected were diethyl sulfide and diethyl disulfide. When methylene chloride was mixed with the pyrolysis product, and the liquid extract was analyzed with GC/MS, the primary compound identified was diethyl disulfide along with trace amounts of diethyl sulfone. Finally, infrared spectroscopy was used to inspect the 150 °C ethylxanthate pyrolysis product. The infrared spectra confirmed the presence of $-CH_2-$ and $-CH_3$ groups but also indicated that some combination of diethyl sulfone, diethylsulfoxide, and even intact zinc ethylxanthate could be present as well.

Thus it appears, at a pyrolysis temperature of 150 °C, zinc sulfide is formed with various xanthate decomposition products attached to the surface such as diethyl sulfide, diethyl disulfide, and diethyl sulfone along with sulfate and perhaps some unreacted zinc ethylxanthate. Incorporating all the information related to the 150 °C xanthate firing product from elemental anaylsis and ceramic yields, the overall mass composition is: Zn, 55.3; S, 30.8; C, 6.0; H, 1.2; O, 6.7 %.

To verify that ZnS was indeed the primary species formed by the thermal decomposition, XRD patterns were obtained on the powders. The diffractogram shown in Figure 5.3 suggests that the ZnS is in the sphaelerite or cubic phase for the particles

prepared by pyrolyzing zinc ethylxanthate in air at 150 °C. The broad peaks can be credited to the small grain size of the particles. The average crystallite size was estimated

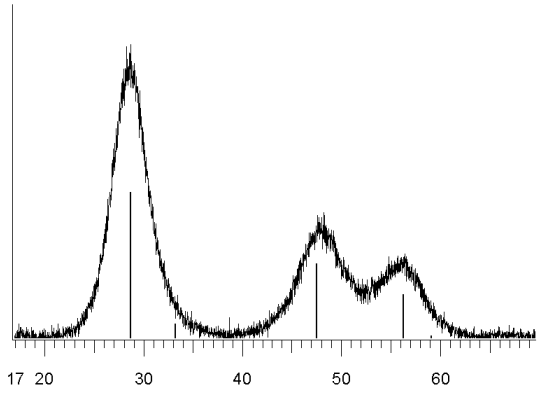

Figure 5.3: Powder X-ray diffraction pattern of nanocrystalline ZnS. The ZnS is the result of pyrolyzing zinc xanthate at 150 °C. The vertical lines represent cubic ZnS, ICDD 05-0566.

for the ZnS using the Warren-Averbach band-broadening method. The sulfide particles had an average crystallite size of 1.5 nm. As one might expect, heating at higher temperatures caused the ZnS crystallite size to increase. The XRD patterns shown in Figure 5.4 demonstrate how varying the zinc ethylxanthate firing temperature influences the crystallite size and eventually the pyrolysis product. From 125-400 °C, ZnS is the only solid material formed by the decomposition. At 500 °C, both ZnS and ZnO are apparent in the pattern, while at 600 °C and higher, ZnO was the only species detected by the diffractometer (ICDD 36-1451).

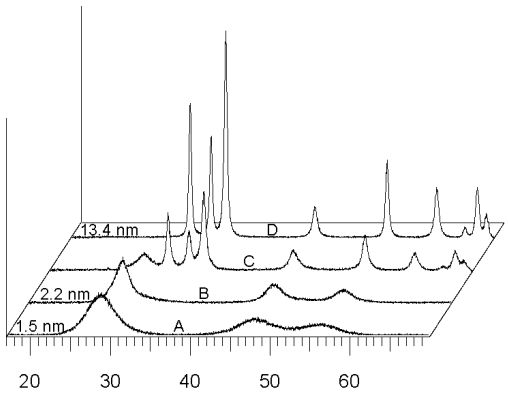

Figure 5.4: Powder X-ray diffractograms of the pyrolysis product from zinc xanthate at (A) 150 °C, (B) 400 °C, (C) 500 °C, and (D) 600 °C. The average crystallite sizes are written next to the corresponding pattern.

Surface area analyses of ZnS and ZnO nanocrystals. BET isotherms were generated to determine the specific surface areas of the ZnS and ZnO powders. Figure 5.5 is a simple bar graph that indicates the surface areas of the commercial zinc sulfide sample (a nanocrystalline sample – 27 nm – in the hexagonal phase), the zinc ethylxanthate precursor, and the thermal decomposition products. The surface area of fused ZnS was also measured, but had a specific surface area of less than 1.0 m^2g^{-1}. To the best of our knowledge, no one has reported a surface area for zinc sulfide as high as 364 m^2g^{-1}. As expected, the specific surface area of the nanocrystals decreases as firing temperature increases due to sintering.

By the time you get to temperatures high enough to produce ZnO, the surface area has reduced to 16.0 m^2g^{-1}. In the P/P^o range of zero to 0.6, the commercial ZnS (hexagonal phase) powder exhibited characteristics of a layer-by-layer adsorption isotherm, while the synthesized nanocrystalline ZnS exhibited the less common type III behavior according to the Brunauer, Denning, Denning, Teller (BDDT) classification

scheme.[31-33] Figure 5.6 contains the isotherms for both the commercial and synthesized nanometric zinc sulfide. Type III behavior indicates that interactions between the nitrogen adsorbate and the surface of the zinc sulfide adsorbant are relatively weak.

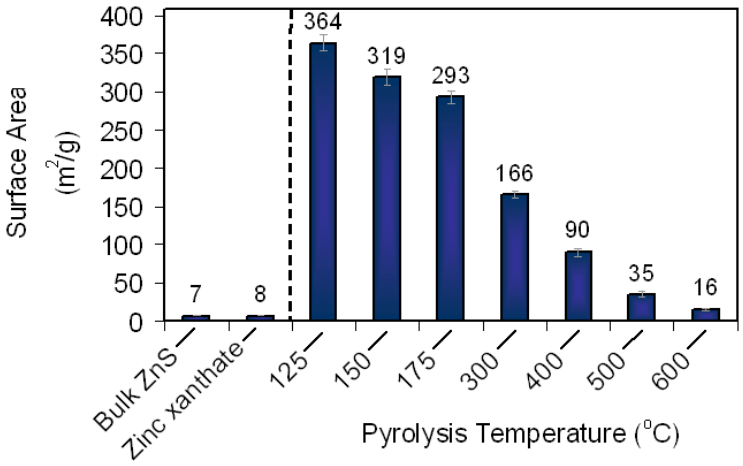

Figure 5.5: Average surface areas for commercial zinc sulfide, zinc ethylxanthate, and the pyrolysis products of zinc ethylxanthate at various temperatures.

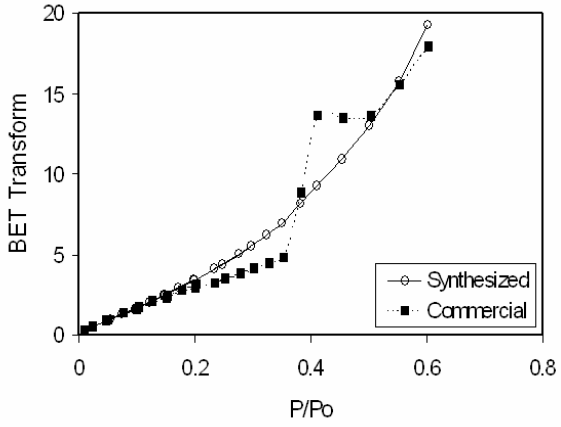

Figure 5.6: BET isotherms of hexagonal commercial zinc sulfide and the cubic synthetic zinc sulfide. The two isotherms have been normalized. The actual BET transform data for the commercial ZnS is 32.8 times higher than for the synthesized sulfide.

Fluorescence spectra of ZnS and ZnO nanocrystals. Figures 5.7 and 5.8 show the emission spectra for both pure and doped (Mn^{2+} or Al^{3+}) ZnS nanocrystals. With either excitation energy, the broad emission from the ZnS spans about 85% of the visible region with only a slight bias to the blue portion of the spectrum. There is no obvious correlation between the dopant concentration and emission intensity. While the dopants do not significantly shift the λ_{mzx} value or change the basic shape of the glow curve, it is clear that they inhibit fluorescence intensity, especially the Mn^{2+} dopant. The dopant quenching along with the lack of correlation between emission characteristics and dopant concentration suggest that particle size, surface states, and surface defects were probably the driving forces behind the luminescence. Additionally, it is possible that the dopants simply migrate to the surface of the particles and are not homogeneously dispersed throughout the ZnS.

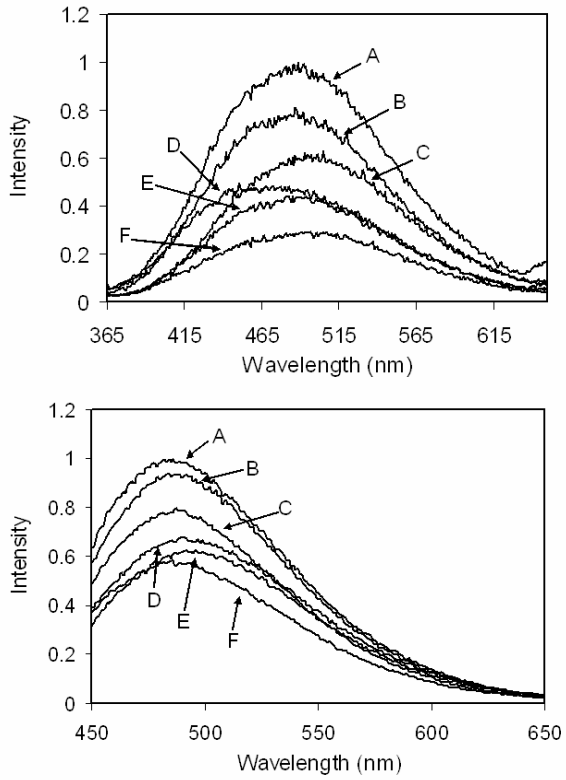

Figure 5.7: Fluorescence spectra of neat and Al^{3+}-doped ZnS. The excitation wavelengths used were 340 nm (top) and 425 nm (bottom). The molar dopant percentages are (A) 0.00%, (B) 3.00%, (C) 2.00%, (D) 0.50%, (E) 0.25%, and (F) 1.00%.

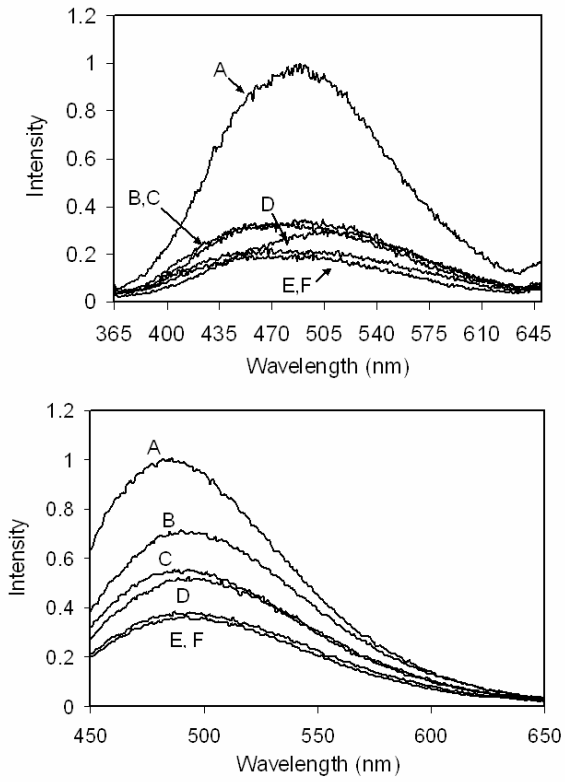

Figure 5.8: Fluorescence spectra of neat and Mn^{2+}-doped ZnS. The excitation wavelengths used were 340 nm (top) and 425 nm (bottom). The molar dopant percentages are (A) 0.00%, (B) 2.00%, (C) 0.50%, (D) 0.25%, (E) 1.00%, and (F) 3.00%.

The effect of pyrolysis temperature on the luminescence properties of the ZnS and ZnO were monitored. Figure 5.9 contains the fluorescence data for the sulfide and oxide nanocrystals prepared at different temperatures. The various spectra indicate that the intensity of the ZnS decreases with increasing temperature until ZnO begins to form. However, once the oxide is the only solid decomposition product, the intensity increases with increasing temperature and λ_{max} has red shifted by about 40 nm. Typically, one would think that the larger band gap of ZnO would cause a blue shift when compared to ZnS. However, the diameter of the ZnS nanocrystals is much smaller than for the ZnO nanocrystals. Beyond that, the deep levels formed from the surface phenomena are the primary driving force of the luminescence. The relative number of surface defects

present on the ZnO particles is presumably much lower than the ZnS particles due to sintering at the high temperature that is required to prepare the oxide. Since neither the diameter nor the surface properties of the two phosphors are similar, trying to predict the luminescence peak position from bulk band gap considerations is precarious. Figure 5.10 contains a photograph of the nanocrystalline ZnS and ZnO powders when excited with a 365 nm ultraviolet lamp.

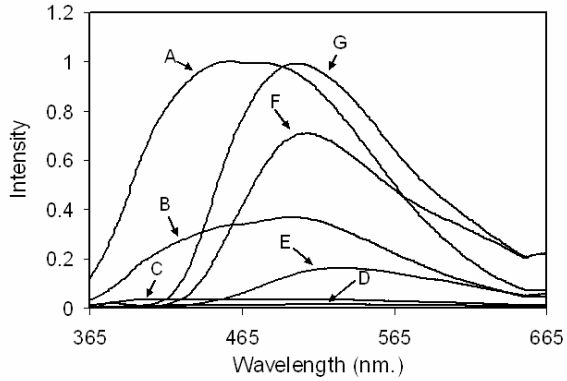

Figure 5.9: Fluorescence spectra of the pyrolysis product of zinc xanthate obtained at various temperature: (A) 150 °C, (B) 175°C, (C) 300 °C, (D) 400 °C, (E) 500 °, (F) 600 °C, and (G) 700 °C.

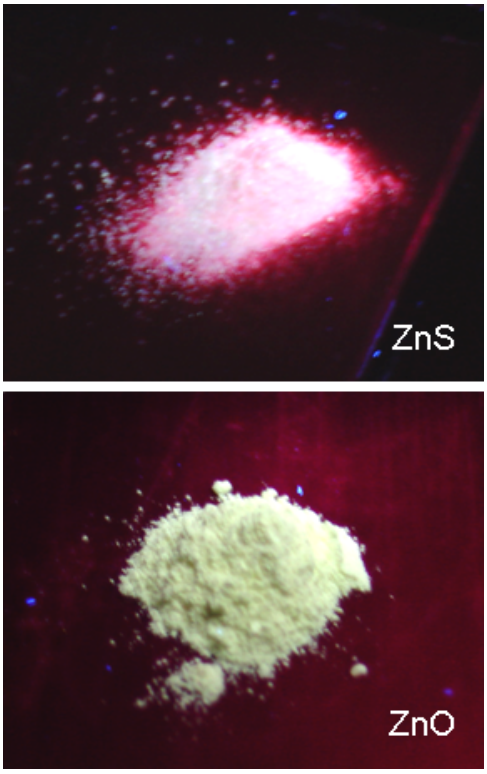

Figure 5.10: Images of nanocrystalline ZnS (top) and ZnO (bottom) irradiated with a 365 nm ultraviolet lamp. The red glow around the ZnS samples is an artifact from the camera.

CONCLUSIONS

Very small nanocrystals (1.5 nm) of zinc sulfide were prepared from the low temperature thermal decomposition of zinc ethyldithiocarbonate. The ZnS prepared from this method can have a specific surface area up to 360 m^2g^{-1}, which is the largest reported surface area for zinc sulfide of which we are aware. Although the nanocrystals are combined in larger aggregates, the photoluminescence properties differ greatly from bulk ZnS. White-light emission is achieved arising, most likely, from the sizeable surface-to-volume ratio. The absence of a strong band edge emission feature, which often accompanies ultra small nanocrystals is beneficial since there is no biasing of the white-

light to a specific color. Broadband yellow emission was also achieved by decomposing the ethylxanthate precursor at higher temperatures, which yielded nanocrystalline zinc oxide. The low cost and great abundance of the needed preparative materials along with the remarkably simple synthetic procedure, make this approach to fabricating white-light phosphors very promising. Deeper and more fundamental studies of these materials could aid in the development of more energy-efficient/environmentally-friendly devices, which could be used for future solid-state lighting equipment.

The next chapter in this dissertation explores what happens to the luminescent properties of ZnS and ZnO prepared from zinc ethylxanthtate when the nanocrystals are embedded in various matrices.

REFERENCES

[1] Eugene Hong, L. C., Michael Scholand **2005**, *II: Energy Efficient Lighting Technology Options*, 1-286.

[2] Chakhovskoi, A. G.; Hunt, C. E.; Malinowski, M. E.; Felter, T. E.; Tallin, A. A. *Journal of Vacuum Science & Technology, B: Microelectronics and Nanometer Structures* **1997**, *15*, 507-511.

[3] Bulur, E.; Goeksu, H. Y.; Wieser, A.; Figel, M.; Oezer, A. M. *Radiation Protection Dosimetry* **1996**, *65*, 373-379.

[4] Chakrabarty, B. S.; Murthy, K. V. R.; Joshi, T. R. *Indian Journal of Pure and Applied Physics* **1999**, *37*, 136-141.

[5] Mueller, A. H.; Petruska, M. A.; Achermann, M.; Werder, D. J.; Akhadov, E. A.; Koleske, D. D.; Hoffbauer, M. A.; Klimov, V. I. *Nano Letters* **2005**, *5*, 1039-1044.

[6] Achermann, M.; Petruska, M. A.; Kos, S.; Smith, D. L.; Koleske, D. D.; Klimov, V. I. *Nature (London, United Kingdom)* **2004**, *429*, 642-646.

[7] Yu, W. W.; Qu, L.; Guo, W.; Peng, X. *Chemistry of Materials* **2003**, *15*, 2854-2860.

[8] Tamura, T.; Setomoto, T.; Taguchi, T. *Journal of Luminescence* **2000**, *87-89*, 1180-1182.

[9] Schlotter, P.; Baur, J.; Hielscher, C.; Kunzer, M.; Obloh, H.; Schmidt, R.; Schneider, J. *Materials Science & Engineering, B: Solid-State Materials for Advanced Technology* **1999**, *B59*, 390-394.

[10] Nakamura, S.; Fasol, G. *The Blue Laser Diode: GaN Based Light Emitters and Lasers*, 1997.

[11] Shimizu, Y.; Sakano, K.; Noguchi, Y.; Moriguchi, T.; (Nichia Kagaku Kogyo Kabushiki Kaisha, Japan). Application: WO
WO, 1998, p 84 pp.

[12] Huang, Y.-S.; Jou, J.-H.; Weng, W.-K.; Liu, J.-M. *Applied Physics Letters* **2002**, *80*, 2782-2784.

[13] Tang, C. W.; VanSlyke, S. A. *Applied Physics Letters* **1987**, *51*, 913-15.

[14] Xu, Y.; Peng, J.; Mo, Y.; Hou, Q.; Cao, Y. *Applied Physics Letters* **2005**, *86*, 163502/1-163502/3.

[15] Bowers, M. J., II; McBride, J. R.; Rosenthal, S. J. *Journal of the American Chemical Society* **2005**, *127*, 15378-15379.

[16] Hill, N. A.; Whaley, K. B. *Journal of Chemical Physics* **1994**, *100*, 2831-7.

[17] Underwood, D. F.; Kippeny, T.; Rosenthal, S. J. *Journal of Physical Chemistry B* **2001**, *105*, 436-443.

[18] Chen, X.; Samia Anna, C. S.; Lou, Y.; Burda, C. *J Am Chem Soc FIELD Full Journal Title:Journal of the American Chemical Society* **2005**, *127*, 4372-5.

[19] Li, H.; Shih, W. Y.; Shih, W.-H. *Nanotechnology* **2007**, *18*, 205604/1-205604/6.

[20] Kawazu, Z.; Kawakami, Y.; Taguchi, T.; Hiraki, A. *Technology Reports of the Osaka University* **1989**, *39*, 203-14.

[21] McClean, I. P.; Thomas, C. B. *Semiconductor Science and Technology* **1992**, *7*, 1394-9.

[22] Peng, W. Q.; Qu, S. C.; Cong, G. W.; Zhang, X. Q.; Wang, Z. G. *Journal of Crystal Growth* **2005**, *282*, 179-185.

[23] Tanaka, M.; Qi, J.; Masumoto, Y. *Journal of Luminescence* **2000**, *87-89*, 472-474.

[24] Chen, W.; Malm, J.-O.; Zwiller, V.; Wallenberg, R.; Bovin, J.-O. *Journal of Applied Physics* **2001**, *89*, 2671-2675.

[25] Rao, S. R. *Xanthates and Related Compounds*, 1971.

[26] The International Centre for Diffraction Data, Newton Square, PA: (The International Centre for Diffraction Data, Newton Square, PA); Vol. File Nos. 05-0566 & 36-1451.

[27] Topas 1.0.1 ed.; Bruker AXS, GmbH: 1998.

[28] Warren, B. E. *Prog. Metal Phys. (Bruce Chalmers and R. King, editors. Pergamon Press)* **1959**, *8*, 147-202.

[29] Warren, B. E.; Averbach, B. L. *Journal of Applied Physics* **1950**, *21*, 595-8.

[30] ChemDraw Ultra 9.0 ed. 2004.

[31] Brunauer, S.; Emmett, P. H.; Teller, E. *Journal of the American Chemical Society* **1938**, *60*, 309-19.

[32] Brunauer, S.; Emmett, P. H. *Journal of the American Chemical Society* **1940**, *62*, 1732-46.

[33] Brunauer, S.; Deming, L. S.; Deming, W. E.; Teller, E. *Journal of the American Chemical Society* **1940**, *62*, 1723-32.

CHAPTER 6

INTENSE BROADBAND FLUORESCENCE FROM NANOCRYSTALLINE ZINC SULFIDE-SILICA AND CADMIUM SULFIDE-SILICA COMPOSITES

High surface area zinc sulfide (>300 m^2g^{-1}) was produced from the low temperature decomposition of zinc ethylxanthate. Nanometric zinc oxide and cadmium sulfide, each with high surface area, were prepared in an analogous way. The nanoscale ZnS crystals (1.5 nm) exhibit broad white-light luminescence when excited with ultraviolet or near-ultraviolet radiation, while the CdS particles (2.8 nm) exhibit broad yellow-light under excitation. When either the CdS or ZnS particles are grown in a SiO_2 matrix by a sol-gel method, the broadband fluorescence is maintained with, in some cases, a drastic increase in intensity. The mole fraction of metal sulfide to SiO_2 was varied between roughly 0.02 and 0.07. The mean surface area of the ZnS-SiO_2 phosphors was determined to be 120 m^2g^{-1} while that of the CdS-SiO_2 was 3.0 m^2g^{-1}. Chromaticity coordinates and quantum efficiencies were determined for all of the tested phosphors. A comparison to commercial phosphors is presented and embedding agents other than silica are discussed. In addition to emission and excitation spectroscopy, powder X-ray diffraction, thermogravimetric analysis, BET surface area analysis, Raman and Fourier transform infrared spectroscopy were the primary characterization techniques used in this study.

INTRODUCTION

The United States Department of Energy has recently set a goal to create new materials and methodologies that would conserve 50% of the electric lighting consumption by 2025.[1] While part of that goal relies on light utilization and human factors, an increase of light source efficiency will also be required. Despite the availability of alternatives, incandescent lamps are still a major competitor in the residential sector. In fact, incandescent sources are estimated to generate 12% of all the light in the United States. However, these incandescent sources are responsible for 42% of all lighting energy consumed.[2] Familiarity and overall light quality are presumably the main factors that would explain the continued popularity of incandescent bulbs. Therefore, replacement technology must generate light that has as similar qualities to incandescent bulbs as possible while increasing device efficiency.

The inherent inefficiency of incandescent bulbs is due to the high temperatures required and the corresponding loss of energy in the form of heat. To get away from the heat loss problem, researchers have shifted to cool-light sources such as fluorescent bulb technology, and more recently, light emitting diode (LED) technology. As for phosphors in fluorescent lamps, the traditional coatings have been mixtures of rare-earth containing oxides with complicated doping schemes[3-5] or doped calcium halophosphates.[6,7] Not only are there relative abundance and cost issues for these mixtures, but difficulties can arise from stoichiometry control and complex doping schemes. Thus, there is a need to develop materials, which could be used as phosphors that do not require mixtures of rare/expensive compounds, elaborate doping recipes, or difficult synthetic protocols.

A promising alternative to incandescent or fluorescent lighting solutions is light emitting diode (LED) technology. Recently, mixtures of semiconductor nanocrystals have been demonstrated as strong emitters in LED-based devices.[8,9] Semiconductor nanocrystals can have high luminescent efficiencies and respectable molar absorptivities on their own, but mixtures that produce white emission can suffer from self absorption, which decreases overall device efficiency.[8,10] There are three widely used general approaches for fabricating LEDs that produce white light: (1) mix light from three (or more) monochromatic sources, red, green, and blue (RGB); (2) use a blue LED to pump a yellow emitting phosphor; (3) use an ultraviolet LED to pump one or more visible-emitting phosphors.[11] Based on a search of the relevant scientific literature and patents, devices based on the second category are currently the most prevalent. Coating a blue emitter, such as InGaN, with a broad yellow phosphor, such as $Y_3Al_5O_{12}$:Ce (cerium doped YAG) is a widely used method for manufacturing white-light emitting diodes.[12-15]

Another device that is poised for extensive use in white lighting solutions is the organic light emitting diode (OLED).[16-18] Likewise, polymer light emitting diodes (PLEDs) have been prepared and proven as white-light emitters.[19] In the short term, from an economic standpoint, organic-based devices are not as favorable as the analogous inorganic devices. Additionally, the synthetic routes required for current OLEDs rely on combinatorial processes that are slow and expensive.[16] While there is definite promise in organic light emitting diode technology, the realization of widespread use will not likely occur before the 2025 Department of Energy goal.

Developing cheaper, more efficient, and easier to make materials for incorporation into fluorescent lamps or inorganic-based light emitting diodes seems to be

a reasonable solution for fulfillment of both short- and long-term energy goals. It has been demonstrated that ultra small CdSe can emit white light (420-710 nm) without displaying the obstacle of significant self absorption.[20] The emission mechanism attributed to the "magic-sized" CdSe depends on the surface of the nanocrystals.[20-22] Incorporating CdSe quantum dots into a blue- or ultraviolet-pumping light emitting device is a simple way to generate white light without the need for complex mixtures of phosphors. The toxicity of cadmium is a drawback. However, it has been shown that ZnSe quantum dots can also as a white-light phosphor.[23] The findings presented in the CdSe and ZnSe studies are encouraging since ways to generate white light that do not rely on the combination of multiple phosphors and elaborate doping patterns are elucidated. The disadvantages of both cases are that the nanoparticles require organic coordinating agents (e.g. trioctylphosphine oxide) or solvents, and incorporating them into stable, long-lasting coatings can be difficult.

If a non-toxic, nanocrystalline system that efficiently produced white light when excited with blue or ultraviolet radiation, which did not rely on intricate mixtures, doping, or harsh organic stabilizers could be realized, a new avenue for lighting solutions would be available. In this chapter we present broadband emission from ZnS nanocrystals embedded in a silica matrix. Normally, nanometric ZnS emits blue light[24-26] when excited with ultraviolet radiation, but with dopants and/or size-control, other colors can be obtained.[27-29] In addition to zinc sulfide, nanocrystalline zinc oxide and cadmium sulfide will be discussed. In each case, the nanocrystals were grown from the decomposition of zinc or cadmium ethylxanthate. Our method does not require harsh organic solvents or coordinating agents, nor does it require inert or protective

environments. As an alternative to the silica matrix, ZnS particles were also grown inside thin films of polystyrene to explore coating options.

EXPERIMENTAL

Materials. Reagent grade cadmium chloride (Fisher), zinc sulfate heptahydrate (J. T. Baker), and O-ethylxanthic acid, potassium salt (potassium ethylxanthate) (Aldrich) were obtained commercially along with 98% tetraethyl orthosilicate (Aldrich), absolute ethanol (Pharmco), polystyrene (c.a. 100,000 amu), toluene ($C_6H_6CH_3$, Pharmco), and 0.100 N hydrochloric acid (Fisher) and used as received without further purification. Zinc ethylxanthate was generated by reacting aqueous solutions of zinc sulfate and potassium ethylxanthate in a stoichiometric fashion as described in the literature.[30] Typically, $ZnSO_4 \bullet 7H_2O$ (5.00 g, 17.4 mmol) was dissolved in water (150 mL) and $KS_2COCH_2CH_3$ (5.57 g, 34.8 mmol) was dissolved in a similar amount of water. The potassium ethylxanthate solution was slowly poured into the zinc sulfate solution immediately generating the white zinc ethylxanthate, $Zn(S_2COCH_2CH_3)_2$, precipitate in high yield (97.6 %). The solid was collected by vacuum filtration and washed thoroughly with water. The zinc ethylxanthate was stored in a sealed glass bottle away from light and remained stable for several months. Carbon and hydrogen elemental analysis (Found: C, 23.3; H, 3.2. $C_6H_{10}O_2S_4Zn$ requires C, 23.4; H, 3.3 %). ^{1}H NMR chemical shifts for zinc ethylxanthate: δ 1.29, 4.35 (CH_3CH_2O-). ^{13}C NMR shifts for zinc ethylxanthate: δ 13.9, 69.7 (CH_3CH_2O-), 225.1 (-OCS_2-). A similar approach was used to prepare cadmium ethylxanthate. Stoichiometric amounts of $CdCl_2 \bullet 2$ ½ H_2O and potassium ethylxanthate

were dissolved in deionized water and the resulting solutions were mixed together which generated the cream-colored cadmium ethylxanthate at a yield of 95.3 %.

Synthesis of ZnS, CdS, ZnS-SiO_2, and CdS-SiO_2. ZnS powder was obtained by heating freshly prepared $Zn(S_2COCH_2CH_3)_2$ in air at 150 °C. Neat CdS powder was prepared by firing $Cd(S_2COCH_2CH_3)_2$ in air at 150 °C as well.

To embed the ZnS or CdS nanocrystals in silica, either the zinc or cadmium ethylxanthate precursor was incorporated into a sol-gel method. For instance, $Zn(S_2COCH_2CH_3)_2$ (0.8 g, 2.6 mmole) was dissolved in a mixture of absolute ethanol (20.0 ml), deionized water (2.0 ml), and tetraethyl orthosilicate (16 ml). When the xanthate was completely dissolved, 0.1 M hydrochloric acid (2.0-3.0 ml) was added to act as a catalyst. The solution was allowed to gel and then age in a sealed container over a range of different times. When the gel had set and the desired aging time had elapsed, the precursor was allowed to dry before it was pyrolyzed at 150 °C. Refer to Scheme 6.1 for a schematic of the metal sulfide/silica composite preparation.

Synthesis of ZnS-polystyrene. The incorporation of nanocrystalline zinc sulfide into polystyrene was accomplished by co-dissolving zinc ethylxanthate and the polymer in toluene. For homogenous mixtures, a relatively low ratio of xanthate to polystyrene is required (~1-10% by mass). Once the ethylxanthate-polystyrene mixture is dry (free from toluene), it can simply be heated to 150 °C to decompose the precursor in the polymer leaving behind ZnS in an evenly dispersed fashion. Scheme 6.2 is a roadmap for the ZnS-polystyrene hybrid.

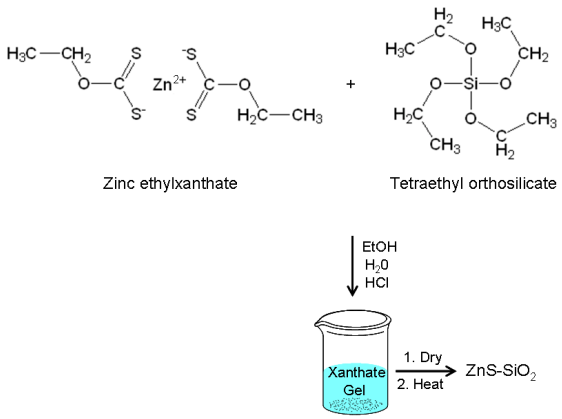

Scheme 6.1: Reaction scheme corresponding to the preparation of a ZnS-SiO_2 nanocomposite. Drying and aging times were varied throughout the experiment. The decomposition temperature was 150 °C.

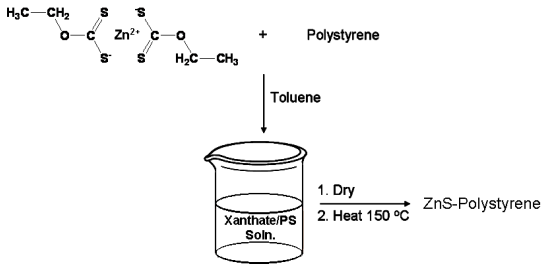

Scheme 6.2: Roadmap for the preparation of ZnS-polystyrene nanocomposites from the ethylxanthate precursor.

Characterization. A Horiba Jobin Yvon Fluorolog FL-1039 was used to measure the luminescence spectra of the ZnS, CdS, ZnS-SiO_2, and CdS-SiO_2 solids. An equal volume of solid was used for each scan. While many different excitation wavelengths were utilized, only spectra recorded for 280nm or 365 nm excitation will be reported here. Chromaticity coordinates were determined using the 1931 Commission Internationale de l'Eclairage (CIE) color matching functions and corresponding color space map.

For infrared spectroscopic measurements, approximately 10 mg of the ethylxanthate precursors or sulfide nanocrystals were mixed with approximately 100 mg FTIR-grade potassium bromide and the blend was finely ground. Spectra in the 4000-

400 cm^{-1} region were collected by diffuse reflectance of the ground powder with a Nicolet Magna-IR 750 spectrometer. Normally, 128 scans were recorded and averaged for each sample (4.0 cm^{-1} resolution) and the background was automatically subtracted. Prominent IR adsorption signals for zinc ethylxanthate (cm^{-1}): 2990(m), 2941(m), 2888(w), 1467(m, sh), 1442(s), 1383(m, sh), 1364(m), 1210(vs), 1126(vs), 1031(vs), 868(m), 817(m), 657(m), 451(s). Very similar signals are present in the cadmium ethylxanthate spectrum (cm^{-1}): 2985(s), 2933(m), 2893(m), 2376(w), 1689(w), 1461(m, sh), 1448(s), 1390(m), 1366(m), 1199(vs), 1123(vs), 1034(vs), 869(m), 818(m), 660(m), 451(s).

Raman spectroscopy was also used to characterize the precursors as well as the sulfide nanocrystals and their silica composites. A Nicolet NXR 9610 Raman Spectrometer was used for the analysis and a neat pressed pellet was used for each measurement. Typically, 32 scans were averaged at a resolution of 4.0 cm^{-1}.

Powder X-ray diffraction (XRD) measurements were obtained on a Bruker AXS D8 Advance diffractometer using Cu Kα radiation with an acceleration voltage of 40 kV and current flux of 30 mA. The diffractograms were recorded for a 2θ range of 17-70° with a step size of 0.02° and a counting time of 18 seconds per step. All the XRD patterns where collected at ambient temperature, and the phases were identified using the ICDD database.[31] The peaks were profiled with a Pearson 7 model using Topas P version 1.01 software.[32] The profiles of the standard and the sample were put into the Win-Crysize program version 3.05, which uses the Warren-Averbach evaluation method to determine crystallite size.[33,34]

The specific surface areas were obtained with a conventional Brunauer-Emmett-

Teller (BET) multilayer nitrogen adsorption method using a Quantachrome Nova 1200 instrument.

Thermogravimetric analysis (TGA) was performed on the zinc and cadmium ethylxanthate complexes at a rate of 2.0°/min from room temperature to 600 °C using a Seiko Instruments Exstar 6200. Neither zinc nor cadmium ethylxanthate melts congruently, but a well behaved decomposition curve was observed for each precursor and a defined onset temperature of roughly 115 ^{o}C.

RESULTS AND DISCUSSION

Low temperature decomposition of $Zn(S_2COCH_2CH_3)_2$ and $Cd(S_2COCH_2CH_3)_2$ to form ZnS and CdS nanocrystals. To determine what temperature was necessary to convert the ethylxanthate precursors into either ZnS or CdS, thermogravimetric analysis was performed on the solid zinc or cadmium ethylxanthate respectively, and the traces can be seen in Figure 6.1. The first derivative of either curve suggests decomposition occurs rapidly in a single step. For both the zinc and cadmium precursors, decomposition commences at roughly 115 °C and is virtually completed by 165 °C. Therefore, 150 °C was chosen as the pyrolysis temperature which would be used throughout the experiment. A more detailed account of the elimination byproducts and decomposition pathway was presented in Chapter 3, but Scheme 6.3 demonstrates the balanced reaction involved in going from the metal xanthate to the metal sulfide. Only the major products detected are included in the scheme. Byproducts present in trace amounts from the decomposition

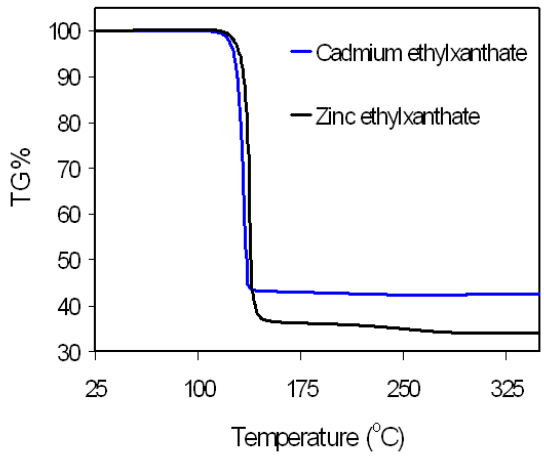

Figure 6.1: Thermalgravimetric analysis traces of zinc ethylxanthate (black) and cadmium ethylxanthate (blue).

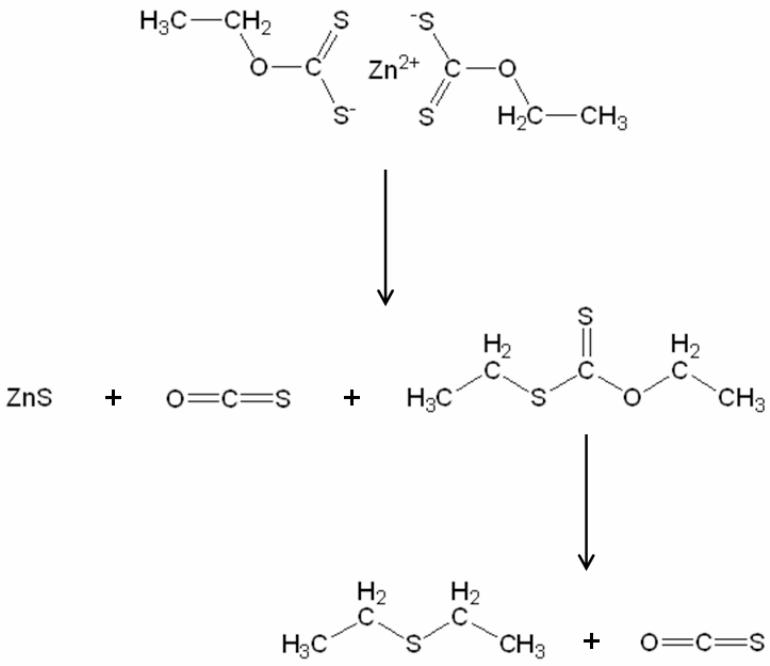

Scheme 6.3: Balanced elimination reaction detailing the conversion of zinc ethylxanthate to zinc sulfide.

were left out for clarity. The second step may or may not go to completion depending on the reaction time and temperature. The heating times used in this study were sufficient to drive away all of the byproducts as gases.

To confirm that ZnS and CdS were, in reality, the species formed due to the thermal breakdown, XRD patterns were obtained for each of the pyroloysis powders. The diffractograms shown in Figure 6.2 suggest that the zinc and cadmium sulfides are

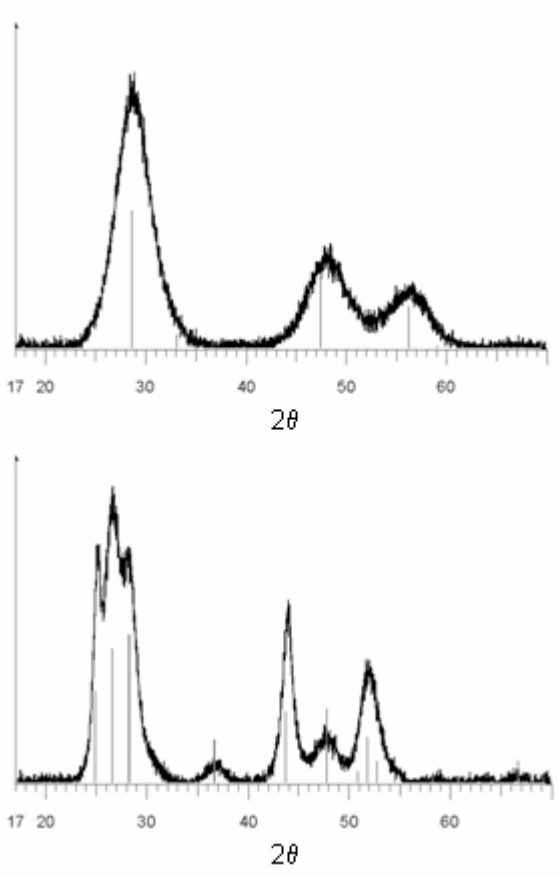

Figure 6.2: XRD images of ZnS (top) and CdS (bottom). Vertical bars represent the ICDD indexes of (05-0566, Zns) and (41-1049, CdS).

the products and that they adopt cubic and hexagonal crystal phases respectively. The broad peaks can be explained by the small grain size of the particles. The average

crystallite size was estimated for the particles using the Warren-Averbach band-broadening method. The ZnS particles had a crystallite size of 1.5 nm while the CdS particles had an average size of 2.8 nm.

It is expected that such ultra small crystals would have the potential for a very large surface area. Indeed, the specific surface area was measured for the neat ZnS and CdS powders, and it was determined that the ZnS had 320 m^2 of exposed surface for every gram while CdS had a value of 137 m^2g^{-1}.

As one might expect, incorporation of the CdS and ZnS into a SiO_x matrix affected the material properties (as compared to the neat sulfides). However, the required decomposition temperature was not greatly affected and 150 °C was sufficient to convert the sol-gel composites of the zinc and cadmium ethylxanthates to ZnS-SiO_2 and CdS-SiO_2. The thermogravimetric analysis traces for the pyrolyzed silica composites are shown in Figure 6.3. Most of the mass loss is due to the condensation of the SiO_x network. The silica-based matrix took on an amorphous structure, and since the relative concentration of metal sulfide to SiO_2 was rather small (~ five mole percent), X-ray powder diffraction was not able to definitely prove the formation of ZnS and CdS within the composite. Therefore, an average crystallite size was not determined for either the ZnS-SiO_2 or the CdS-SiO_2 system. However, using techniques such as Raman and FTIR spectroscopy along with simple yield calculations, there is no doubt the ethylxanthate ligands decomposed leaving the sulfide behind. Figure 6.4 contains the Raman spectra of the pre- and post-pyrolyzed zinc composite whereas Figure 6.5 contains information about the cadmium composite. The disappearance of the alkyl stretches at just under

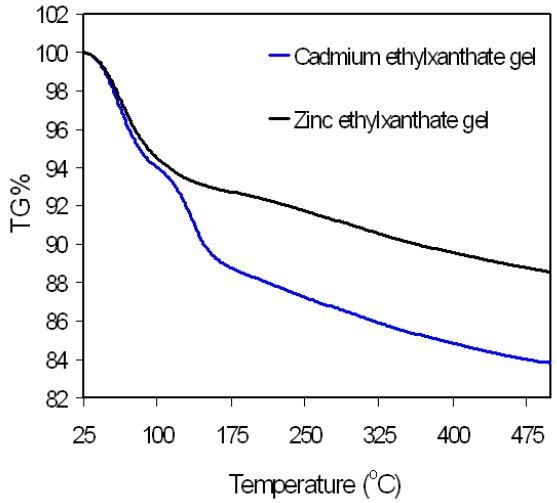

Figure 6.3: Thermalgravimetric analysis traces of $Zn(S_2COCH_2CH_3)_2$-SiO_2 and $Cd(S_2COCH_2CH_3)_2$-SiO_2. The zinc-based gel had a higher metal loading.

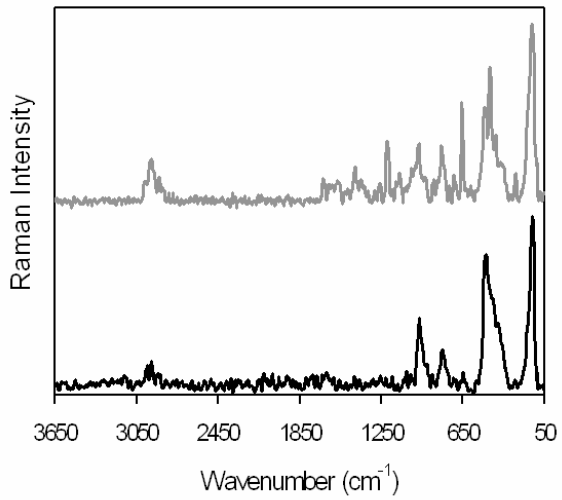

Figure 6.4: Raman spectra of $Zn(S_2COCH_2CH_3)_2$-SiO_2 (GRAY) and ZnS-SiO_2 (BLACK). The disappearance of the signals at just under 3000 cm^{-1}, 660 cm^{-1}, and in the range from 1000 to 1700 cm^{-1} indicate that the xanthate is no longer present and that the sulfide has formed.

3000 cm^{-1} indicate that the ethyl units have been removed. Similarly, the absence of peaks in the region from 1000-1700 cm^{-1} and 660 cm^{-1} suggest that the $ROCS_2$ group is no longer intact.

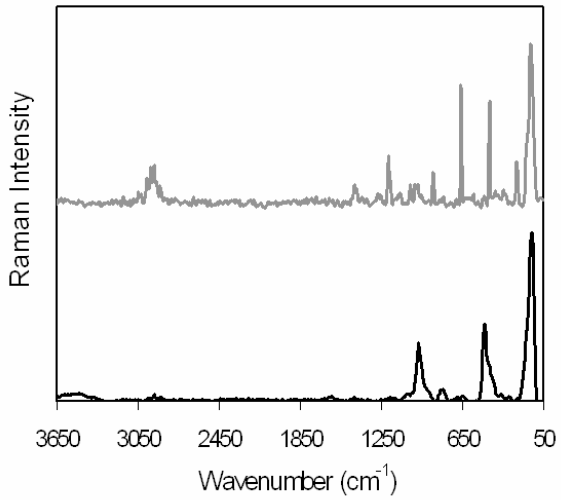

Figure 6.5: Raman spectra of $Cd(S_2COCH_2CH_3)_2$-SiO_2 (TOP) and CdS-SiO_2 (BOTTOM). As with the zinc compounds, the disappearance of the signals at just under 3000 cm^{-1}, at 660 cm^{-1}, and in the range from 1000 to 1700 cm^{-1} indicate that the xanthate is no longer present and that the sulfide has formed.

Compared to the neat metal sulfides, the specific surface areas of the composites are lower. The measured surface areas were determined to be 120 m^2g^{-1} and 3.0 m^2g^{-1} for the ZnS-SiO_2 and CdS-SiO_2 respectively.

Luminescence spectra and efficiencies of both neat and silica composite ZnS and CdS nanocrystals. Figure 6.6 shows the normalized emission spectra for pure CdS (2.8 nm) and ZnS (1.5 nm) when excited with either 280 nm or 365 nm light respectively.

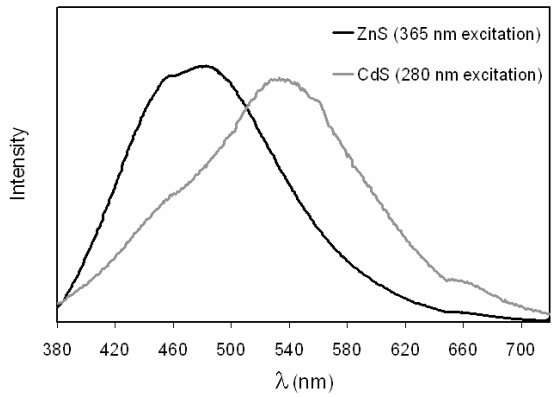

Figure 6.6: Fluorescence spectra of neat ZnS and CdS nanocrystals. The intensities have been normalized since the ZnS emits much more strongly than the CdS.

Although the cadmium sulfide appears yellow when excited with 365 nm light, it does not emit very strongly, which is why 280 nm was chosen for the excitation. *Keep in mind, when comparing the ZnS/CdS fluorescence curves, that two different excitation energies were used for this portion of the experiment.* Both luminescence curves are quite broad with the CdS envelope red shifted by about 50 nm compared to the ZnS. The breadth of the emission profiles is most likely due to surface phenomena. The rapid decomposition from ethylxanthate to sulfide is not conducive to significant surface reorganization. Along this same train of thought, due to the relatively low preparative temperature required, very little sintering occurs. The combination of rapid growth and low temperature contribute to a particle surface containing a high density of defects. The wide array of surface defects corresponds to a wide array of deep trap levels, which results in broadband emission.

To the naked eye, the ZnS emits white light and the CdS emits pale-green/yellow light correspondingly when excited with 365 nm and 280 nm radiation. The actual chromaticity coordinates based on the 1931 CIE system are (0.20, 0.27) and (0.31, 0.43)

for the zinc and cadmium sulfides in that order. The ZnS coordinates are near the white/blue border while the CdS coordinates are within the typical yellow to yellowish-green region. Determining the absolute quantum efficiency of a powder can be rather challenging. Phenomena such as self-absorption, re-absorption, and polarization all contribute to the difficulty of achieving a reliable absolute efficiency. It is also challenging and time consuming to determine how much of a given solid sample is actually participating in the excitation/emission process. However, a rough estimate of the relative quantum efficiency can be straightforwardly determined. Relative quantum yields were acquired using an ethanolic solution of Rhodamine 6G excited at 365 nm as a standard. Rhodamine 6G has a reported quantum efficiency of 0.95. Equal volumes of finely powdered samples were used throughout the experiment and great care was taken to keep the powder thickness uniform from one measurement to the next. The emission window used for comparison was from 380 to 720 nm. The values obtained were 0.18 for the nanocrystalline ZnS and less than 0.05 for the CdS as compared to the Rhodamine dye.

Figure 6.7 contains the emission spectra of three different mole fraction ZnS-SiO_2 powders while Figure 6.8 illustrates similar information concerning a CdS-SiO_2 analog. *Note that for the silica composites, 365 nm is sufficient to excite both the zinc and cadmium sulfides.* It is clear that luminescence intensity increases as the mole fraction of the metal sulfide increases.

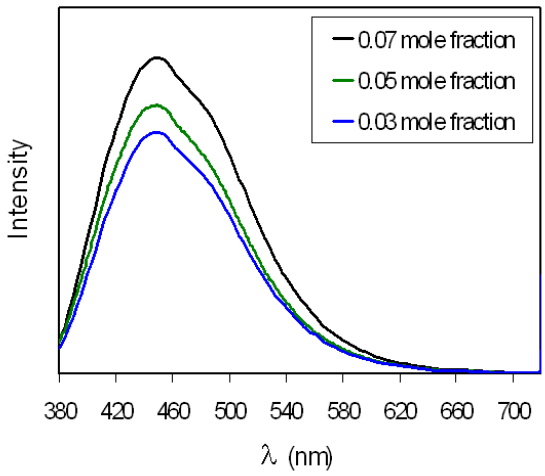

Figure 6.7: Fluorescence spectra of ZnS-SiO_2 for different mole fractions of ZnS excited with 365 nm radiation. The relative intensities have not been adjusted so as to give the correct intensity ratio.

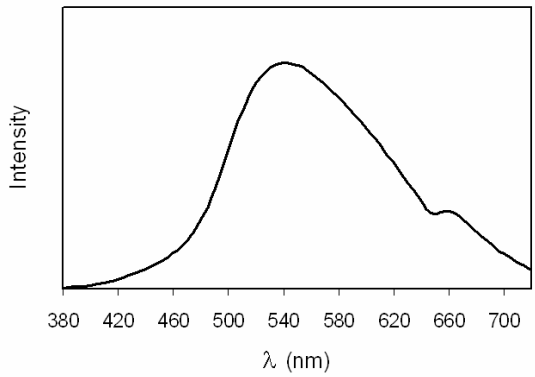

Figure 6.8: Fluorescence spectra of CdS-SiO_2 for a 0.02 mole fraction CdS sample. The composite was excited with 365 nm photons.

However, it appears that the general shape of the emission spectra is not greatly affected by changes in sulfide concentration. On a metal sulfide basis, the silica composites emit much more intensely than their neat counterparts. For instance, when exciting an equal volume of ZnS and ZnS-SiO_2 (0.07 mole fraction ZnS) under the same conditions, the composite peak area (in the range of 400 to 700 nm) is roughly the same (1.02 times) as

the area for the pure compound. A similar but more pronounced phenomenon is observed for the cadmium system where the composite (0.02 mole fraction CdS) area is nearly 1700 times as large as the pure CdS. The efficiencies for 0.07 mole fraction ZnS-SiO_2 and 0.02 mole fraction CdS-SiO_2 were estimated to be 0.27 and 0.11 times that of the Rhodamine 6G respectively. These quantum efficiency results are not intended to be absolute values. There was no way to determine the actual number of metal sulfide particles that participated in the emission processes in the solid samples. There is little doubt that a significant portion of each powder sample played no part in the luminescence. To accurately determine the efficiency, one of two things would be required. The first would be to find a solvent/dispersant that would work with the ZnS-SiO_2 powders so that precise concentrations could be determined. So far, any solvent that successfully dissolved the composite also destroyed the sample. The second approach would be to make a very thin film of the silica composite on a mirror. The ratio between the number of photons detected from the mirror itself and the coated mirror would give a good indication of the quantum efficiency. The difficulty so far has been making a film that is thin enough to insure that self absorption is not an issue. The CIE chromaticity coordinates for the CdS-SiO_2 composite were calculated to be (0.39, 0.51) while the values for the zinc composite were (0.17, 0.19).

Phosphor mixtures. Although the ZnS and ZnS-SiO_2 phosphors appear to be promising media for cool white-light sources, the emission is somewhat biased to blue wavelengths. The center of the white light region in the 1931 CIE diagram is roughly at position (0.33, 0.33), which is known as the achromatic point. If a less biased white-light is desired, we

have found several ways to shift the emission profile, so that a different chromaticity is produced. The first approach is to mix the ZnS-SiO_2 and CdS-SiO_2 phosphors. By varying the percent composition of one to the other, the CIE coordinates can be tuned (see Figure 6.9). Mixing the phosphors does not result in a linearly additive spectral distribution due in large part to self absorption, which is why the chromaticity coordinates do not very linearly with composition. However, low CdS-SiO_2 containing mixtures yield coordinates that are shifted away from the blue and more toward the yellow region.

Another approach to mitigate the slight blue bias is to mix the ZnS-SiO_2 which was prepared at 150 °C with ZnO-SiO_2. To prepare ZnO-SiO_2, the exact same precursor

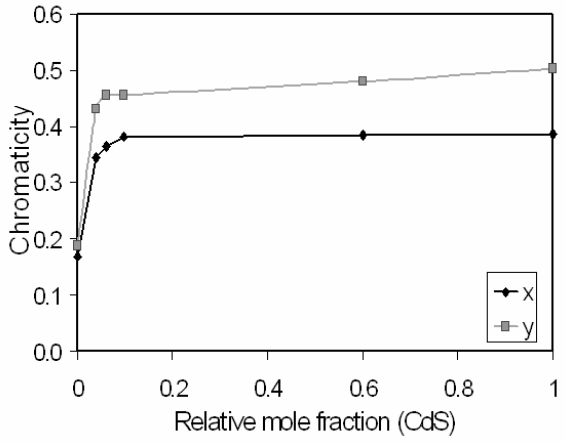

Figure 6.9: The CIE x and y chromaticity coordinates versus relative CdS mole fraction. The CdS mole fraction is relative to ZnS. Bear in mind that 95% of the phosphor is still SiO_2. The SiO_2 was left out of the mole fraction calculations for simplicity.

used to synthesize ZnS-SiO_2 can be used. The only difference is that a higher pyrolysis temperature is required (700 °C). A 1:1 (mass:mass) mixture of ZnS-SiO_2 (0.03 mole fraction) and ZnO-SiO_2 (0.05 mole fraction) yields the CIE coordinates of (0.19, 0.23).

while a 1:3 (mass:mass) mixture of ZnS-SiO_2 (0.03 mole fraction) and ZnO-SiO_2 (0.05 mole fraction) yields the CIE coordinates of (0.21, 0.30). Figure 6.10 shows the relationship between chromaticity and relative composition for the ZnS-SiO_2 and ZnO-SiO_2 mixtures. The ZnS/ZnO silica composite mixture is probably more favorable from a commercial standpoint since cadmium has a greater toxicity and cost when compared to zinc. Not to mention that having CdS in a fluorescent bulb phosphor will cause the unexcited powder to have a yellow color, which may be unappealing. Photographs of some of the phosphors are provided in Figure 6.11. A long-wave mercury ultraviolet lamp was used as the excitation source.

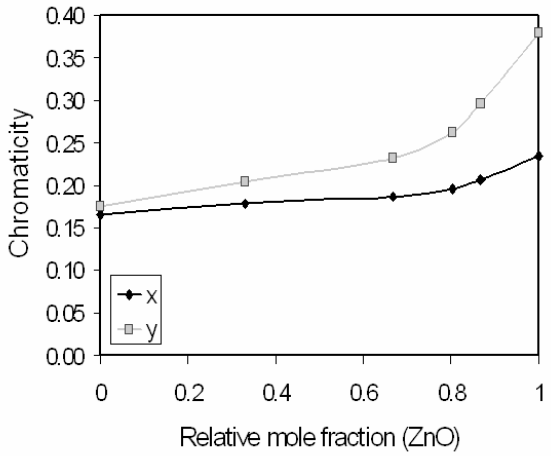

Figure 6.10: The CIE x and y chromaticity coordinates versus relative ZnO mole fraction. The ZnO mole fraction is relative to ZnS. As with the previous figure, remember that 95% of the phosphor is still SiO_2.

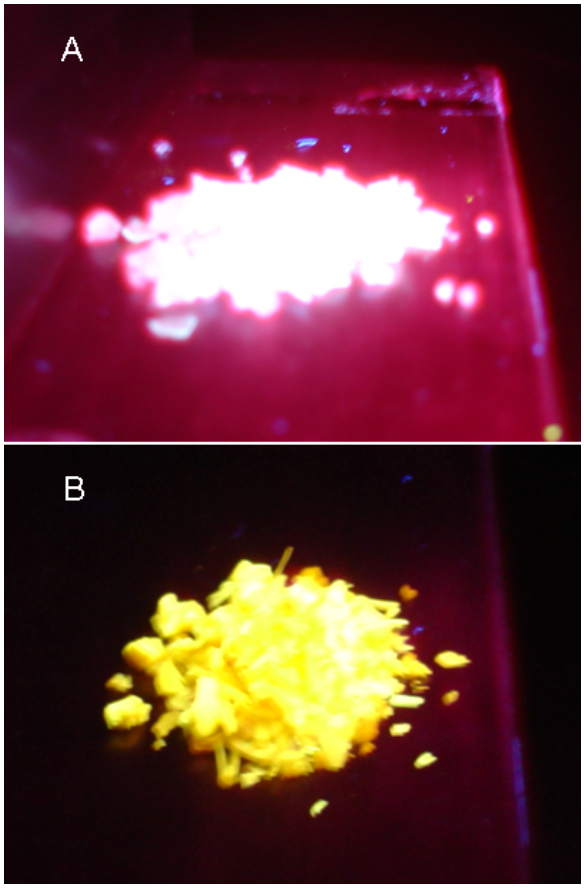

Figure 11: Photographs of: (A) $ZnS\text{-}SiO_2$ and (B) $CdS\text{-}SiO_2$. Each powder is excited with a long-wave mercury ultraviolet lamp.

Commercial Comparison. To explore the usefulness of the $ZnS\text{-}SiO_2$ and $CdS\text{-}SiO_2$ composites as phosphors in fluorescent bulbs, the phosphor mixture from a commercial bulb[35] was obtained. Mercury is used to excite the phosphors in current light bulbs. The two major wavelengths emitted by mercury are 365 nm and 254 nm. Therefore, comparisons were made at each of those wavelengths both separately and in tandem. Figure 6.12 shows the emission details of the commercial phosphor compared to 0.03 mole fraction $ZnS\text{-}SiO_2$ when excited at 365 nm.

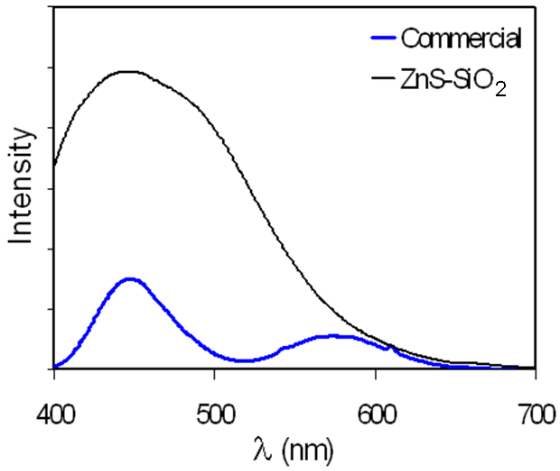

Figure 6.12: Fluorescence spectra for a commercial phosphor and a sample of 0.03 mole fraction $ZnS\text{-}SiO_2$. The excitation wavelength was 365 nm.

Under the conditions of the lower energy excitation, the zinc sulfide composite emits light that is much more intense than the commercial bulb. The chromaticity coordinates for the two phosphors under the given excitation conditions are: commercial (0.24, 0.18) and $ZnS\text{-}SiO_2$ (0.17, 0.19).

When 254 nm ultraviolet light is used to excite the two phosphors, a drastically different pattern results (refer to Figure 6.13). It is clear that the commercial material emits much more strongly when excited with the higher of the two energies. However, the silica composite still emits rather strongly even at the lower wavelength. The chromaticity coordinates do not change appreciably for the composite, but the values for the commercial phosphor change dramatically (0.32, 0.36).

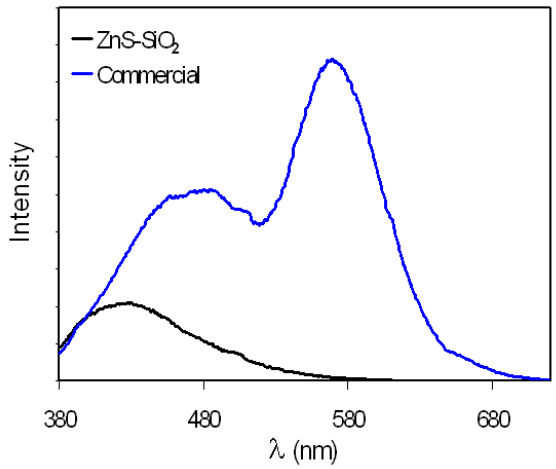

Figure 6.13: Fluorescence spectra for a commercial phosphor and a sample of 0.03 mole fraction ZnS-SiO_2. The excitation wavelength was 254 nm.

When the spectra from the two previous figures are combined, the results can be seen in Figure 6.14. While the actual power ratio for the two different excitations do not perfectly mimic that of mercury emission (the excitation was done by the Fluorolog mentioned in the characterization section), the combined spectra give the most realistic comparison. When the emissions from both excitations are summed, the chromaticity coordinates become: commercial (0.33, 0.37) and ZnS-SiO_2 (0.16, 0.18).

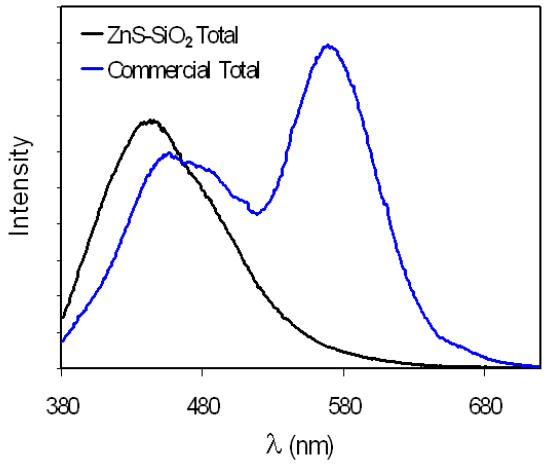

Figure 6.14: Emission spectra for a commercial phosphor and a sample of 0.03 mole fraction ZnS-SiO_2. The excitation wavelengths 254 nm and 365 nm were both used and the emissions were summed.

While the intensity of the lowest mole fraction ZnS-SiO_2 sample is comparable to the commercial phosphor mixture, the chromaticity is too biased to be used in a fluorescent bulb. Adding CdS-SiO_2 would help shift the emission color to the white, but due to the toxicity of cadmium, that may not be the best solution. However, combining the zinc sulfide and zinc oxide composites may provide a reasonable alternative to current phosphors which rely on rare-earth oxides and elaborate doping schemes.

ZnS-polystyrene hybrid. As a proof of concept reaction, hybrid thin films of ZnS nanocrystals in polystyrene were prepared and some of the luminescent properties were examined. In hindsight, polystyrene was not the best choice for light-emitting performance due to the fact that it does have some absorbance in the ultraviolet region of the spectrum and one of the relaxation processes is to emit photons in the blue/long ultraviolet region. Other polymers, such as those mentioned by Uthirakumar *et. al.*[36]

when they synthesized polymer/zinc oxide hybrids for the same purpose could be of interest. However, for ease of synthesis and characterization, polystyrene is sufficient for a starting point. The luminescence spectrum of ZnS-polystyrene can be seen in Figure 6.15. The chromaticity coordinates are shifted even further to the blue than the neat ZnS particles due to the contribution of the polystyrene itself.

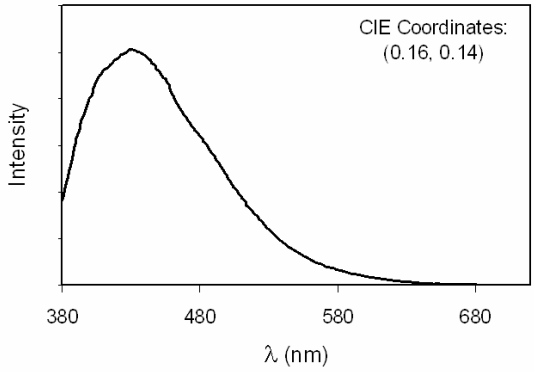

Figure 6.15: Luminescence spectrum of a ZnS-polystyrene thin film. The excitation wavelength used was 365 nm.

The two photographs in Figure 6.16 correspond to a thin coating of ZnS-polystyrene on the inside of a glass scintillation vial under normal laboratory light and then long wave ultraviolet light. The average thickness of the film was 235 μ and the ZnS mass percentage was just over 6%. The purple glow in the second image is due to the glass bottle itself and not the polymer nanocomposite. It is clear to see that through the purple glow, the thin film is emitting white light. If the excitation energy source was coming from inside the vial, as it would in a fluorescent bulb, the glass would not create

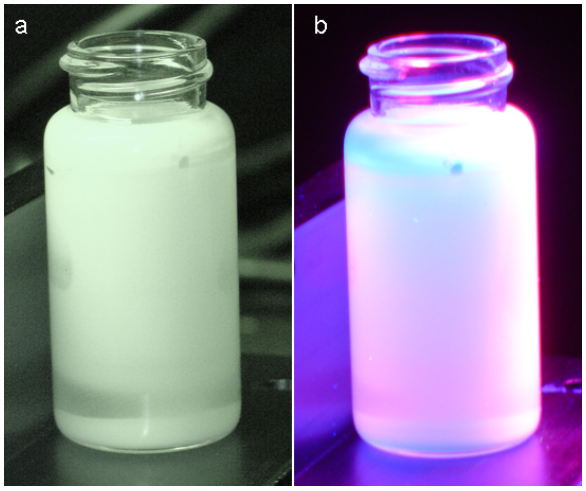

Figure 6.16: Photographs of a ZnS-polystyrene coating under (a) normal laboratory lights and (b) long wave mercury ultraviolet lamp.

interference. The image is included to prove that a thin film of the phosphor can easily be coated on the inside of a glass tube. Figure 6.17a demonstrates the contribution of polystyrene to the overall emission, while 6.17b shows two isolated ZnS-polystyrene films when excited with 365 nm ultraviolet radiation. While the CIE coordinates are blue biased, the high intensity emission of the phosphor seems to diminish the effect.

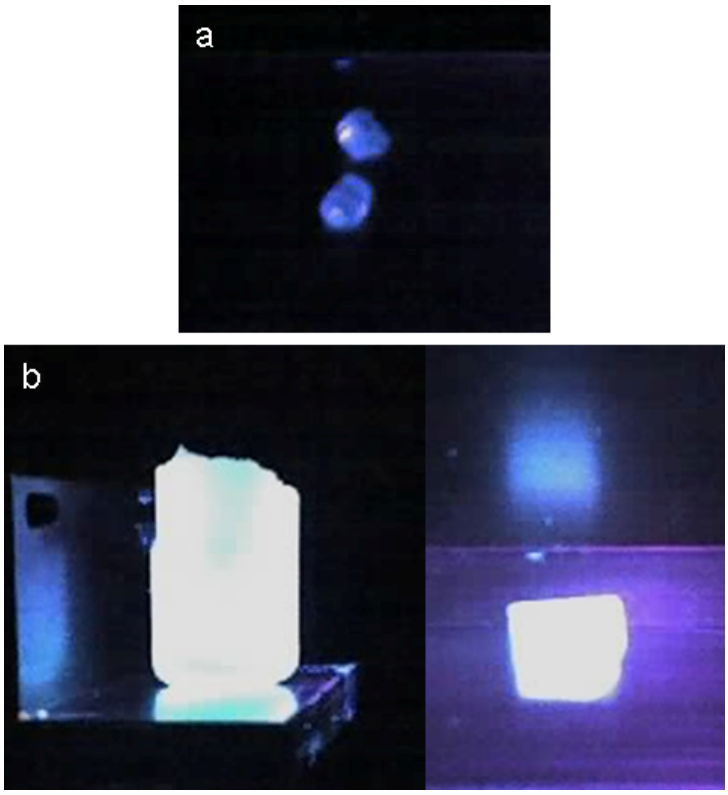

Figure 6.17: Photographs of (a) some polystyrene beads and (b) some thin film of ZnS-polystyrene when excited with a long wave mercury lamp.

CONCLUSIONS

Very small nanocrystals of zinc sulfide (1.5 nm) and CdS (2.8 nm) were prepared from the low temperature thermal decomposition of their corresponding ethylxanthate precursors. The ZnS particles prepared from this method can have a specific surface area over 300 m^2g^{-1} while the CdS particles have a value of 137 m^2g^{-1}. Although the ZnS and CdS nanocrystals are combined in larger bulk-like aggregates (no solution growth is necessary so no capping agent is present), the photoluminescence properties differ greatly from the bulk sulfides. White- and yellow-light emission is achieved due the sizeable surface-to-volume ratio of the phosphors. The high density of surface defects is due

primarily to the low preparative temperature and rapid, single-step decomposition of the ethylxanthate precursors.

$ZnS\text{-}SiO_2$, $ZnO\text{-}SiO_2$, $CdS\text{-}SiO_2$, ZnS-polystyrene and their mixtures show even more promise for lighting applications than the pure metal sulfides, since the luminescence intensity is increased and far less metal chalcogenide is needed for the same volume of phosphor. If necessary, the chromaticity coordinates can be tuned by mixing the various composites. The low cost and great abundance of the required preparative materials along with the remarkably simple synthetic procedure, make this approach to fabricating white-light phosphors very promising. This and further studies of these materials could aid in the development of more efficient/green devices, which could be used for future solid-state lighting equipment.

REFERENCES

[1] Eugene Hong, L. C., Michael Scholand **2005**, *II: Energy Efficient Lighting Technology Options*, 1-286.

[2] U.S. Lighting Market Characterization Volume I:National Lighting Inventory and Energy Consumption Estimate, 2002.

[3] (Tokyo Shibaura Electric Co., Ltd.). GB, 1968, p 9 pp.

[4] (Westinghouse Electric Corp.). GB, 1968, p 10 pp.

[5] Juestel, T.; Mayr, W.; Schmidt, P. J.; (Philips Intellectual Property & Standards GmbH, Germany; Koninklijke Philips Electronics N. V.). Application: WO WO, 2004, p 18 pp.

[6] Bulur, E.; Goeksu, H. Y.; Wieser, A.; Figel, M.; Oezer, A. M. *Radiation Protection Dosimetry* **1996**, *65*, 373-379.

[7] Chakrabarty, B. S.; Murthy, K. V. R.; Joshi, T. R. *Indian Journal of Pure and Applied Physics* **1999**, *37*, 136-141.

[8] Mueller, A. H.; Petruska, M. A.; Achermann, M.; Werder, D. J.; Akhadov, E. A.; Koleske, D. D.; Hoffbauer, M. A.; Klimov, V. I. *Nano Letters* **2005**, *5*, 1039-1044.

[9] Achermann, M.; Petruska, M. A.; Kos, S.; Smith, D. L.; Koleske, D. D.; Klimov, V. I. *Nature (London, United Kingdom)* **2004**, *429*, 642-646.

[10] Yu, W. W.; Qu, L.; Guo, W.; Peng, X. *Chemistry of Materials* **2003**, *15*, 2854-2860.

[11] Steigerwald, D. A.; Bhat, J. C.; Collins, D.; Fletcher, R. M.; Holcomb, M. O.; Ludowise, M. J.; Martin, P. S.; Rudaz, S. L. *IEEE Journal of Selected Topics in Quantum Electronics* **2002**, *8*, 310-320.

[12] Tamura, T.; Setomoto, T.; Taguchi, T. *Journal of Luminescence* **2000**, *87-89*, 1180-1182.

[13] Schlotter, P.; Baur, J.; Hielscher, C.; Kunzer, M.; Obloh, H.; Schmidt, R.; Schneider, J. *Materials Science & Engineering, B: Solid-State Materials for Advanced Technology* **1999**, *B59*, 390-394.

[14] Nakamura, S.; Fasol, G. *The Blue Laser Diode: GaN Based Light Emitters and Lasers*, 1997.

[15] Shimizu, Y.; Sakano, K.; Noguchi, Y.; Moriguchi, T.; (Nichia Kagaku Kogyo Kabushiki Kaisha, Japan). Application: WO
WO, 1998, p 84 pp.

[16] D'Andrade, B. W.; Forrest, S. R. *Advanced Materials (Weinheim, Germany)* **2004**, *16*, 1585-1595.

[17] Huang, Y.-S.; Jou, J.-H.; Weng, W.-K.; Liu, J.-M. *Applied Physics Letters* **2002**, *80*, 2782-2784.

[18] Tang, C. W.; VanSlyke, S. A. *Applied Physics Letters* **1987**, *51*, 913-15.

[19] Xu, Y.; Peng, J.; Mo, Y.; Hou, Q.; Cao, Y. *Applied Physics Letters* **2005**, *86*, 163502/1-163502/3.

[20] Bowers, M. J., II; McBride, J. R.; Rosenthal, S. J. *Journal of the American Chemical Society* **2005**, *127*, 15378-15379.

[21] Hill, N. A.; Whaley, K. B. *Journal of Chemical Physics* **1994**, *100*, 2831-7.

[22] Underwood, D. F.; Kippeny, T.; Rosenthal, S. J. *Journal of Physical Chemistry B* **2001**, *105*, 436-443.

[23] Chen, X.; Samia Anna, C. S.; Lou, Y.; Burda, C. *J Am Chem Soc FIELD Full Journal Title:Journal of the American Chemical Society* **2005**, *127*, 4372-5.

[24] Li, H.; Shih, W. Y.; Shih, W.-H. *Nanotechnology* **2007**, *18*, 205604/1-205604/6.

[25] Kawazu, Z.; Kawakami, Y.; Taguchi, T.; Hiraki, A. *Technology Reports of the Osaka University* **1989**, *39*, 203-14.

[26] McClean, I. P.; Thomas, C. B. *Semiconductor Science and Technology* **1992**, *7*, 1394-9.

[27] Peng, W. Q.; Qu, S. C.; Cong, G. W.; Zhang, X. Q.; Wang, Z. G. *Journal of Crystal Growth* **2005**, *282*, 179-185.

[28] Tanaka, M.; Qi, J.; Masumoto, Y. *Journal of Luminescence* **2000**, *87-89*, 472-474.

[29] Chen, W.; Malm, J.-O.; Zwiller, V.; Wallenberg, R.; Bovin, J.-O. *Journal of Applied Physics* **2001**, *89*, 2671-2675.

[30] Rao, S. R. *Xanthates and Related Compounds*, 1971.

[31] The International Centre for Diffraction Data, Newton Square, PA: (The International Centre for Diffraction Data, Newton Square, PA); Vol. File Nos. 05-0566 & 36-1451.

[32] Topas 1.0.1 ed.; Bruker AXS, GmbH: 1998.

[33] Warren, B. E. *Prog. Metal Phys. (Bruce Chalmers and R. King, editors. Pergamon Press)* **1959**, *8*, 147-202.

[34] Warren, B. E.; Averbach, B. L. *Journal of Applied Physics* **1950**, *21*, 595-8.

[35] Philips Alto Collection F34C/RS/EW.

[36] Uthirakumar, P.; Hong, C.-H.; Suh, E.-K.; Lee, Y.-S. *Chemistry of Materials* **2006**, *18*, 4990-4992.

CHAPTER 7

WATER SOLUBLE METAL SULFIDE QUANTUM DOTS: WHITE-LIGHT EMISSION FROM CADMIUM SULFIDE

Water-soluble cadmium sulfide quantum dots were prepared from the low temperature (125 °C) thermal breakdown of the single-source precursor, cadmium isethionic xanthate. In some cases, no external capping agent is required to produce stable nanoparticulate suspensions since the precursor byproducts act as stabilizers. For indefinitely stable quantum dot suspensions, dilute mercaptoacetic acid was used to saturate the nanoparticle surface. The luminescence profile of the CdS particles showed intense white emission when excited with 365 nm radiation. The broad fluorescence is attributed, primarily, to surface defects that generate a wide assortment of deep trap energy levels. With CIE chromaticity coordinates of (0.32, 0.38), the CdS nanocrystals demonstrate great potential for use in future lighting equipment.

INTRODUCTION

The scientific literature contains numerous examples of successful preparation of stable colloids of various semiconducting nanoparticles.[1-9] The referenced authors, along with many others, have proven that semiconducting nanocrystals in the range of 1-20 nm exhibit properties that are distinct from their bulk counterparts. For example, the optical, electrical, and mechanical properties can all be tuned by simply changing the size of the nanocrystal. Beyond the unique tunable properties of these so-called quantum dots, there is a driving force in technology to further miniaturize optical and electrical devices.[10,11] Current optical lithographic methods do not have the resolution necessary to sculpt features in the quantum confinement region (1-20 nm).[12] Nanoimprint lithography demonstrates better resolution than optical lithography, but there are still practical constraints associated with the technology.[13] As an alternative to lithographic fabrication schemes, there is a continuing effort within the scientific community to prepare devices and device material from chemical methods.

Two of the most commonly studied semiconducting nanocrystal systems are the II/VI metal chalcogenides, CdSe and CdS. Early on, both cadmium selenide and sulfide found success in photovoltaic devices.[14-17] Other potential applications for CdS and CdSe have been discovered, such as light emission[18,19] and sensing.[20,21] This chapter focuses on the utilization of CdS as a light emitter.

An important factor inherent with ultra-small particles is that they must be stabilized with a capping agent, usually an organic ligand.[22] Tri-*n*-octylphosphine oxide was the stabilizing agent of choice for years and is still presently used.[23-27] Alternative stabilizers are sought for many reasons. Two such reasons are that residual tri-*n*-

octylphosphine oxide diminishes optical clarity and quenches photoluminescence.[28-30] An added downside to using trioctylphosphine and trioctylphosphine oxide coordinators is that organic solvents are required as dispersants. If there was a way to prepare water-soluble nanocrystals without significantly impairing the desirable features, it would be a much more cost-effective and environmentally-favorable process. Water-soluble quantum dots would be much more compatible for biological reasons as well.[31-33] Replacing the tri-*n*-octylphosphine based capping agents with mercaptopropanoic acid provides water solubility at the expense of reduced photoluminescent efficiency.[34,35]

It seems reasonable to search for a chemical system that generates water-soluble, ultra-small nanocrystals where the stabilizing agent does not negatively affect the material properties. With energy costs and demands as they are, the preparative method should be as straightforward as possible and consume as little energy as possible. Single precursors used to grow metal sulfide and metal selenide particles offer advantages to dual-source synthetic methods since dual precursors can undergo premature reactions, which leads to non-stoichiometric and/or inhomogeneous products. Even single-source precursor growth methods require that the capping agent is added separately. If the stabilizing agent was built into the precursor, the complexity of the reaction would substantially decrease. We have developed a single precursor for CdS where the decomposition products of that precursor act as "in-house" stabilizers for the nanocrystals. This chemical system corresponds to a truly single-source synthetic technique.

EXPERIMENTAL

Materials. Reagent grade cadmium chloride ($CdCl_2 \cdot 2½H_2O$, Fisher), silver nitrate ($AgNO_3$, 0.1M, Fisher), sodium isethionate ($NaO_3SCH_2CH_2OH$, Aldrich), sodium hydroxide (NaOH, EMD), carbon disulfide (CS_2, Alfa Aesar), and mercaptoacetic acid ($HSCH_2COOH$, Aldrich) were obtained commercially and used as received without further purification. All water used throughout the experiment was deionized with a resistivity of 18.1 MΩcm.

Synthesis of sodium and cadmium isethionic xanthate. Sodium isethionic xanthate was prepared by mixing sodium hydroxide, carbon disulfide, and sodium isethionate in a stoichiometric fashion. Usually, NaOH (6.00 g, 150 mmole) was dissolved in water (200 ml) and placed in an ice bath. Sodium isethionate (22.22 g, 150 mmole) was also dissolved in water (200 ml) and then added to the sodium hydroxide solution. Finally, carbon disulfide (11.45 g, 150 mmole) was slowly dispensed into the mixture. The three reagents were allowed to mix until the CS_2 had completely reacted (roughly 24 hours). The product of the reaction was water-soluble sodium isethionic xanthate ($NaS_2COCH_2CH_2SO_3Na$), and the yield was approximately 92 %. Water was easily driven off with a steady stream of air, and solid sodium isethionic xanthate was obtained. The xanthate was purified and stored in a brown glass bottle at room temperature and remained indefinitely stable.

Cadmium isethionic xanthate, $Cd(S_2COCH_2CH_2SO_3Na)_2$, was synthesized by stoichiometrically reacting aqueous solutions of cadmium chloride and sodium isethionic xanthate (1 to 2 mole equivalents respectively). Cadmium isethionic xanthate is

moderately soluble in water, which is different from most xanthic acid derivatives of cadmium that normally suffer from poor solubility. When the two reagents are mixed, after a time, a pale yellow solid forms which eventually sinks to the bottom of the container. It was determined this solid was cadmium carbonate. Do to the partial decomposition and high water solubility, an accurate xanthate yield was not determined.

Synthesis of CdS colloids. For the particles prepared in this study, an aqueous saturated solution of cadmium isethionic xanthate was prepared and the excess solid was removed by simple filtration. The precursor solution was either used as is or diluted with water depending on the application. Regardless of precursor concentration, to get CdS particles, the solution was placed in a sealed tube and heated to 125 °C. Thirty minute heating times were used throughout the experiment for consistency.

To get nanoparticle suspensions without the addition of an external capping agent, a saturated cadmium isethionic xanthate sample was diluted by a factor of at least ten times (greater dilution factors were also used) and then warmed in a preheated 125 °C oven. After the thirty minute heating period, the CdS colloids were stored in glass vials under ambient conditions. For stable quantum dot suspensions, a saturated precursor solution was diluted by a factor of ten (or greater) and enough mercaptoacetic acid was added to achieve a final mercaptoacetic acid concentration of 5%. The 5% concentration was an arbitrary choice, and it is possible that less stabilizing agent would be sufficient. Again, the precursor was placed in a preheated 125 °C oven and warmed for thirty minutes. The resulting CdS quantum dots were kept in glass vials under ambient conditions.

Characterization. The UV adsorption spectra of the xanthate compounds were measured with a Perkin-Elmer Lamda EZ201 spectrometer. Spectra were measured at 200 nm/min from 200-500 nm in a quartz cuvette.

A Horiba Jobin Yvon Fluorolog FL-1039 was used to measure the luminescence spectra of the precurosor and CdS suspensions. While many different excitation wavelengths were utilized, only spectra recorded for 365 nm excitation will be reported here. Emission measurements of the precursor were performed in the solid-state, while the quantum dots were measured as aqueous suspensions in a quartz cuvette. Chromaticity coordinates were determined using the 1931 Commission Internationale de l'Eclairage (CIE) color matching functions and corresponding color space map.[36]

For infrared spectroscopic measurements, approximately 10 mg of the sodium or cadmium isethionic xanthate precursors were mixed with approximately 100 mg FTIR-grade potassium bromide and the blend was finely ground. Spectra in the 4000-400 cm^{-1} region were collected by diffuse reflectance of the ground powder with a Nicolet Magna-IR 750 spectrometer. Normally, 128 scans were recorded and averaged for each sample (4.0 cm^{-1} resolution) and the background was automatically subtracted. Prominent IR adsorption signals for sodium isethionic xanthate (cm^{-1}): 2990(m), 2941(m), 2888(w), 1467(m, sh), 1442(s), 1383(m, sh), 1364(m), 1210(vs), 1126(vs), 1031(vs), 868(m), 817(m), 657(m), 451(s).

Raman spectroscopy was also used to characterize the sodium and cadmium precursors. A Nicolet NXR 9610 Raman Spectrometer was used for the analysis and a neat pressed pellet was used for each measurement. Typically, 32 scans were averaged in the 4500-50 cm^{-1} range at a resolution of 4.0 cm^{-1}. Prominent Raman signals for sodium

isethionic xanthate (cm^{-1}): 2987(m), 2937(s), 2887(m), 1463(m), 1436(m), 1393(m), 1318(m), 1227(m), 1164(m), 1073(vs), 971(w), 849(m), 755(s), 620(m), 591(w), 537(s), 501(m), 449(m), 361(m), 313(m), 140(m). Raman peaks for cadmium isethionic xantahte (cm^{-1}): 2970(m), 2934(m), 1396(m), 1083(vs), 1039(m, sh), 797(m), 737(m), 657(m), 523(m), 269(s), 156(s).

Powder X-ray diffraction (XRD) measurements were obtained on a Bruker AXS D8 Advance diffractometer using Cu Kα radiation with an acceleration voltage of 40 kV and current flux of 30 mA. The diffractograms were recorded for a 2θ range of 17-70° with a step size of 0.02° and a counting time of 18 seconds per step. All the XRD patterns where collected at ambient temperature, and the phases were identified using the ICDD database.[37] The peaks were profiled with a Pearson 7 model using Topas P version 1.01 software.[38] The profiles of the standard and the sample were put into the Win-Crysize program version 3.05, which uses the Warren-Averbach evaluation method to determine crystallite size.[39,40]

The specific surface areas were obtained with a conventional Brunauer-Emmett-Teller (BET) multilayer nitrogen adsorption method using a Quantachrome Nova 1200 instrument.

Thermogravimetric analysis (TGA) was performed on the sodium and cadmium isethionic xanthate complexes at a rate of 2.0°/min from room temperature to 600 °C using a Seiko Instruments Exstar 6200. Neither sodium nor cadmium isethionic xanthate melts congruently, but a well behaved decomposition curve was observed for each precursor.

Dynamic light scattering (DLS) measurements were performed on the CdS nanosuspensions with a Malvern HPPS 3001 instrument. Particle size measurements were obtained at 25.0 °C with dispersant viscosity and refractive index values of 0.887 cP and 1.330 respectively.

Transmission electron micrographs (TEM) were obtained using a JEOL JEM-100CXII electron microscope operated at 200 kV. The water-soluble CdS particles were deposited on a carbon-coated copper TEM grid.

RESULTS AND DISCUSSION

Low temperature formation of CdS nanoparticles from a single precursor with built in stabilizing agent. As previously mentioned, when one molar equivalent of $Cd^{2+}(aq)$ is mixed with 2 molar equivalents of $^{-}S_2COCH_2CH_2SO_3Na(aq)$, a new complex is formed. The pale yellow cadmium isethionic xanthate complex is relatively soluble in water due to the terminal $–SO_3^-$ (sulfonate) groups. To the best of our knowledge, there has been no report of this compound in the available literature, so some basic characterization information is presented. The ultraviolet absorption spectrum measured for a 1.5×10^{-4} M sample is shown in Figure 7.1. The extinction coefficient was estimated for cadmium isethionic xanthate to be 4.58×10^{3} $L\cdot mole^{-1}\cdot cm^{-1}$ based on the 301 nm peak from a plot of five different precursor concentrations. The Beer's Law plot can be seen in Figure 7.2. An estimate for the concentration of a saturated solution is 0.03 M $Cd(S_2COCH_2CH_2SO_3Na)_2$. On a weight percent basis, this molar concentration corresponds to just under 17 g per liter. The cadmium salt will begin to fall out of a

saturated solution after a few hours if not mixed periodically implying that the solution becomes supersaturated when mixed.

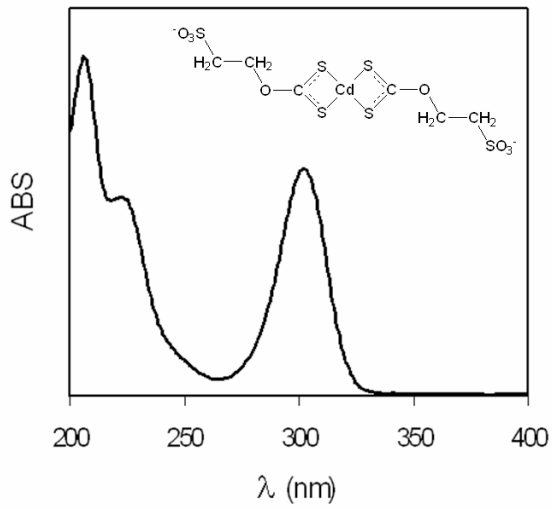

Figure 7.1: Ultraviolet absorbance spectrum for cadmium isethionic xanthate in water. A simplified structure of the xanthate complex is shown above the spectrum.

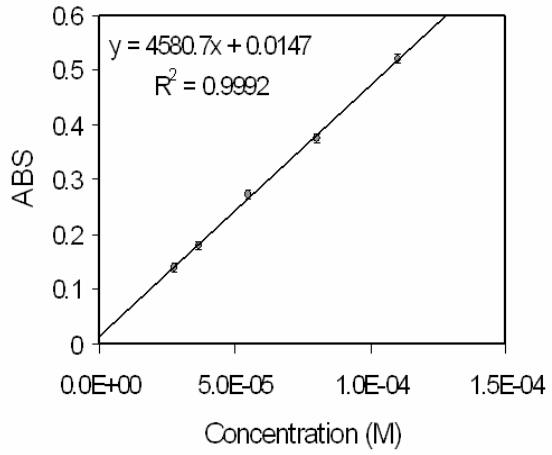

Figure 7.2: Beer's Law plot of absorbance versus cadmium isethionic xanthate concentration for the 301 nm peak.

Raman spectra for both sodium and cadmium isethionic xanthate are shown in Figure 7.3. Based on previous Raman[41] and IR[42-45] studies of xanthate compounds, the peaks can be identified. Refer to Table 7.1 for a summary of the various signals and corresponding motions for the cadmium and sodium xanthates.

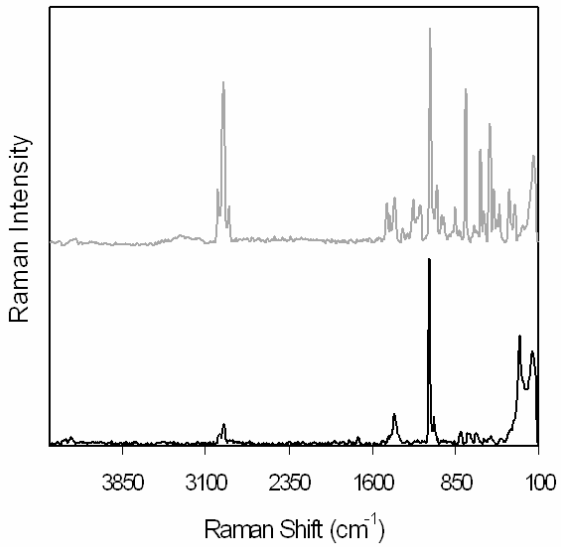

Figure 7.3: Raman spectra of sodium isethionic xanthate (top) and cadmium isethionic xanthate (bottom).

Raman and infrared spectroscopy were useful in validating the product structure. The exact crystal structure, however, of $Cd(S_2COCH_2CH_2SO_3Na)_2$ is not known. The instability, which is a positive for its use as a low temperature precursor, makes isolating the compound difficult. However, a powder diffraction pattern was obtained for the sodium salt. The sodium isethionic xanthate diffractogram can be seen in Figure 7.4. The peak pattern for the compound does not match any reported crystal structure.

Table 7.1: Selected Raman/IR signals and corresponding assignments for sodium isethionic xanthate and cadmium isethionic xanthate.

Infrared Frequency (cm^{-1})	Raman Frequency (cm^{-1})	Assigned Motion
	< 100	Lattice vibrations
	140	Na-S vibrations
	156	Cd-S vibrations
	269	Cd-S stretching vibrations
	313	SCS in-phase bending
	362	SCS out-of-phase bending, Cd-S vibrations
474	449	COC in-phase bending
530-675	500-650	Various OCS_2 and CS motions
750-850	750-850	CS stretches
950	971	Cd-S
	1015-1040	CS_2 out-of-phase stretching, S-O stretch
1010-1120	1070-1085	S-O movements
	1164	CH_2, (S)CO stretching
1201	1227	COC out-of-phase stretching
1318-1435	1390-1460	CH wagging, CH_2 deformation
2888, 2937	2885-2990	CH_2 stretchings

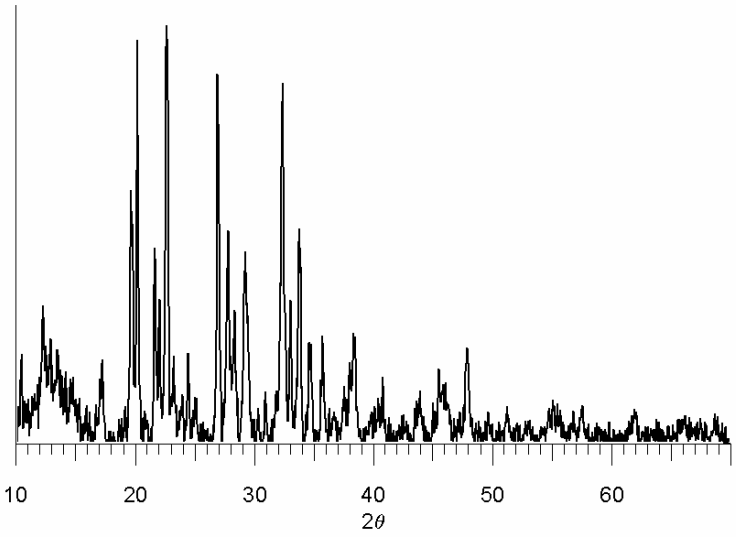

Figure 7.4: Powder X-ray diffraction patterns for $NaS_2COCH_2CH_2SO_3Na$.

Thermalgravimetric anaylsis traces for the sodium and cadmium xanthate complexes can be seen in Figure 7.5. Determining an onset elimination temperature for the cadmium compound is challenging due to the lack of any drastic features in the TGA profile between room temperature and 300 °C. The presence of the sodium sulfonate

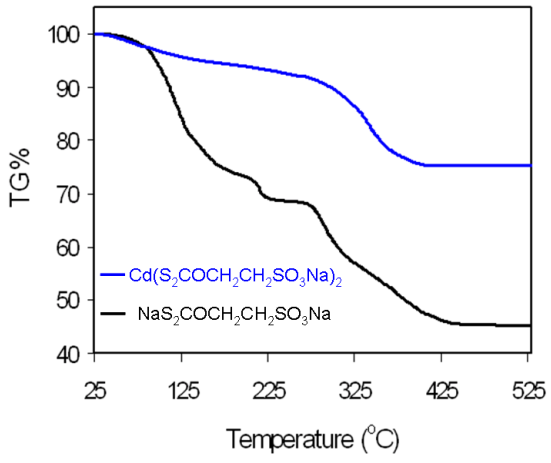

Figure 7.5: Thermalgravimetric analysis traces of $NaS_2COCH_2CH_2SO_3Na$ and $Cd(S_2COCH_2CH_2SO_3Na)_2$**.**

functionality in the precursor complicates the decomposition compared to the ethylxanthate analog. The composition of the cadmium xanthate compound after firing at 400 °C was determined by powder X-ray diffraction. The pyrolysis product was phase-pure cadmium sulfide. The mass loss at roughly 300 to 400 °C provided a starting point for selecting the optimal decomposition conditions. Previously, however, it has been established that the presence of a coordinating solvent lowers the necessary conversion temperature.[46] Additionally, the sodium isethionic xanthate trace shows a significant mass loss which occurs in the 100-125 °C range. Therefore, the range of 100-125 °C was chosen as the reaction temperature for $Cd(S_2COCH_2CH_2SO_3Na)_2$ (when in solution), and that range seemed to provide the most favorable conditions for nanoparticle growth. It should be mentioned, that while elevated temperatures are required to rapidly convert the precursor in its entirety, some decomposition does occur at ambient temperature. Figure 7.6 shows dynamic light scattering results for saturated cadmium isethionic xanthate after only three hours at room temperature. The occurrence of nanometric particles indicates that some CdS has formed. The relative amount of decomposition that occurs at room temperature is small enough that the CdS does not significantly affect the absorption or Raman spectra. However, the emission spectrum confirms CdS formation (Figure 7.7). Thus, it appears that the conversion of cadmium isethionic xanthate to cadmium sulfide at room temperature is thermodynamically acceptable, just kinetically hindered. The most likely reason for the room temperature decomposition is that the nucleophilic character of the oxygen in a water molecule or the presence of hydroxide ions from the autoionization of water causes a base-catalyzed elimination.

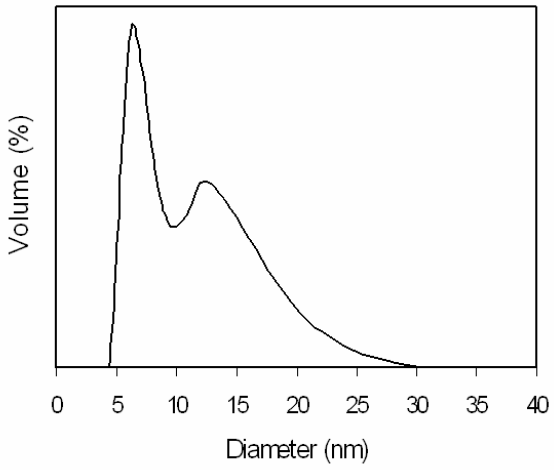

Figure 7.6: Dynamic light scattering data for CdS particles that formed from the room temperature decomposition of a saturated aqueous solution of cadmium isethionic xanthate. The solution had rested for three hours.

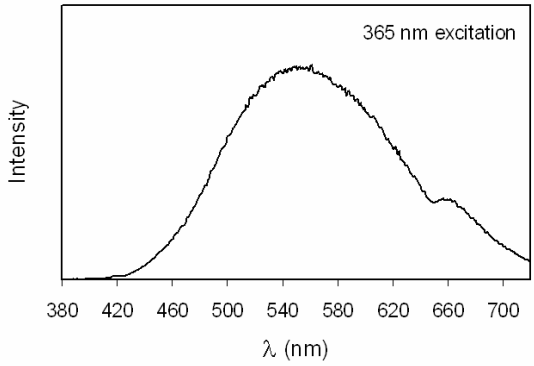

Figure 7.7: Luminescence emission data for CdS particles that formed from the room temperature decomposition of a saturated aqueous solution of cadmium isethionic xanthate. The solution had rested for three hours.

If a dilute aqueous solution of cadmium isethionic xanthate is freshly prepared and pyrolyzed for 30 minutes at 125 °C, CdS particles in the quantum dot range are formed (see Figure 7.8A). The ultra small nanocrystals remain stable for some time due to the isethionic xanthate byproducts acting as capping agents. After the thirty minute

warming period, if left at room temperature, the CdS nanocrystals will eventually grow out of the quantum dot range and stabilize with average diameters of roughly 50 nm (Figure 7.8B). Typically, depending on the starting xanthate concentration, it takes about

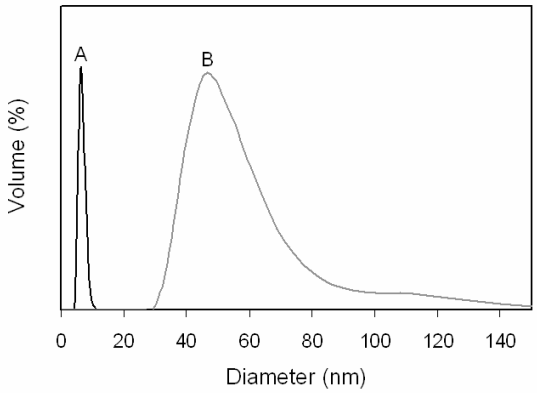

Figure 7.8: Dynamic light scattering data for CdS particles that formed from: (A) a dilute cadmium isethionic xanthate solution which was heated at 125 °C for 30 minutes and (B) the same dilute aqueous solution of cadmium isethionic xanthate that was heated for 30 minutes and then left at room temperature for 18 hours.

18-24 hours for the ripening to go to completion. To prove that cadmium sulfide particles were actually grown as a result of the xanthate decomposition, a dilute (~0.005 M) $Cd(S_2COCH_2CH_2SO_3Na)_2$ solution was prepared and pyrolyzed at 125 °C for four hours. After such an extended heating time, a bright orange precipitate can be seen in the reaction flask. The X-ray diffraction pattern for the orange solid is presented in Figure 7.9, and it is apparent that CdS is, indeed, forming from the thermal breakdown of the isethionic xanthate precursor.

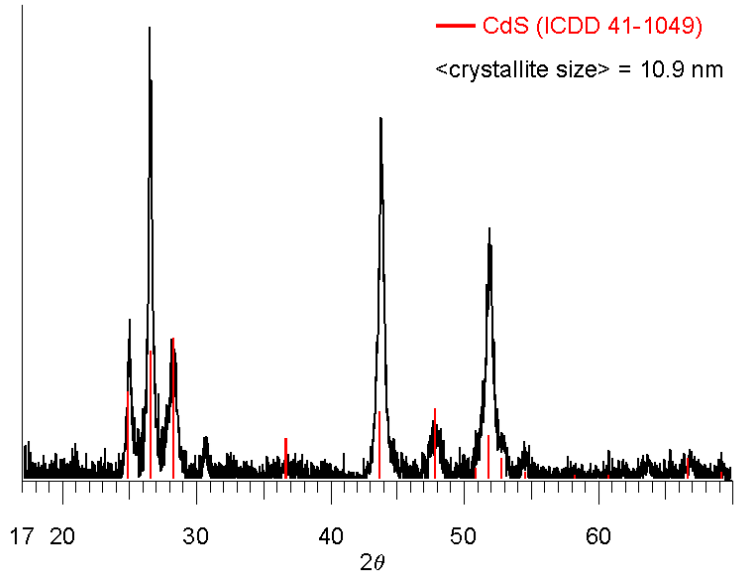

Figure 7.9: Powder X-ray diffraction pattern of the solid formed from aqueous $Cd(S_2COCH_2CH_2SO_3Na)_2$ heated to 125 °C for four hours.

Even though the diameter of the cadmium sulfide particles slowly increases from the quantum dot region to aggregates of roughly 50-60 nm, the finding is significant. This growth method uses a single-source precursor, so stoichiometry is not a problem. The precursor requires very little heating at a relatively low temperature to achieve conversion, so only modest amounts of energy are required. The precursor and the nanoparticulate suspensions are both water-soluble, which is both economically and environmentally favorable. The water-solubility and "in-house" particle stabilization come from the unique xanthate ligands (or decomposition products of the ligands), and specifically from the sulfonate groups on each ligand.

Emission characteristics of mercaptoacetic acid stabilized CdS quantum dots. Water soluble CdS quantum dots, which appear to be indefinitely stable, can be

synthesized from cadmium isethionic xanthate if 5% mercaptoacetic acid is used as a solvent instead of pure water. For example, a saturated $Cd(S_2COCH_2CH_2SO_3Na)_2$ solution which is diluted by a factor of ten and brought to a mercaptoacetic acid concentration of roughly 5%, which is then heated for 30 minutes at 125 °C yields CdS nanocrystals with 5 nm average diameters. In Figure 7.10 there are two transmission electron microscopy images of mercaptoacetic acid capped cadmium sulfide. The particles vary in size from approximately 2-8 nm and have no uniform shape. Some particles are spherical; others are slightly elongated along a particular axis, while others may be best described as polyhedral. Figure 7.11 shows the emission spectra for mercaptoacetic acid stabilized CdS particles when excited with 365 nm radiation. As one might expect from the broad luminescence spectrum, the cadmium sulfide colloid appears white when excited with 365 nm light (Figure 7.12). The breadth of the emission curve cannot be explained solely by the quantum confinement effect of varying particle sizes, but is partially attributed to surface phenomena.[18,47,48]

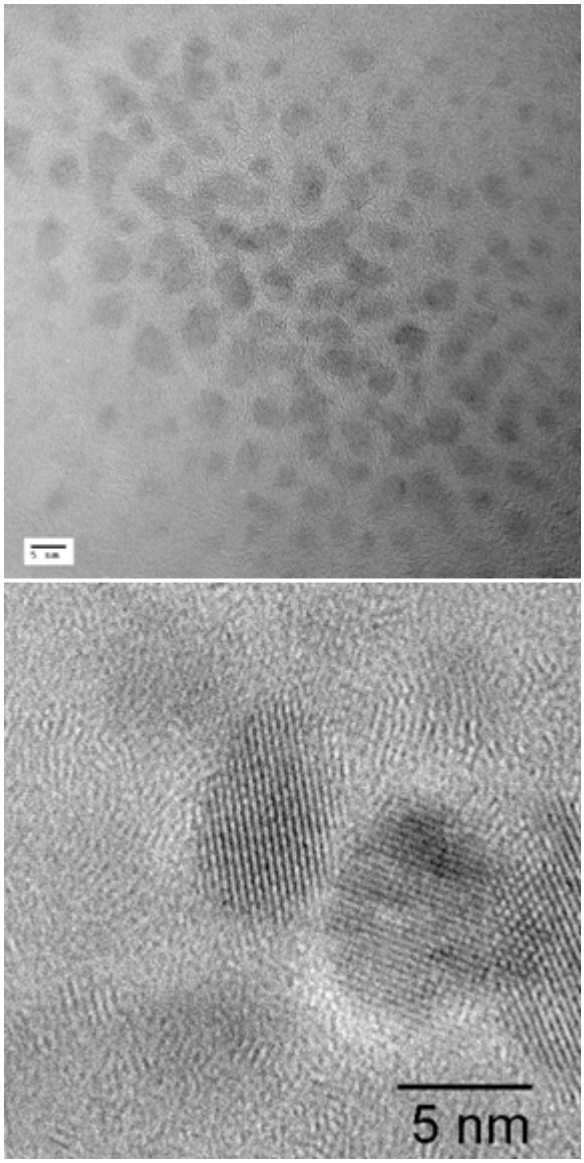

Figure 7.10: Transmission electron microscope images of CdS quantum dots. Both images are of the same sample taken at the same magnification. The magnification of the bottom picture was done digitally.

The rapid decomposition from xanthate to sulfide does not allow significant surface reorganization, which contributes to a defect laden surface. Similarly, the relatively low

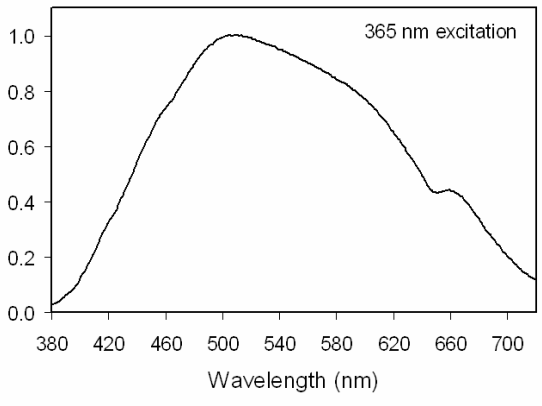

Figure 7.11: Emission spectrum of CdS quantum dots dispersed in water.

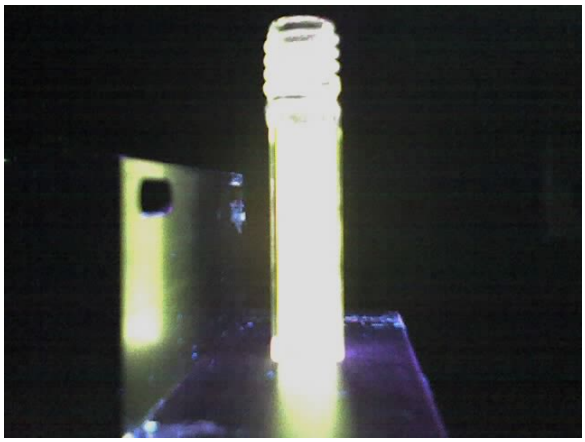

Figure 7.12: Photograph of a dilute CdS nanocrystal suspension excited with a mercury long-wave ultraviolet lamp. The particles are in water with 5% mercaptoacetic acid.

preparative temperature used is not conducive to extensive sintering. The combination of low temperature and rapid particle growth contribute to irregular particle shapes and surfaces with large defect densities. This considerable assortment of surface defects corresponds to a wide variety of deep trap levels, which give rise to broadband emission.

To the naked eye, the CdS nanoparticles emit white light, and the actual chromaticity coordinates based on the 1931 CIE system are (0.32, 0.38). For comparison, the achromatic point in the CIE color space map is at point (0.33, 0.33), so the CdS

emission in well within the typical white-light region. The photoluminescence quantum efficiency was assessed using Rhodamine 6G as a standard.[49] The value obtained, is at best, an estimate since determining a precise cadmium sulfide concentration is problematical. The complicated nature of the decomposition makes gauging the completeness of the xanthate-to-sulfide conversion rather difficult. However, a relative efficiency of 20-30% was calculated. This number will have to be revisited once a protocol to find a more definite CdS concentration is brought to fruition.

The distinctive optical characteristics of the CdS nanocrystals indicate that they would be a promising material for use as a phosphor in fluorescent bulbs or more likely as an emitting layer in light emitting diodes. The simple, low-cost, low-temperature preparation from the single precursor only adds to the appeal of the cadmium sulfide quantum dots.

Formation of Ag_2S nanoparticles. The isethionic xanthate anion can be used with other metals to form various metal sulfide precursors. Copper and nickel isethionic xanthates were prepared in the same way the cadmium salt was. Beyond demonstrating that the corresponding sulfides can be prepared from the copper and nickel salts very little was done to study those 2+ metals. To investigate if a 1+ transition metal would form a useful complex with the isethionic xanthate ligand, $AgNO_3$ was reacted in a one-to-one fashion with $NaS_2COCH_2CH_2SO_3Na$. The silver did form a complex through the xanthate functionality as evidenced by Raman and infrared spectroscopies. It was also established that the decomposition of $AgS_2COCH_2CH_2SO_3Na$ led to phase-pure Ag_2S formation. For example, if a dilute aqueous solution of silver isethionic xanthate is

heated to 100-125 °C for approximately four hours, a dark precipitate forms in the reaction vessel. The dark precipitate was determined to be Ag_2S by powder X-ray diffraction (refer to Figure 7.13).

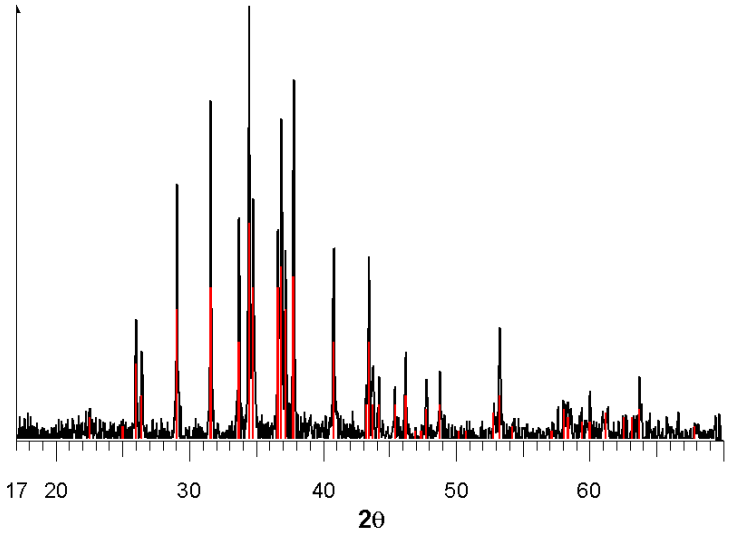

Figure 7.13: Powder X-ray diffraction pattern of the solid product formed from the 125 °C pyrolysis of aqueous $AgS_2COCH_2CH_2SO_3Na$. The red vertical lines are the database peaks for Acanthite, Ag_2S (ICDD, 14-0072).

Both the solubility and stability for the silver complex is similar to that of the cadmium species. The facile formation of water-soluble quantum dots is also possible with the silver isethionic xanthate system. Heating a dilute sample for roughly 30 minutes at 100-125 °C in 5% mercaptoacetic acid produces Ag_2S nanoparticles in the 1-10 nm size range. Transmission electron microscopy images of mercaptoacetic acid stabilized silver sulfide particles are shown in Figure 7.14. The average size of the silver sulfide particles is 8 nm. In contrast to the cadmium sulfide case, most of the Ag_2S particles are the same shape and there is much less size variability.

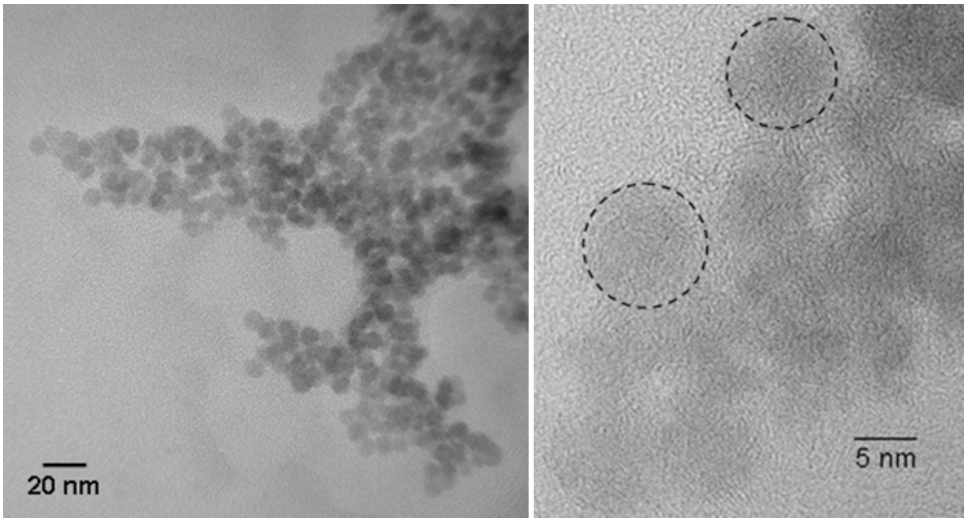

Figure 7.14: Transmission electron microscopy images of Ag_2S prepared by heating silver isethionic xanthate for 30 minutes at 125 °C in a 5% mercaptoacetic acid solution.

CONCLUSIONS

Water-soluble CdS nanoparticles were prepared by the controlled decomposition of the single precursor, cadmium isethionic xanthate at low temperature. The unique properties of the sulfonated xanthate ligand not only allow a high degree of water solubility, but the precursor byproducts act as nanocrystal stabilizing agents. However, if additional stabilization is required, dilute mercaptoacetic acid works well. Stable quantum dot suspensions, which consist of a variety of shapes and sizes (2-8 nm) are easily achievable. The CdS growth conditions promote particle surfaces that are laden with defects. The large surface-to-volume ratio and defect density give rise to a material with favorable optical properties. With efficiencies estimated to be roughly 30%, and chromaticity coordinates of (0.32, 0.38), the cadmium sulfide quantum dots seem to be ideal for use in fluorescent bulbs or light emitting diodes.

Beyond the useful optical properties, the preparative approach used in this study provides additional benefits. In the past, white-emission from II-VI quantum dots has been achieved with selenides or tellurides. Moving up the periodic table to sulfur not only reduces cost and toxicity, but opens up easier synthetic pathways. The single precursor technique eliminates stoichiometry mismatches, and in this case the decomposition products are not wasted but rather aid in particle surface stabilization. Further fine-tuning of this experimental system could advance the status of solid-state cool-lighting and aid in the production of next-generation devices.

Not only can divalent metal sulfides be grown from the corresponding isethionic xanthate complexes, but monovalent metal sulfides such as Ag_2S can be formed as well. The versatility of the isethionic xanthate anion makes it a useful species worthy of further and more intense research.

REFERENCES

[1] Trindade, T.; O'Brien, P.; Pickett, N. L. *Chemistry of Materials* **2001**, *13*, 3843-3858.

[2] Murray, C. B.; Kagan, C. R.; Bawendi, M. G. *Annual Review of Materials Science* **2000**, *30*, 545-610.

[3] Alivisatos, A. P. *Journal of Physical Chemistry* **1996**, *100*, 13226-13239.

[4] Weller, H. *Angewandte Chemie* **1993**, *105*, 43-55 (See also Angew Chem, Int Ed Engl, 1993, 32(1), 41-53).

[5] Steigerwald, M. L.; Brus, L. E. *Accounts of Chemical Research* **1990**, *23*, 183-8.

[6] Henglein, A. *Chemical Reviews (Washington, DC, United States)* **1989**, *89*, 1861-73.

[7] Weller, H. *Advanced Materials (Weinheim, Germany)* **1993**, *5*, 88-95.

[8] Hagfeldt, A.; Graetzel, M. *Chemical Reviews (Washington, D. C.)* **1995**, *95*, 49-68.

[9] Fendler, J. H.; Meldrum, F. C. *Advanced Materials (Weinheim, Germany)* **1995**, *7*, 607-32.

[10] Stroscio, J. A.; Eigler, D. M. *Science (Washington, DC, United States)* **1991**, *254*, 1319-26.

[11] Lieber, C. M.; Liu, J.; Sheehan, P. E. *Angewandte Chemie, International Edition in English* **1996**, *35*, 687-704.

[12] Bruning, J. H. *Proceedings of SPIE-The International Society for Optical Engineering* **2007**, *6520*, 652004/1-652004/13.

[13] Guo, L. J. *Advanced Materials (Weinheim, Germany)* **2007**, *19*, 495-513.

[14] Robel, I.; Subramanian, V.; Kuno, M.; Kamat Prashant, V. *J Am Chem Soc FIELD Full Journal Title:Journal of the American Chemical Society* **2006**, *128*, 2385-93.

[15] Sun, B.; Greenham Neil, C. *Phys Chem Chem Phys FIELD Full Journal Title:Physical chemistry chemical physics: PCCP* **2006**, *8*, 3557-60.

[16] Rappaport, P.; Wysocki, J. J. *Acta Electronica* **1961**, *5*, 364-78.

[17] Kandilarov, B.; Andreytchin, R. *Physica Status Solidi* **1965**, *8*, 897-901.

[18] Bowers, M. J., II; McBride, J. R.; Rosenthal, S. J. *Journal of the American Chemical Society* **2005**, *127*, 15378-15379.

[19] Wankhede, M. E.; Haram, S. K. *Chemistry of Materials* **2003**, *15*, 1296-1301.

[20] Jiang, H.; Ju, H. *Analytical Chemistry (Washington, DC, United States)* **2007**, *79*, 6690-6696.

[21] Hansen, J. A.; Sumbayev, V. V.; Gothelf, K. V. *Nano Letters* **2007**, *7*, 2831-2834.

[22] Kim, S.; Bawendi, M. G. *Journal of the American Chemical Society* **2003**, *125*, 14652-14653.

[23] Trindade, T.; O'Brian, P. *Advanced Materials (Weinheim, Germany)* **1996**, *8*, 161-3.

[24] Malik, M. A.; Zulu, M. M.; O'Brien, P.; Wakefield, G. *Journal of Materials Chemistry* **1998**, *8*, 1885-1888.

[25] Ludolph, B.; Malik, M. A. *Chemical Communications (Cambridge)* **1998**, 1849-1850.

[26] Lorenz, J. K.; Ellis, A. B. *Journal of the American Chemical Society* **1998**, *120*, 10970-10975.

[27] Revaprasadu, N.; Azad Malik, M.; O'Brien, P.; Wakefield, G. *Chemical Communications (Cambridge)* **1999**, 1573-1574.

[28] Sharma, H.; Sharma, S. N.; Singh, G.; Shivaprasad, S. M. *Colloid and Polymer Science* **2007**, *285*, 1213-1227.

[29] Murray, C. B.; Norris, D. J.; Bawendi, M. G. *Journal of the American Chemical Society* **1993**, *115*, 8706-15.

[30] Lee, J.; Sundar, V. C.; Heine, J. R.; Bawendi, M. G.; Jensen, K. F. *Advanced Materials (Weinheim, Germany)* **2000**, *12*, 1102-1105.

[31] Chan, W. C. W.; Maxwell, D. J.; Gao, X.; Bailey, R. E.; Han, M.; Nie, S. *Current Opinion in Biotechnology* **2002**, *13*, 40-46.

[32] Dubertret, B.; Skourides, P.; Norris, D. J.; Noireaux, V.; Brivanlou, A. H.; Libchaber, A. *Science (Washington, DC, United States)* **2002**, *298*, 1759-1762.

[33] Bruchez, M., Jr.; Moronne, M.; Gin, P.; Weiss, S.; Alivisatos, A. P. *Science (Washington, D. C.)* **1998**, *281*, 2013-2016.

[34] Mitchell, G. P.; Mirkin, C. A.; Letsinger, R. L. *Journal of the American Chemical Society* **1999**, *121*, 8122-8123.

[35] Mattoussi, H.; Mauro, J. M.; Goldman, E. R.; Anderson, G. P.; Sundar, V. C.; Mikulec, F. V.; Bawendi, M. G. *Journal of the American Chemical Society* **2000**, *122*, 12142-12150.

[36] http://hyperphysics.phy-astr.gsu.edu/hbase/vision/cie.html.

[37] The International Centre for Diffraction Data, Newton Square, PA: (The International Centre for Diffraction Data, Newton Square, PA); Vol. File Nos. 05-0566 & 36-1451.

[38] Topas 1.0.1 ed.; Bruker AXS, GmbH: 1998.

[39] Warren, B. E.; Averbach, B. L. *Journal of Applied Physics* **1950**, *21*, 595-8.

[40] Warren, B. E. *Prog. Metal Phys. (Bruce Chalmers and R. King, editors. Pergamon Press)* **1959**, *8*, 147-202.

[41] Barreca, D.; Gasparotto, A.; Maragno, C.; Seraglia, R.; Tondello, E.; Venzo, A.; Krishnan, V.; Bertagnolli, H. *Applied Organometallic Chemistry* **2005**, *19*, 59-67.

[42] Little, L. H.; Poling, G. W.; Leja, J. *Canadian Journal of Chemistry* **1961**, *39*, 745-54.

[43] Shankaranarayana, M. L.; Patel, C. C. *Spectrochimica Acta* **1965**, *21*, 95-103.

[44] Shankaranarayana, M. L.; Patel, C. C. *Canadian Journal of Chemistry* **1961**, *39*, 1633-7.

[45] Watt, G. W.; McCormick, B. J. *Spectrochimica Acta* **1965**, *21*, 753-61.

[46] Pradhan, N.; Katz, B.; Efrima, S. *Journal of Physical Chemistry B* **2003**, *107*, 13843-13854.

[47] Chen, X.; Samia Anna, C. S.; Lou, Y.; Burda, C. *J Am Chem Soc FIELD Full Journal Title:Journal of the American Chemical Society* **2005**, *127*, 4372-5.

[48] Hill, N. A.; Whaley, K. B. *Journal of Chemical Physics* **1994**, *100*, 2831-7.

[49] Kubin, R. F.; Fletcher, A. N. *Journal of Luminescence* **1983**, *27*, 455-62.

CHAPTER 8

METALLIC NICKEL SULFIDE AND NICKEL SULFIDE-BASED ELECTRICALLY CONDUCTIVE POLYMER NANOCOMPOSITES

The use of plastics in housings for electronic devices is often desired, but non-electrically conductive plastics are relatively transparent to electromagnetic radiation. To avoid this problem of electromagnetic interference (EMI), the plastic must be made conductive. Conductive plastics are also important in packaging for electronic devices that are susceptible to damage from electrostatic discharge. One of the most common methods used to render a plastic conductive is to incorporate electrically conductive fillers such as carbon black into the bulk of the polymer. We have developed an alternative based on metallically conducting nickel sulfide nanoparticles. NiS-polystyrene thin films with tunable specific resistivities were achieved by co-dissolving varying amounts of polystyrene and nickel ethylxanthate in toluene. The toluene mixture was added dropwise onto an aluminum surface where the toluene was allowed to evaporate leaving behind nickel ethylxanthate embedded in polystyrene. Upon heating the xanthate-polystyrene film at 150 °C, nickel ethylxanthate decomposes to leave behind nanometric NiS particles contained in the plastic.

INTRODUCTION

Nickel(I) and nickel(III) chemistries are well known – there are even rare reports of Ni^{-} and Ni^{4+} compounds – and complexes with 1+ and 3+ oxidation states such as $K_4[Ni_2(CN)_6]$ and $[Ni(PEt_3)_2Br_3]$ were reported as early as 1913 and 1936 respectively,[1] but nickel(II) and nickel-solid have dominated both industry and the scientific literature. Nickel ranks only 24th in natural abundance and makes up less than 0.01% of the Earth's mass. Nickel is generally found in nature as sulfide (over 55%) or laterite ores, and the largest consumer of nickel is the stainless steel industry, which is responsible for over 60% of all sales.[2] With nearly all natural nickel coming from ores, mineral flotation is an important aspect of Ni recovery.[3,4] While there have been many collection or flotation species used in the mineral processing industry, xanthate-based materials are some of the most common.[5-7] Many alkylxanthates have high affinities for metal ions, whether solvated or as part of a sulfide ore.[8] The most commonly used xanthate in flotation is the ethylxanthate ion (from potassium ethylxanthate), and while the mining/mineral industry is the biggest user of potassium ethylxanthate, other functions for ethylxanthate and xanthate-based compounds are being discovered. In this chapter, one of these alternate uses of the ethylxanthate anion, in the form of nickel(II) ethylxanthate, will be presented.

With 2+ oxidation states and d^8 electron configurations, Ni(II) complexes typically have square-planar or octahedral geometries. The octahedral complexes are paramagnetic (S = 1) whereas the square-planar complexes are diamagnetic (S = 0).[9-11] Nickel(II) ethylxanthate has a known crystal structure and is a d^8, low-spin, square-planar complex.[12-14] In the laboratory, nickel(II) ethylxanthate is prepared via a quantitative precipitation reaction using aqueous potassium ethylxanthate and any water-soluble Ni^{2+}

salt.[15] The complex has a reddish-brown color and is particularly hydrophobic. It was realized that heating nickel(II) ethylxanthate – as well as similar nickel compounds known as carbamates – would eventually decompose the complex and generate nickel sulfide.[16] Since that discovery, there have been numerous studies on the usefulness of nickel dithiocarbamates[17,18] and xanthates[19,20] as single precursors for NiS. There are more reports in the literature about employing dithiocarbamates as precursors largely because they are more stable than the corresponding xanthates. However, that increased stability can be thought of as a disadvantage since higher decomposition temperatures are required to convert the carbamate into a sulfide. Xanthates decompose at a much lower temperature and, therefore, require much less energy to produce. The reported decomposition temperature of nickel(II) ethylxanthate ranges from 150-180 °C,[16] while nickel(II) ethyldithiocarbamate requires a temperature of 290-390 °C to achieve the same end.[21,22]

Nickel sulfide, depending on the crystal structure, impending pressure, and temperature, can have a range of electrical properties. The transition from metallic to semiconducting NiS as a function of temperature is well-known.[23,24] The relatively high conductivity of nickel sulfide makes it a reasonable candidate for use as electrode material,[25] filler material in conductive polymer composites,[26] and in any other number of systems. Conductive polymers or polymer composites are necessary for a variety of reasons. Among the myriad uses of conductive polymers are electroluminescence,[27] electromagnetic shielding,[28] anti-static packaging,[29] information storage,[30] and sensing along with some biological applications.[31]

There are two main categories of electrically conductive plastics: (1) organic polymers[32-34]; and (2) composites made from a non-conductive polymer and a conductive filler material (carbon black, metal powders, etc.).[35-38] The first class relies on an extended system of delocalized bonds (a conjugated system) where charge carries are then introduced through oxidation or reduction. Conductive plastics of the second class are easier to make and the conductivities can be more easily tuned by simply changing the filler-component concentration. In this chapter, a conductive polymer composite system based on a highly conductive NiS filler and polystyrene plastic backbone will be presented. Homogeneity issues of the filler inside the plastic, which often accompany this type of system, will be considered and discussed in regards to the preparative approach, xanthate-to-sulfide thermal decomposition.

EXPERIMENTAL

Materials. Reagent grade quality nickel(II) sulfate hexahydrate ($NiSO_4 \bullet 6H_2O$, GFS), potassium ethylxanthate ($KS_2COCH_2CH_3$, Aldrich), toluene ($C_6H_6CH_3$, Pharmco), polystyrene (c.a. 100,000 amu, Avocado), dioctyl terephthalate ($C_{24}H_{38}O_4$, Aldrich), polyvinyl alcohol (72,000 amu, Fluka), and carbon disulfide (CS_2, Aldrich) were obtained commercially and used as received without further purification. All water used throughout the experiment was deionized with a resistivity of approximately 18.0 MΩcm.

Synthesis of nickel ethylxanthate and metallic nickel sulfide. Nickel(II) ethylxanthate was generated by reacting aqueous solutions of nickel(II) sulfate hexahydrate and potassium ethylxanthate in a stoichiometric fashion as described in the literature.[15]

Typically, $NiSO_4 \bullet 6H_2O$ (5.00 g, 19.0 mmol) was dissolved in water (150 mL) and $KS_2COCH_2CH_3$ (6.10 g, 38.0 mmol) was dissolved in a similar amount of water. The potassium ethylxanthate solution was slowly poured into the nickel sulfate solution immediately generating the brownish-red nickel ethylxanthate precipitate in nearly quantitative amounts (98.8 %). The solid was collected by vacuum filtration and washed thoroughly with water. The nickel ethylxanthate was stored in a sealed glass bottle away from light and remained stable for several months. Prominent infrared signals for nickel(II) ethylxanthate (cm^{-1}): 2994, 2979, 2946, 2891 (m); 2504 (w); 1467, 1451, 1437, 1390 (m); 1372 (s); 1255 (vs); 1144 (m); 1123 (s); 1057 (m); 1028, 1002 (s); 861 (m); 811 (w); 662, 546 (w); 436 (m).

To obtain nickel sulfide (1.00 g), an appropriate amount (3.32 g) of nickel ethylxanthate was baked, in air, at a temperature in the range of 120 °C to nearly 400 °C. Temperatures below 120 °C were not sufficiently high enough to decompose the ethylxanthate ligand in a timely fashion. For temperatures at or above 400 °C, the nickel sulfide would begin to oxidize.

Synthesis of polystyrene–nickel ethylxanthate composites and polystyrene–nickel sulfide nanocomposites. For the purpose of making thin composite films, various masses of nickel ethylxanthate were dissolved in toluene. Likewise, various masses of polystyrene were dissolved in toluene. The two toluene solutions were combined in such a way to give nickel ethylxanthate-to-polystyrene ratios of 1:3, 1:2, 1:1, and 2:1 by mass. The xanthate-polystyrene mixtures were poured into either glass or aluminum flat-bottomed dishes and placed on an orbital shaker. The composites were slowly shaken as

the toluene evaporated, which eventually resulted in a dried thin film (film thickness ranged from a few hundred microns to several millimeters). The nickel ethylxanthate-polystyrene composite films appear to be indefinitely stable at room temperature.

NiS–polystyrene nanocomposites were fabricated by heating the xanthate-polystyrene films at 150 °C. The NiS-polystyrene composites are sturdy and fairly brittle. To soften the films and make them increasingly flexible, a plasticizer can be incorporated. The addition of a plasticizer is most easily accomplished by adding it at the beginning of the synthetic process. Specific masses of dioctyl terephthalate (in the range of 10 – 100 % as compared to polystyrene) were co-dissolved with the polystyrene in the first step of the composite preparation. Refer to Scheme 8.1 for a pictorial representation of the composite construction. **Note**: all ratios referring to the NiS-polymer composites are mass ratios corresponding to the mass of $Ni(S_2COCH_2CH_3)_2$ relative to the mass of polystyrene.

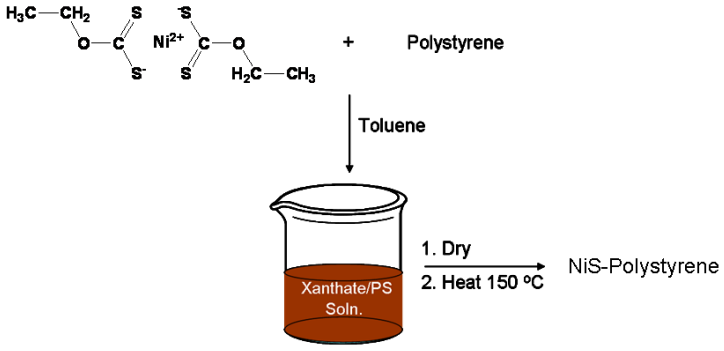

Scheme 8.1: Preparation of NiS-polystyrene nanocomposites from nickel ethylxanthate.

Preparation of polyvinyl–nickel ethylxanthate composites and polyvinyl–nickel sulfide nanocomposites. Normally, 8.61 g (200 mmole) of finely powdered polyvinyl alcohol was dispersed in 150 ml of deionized water. An aqueous solution of potassium

hydroxide, 11.22 g (200 mmole), was added to the polyvinyl alcohol suspension. To complete the conversion from alcohol to xanthate, 15.20 g (200 mmole) of carbon disulfide was slowly poured into the mixture. After a substantial reaction period (usually 24 to 48 hours) a completely water soluble orange polymer develops. Finally, 26.28 g (100 mmole) of nickel(II) sulfate hexahydrate is dissolved in water and added to the potassium polyvinyl xanthate solution. Immediately upon the addition of Ni^{2+}, a black solid falls out of solution. If the supernatant is decanted, the remaining wet nickel polyvinyl xanthate has the texture and spreadability of many common types of toothpaste.

The nickel(II) polyvinyl xanthate was evenly spread on a glass microscope slide or some other smooth surface before it completely dried. The thin polyvinyl xanthate film was then allowed to dry before being heated to 150 °C to convert the nickel xanthate into nickel sulfide. Scheme 8.2 contains a balanced reaction schematic for the preparation of nickel(II) polyvinyl xanthate.

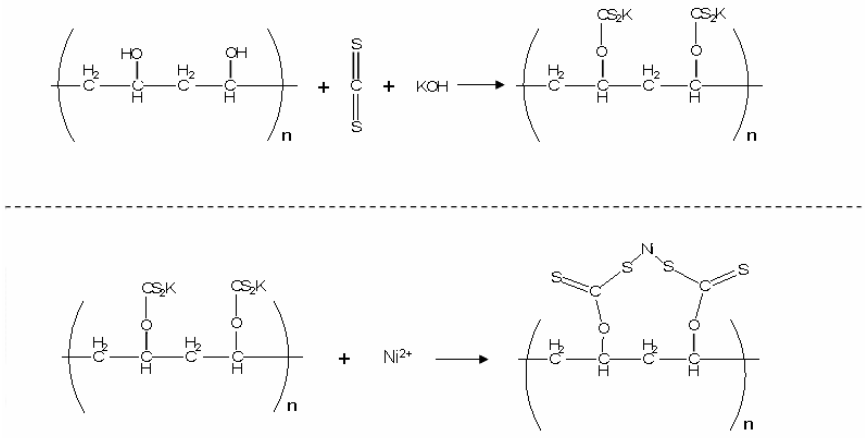

Scheme 8.2: Preparation of potassium polyvinyl xanthate (top) and nickel(II) polyvinyl xanthate (bottom).

Characterization. The UV adsorption spectrum of nickel ethylxanthate was measured with a Perkin-Elmer Lamda EZ201 spectrometer. The spectrum was measured at a rate of 200 nm/min in the range from 200 nm to 500 nm in a quartz cuvette. Methanol was used as the solvent.

For infrared spectroscopic measurements, approximately 10 mg of the desired sample was mixed with approximately 100 mg FTIR-grade potassium bromide and the blend was finely ground. Spectra in the 4000-400 cm^{-1} region were collected by diffuse reflectance of the ground powder with a Nicolet Magna-IR 750 spectrometer. Typically, 128 or more scans were recorded and averaged for each sample (4.0 cm^{-1} resolution) and the background was automatically subtracted.

Raman spectroscopy was also used to characterize the nickel ethylxanthate and nickel sulfide powders. A Nicolet NXR 9610 Raman Spectrometer was used for the analysis and a neat pressed pellet was used for each measurement. Typically, 32 scans were averaged in the 4500-50 cm^{-1} range at a resolution of 4.0 cm^{-1}.

Powder X-ray diffraction (XRD) measurements were obtained on a Bruker AXS D8 Advance diffractometer using Cu Kα radiation with an acceleration voltage of 40 kV and current flux of 30 mA. The diffractograms were recorded for a 2θ range of either 5-70° or 17-70° with a step size of 0.02° and a counting time of 18 seconds per step. All the XRD patterns where collected at ambient temperature, and the phases were identified using the ICDD database.[39] The peaks were profiled with a Pearson 7 model using Topas P version 1.01 software.[40] The profiles of the standard and the sample were put into the Win-Crysize program version 3.05, which uses the Warren-Averbach evaluation method to determine crystallite size.[41,42]

The specific surface areas were obtained with a conventional Brunauer-Emmett-Teller (BET) multilayer nitrogen adsorption method using a Quantachrome Nova 1200 instrument.

Thermogravimetric analysis (TGA) was performed on the nickel ethylxanthate complex at a rate of 2.0°/min from room temperature to 600 °C using a Seiko Instruments Exstar 6200. A well behaved decomposition curve was observed for the precursor with a defined onset temperature of roughly 120 ^{o}C.

Bulk and surface electrical resistivity measurements were carried out using a Fluke 189 True RMS Multimeter. For surface measurements, the imparted voltage came only from the digital multi-meter. Refer to Figure 8.1 for a representation how the surface

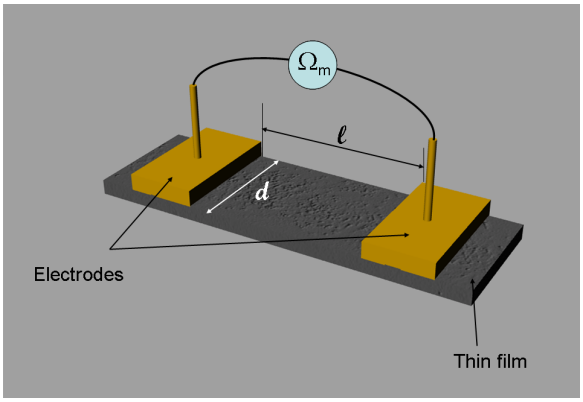

Figure 8.1: Thin film orientation with respect to the electrodes for surface resistivity measurements.

resistivity was measured. The equation necessary to determine the surface resistivity is

$$\rho_s = \frac{R_s d}{l}$$

where R_s is the measured resistance, and *d* and *l* are the distances shown in Figure 1. The units for surface resistivity are $\Omega square^{-1}$ or $\Omega\square^{-1}$. For bulk measurements, two different power supplies were used. An Agilent E3610A DC power supply was used for applied voltages up to 10.0 volts, while a Hewlett Packard 6116A DC power supply was used for applied voltages in the range of 10 to 100 volts. A simple circuit schematic along with a rendered image of the film/electrode orientation is depicted in Figure 8.2. The equation

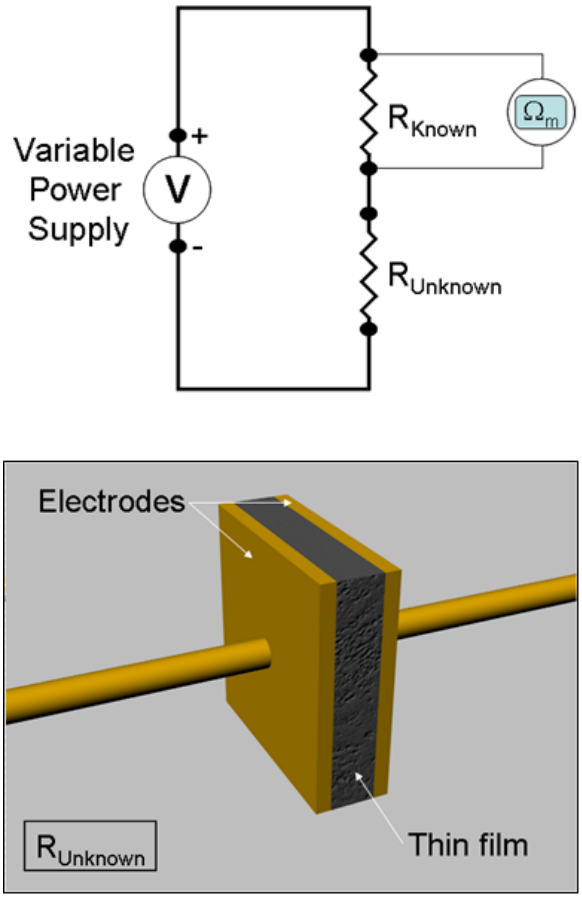

Figure 8.2: (Top) Circuit used to measure the resistivity of an unknown. (Bottom) Thin film orientation with respect to the two electrodes, which is different than the orientation for the surface measurement.

governing bulk resistivity is

$$\rho = \frac{RA}{l}$$

where R is the measured resistance, A is the contact area between the electrodes and the material, and l is the distance between the two electrodes. The resistance of each film was measured as a voltage drop across a known resistor and then back calculated using Ohm's Law.

RESULTS AND DISCUSSION

Low temperature formation of metallic NiS nanoparticles and mirror films from the single precursor, $Ni(S_2COCH_2CH_3)_2$. A simple process for preparing nanoscale NiS powder and mirror thin films was used. Whether the powder or thin film nickel sulfide was desired, the starting point was the same, nickel(II) ethylxanthate. The ethylxanthate precursor is easily prepared using a quantitative precipitation reaction under aqueous conditions. The ultraviolet absorption spectrum of nickel ethylxanthate in methanol is shown in Figure 8.3. The three signals at 217, 251, and 315 nm are most likely due to $d\rightarrow\pi^*/p$, $S\pi\rightarrow\pi^*$ ligand, and $S\sigma\rightarrow d\sigma^*$ transitions respectively while the two less prominent signals at 416 and 479 nm can be correspondingly attributed to $S_{lp}\rightarrow d\sigma^*$ and $Sn\rightarrow d\sigma^*$ absorptions.[43]

To further confirm the identity of the nickel ethylxanthate precursor, infrared and Raman spectroscopy were used along with X-ray powder diffraction. Figure 8.4 contains both the IR and Raman spectra for nickel ethylxanthate. Both spectra match well with

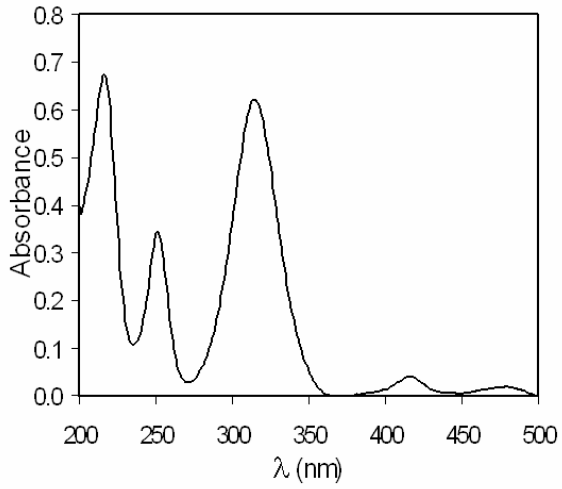

Figure 8.3: Electronic absorption spectrum of nickel ethylxanthate in methanol versus methanol.

previous reports and based on earlier Raman[44] and IR[45-47] studies of xanthate compounds, the peaks can be identified. Refer to Table 8.1 for a summary of the various signals and corresponding motions for the nickel ethylxanthate complex. X-ray powder diffraction demonstrated a crystalline, pure (no peaks from the starting materials were present) material.

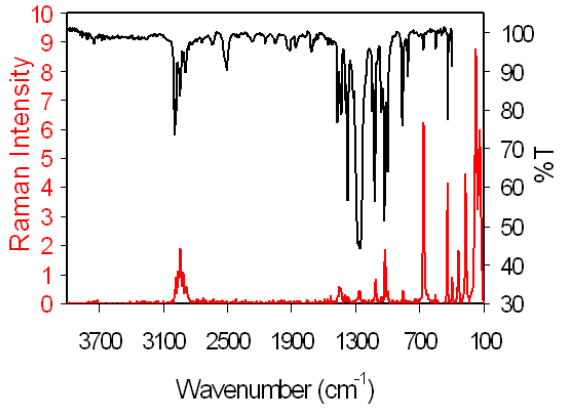

Figure 8.4: Raman (red) and infrared (black) spectra for nickel ethylxanthate.

Table 8.1: Selected Raman/IR signals and corresponding assignments for nickel ethylxanthate.

Infrared Frequency (cm^{-1})	**Raman Frequency (cm^{-1})**	**Assigned Motion**
	< 100	Lattice vibrations
	140	Ni-S vibrations
	156	Ni-S vibrations
	269	Ni-S stretching vibrations
	313	SCS in-phase bending
	362	SCS out-of-phase bending, Cd-S vibrations
474	449	COC in-phase bending
530-675	500-650	Various OCS_2 and CS motions
750-850	750-850	CS stretches
950	971	Cd-S
	1015-1040	CS_2 out-of-phase stretching, S-O stretch
1010-1120	1070-1085	S-O movements
	1164	CH_2, (S)CO stretching
1201	1227	COC out-of-phase stretching
1318-1435	1390-1460	CH wagging, CH_2 deformation
2888, 2937	2885-2990	CH_2 stretchings

Figure 8.5 contains the diffractogram of nickel ethylxanthate. There is no pattern in the International Center for Diffraction Data database of the ethylxanthate precursor

that can be used for matching purposes. However, the pattern compares well with that of other patterns in the literature.[13]

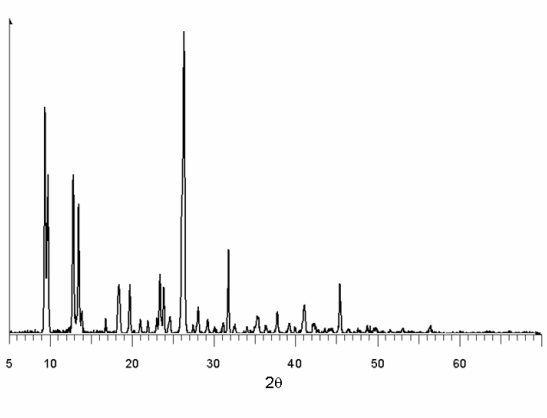

Figure 8.5: X-ray powder diffraction pattern for nickel(II) ethylxanthate.

To determine what temperature was necessary to convert the nickel ethylxanthate complex into nickel sulfide, thermal gravimetric anaylsis was performed. The trace for the ethylxanthate precursor can be seen in Figure 8.6. The onset elimination temperature

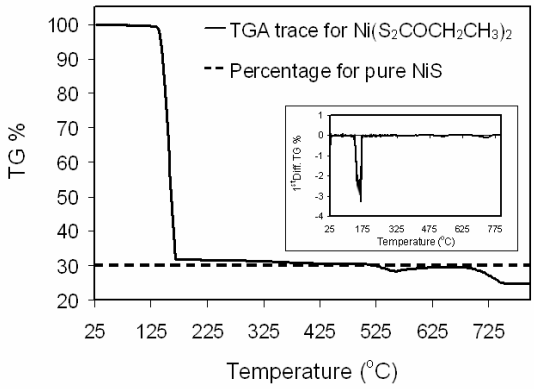

Figure 8.6: Thermal gravimetric analysis trace of nickel ethylxanthate, $Ni(S_2COCH_2CH_3)_2$. The inset is the first derivative of the TGA curve with respect to temperature.

for the nickel compound occurs at about 125 °C. The first derivative of the TGA curve suggests the decomposition occurs in a single step. The horizontal dashed line in the figure represents the percentage for pure NiS. The minor disagreement between the actual sample mass and theoretical mass can be explained by the presence of slight amounts of sulfate and carbonaceous species on the surface. X-ray photoelectron spectroscopy confirms the presence of sulfate and residual carbon compounds on the NiS surface. The sulfate arises from sulfide oxidation and the carbonaceous species are decomposition products that stick to the particle surface during the decomposition.

The elimination process in going from xanthate to sulfide is analogous to that of zinc ethylxanthate, which was mentioned in an earlier chapter. The ethyl group from one of the xanthate ligands transfers to the other, which leads to the formation of diethylxanthate, carbonyl sulfide, and the desired nickel sulfide. At the temperature required for decomposition, both carbonyl sulfide and diethylxanthate exit the system as gases leaving behind nickel sulfide as the sole solid product of an essentially irreversible process. The ceramic yield of the ethylxanthate $\rightarrow$ sulfide reaction at 150 °C for two hours is 28%. The theoretical yield for NiS formation is 30%. In this case, the actual yield is lower than the theoretical, which is in contrast to the TGA data where the actual yield at 150 °C is higher. The reason for this difference is an interesting phenomenon. When solid nickel ethylxanthate is brought to a temperature of greater than 125 °C and held there, a pseudo chemical vapor deposition process occurs. As the xanthate decomposes, the byproducts temporarily boil before they are converted to the gas phase and depart from the system. During this boiling period and shortly thereafter, a small amount of either yet-to-be-decomposed nickel ethylxanthate or newly-formed nickel

sulfide is spontaneously transported along the walls of the crucible into the atmosphere of the oven. After the heating period, there is a thin black film of NiS deposited along the walls of the crucible and even portions of the oven walls are covered in a thin black film. Similarly, if a glass slide is suspended above powdered nickel ethylxanthate and the precursor is heated to 150 °C, the glass slide is coated with a thin film of NiS. Thus, the low yield is due to loss of product to the surroundings because of this "vapor phase" deposition. The unique nature of the decomposition process allows for the preparation of very smooth, and in some cases, mirror thin films of NiS. The actual mechanism of the vapor phase transport is not completely understood. A possibility is that carbonyl sulfide and carbon disulfide act as volatilizers/carriers for the NiS. This would be analogous to the preparation of Ni nanoparticles from nickel tetracarbonyl. It has been demonstrated that nickel can be transported as $Ni(CO)_4$ in the vapor phase yielding nanoscale Ni particles.[48-50]

Consider two parallel experiments, both of which involve heating a similar mass of solid nickel ethylxanthate at 150 °C for two hours. In the first case, the xanthate is finely ground and placed in a ceramic crucible before heating. After the pyrolysis period, a black powder is all that remains in the crucible (barring the thin film along the walls mentioned in the previous paragraph). The X-ray powder diffraction pattern of the pyrolysis product is shown in Figure 8.7. The pattern matches a calculated NiS structure with an orthorhombic configuration. The average crystallite size of the NiS particles is 11.6 nm while the specific surface area is 2.2 m^2/g. In the second case, the precursor is finely ground and evenly spread between two glass microscope slides. After baking, at each glass interface, there is a mirror film of NiS. The NiS mirror adheres to

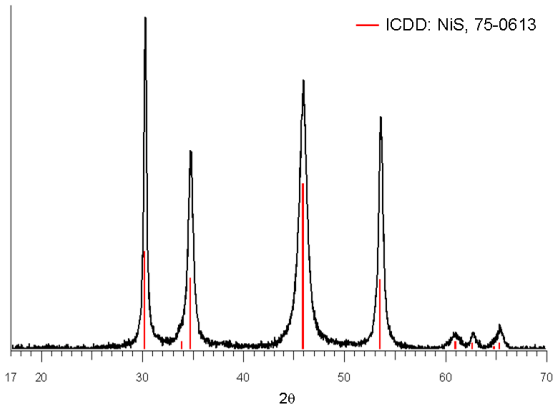

Figure 8.7: X-ray powder diffraction pattern of nickel ethylxanthate heated to 150 °C.

the glass surface unless it is mechanically scraped off. If the mirror film is scraped from the slide, ground into a powder, and measured by X-ray powder diffraction, the resulting XRD pattern is virtually indistinguishable from that shown in Figure 8.7. Figure 8.8 contains two scanning electron microscope images of the NiS formed in the two cases. The morphology difference between the nanocrystalline powder and the mirror film is obvious. The image of the mirror film is not entirely representative of the sample. The concentration of bumps and imperfections in the picture is higher than most places on the film. The features did, however, allow for a better focus. A picture of two mirror films is shown in Figure 8.9. The glass slides are still attached to the mirrors. The masking tape that held the slides together during the heating process was left on to provide some contrast.

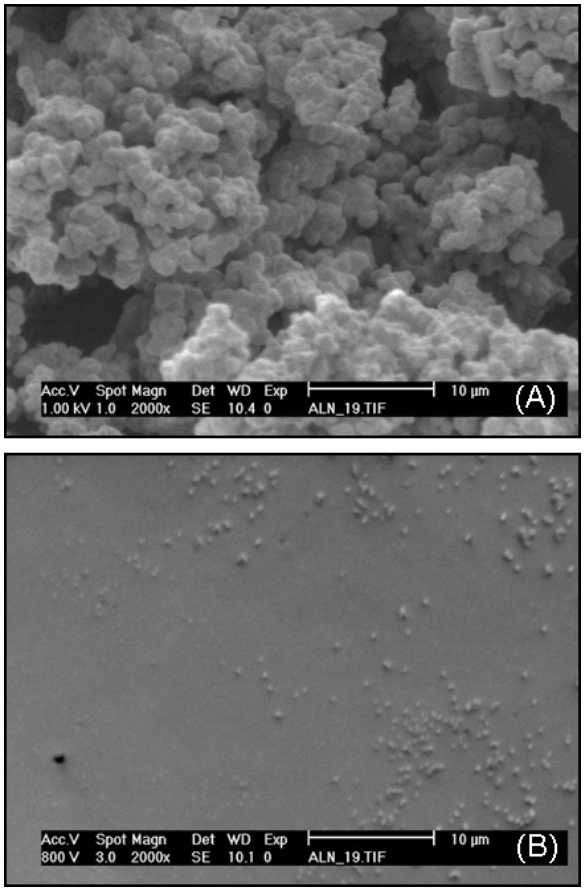

Figure 8.8: Scanning electron microscope images of (A) NiS poweder and (B) a NiS mirror thin film.

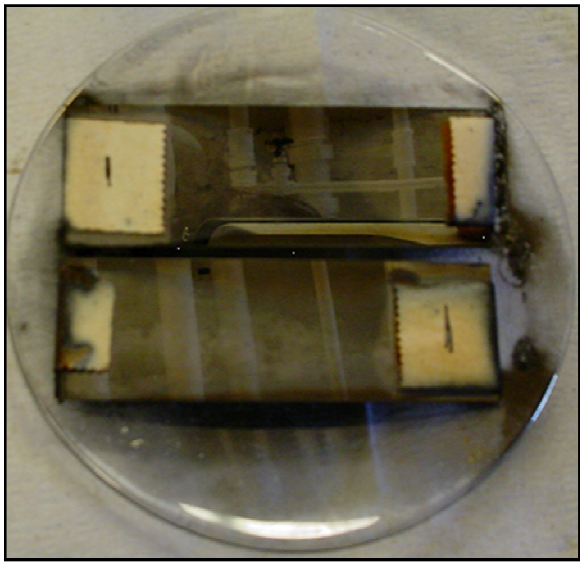

Figure 8.9: Picture of two NiS mirror films grown on glass substrates.

Temperature dependence of nickel sulfide formation. Several experiments were performed to explore what effects the decomposition temperature had on the nickel ethylxanthate→nickel sulfide route. Decomposition temperatures in the range of 125 °C to 1000 °C were employed. Up until about 400 °C, there is very little change in the decomposition process. However, at temperatures greater than 400 °C, new solid-state products begin to form. Table 8.2 lists the solid decomposition products for a variety of conversion temperatures. The identity of the products was determined by X-ray powder diffraction. The ICDD database numbers are included in the table. The oxidation pathway of going from NiS to NiO passes through two intermediate compounds, $Ni_{17}S_{18}$ and $NiSO_4$. Pure NiO is not formed until roughly 700 °C. The theoretical ceramic yield for NiO is 24.8%, which matches well with the yield measured for the 1000 °C elimination. In contrast to other metal sulfides (mentioned in Chapter 3), the surface area of NiS obtained from $Ni(S_2COCH_2CH_3)_2$ is relatively small. The reason for the lower surface area is most probably related to the distinctive vapor deposition phenomenon that accompanies the decomposition. A chart of surface area versus pyrolysis temperature is shown in Figure 8.10. The surface area remains essentially constant in the temperature range of 125 ° to 400 °C (the temperatures at which Ni_xS_y is formed) and is comparable to commercial, bulk nickel sulfide. A modest increase of surface area accompanies the formation of oxygen containing pyrolysis products.

Table 8.2: Effects of nickel ethylxanthate decomposition temperature on ceramic yield, crystallite size, and product identity.

Decomposition Temperature (°C)	**Ceramic Yield (%)**	**Crystallite Size (nm)**	**Identity (ICDD #)**
125	28.3	6.9	NiS (75-0613)
150	28.3	8.3	NiS (75-0613)
200	26.1	13.5	NiS (75-0613)
300	26.3	15.7	NiS (75-0613)
400	25.8	18.1	$Ni_{17}S_{18}$ (76-2306)
500	26.8	NA	$Ni_{17}S_{18}$ (76-2306) $NiSO_4$ (13-0435) NiO (47-1049)
600	24.1	NA	$NiSO_4$ (13-0435) NiO (47-1049)
700	21.0	20.2	NiO (47-1049)
1000	24.3	26.1	NiO (47-1049)

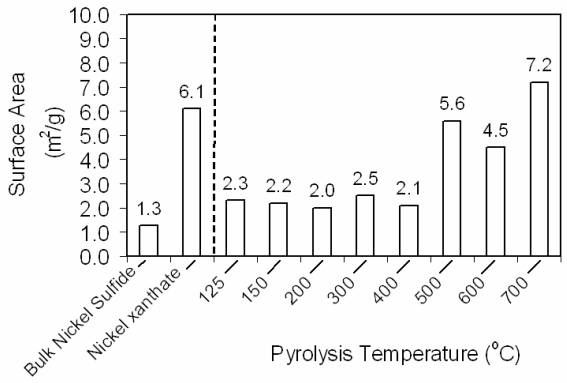

Figure 8.10: Specific surface areas of commercial (bulk) NiS, nickel ethylxanthate, and nickel ethylxanthate thermal decomposition products.

Electrically conductive polymer nanocomposites. It is known that NiS can be electrically conductive. In fact, it is frequently referred to as metallic due to its lustrous appearance and high conductivity. For the purposes of preventing electromagnetic interference and providing anti-static packing materials, plastics are often made electrically conductive through incorporation of metallic fillers into the polymers. By co-dissolving nickel ethylxanthate and polystyrene, NiS-loaded plastics are easily achieved. Scheme 8.1, shown earlier in this chapter depicts how the NiS-polystyrene thin films are made. Figure 8.11 contains pictures of a polymer-xanthate composite and a polymer-sulfide composite. Scanning electron microscope images of the film shown in Figure 8.11B can be seen in Figure 8.12. Both secondary and backscattered electrons were used to obtain the micrographs, so that different distances in the surface region could be probed.

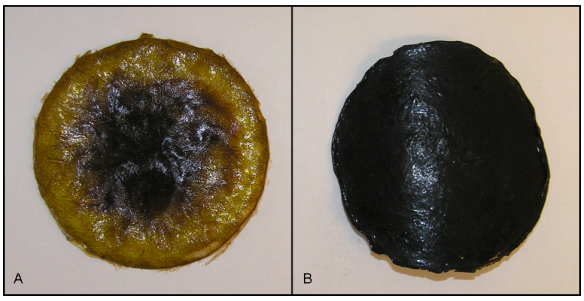

Figure 8.11: A saturated nickel(II) ethylxanthate-polystyrene composite, (A). The same composite after a two-hour baking period at 150 °C, (B). The conversion from xanthate to sulfide is visually evident.

The NiS-polymer film is relatively homogeneous, and with exception of a few cracks and vent holes, featureless. By systematically varying the concentration of xanthate-to-polystyrene, both bulk and surface resistivities can be tuned.

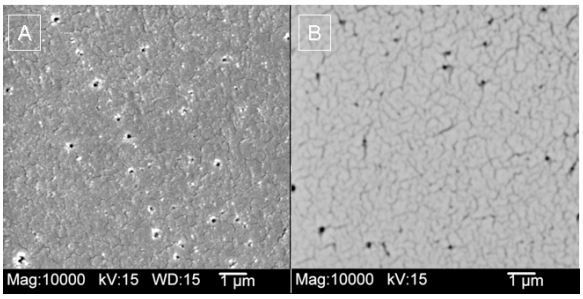

Figure 8.12: (A) Secondary SEM image of a typical NiS-polystyrene film. (B) Backscattered SEM image of the same NiS-polystyrene film.

Again, due to the unusual decomposition route for the elimination of nickel ethylxanthate to nickel sulfide, the NiS migrates towards the edges of the polymer composites, creating a larger concentration of charge carriers at the film surfaces. For NiS concentrations corresponding to an initial mass ratio of less than 2:1, nickel ethylxanthate:polystyrene, the conductivity occurs only in the surface regions. The surface resistivity trend can be seen in Figure 8.13. Expectedly, the more NiS present in

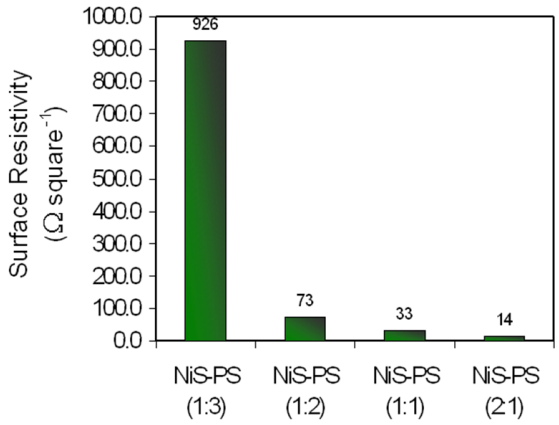

Figure 8.13: Surface resistivities for various NiS-polystyrene composites. The ratios refer to nickel ethylxanthate-to-polystyrene on a mass basis.

the plastic composite, the lower the resistivity. A neat NiS mirror film has a surface resistivity of about 5 Ωsquare^{-1}, so the polymer does very little to inhibit the conductivity at or near the film boundaries. The low-level concentration of NiS that would still produce a non-negligible surface current is not known. Presumably, a large tunable range of surface resistivity is possible. Figure 8.14 contains the X-ray powder diffraction scans of films with various NiS concentrations. In all cases, the pattern matches a known orthorhombic pattern for NiS (the same pattern as the neat NiS). The average crystallite sizes for sample A, B, C, and D are 7.8, 3.4, 18.8, and 10.5 nm respectively. It is apparent that metal sulfide concentration is not the primary driving force for determining the crystallite size. The lack of any obvious trend between NiS loading and crystallite size is puzzling. To test for anomalous behavior, the experiment was repeated and with each successive try there was less variability between the average crystallite sizes, but

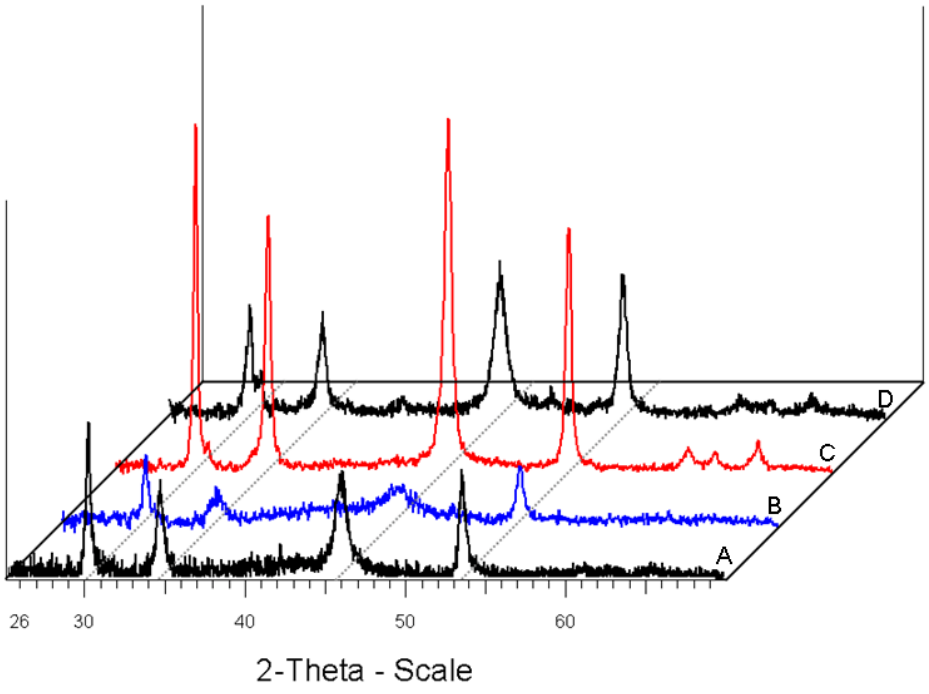

Figure 8.14: X-ray powder diffraction patterns for polymer composites with (A) 7.5% NiS, (B) 10.0% NiS, (C) 15.0% NiS, and (D) 20.0% NiS.

still no evident trend. Two possible explanations exist as to why there is this lack of consistency. The first is that the nickel ethylxanthate rarely crystallizes the same within the polymer as the solvent is evaporated. Sometimes there are larger crystals and sometimes smaller. Sometimes the crystals congregate together more strongly than others and sometimes the xanthate is spread relatively homogenously throughout the film. The second conceivable reason is that the presence of remnant toluene in the film during the heating process could effect the decomposition enough to affect crystallite size.

Bulk resistivity measurements on a 2:1 $Ni(S_2COCH_2CH_3)_2$-polystyrene film, which was pyrolyzed for two hours yielded the results seen in Table 8.3. The applied

Table 8.3: Applied voltage versus bulk resistivity for a 2:1 polymer nanocomposite.

Applied Voltage (V)	Bulk Resistivity (Ω cm)
10.0	25.2
20.0	25.2
30.0	26.2
40.0	26.0
50.0	26.5
60.0	26.7
90.0	28.9

voltage was varied to see if the composite behaved as a variable resistor. The trend between applied voltage and resistivity can be more readily compared using Figure 8.15. While there is a direct, increasing correlation between the applied voltage and resistivity, the relative change in conductivity is effectively negligible. A pressed pellet of finely ground NiS powder prepared from heating nickel ethylxanthate to 150 °C has a bulk resistivity of roughly 1.0 Ωcm. The bulk resistivity can be tuned between 25 Ωcm and 1.0 Ωcm by preparing polymer composites with $Ni(etxan)_2$ concentrations between 2:1 and the neat powder.

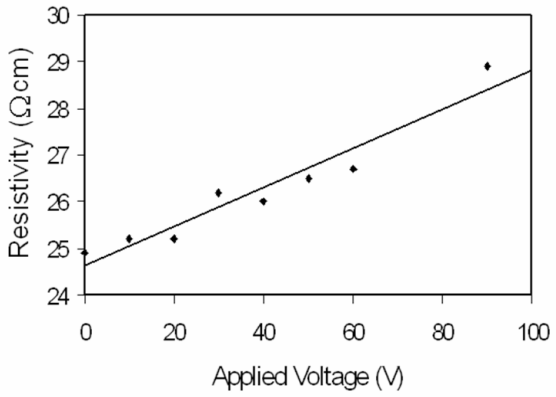

Figure 8.15: Bulk resistivity of a 2:1 NiS-polymer composite thin film versus applied voltage. Note: Zero applied voltage refers to the external power supply and not the applied voltage of the multimeter.

The NiS-polymer composites are relatively inflexible once thicknesses of a several hundred microns and greater are reached. To introduce flexibility, dioctyl terephthalate was added to the films. For instance, if a starting mass mixture of 1.00 g nickel ethylxanthate, 1.00 g polystyrene, and 0.10 g dioctyl terephthalate are co-dissolved in toluene, dried, and fired at 150 °C, the film has a much greater plasticity. However, the presence of the plasticizer inhibits the conductivity. The surface resistivity of a 1:1:0.1 film is 5.40×10^{3} Ω square^{-1}, which is two orders of magnitude greater than the analogous film with no plasticizer.

An alternative method for synthesizing NiS-polymer composites without the necessity of organic solvents was developed. As mentioned in the introductory chapters, transition metal ethylxanthate compounds are strongly hydrophobic and do not dissolve in water. Due to this intense water-insolubility, a simple co-dissolving of the nickel ethylxanthate and a water-soluble polymer is not possible. However, using the process described in the experimental section of this chapter, NiS-polyvinyl nanocomposites are readily attained. Having the xanthate functionality built into the polymer backbone slightly changes the decomposition, so that the vapor deposition process does not occur. Therefore, after heating the polymer-ethylxanthate hybrid, the resulting NiS nanocrystals are evenly distributed among the film and there is no apparent segregation at the surface.

While this method for preparing conductive polymer composites sidesteps the NiS segregation issue, and requires only water as a solvent, there is one major drawback. Tuning the conductivity is difficult since the Ni-S unit is part of the polymer and not just an additive. For full nickel loading (one nickel ion for every two xanthate functionalities and greater than 90% conversion of –OH into $–OCS_2^-$), the measured resistivity is 380

Ωcm. There are two major ways to reduce the concentration of Ni-S units in the polymer if a larger resistivity is desired. The first is to convert only some of the hydroxyl groups into xanthate groups. However, the water-solubility of polyvinyl xanthate is much greater than the solubility of polyvinyl alcohol, so it is nearly impossible to get a homogenous distribution of xanthate and hydroxyl groups. Despite the inhomogeneity issue, a resistivity as high as 900 MΩcm was achieved for a 1:1 mole ratio of xanthate to hydroxyl sample. The second approach that can be used to reduce the concentration of NiS is to substitute a portion of the nickel with another divalent metal such as zinc. In this way, you can completely convert the hydroxyls into xanthates (avoiding the solubility issue) and then incorporate whatever Ni^{2+}/Zn^{2+} ratio into the polymer that is needed. The conductivity limits and range for the Ni^{2+}/Zn^{2+} approach are not completely known as yet.

CONCLUSIONS

Electrically conductive mirror films and polymer nanocomposites were easily prepared from the single precursor, nickel(II) ethylxanthate. Neat NiS powders and thin films can have resistivities as low as 10^{-1} to 10^{1} Ωcm. The highly conductive mirror films are a direct result of the unusual vapor deposition process that is associated with the $Ni(S_2COCH_2CH_3)_2$ decomposition. Both the NiS-polystyrene and the NiS-polyvinyl nanocomposites were prepared, and the electrical properties can be tuned based on the concentration of Ni-S units present in the plastic. At lower NiS concentrations, the conductivity can be selectively located near film surfaces using the nickel(II) ethylxanthate and polystyrene preparative approach. However, using the polyvinyl

alcohol method, bulk resistivities are possible at the same nickel sulfide concentrations. With a resistivity range of 10^1 to 10^8 Ωcm, the polymer composites appear to be useful for many applications, such as electrodes, anti-static packing material, and electromagnetic interference-reducing media. The plasticity of the composites can be altered with the incorporation of a plasticizer such as dioctyl terephthalate. The facile nature of preparing these materials and the versatility afforded by them, make their use in technological systems or devices appealing.

REFERENCES

[1] Nag, K.; Chakravorty, A. *Coordination Chemistry Reviews* **1980**, *33*, 87-147.

[2] Moskalyk, R. R.; Alfantazi, A. M. *Mineral Processing and Extractive Metallurgy Review* **2002**, *23*, 141-180.

[3] Marabini, A. M.; Ciriachi, M.; Plescia, P.; Barbaro, M. *Minerals Engineering* **2007**, *20*, 1014-1025.

[4] Vanthuyne, M.; Maes, A. *Science of the Total Environment* **2002**, *290*, 69-80.

[5] Farr, I. *Minerals Engineering* **1992**, *5*, 1169-83.

[6] Wang, X. H.; Forssberg, K. S. E. *Minerals Engineering* **1996**, *9*, 527-546.

[7] Kirjavainen, V.; Schreithofer, N.; Heiskanen, K. *International Journal of Mineral Processing* **2002**, *65*, 59-72.

[8] Szymula, M.; Koziol, A. E.; Szczypa, J. *International Journal of Mineral Processing* **1996**, *46*, 123-135.

[9] Dag, O.; Yaman, S. O.; Onal, A. M.; Isci, H. *Journal of the Chemical Society, Dalton Transactions* **2001**, 2819-2824.

[10] Shriver, D. F.; Atkins, P. W.; Langford, C. H. *Inorganic Chemistry, Pt. 1. 2nd Ed*, 1996.

[11] Shriver, D. F.; Atkins, P. W.; Langford, C. H. *Inorganic Chemistry, Pt. 2. 2nd Ed*, 1996.

[12] Franzini, M. *Min. Crist. C.N.R. Ist. Min. (Univ. Pisa, Italy). Z. Krist.* **1963**, *118*, 393-403.

[13] Shugam, E. A.; Agre, V. M. *Trudy IREA* **1967**, *No. 30*, 364-8.

[14] Coucouvanis, D.; Fackler, J. P., Jr. *Inorganic Chemistry* **1967**, *6*, 2047-53.

[15] Rao, S. R. *Xanthates and Related Compounds*, 1971.

[16] Natu, G. N.; Kulkarni, S. B.; Dhar, P. S. *Thermochimica Acta* **1982**, *54*, 297-307.

[17] Lazell, M.; Norager, S. J.; O'Brien, P.; Revaprasadu, N. *Materials Science & Engineering, C: Biomimetic and Supramolecular Systems* **2001**, *C16*, 129-133.

[18] Brinkhoff, H. C. *Recueil des Travaux Chimiques des Pays-Bas* **1971**, *90*, 377-80.

[19] Pradhan, N.; Katz, B.; Efrima, S. *Journal of Physical Chemistry B* **2003**, *107*, 13843-13854.

[20] Cheon, J.; Talaga, D. S.; Zink, J. I. *Chemistry of Materials* **1997**, *9*, 1208-1212.

[21] Madhusudanan, P. M.; Yusuff, K. K. M.; Nair, C. G. R. *Journal of Thermal Analysis* **1975**, *8*, 31-43.

[22] Hill, J. O.; Murray, J. P.; Patil, K. C. *Reviews in Inorganic Chemistry* **1994**, *14*, 363-87.

[23] Townsend, M. G.; Tremblay, R.; Horwood, J. L.; Ripley, L. J. *Journal of Physics C: Solid State Physics* **1971**, *4*, 598-606.

[24] Brusetti, R.; Coey, J. M. D.; Czjzek, G.; Fink, J.; Gompf, F.; Schmidt, H. *Journal of Physics F: Metal Physics* **1980**, *10*, 33-51.

[25] Shimizu, Y.; Okimoto, M.; Souda, N. *International Journal of Applied Ceramic Technology* **2006**, *3*, 193-199.

[26] Yamamoto, T.; Taniguchi, A.; Dev, S.; Kubota, E.; Osakada, K.; Kubota, K. *Colloid and Polymer Science* **1991**, *269*, 969-71.

[27] Bernanose, A.; Vouaux, P. *Journal de Chimie Physique et de Physico-Chimie Biologique* **1953**, *50*, 261-3.

[28] Yu, D.; Cheng, J.; Yang, Z. *Journal of Materials Science & Technology (Shenyang, China)* **2007**, *23*, 529-534.

[29] Maki, N.; Nakano, S.; Sasaki, H. *Packaging Technology & Science* **2004**, *17*, 249-256.

[30] Wisseroth, K.; Scholl, R.; (BASF A.-G., Fed. Rep. Ger.). Application: DE DE, 1987, p 11 pp.

[31] Riul Junior, A.; Malmegrim, R. R.; Fonseca, F. J.; Mattoso, L. H. C. *Biosens Bioelectron FIELD Full Journal Title:Biosensors & bioelectronics* **2003**, *18*, 1365-9.

[32] Dalas, E. *Solid State Communications* **1991**, *77*, 63-4.

[33] Ruckenstein, E.; Park, J. S. *Polymer Composites* **1991**, *12*, 289-92.

[34] Vincent, B. *Polymers for Advanced Technologies* **1995**, *6*, 356-61.

[35] Alonso, M.; Satoh, M.; Miyanami, K.; Higashi, K.; Ito, T. *Powder Technology* **1991**, *67*, 11-13.

[36] Crossman, R. A. *Polymer Engineering and Science* **1985**, *25*, 507-13.

[37] Duggal, A. R.; Levinson, L. M. *Applied Physics Letters* **1997**, *71*, 1939-1941.

[38] Duggal, A. R.; Levinson, L. M. *Journal of Applied Physics* **1997**, *82*, 5532-5539.

[39] The International Centre for Diffraction Data, Newton Square, PA: (The International Centre for Diffraction Data, Newton Square, PA); Vol. File Nos. 05-0566 & 36-1451.

[40] Topas 1.0.1 ed.; Bruker AXS, GmbH: 1998.

[41] Warren, B. E. *Prog. Metal Phys. (Bruce Chalmers and R. King, editors. Pergamon Press)* **1959**, *8*, 147-202.

[42] Warren, B. E.; Averbach, B. L. *Journal of Applied Physics* **1950**, *21*, 595-8.

[43] Isci, H.; Dag, O.; Mason, W. R. *Inorganic Chemistry* **1993**, *32*, 3909-14.

[44] Barreca, D.; Gasparotto, A.; Maragno, C.; Seraglia, R.; Tondello, E.; Venzo, A.; Krishnan, V.; Bertagnolli, H. *Applied Organometallic Chemistry* **2005**, *19*, 59-67.

[45] Shankaranarayana, M. L.; Patel, C. C. *Canadian Journal of Chemistry* **1961**, *39*, 1633-7.

[46] Shankaranarayana, M. L.; Patel, C. C. *Spectrochimica Acta* **1965**, *21*, 95-103.

[47] Watt, G. W.; McCormick, B. J. *Spectrochimica Acta* **1965**, *21*, 753-61.

[48] Sahoo, Y.; He, Y.; Swihart, M. T.; Wang, S.; Luo, H.; Furlani, E. P.; Prasad, P. N. *Journal of Applied Physics* **2005**, *98*, 054308/1-054308/6.

[49] Erber, D.; Cammann, K. *Analyst (Cambridge, United Kingdom)* **1995**, *120*, 2699-705.

[50] Fau-Canillac, F.; Maury, F. *Surface and Coatings Technology* **1994**, *64*, 21-7.

CHAPTER 9

UNIQUE XANTHATE-BASED PRECURSORS FOR PHOTOVOLTAIC MATERIALS: COPPER INDIUM DISULFIDE AND COPPER GALLIUM DISULFIDE

The ternary metal sulfides $CuInS_2$, $CuGaS_2$, and $CuIn_xGa_{1-x}S_2$ were grown from mixed-metal xanthate precursors at low temperature. By tailoring the alkyl substituent on the xanthate precursor, multiple synthetic routes are available to prepare $CuInS_2$. The solid-state route will work with essentially any substituent. Introducing an –OH group provided water solubility, which resulted in the formation of water-soluble $CuInS_2$ nanoparticles. Lengthening the carbon chain and introducing ether linkages into the precursor enhanced solubility in acetone and methylene chloride. Precursor solutions in methylene chloride were shown to be ideal for chemical vapor deposition preparative techniques. $CuInS_2$-polystyrene composites with low sulfide loading were tested for photovoltaic activity. Different light sources did indeed influence film conductivity. It is presumed that higher loadings will display a more pronounced effect with respect to photovoltaic conversion. Early experiments reveal that other ternary systems such as mercury cadmium sulfide and nickel cadmium sulfide are also accessible from mixed-metal xanthate precursors.

INTRODUCTION

For solar cell technology to play a significant role in world-wide power generation, the unit cost per area of panel material must be competitive with other technologies in the market.[1] Along with the price, issues such as product stability, longevity, and the possibility of making large surface area units are some of the key factors in determining the likelihood of widespread use.[2] To this point, crystalline silicon is still the best option to meet the aforementioned requirements, and for that reason, dominates the photovoltaic market. There are difficulties in fabricating large surface area silicon panels, and current methods to maximize surface area are expensive.[1] Therefore, researchers and development teams are exploring alternate technologies for solar energy equipment.

Ternary chalcogenides of the general form $CuEX_2$ (E = Ga, In; X = S, Se) are some of the most studied and most promising absorber layer compounds.[3,4] Copper indium sulfide, $CuInS_2$, is a known semiconductor with the chalcopyrite structure[5] and has been reported to have photovoltaic efficiencies on the order of up to 13 %.[6-8] Not only is the efficiency of $CuInS_2$ respectable, but large area films have been produced via a roll-to-roll process on copper tape for less cost than a silicon panel of the same size.[1,9-11] Due to the ideal bandgap (1.3-1.5 eV) and high efficiency, numerous groups have prepared $CuInS_2$ using an assortment of synthetic techniques such as co-precipitation,[12] modulated flux deposition,[13] sequential sulfurization,[14] molecular beam epitaxy,[15] solvothermal preparation,[16] radio-frequency sputtering,[17,18] spray pyrolysis,[19] and chemical vapor deposition[20-23] among others.

The metal organic chemical vapor deposition technique offers advantages in terms of film homogeneity, composition, and structure if a suitable single-source precursor is available. Difficulties do arise in terms of stoichiometry if multiple precursors are necessary, which often occurs for ternary compounds. Finding a single precursor with Cu, In, and S in the correct proportion is rare.[24,25] One such precursor, $[(C_6H_5)_3P]_2Cu(SC_2H_5)_2In(SC_2H_5)_2$, has been proven to generate $CuInS_2$, but it is moisture and air sensitive and suffers from slow growth rates.[24,26] Success from dual carbamate ($^-S_2CNR_2$) precursors similar to material grown from single precursors has been demonstrated.[20,21,23] The downside of current single precursors and dual carbamate precursors is that substrate temperatures over 300 °C are needed for decomposition. Since carbamate ($^-S_2CNR_2$) and xanthate (^-S_2COR) functional groups differ only by a nitrogen/oxygen interchange, probing xanthates as low-temperature precursors for ternary sulfides seems a logical undertaking.

There are no reports on the preparation of $CuInS_2$ or $CuGaS_2$ from dual xanthate precursors, but copper(II) ethylxanthate,[27] gallium(III) ethylxanthate, and indium(III) ethylxanthate[28,29] have been prepared, and the formation of sulfides from ethylxanthates has been extensively established throughout this dissertation. In this chapter, the combination of cupric ethylxanthate and indium(III) ethylxanthate to form a physical single-source precursor for copper indium disulfide is presented. A brief discussion on the combination of $Cu(S_2COCH_2CH_3)_2$ and $Ga(S_2COCH_2CH_3)_3$ as a precursor for $CuGaS_2$ will also be provided.

EXPERIMENTAL

Materials. Reagent grade or higher purity cupric nitrate ($Cu(NO_3)_2 \bullet 2½H_20$, Fisher), indium(III) chloride ($InCl_3$, Acros), gallium(III) nitrate ($Ga(NO_3)_3$, GFS), potassium ethylxanthate ($KS_2COCH_2CH_3$, Aldrich), potassium hydroxide (KOH, Fisher), carbon disulfide (CS_2, Aldrich), tri(ethylene glycol) monomethyl ether ($C_7H_{16}O_4$, Aldrich), polystyrene (ca 100,000 amu, Avocado), toluene ($C_6H_6CH_3$, Pharmco) and dichloromethane (CH_2Cl_2, Aldrich) were obtained commercially and used as received without further purification. Deionized water with a resistivity of 18.1 MΩcm was used throughout the experiment.

Synthesis of copper indium and copper gallium ethylxanthate. Copper indium ethylxanthate - $CuIn(S_2COCH_2CH_3)_x$ - was generated by stoichiometrically reacting aqueous solutions of indium(III) chloride, copper(II) nitrate, and potassium ethylxanthate. Normally, $Cu(NO_3)_2 \bullet 2½H_2O$ (5.82 g, 25.0 mmol) and $InCl_3$ (5.53 g, 25.0 mmol) were dissolved in water (200 mL each) and temporarily set aside. Five molar equivalents of $KS_2COCH_2CH_3$ (20.0 g, 125.0 mmol) were put in solution (200 mL H_2O), and this xanthate solution was slowly added to the Cu^{2+}/In^{3+} mixture. Immediately, the reaction yielded a light orange precipitate (91.3 %). The solid copper indium ethylxanthate was filtered, washed, dried under vacuum, and stored in a sealed glass bottle away from light.

Copper gallium ethylxanthate was synthesized in a parallel manner by mixing aqueous solutions of copper(II) nitrate, gallium(III) nitrate, and potassium ethylxanthate stoichiometrically. A precipitate of copper gallium ethylxanthate formed in a nearly quantitative yield.

Synthesis of potassium O-2-(2-(2-methoxyethoxy)ethoxy)ethyl carbonodithioate.

Potassium *O*-2-(2-(2-methoxyethoxy)ethoxy)ethyl carbonodithioate (refered to as potassium trietherxanthate, see Figure 9.1) was generated by reacting an aqueous solution

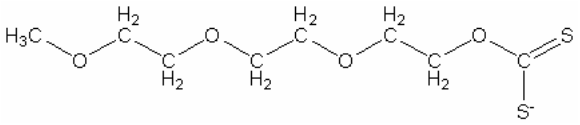

Figure 9.1: Structure of the *O*-2-(2-(2-methoxyethoxy)ethoxy)ethyl carbonodithioate or "trietherxanthate" anion.

of potassium hydroxide with carbon disulfide and tri(ethylene glycol) monomethyl ether in a stoichiometric fashion. Typically, KOH (10.00 g, 178 mmol) was dissolved in water (250 mL) and the solution was placed in an ice bath. Tri(ethylene glycol) monomethyl ether (29.26 g, 178 mmol) was added to the potassium hydroxide solution. Finally, CS_2 (13.55 g, 178 mmol) was added and the mixture was continuously stirred until all of the carbon disulfide had reacted (~ 48 hrs). The reaction yielded the water soluble potassium trietherxanthate in quantitative yields. Solid potassium trietherxanthate was obtained by allowing the water to evaporate which induced crystallization. The potassium trietherxanthate crystals were stored in a sealed glass bottle away from light and remained indefinitely stable.

Synthesis of copper indium O-2-(2-(2-methoxyethoxy)ethoxy)ethyl carbonodithioate.

Copper indium trietherxanthate was obtained by mixing aqueous solutions of cupric nitrate, indium chloride, and potassium trietherxanthate in a 1:1:5 mole ratio. Five equivalents of potassium trietherxanthate are necessary to balance the 2+ charge on the

copper and 3+ charge on the indium. The resulting mixture has a gel-like texture, and it is difficult to drive the excess water out of the gel to obtain the desired precursor. However, when dichloromethane is added to the gel, the CH_2Cl_2 readily extracts the copper indium trietherxanthate via a liquid-liquid extraction since copper indium trietherxanthate is soluble in dichloromethane. The solvent can be driven off to leave behind the solid precursor if required.

An analogous approach can be used to prepare copper gallium trietherxanthate. The gallium system behaves similar to that of the indium.

Synthesis of copper indium and copper gallium disulfide. Copper indium disulfide and copper gallium disulfide are easily prepared from either xanthate (ethyl or triether) precursor. In the solid state, all that is required to convert the xanthate to the sulfide is elevated temperature. For instance, heating a solid sample of copper indium ethylxanthate (2.00 g) to 150 °C triggers decomposition, which results in the production of copper indium sulfide (0.62 g). The same can be said for the gallium-based reaction; 150 °C is sufficient to convert the ethylxanthate precursor into $CuGaS_2$.

An alternate protocol can be used to make $CuInS_2$. Instead of mixing cupric and indium ions in solution, individual copper and indium ethylxanthate complexes can be prepared. If the two solid ethylxanthates are thoroughly mixed in the proper proportions via grinding, and then fired at 150 °C, $CuInS_2$ is exclusively formed.

$CuInS_2$ and $CuGaS_2$ were prepared from trietherxanthate precursors in both solid-state and solution-based reactions. The solid-state preparative approach is identical to that used for the ethylxanthate equivalents; pyrolyzing (150 °C) the precursor initiates

decomposition. Lower temperatures are required for solution-based conversion, since most solvents catalyze the disintegration process.[30,31]

Synthesis of polystyrene–copper indium ethylxanthate composites and polystyrene–copper indium disulfide nanocomposites. For the purpose of making thin composite films, various masses of copper indium ethylxanthate were dissolved in toluene. Likewise, various masses of polystyrene were dissolved in toluene. The two toluene solutions were combined in such a way to give copper indium ethylxanthate-to-polystyrene ratios of 1:5, 1:4, 1:3, and 1:2 by mass. The xanthate-polystyrene mixtures were poured into either glass or aluminum flat-bottomed dishes. The composites were periodically stirred as the toluene evaporated, which eventually resulted in a dried thin film (film thickness ranged from a few hundred microns to several millimeters). The copper indium ethylxanthate-polystyrene composite films appear to be indefinitely stable at room temperature.

$CuInS_2$–polystyrene nanocomposites were fabricated by heating the xanthate-polystyrene films at 150 °C. The dark brown/black $CuInS_2$-polystyrene composites are sturdy and fairly brittle.

Characterization. For infrared spectroscopic measurements, approximately 10 mg of the desired sample was mixed with approximately 100 mg FTIR-grade potassium bromide and the blend was finely ground. Spectra in the 4000-400 cm^{-1} region were collected by diffuse reflectance of the ground powder with a Nicolet Magna-IR 750

spectrometer. Typically, 128 or more scans were recorded and averaged for each sample (4.0 cm^{-1} resolution) and the background was automatically subtracted.

Powder X-ray diffraction (XRD) measurements were obtained on a Bruker AXS D8 Advance diffractometer using Cu Kα radiation with an acceleration voltage of 40 kV and current flux of 30 mA. The diffractograms were recorded for a 2θ range of either 5-70° or 17-70° with a step size of 0.02° and a counting time of 18 seconds per step. All the XRD patterns where collected at ambient temperature, and the phases were identified using the ICDD database.[32] The peaks were profiled with a Pearson 7 model using Topas P version 1.01 software.[33] The profiles of the standard and the sample were put into the Win-Crysize program version 3.05, which uses the Warren-Averbach evaluation method to determine crystallite size.[34,35]

The specific surface areas were obtained with a conventional Brunauer-Emmett-Teller (BET) multilayer nitrogen adsorption method using a Quantachrome Nova 1200 instrument.

Thermogravimetric analyses (TGA) were performed on the ethylxanthate complexes at a rate of 2.0°/min from room temperature to 800 °C using a Seiko Instruments Exstar 6200. A well behaved decomposition curve was observed for the precursor with a defined onset temperature of roughly 120 ^{o}C.

Dynamic light scattering (DLS) measurements were performed on water suspensions with a Malvern HPPS 3001 instrument. One and one-half mL of the suspension was placed in a disposable sample cuvette, and particle size measurements were obtained at 25.0 °C.

Electrical resistivity measurements were carried out using a Fluke 189 True RMS Multimeter. The equation governing bulk resistivity is

$$\rho = \frac{RA}{l}$$

where R is the measured resistance, A is the contact area between the electrodes and the material, and *l* is the distance between the two electrodes.

RESULTS AND DISCUSSION

Structure of copper indium ethylxanthate. Although it behaves as such, copper indium ethylxanthate is not technically a single-source precursor. X-ray diffraction and infrared spectroscopy confirm that $CuIn(S_2COCH_2CH_3)_5$ is, in actuality, a physical mixture of $Cu(S_2COCH_2CH_3)_2$ and $In(S_2COCH_2CH_3)_3$. This is the reason why it does not matter when you mix the cations. The benefit of mixing the metal ions prior to xanthate formation is that a more homogenous blend is produced. Figures 9.2 (X-ray powder patterns) and 9.3 (infrared spectra) provide evidence for the conclusion that copper indium ethylxanthate is not distinct from a physical mixture of the individual xanthates.

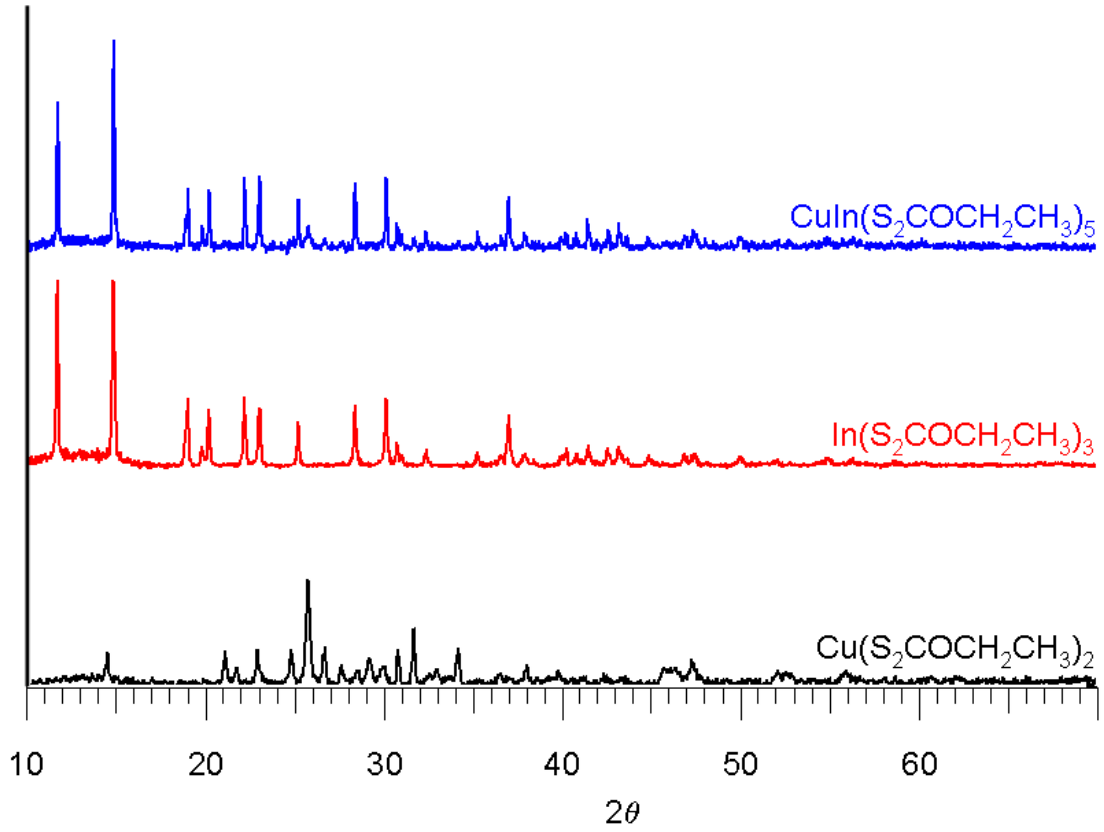

Figure 9.2: Powder X-ray diffraction patterns obtained for copper(II), indium(III), and copper indium ethylxanthate. The diffractograms are not normalized.

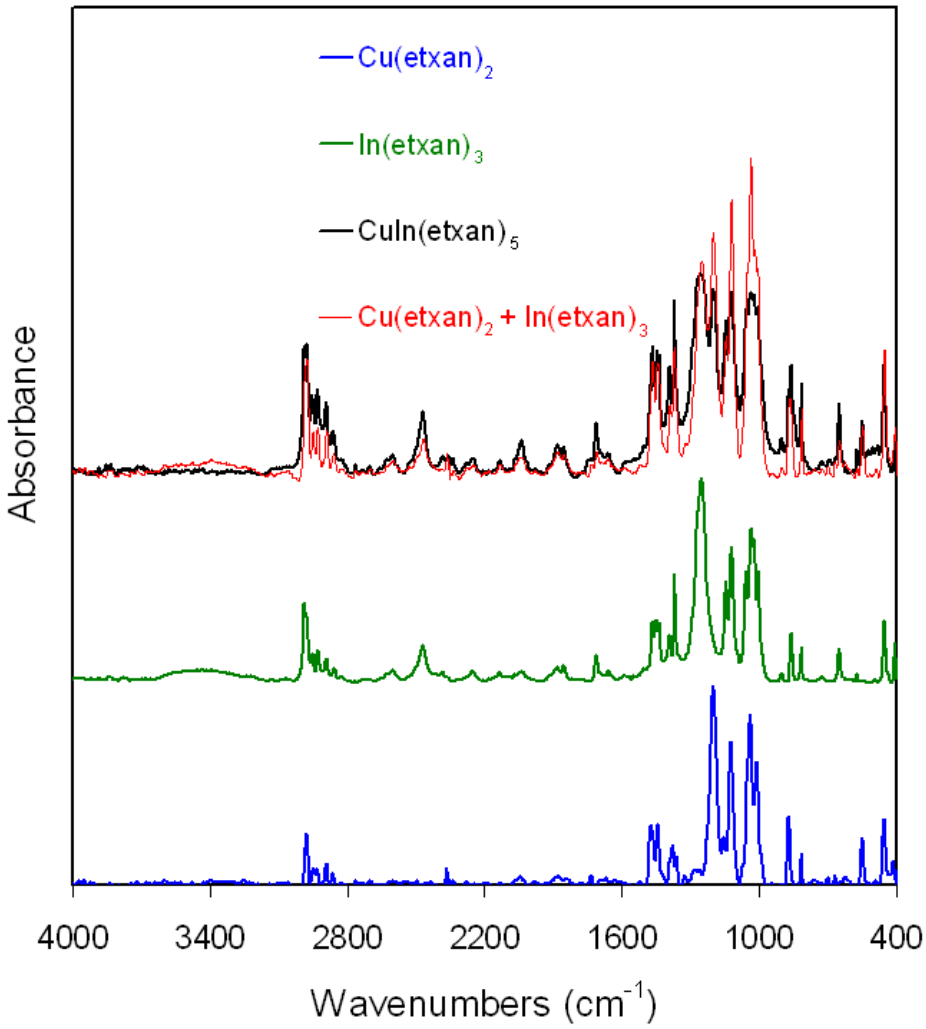

Figure 9.3: Infrared spectra for $Cu(S_2COCH_2CH_3)_2$, $In(S_2COCH_2CH_3)_3$, $CuIn(S_2COCH_2CH_3)_5$, and a spectral addition of $Cu(S_2COCH_2CH_3)_2$ and $In(S_2COCH_2CH_3)_3$.

Copper indium sulfide, copper gallium sulfide, and copper indium/gallium sulfide from ethylxanthate precursors. As previously discussed, heating the solid-state ethylxanthate precursor at 150 °C will generate the sulfide. For copper indium ethylxanthate, 150 °C is more than enough to cause conversion (refer to Figure 9.4). Thermogravimetric analysis results indicate that the decomposition occurs at 120 °C

(peak value of the first derivative). The breakdown process transpires quickly and in a single step. The ceramic yield of the thermal treatment process is 38.7 %, which

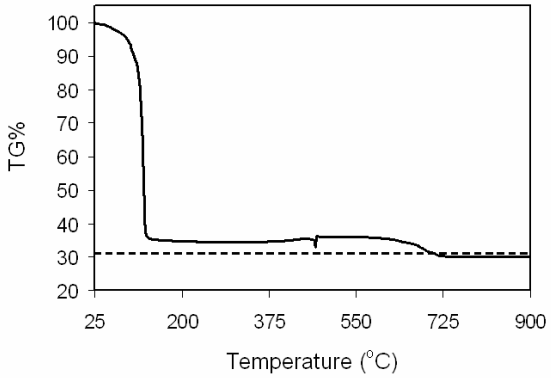

Figure 9.4: Thermogravimetric analysis trace for $CuIn(S_2COCH_2CH_3)_5$. The dashed line represents the theoretical yield for $CuInS_2$.

is slightly higher than the theoretical value of 30.9 %. The excess mass is attributed to xanthate decomposition products that stick to the sulfide surface along with oxidation products such as sulfate. The $CuInS_2$ that is formed by pyrolzing the ethylxanthate precursor has a specific surface area of 15 m^2/g and is nanocrystalline. The degree of crystallinity was estimated from the breadth of the X-ray diffraction peaks (Figure 9.5A). It was determined that the average crystallite size for $CuInS_2$ was 1.5 nm. An interesting discovery was that if Cu^{2+} and In^{3+} are mixed in solution before complexation, the resultant $CuInS_2$ crystallite size is smaller than if the ethylxanthates are mixed post-complexation. In fact, even with rigorous mixing of the individual xanthate powders, larger crystallites and non-uniform peak shapes arise (Figure 9.5B).

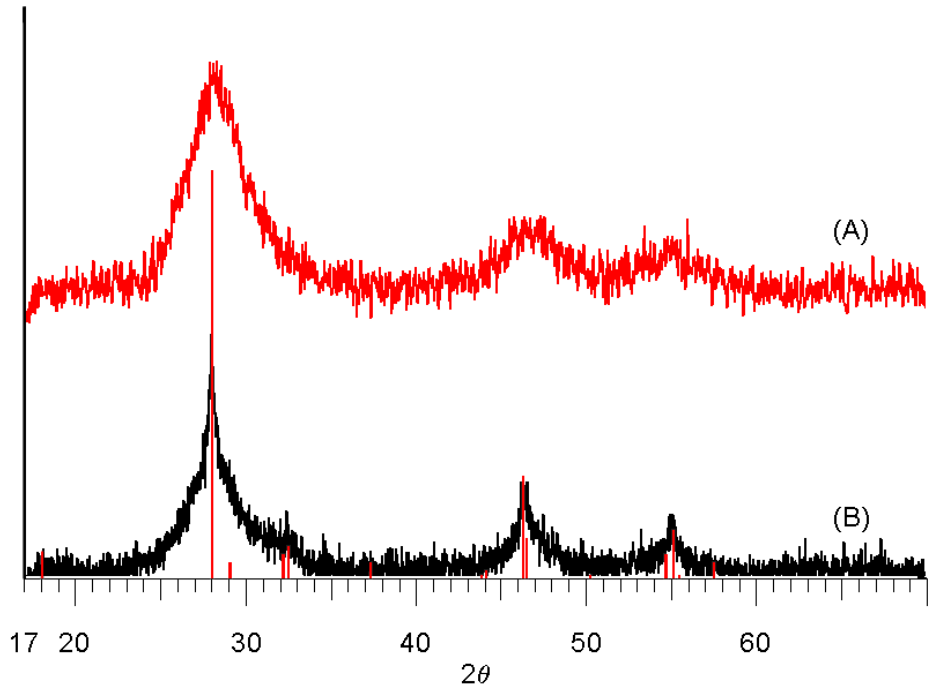

Figure 9.5: X-ray powder diffraction patterns for $CuInS_2$ prepared from (A) pre-complexed mixing and (B) post-complexed mixing of the metal ions. Vertical red lines represent database pattern, Roquesite, $CuInS_2$, ICDD 27-0159.

Copper(I) gallium sulfide, $CuGaS_2$, and copper(I) indium/gallium sulfide, $CuIn_xGa_{1-x}S_2$, are easily synthesized by thermal treatment as well. The powder diffraction pattern of an arbitrary $CuIn_xGa_{1-x}S_2$ sample can be seen in Figure 9.6. Both $CuInS_2$ and $CuGaS_2$ phases are clearly present.

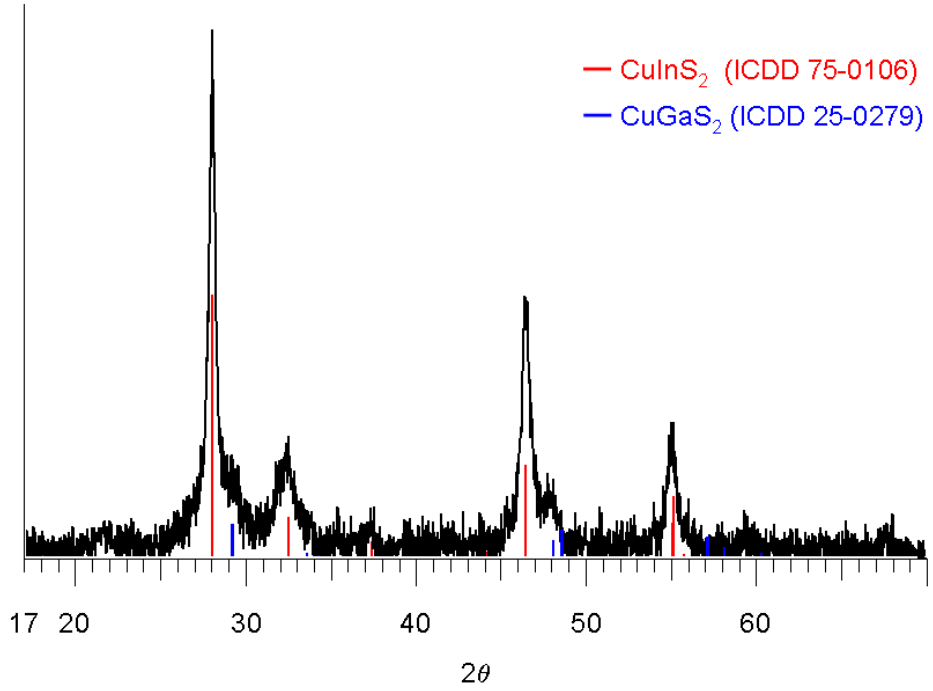

Figure 9.6: Powder X-ray diffraction pattern of $CuIn_xGa_{1-x}S_2$ from the ethylxanthate precursor. The value of x is roughly 0.8.

A question one might ask is related to the fact that copper changes oxidation states at some point in the preparation of these ternary sulfide compounds. Cupric ions are used to make the precursor, but within the sulfide, copper is only present in the cuprous form. This chemistry is known, and has been reported.[27,31,36] Copper(II) first reacts with ethylxanthate to form cupric ethylxanthate. Cupric ethylxanthate is not particularly stable and it decomposes to cuprous xanthate. The other half reaction in the redox process involves the formation of diethyl dixanthogen. A reaction scheme is provided (Scheme 9.1).

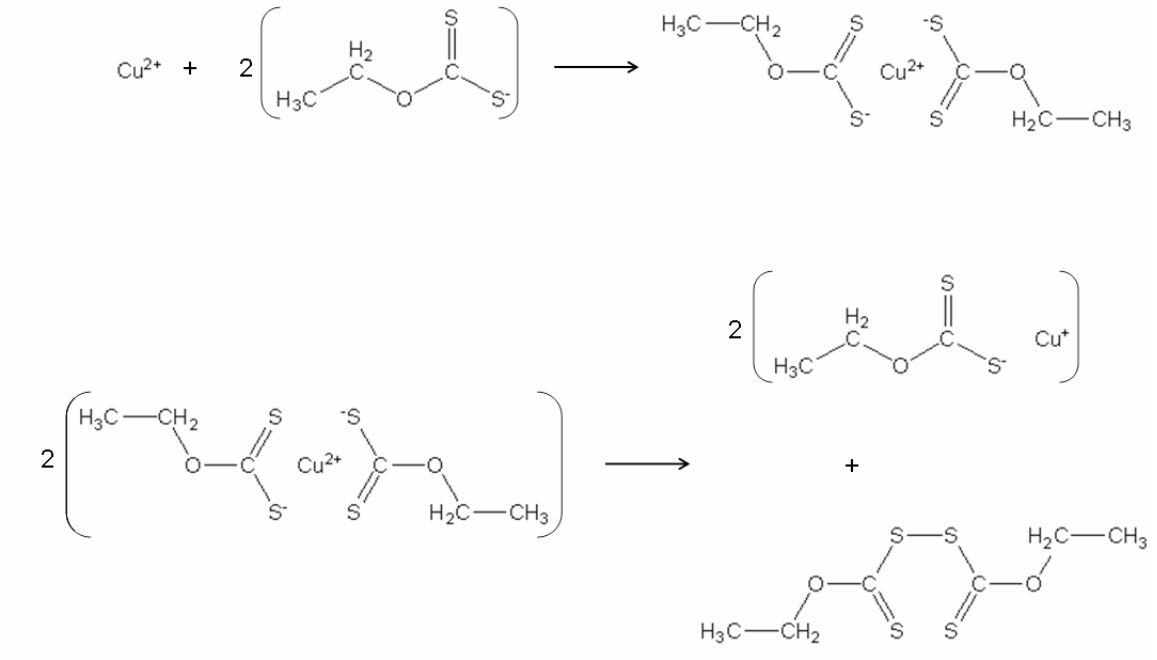

Scheme 9.1: Redox reaction describing the auto-decomposition of cupric ethylxanthate.

Water-soluble $CuInS_2$ nanoparticles. Copper indium 2-hydroxyethylxanthate can be prepared by reacting potassium 2-hydroxyethylxanthate with Cu^{2+} and In^{3+} stoichiometrically. The method to synthesize potassium 2-hydroxyethylxanthate is discussed in Chapter 2. The hydroxyl group provides significant water solubility, such that about a 2 % $CuIn(S_2COCH_2CH_2OH)_5$ solution can easily be prepared. Higher concentrations can be achieved with excess potassium 2-hydroxyethylxanthate present. To demonstrate the usefulness of the water-soluble precursor, a 2.5×10^{-3} M $CuIn(S_2COCH_2CH_2OH)_5$ solution was prepared and heated for thirty minutes in a 125 °C oven. The xanthate solution went into the oven as a deep red solution and came out of the oven as a brown suspension of $CuInS_2$ (determined by powder X-ray diffraction). Dynamic light scattering was used to approximate the $CuInS_2$ particle size after thermal treatment. Figure 9.7 shows the light scattering results. It is speculated that much

smaller particles could be formed if an external stabilizing agent such as a thiol or carboxylate was added. Even without a capping agent, it is reasonable to claim that $CuIn(S_2COCH_2CH_2OH)_5$ is a promising precursor for water-soluble nanoparticles of copper indium sulfide.

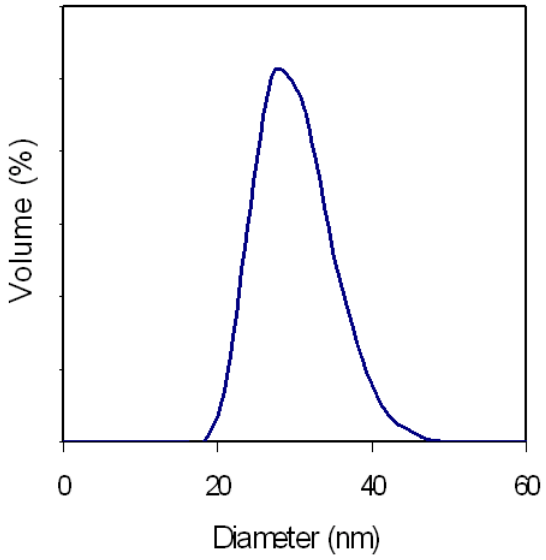

Figure 9.7: Dynamic light scattering plot of $CuInS_2$ diameter.

Photovoltaic character of polymer nanocomposites. It is known that $CuInS_2$, $CuGaS_2$, and $CuIn_xGa_{1-x}S_2$ are useful in photovoltaic devices. For the purpose of making thin films, nanocrystalline $CuInS_2$ was incorporated into polystyrene. By co-dissolving copper(II) indium ethylxanthate and polystyrene, $CuInS_2$-loaded plastics are easily obtained. The preparation is similar to that of the NiS-polymer composites discussed in the previous chapter. Heating a copper indium xanthate loaded polymer film to 150 °C will produce nanocrystalline copper indium sulfide encased in plastic. The $CuInS_2$-polystyrene films are relatively homogeneous, and with exception of a few vent holes, nearly featureless. A representative film (thickness = 1.5 mm, 6 % $CuInS_2$) was prepared

and the resistivity of the film was determined under different lighting conditions. The collected resistivity data are presented in Figure 9.8.

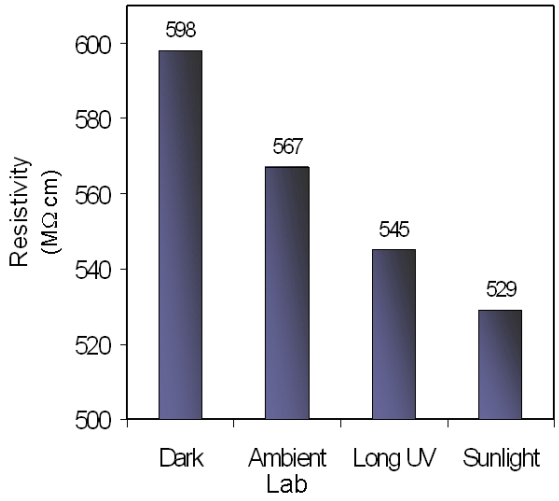

Figure 9.8: Resistivity data for a 6 % $CuInS_2$ polymer nanocomposite exposed to various lighting environments.

Metallo-organic chemical vapor deposition precursor. Copper indium or copper gallium trietherxanthate (*O*-2-(2-(2-methoxyethoxy)ethoxy)ethyl carbonodithioate) have been shown to be effective precursors for plasma assisted chemical vapor deposition. This work is ongoing and it is a collaboration with a research group from the University of Tulsa. We have synthesized stable suspensions (methylene chloride dispersant) of copper indium trietherxanthate and copper gallium trietherxanthate for them to use in their vapor deposition instrument. So far, $CuInS_2$ has been successfully generated. Copper gallium trietherxanthate has yet to be tested as a precursor in their system.

CONCLUSIONS

The previous chapters contain information regarding the formation of binary metal sulfide materials. However, using the same ligands, ternary sulfides are readily achievable. $CuInS_2$, $CuGaS_2$, and $CuIn_xGa_{1-x}S_2$ were successfully prepared and preliminary experiments indicate that other ternary systems such as mercury cadmium sulfide and nickel cadmium sulfide are obtainable from mixed-metal xanthate precursors. The mixed-metal xanthate precursors are, in fact, physical mixtures of the individual metal xanthate complexes. For this reason, while mixed-metal xanthate precursors behave as such, they are not single-source precursors in the most stringent sense.

$CuInS_2$-polymer composites with low sulfide loading demonstrate photovoltaic activity. It is presumed that higher loadings will display a more pronounced effect with respect to photovoltaic conversion. Efficiencies have been extensively reported for devices based on copper indium/gallium sulfide, but no attempt to determine an efficiency was made in this study.

Finally, by tailoring the alkyl substituent on the xanthate precursor, multiple synthetic routes are available to prepare $CuInS_2$. The solid-state route will work with essentially any substituent. Introducing an –OH group provided water solubility, and the result was the formation of water-soluble $CuInS_2$ nanoparticles. Introducing ether linkages into the precursor was thought to enhance water solubility, but the immediate formation of gels makes water solubility a non-issue. However, when these water-based gels are treated with methylene chloride, the copper indium trietherxanthate preferentially congregates in the organic layer. Precursor solutions in methylene chloride are ideal for chemical vapor deposition preparative techniques.

REFERENCES

[1] Winkler, M.; Griesche, J.; Konovalov, I.; Penndorf, J.; Wienke, J.; Tober, O. *Solar Energy* **2004**, *77*, 705-716.

[2] Hammond, M. *Journal of Power Sources* **2001**, *96*, 173.

[3] Robbins, M.; Bachmann, K. J.; Lambrecht, V. G.; Thiel, F. A.; Thomson, J., Jr.; Vadimsky, R. G.; Menezes, S.; Heller, A.; Miller, B. *Journal of the Electrochemical Society* **1978**, *125*, 831-2.

[4] Klenk, R.; Klaer, J.; Scheer, R.; Lux-Steiner, M. C.; Luck, I.; Meyer, N.; Ruehle, U. *Thin Solid Films* **2005**, *480-481*, 509-514.

[5] Loferski, J. J. *Materials Science & Engineering, B: Solid-State Materials for Advanced Technology* **1992**, *B13*, 271-7.

[6] Klaer, J.; Bruns, J.; Henninger, R.; Siemer, K.; Klenk, R.; Ellmer, K.; Braunig, D. *Semiconductor Science and Technology* **1998**, *13*, 1456-1458.

[7] Unold, T.; Sieber, I.; Ellmer, K. *Applied Physics Letters* **2006**, *88*, 213502/1-213502/3.

[8] Watanabe, T.; Matsui, M. *Japanese Journal of Applied Physics, Part 1: Regular Papers, Short Notes & Review Papers* **1999**, *38*, L1379-L1381.

[9] Das, K.; Datta, A.; Chaudhuri, S. *Crystal Growth & Design* **2007**, *7*, 1547-1552.

[10] Van Gheluwe, J.; Versluys, J.; Poelman, D.; Verschraegen, J.; Burgelman, M.; Clauws, P. *Thin Solid Films* **2006**, *511-512*, 304-308.

[11] Penndorf, J.; Winkler, M.; Tober, O.; Roser, D.; Jacobs, K. *Solar Energy Materials and Solar Cells* **1998**, *53*, 285-298.

[12] Rudnev, N. A.; Malofeeva, G. I. *Talanta* **1964**, *11*, 531-42.

[13] Guillen, C.; Herrero, J. *Thin Solid Films* **2007**, *515*, 5917-5920.

[14] Klaer, J.; Klenk, R.; Schock, H.-W. *Thin Solid Films* **2007**, *515*, 5929-5933.

[15] Kaigawa, R.; Ohyama, A.; Wada, T.; Klenk, R. *Thin Solid Films* **2007**, *515*, 6260-6264.

[16] Peng, S.; Liang, J.; Zhang, L.; Shi, Y.; Chen, J. *Journal of Crystal Growth* **2007**, *305*, 99-103.

[17] He, Y. B.; Kramer, T.; Polity, A.; Hardt, M.; Meyer, B. K. *Thin Solid Films* **2003**, *431-432*, 126-130.

[18] He, Y. B.; Kramer, T.; Polity, A.; Gregor, R.; Kriegseis, W.; Osterreicher, I.; Hasselkamp, D.; Meyer, B. K. *Thin Solid Films* **2003**, *431-432*, 231-236.

[19] Krunks, M.; Kijatkina, O.; Rebane, H.; Oja, I.; Mikli, V.; Mere, A. *Thin Solid Films* **2002**, *403-404*, 71-75.

[20] Lee, S. S.; Seo, K. W.; Park, J. P.; Kim, S. K.; Shim, I.-W. *Inorganic Chemistry* **2007**, *46*, 1013-1017.

[21] Park, J.-H.; Afzaal, M.; Kemmler, M.; O'Brien, P.; Otway, D. J.; Raftery, J.; Waters, J. *Journal of Materials Chemistry* **2003**, *13*, 1942-1949.

[22] Rodriguez, R. G.; Pulsipher, D. J. V.; Lau, L. D.; Shurdha, E.; Pak, J. J.; Jin, M. H.; Banger, K. K.; Hepp, A. F. *Plasma Chemistry and Plasma Processing* **2006**, *26*, 137-148.

[23] Waters, J. P.; Smyth-Boyle, D.; Govender, K.; Green, A.; Durrant, J.; O'Brien, P. *Chemical Vapor Deposition* **2005**, *11*, 254-260.

[24] Kelly, C. V.; Jin, M. H. C.; Banger, K. K.; McNatt, J. S.; Dickman, J. E.; Hepp, A. F. *Materials Science & Engineering, B: Solid-State Materials for Advanced Technology* **2005**, *B116*, 403-408.

[25] O'Brien, P.; Nomura, R. *Journal of Materials Chemistry* **1995**, *5*, 1761-73.

[26] McNatt, J. S.; Dickman, J. E.; Hepp, A. F.; Kelly, C. V.; Jin, M. H. C.; Banger, K. K. *Conference Record of the IEEE Photovoltaic Specialists Conference* **2005**, *31st*, 375-377.

[27] Lar'kova, V. M.; Akhmetshin, A. G. *Izvestiya Vysshikh Uchebnykh Zavedenii, Khimiya i Khimicheskaya Tekhnologiya* **1978**, *21*, 296.

[28] Galsbol, F.; Schaffer, C. E. *Inorganic Syntheses* **1967**, *10*, 42-9.

[29] Delepine, M. *Annali di Chimica Applicata* **1951**, *6*, 645-7.

[30] Pradhan, N.; Katz, B.; Efrima, S. *Journal of Physical Chemistry B* **2003**, *107*, 13843-13854.

[31] Rao, S. R. *Xanthates and Related Compounds*, 1971.

[32] The International Centre for Diffraction Data, Newton Square, PA: (The International Centre for Diffraction Data, Newton Square, PA); Vol. File Nos. 05-0566 & 36-1451.

[33] Topas 1.0.1 ed.; Bruker AXS, GmbH: 1998.

[34] Warren, B. E. *Prog. Metal Phys. (Bruce Chalmers and R. King, editors. Pergamon Press)* **1959**, *8*, 147-202.

[35] Warren, B. E.; Averbach, B. L. *Journal of Applied Physics* **1950**, *21*, 595-8.

[36] Coleman, R. E.; Powell, H. E.; Cochran, A. A. *Transactions of the American Institute of Mining, Metallurgical and Petroleum Engineers* **1967**, *238*, 408-12.

CHAPTER 10

WATER PURIFICATION: REMEDIATION OF ARSENIC AND LEAD; REDUCTION OF HEXAVALENT CHROMIUM

Nanocrystalline (1.5 nm) zinc sulfide with a specific surface area up to 360 m^2g^{-1} was prepared from the thermal decomposition of a single-source precursor, zinc ethylxanthate. Zinc ethylxanthate decomposes to cubic zinc sulfide upon exposure to temperatures greater than or equal to 125 °C. The resulting zinc sulfide was tested as a water impurity extractant. The target impurities used in this study were As^{5+}, As^{3+}, Pb^{2+}, and Cr^{6+}. The reaction of the nanocrystalline ZnS with Pb^{2+} proceeds as a replacement reaction where solid PbS is formed and Zn^{2+} is released into the aqueous system. Removal of lead to a level of less than two parts per billion is achievable. The results of a detailed kinetics experiment between the ZnS and Pb^{2+} are included in this report. Unlike the instance of lead, both As^{5+} and As^{3+} adsorb on the surface of the ZnS extractant as opposed to an ion-exchange process. An uptake capacity of >25 milligrams per gram for the removal of As^{5+} is possible. The uptake of As^{3+} appears to proceed by a slower process than that of the As^{5+} with a capacity of nearly 20 mg/g. Various matrices for embedding the ZnS nanocrystals were prepared, and the results are presented. A brief discussion of other arsenic extractants is also included. Finally, while further study is needed, early experiments indicate that the ZnS nanoparticles can easily reduce hexavalent chromium to the less toxic trivalent species.

INTRODUCTION

There are many areas in the world where the drinking water supply contains unsafe arsenic concentrations.[1-6] In fact, it has been claimed that arsenic contamination in groundwater in Bangladesh is the largest poisoning of a population in known history.[7] There are essentially two main options of providing these areas with safe water: bring in water from a distant source, or removing the arsenic from the polluted water. Transporting large amounts of clean water to certain locations is not always a feasible option, so methods to remove arsenic at the source must be employed. Before current methods of arsenic remediation are discussed, a brief review about the properties of arsenic contaminants is in order.

Arsenic (As) is found almost everywhere, and of all the elements ranks 20th in natural abundance. In seawater, it ranks 14th in natural abundance and 12th in the human body.[8,9] Arsenic is present naturally in over 200 mineral forms and can exist in several oxidation states (-3, 0, +3, +5).[10,11] There are organic forms of arsenic,[12] but the inorganic species are the forms of interest in this chapter. In water, arsenic is most often found in the +3 or +5 states. The pentavalent arsenate form (H_3AsO_4, $H_2AsO_4^-$, $HAsO_4^{2-}$, AsO_4^{3-}) occurs prevalently in oxygen rich environments whereas the trivalent arsenite (H_3AsO_3, $H_2AsO_3^-$ or $HAsO_2$, AsO_2^-) exists more readily in reducing, oxygen deficient conditions.[13] The pK_a values for arsenic acid and arsenous acid are listed in Table 10.1.[14] Arsenic is found in groundwater for natural reasons and as a result of industry. Several industrial examples are ore processing,[15] cotton/wool processing,[16] insecticides/herbicides,[17] power generation (arsenic contaminated coal),[18] and semiconductor manufacturing.[15]

Table 10.1: **A**cid dissociation constants for H_3AsO_4 and $HAsO_2$.

		pK_a
H_3AsO_4	pK_{a1}	2.1
	pK_{a2}	6.7
	pK_{a3}	11.2
$HAsO_2$		9.1

Due to the prevalence and high toxicity of arsenic, the World Health Organization (WHO) has put forth a provisional maximum contaminant level (MCL) of 10 ppb, and this value has been largely adopted as a standard.[19] Based on the value set by the World Health Organization, the United States Environmental Protection Agency (USEPA) set the MCL to 10 ppb.[20] This national and worldwide level makes the need for effective remediation technologies even more necessary.

The most common removal technologies are oxidation/precipitation,[21-23] coagulation/co-precipitation,[24] sorption,[25] ion-exchange,[26] membrane techniques,[27-29] foam flotation,[30] solvent extraction,[31] and bioremediation.[32] Each method has its advantages and disadvantages. For instance, membrane and ion-exchange technologies suffer from high cost whereas in coagulation/co-precipitation a toxic sludge is formed and capacities are not very high. Likewise oxidation/precipitation methods require precise control of pH and sorption extractants often must be replaced after only a few regenerations.[14] Nanomaterials are of considerable interest as adsorbents since they often have large surface areas and low mass-transfer resistances.[33]

In this chapter both free nanoparticles, and immobilized nanoparticles will be presented as potential sorption materials for arsenic. The same adsorbents were tested for lead remediation and hexavalent chromate reduction, and brief descriptions of their performances are included.

EXPERIMENTAL

Materials. Reagent grade zinc sulfate heptahydrate (J. T. Baker), potassium ethylxanthate (Aldrich), lead nitrate (EM Science), sodium arsenate heptahydrate (GFS), sodium arsenite (Alfa Aesar), potassium dichromate (Mallinckrodt), polyvinyl alcohol (Fluka), Amberlite ion exchange resin (Aldrich), Darco activated carbon (Fisher), potassium hydroxide (Spectrum), cobalt(II) chloride hexahydrate (J. T. Baker), and carbon disulfide (Aldrich) were obtained commercially and used as received without further purification. Well samples from Tinker Air Force Base, Oklahoma City were obtained for chromate analysis. Simulated pond water based on data from Suncor Energy Inc. (Alberta, Canada) was prepared and tested for arsenic and lead. Iron(III) fumarate prepared by Allen Apblett and Jimmy Brown was acquired and used in this study.

Synthesis of xanthate precursors. With the exception of Iron(III) fumarate, all the extractants used in the experiment began as xanthate-based complexes. The metals used for each complex were zinc and cobalt while the R-group was varied. The simplest R-group was ethyl. Either aqueous zinc or cobalt was reacted with potassium ethylxanthate in a 1:2 ratio, which resulted in the formation of zinc and cobalt(II) ethylxanthate respectively. For the remainder of the R-groups (from 1. activated carbon, 2. ion

exchange resin, and 3. polyvinyl alcohol) only zinc complexes were prepared. Each of these three materials has a large number of –OH functional groups. The –OH functionalities were converted to xanthates by reaction with potassium hydroxide and carbon disulfide. Finally, divalent zinc was introduced into each system replacing the potassium ions. A general scheme for the synthesis of any poly-zinc-xanthate is shown in Scheme 10.1.

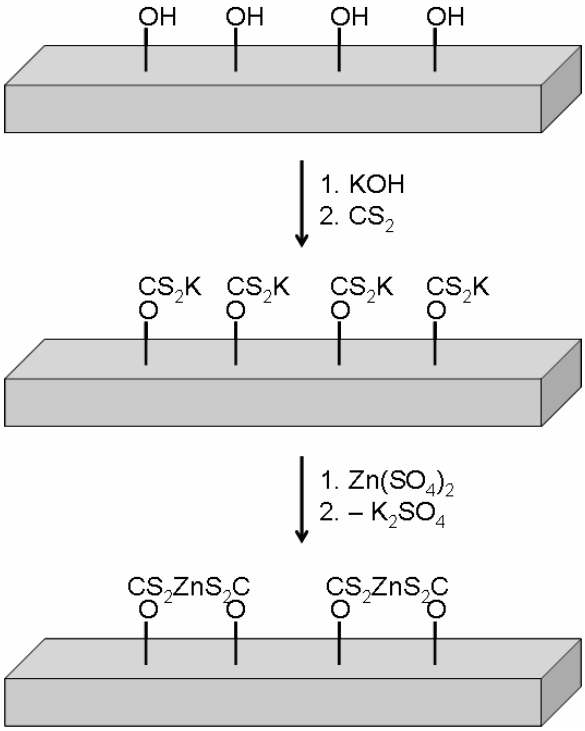

Scheme 10.1: General preparation of any poly-zinc-xanthate. The gray box in the image in not intended to be physically or chemically significant. It serves only to show that there is a poly R-group backbone for the xanthate functionality.

Synthesis of sulfide extractants. Each precursor: zinc ethylxanthate, cobalt(II) ethylxanthate, zinc (activated carbon)xanthate, zinc (polyvinyl)xanthate, and zinc (resin)xanthate was heated to 150 °C to convert the xanthate functionality to sulfide. Thermogravimetric analysis confirmed that 150 °C was a sufficient decomposition temperature. The extractants that are ZnS particles trapped in organic matrices will be referred to as described in Table 10.1.

Table 10.1: Nomenclature and relevant abbreviations.

Full Name	Name Used in Chapter	Pyrolysis Product
zinc (polyvinyl)xanthate	zinc vinylxanthate	zinc vinylsulfide Zn(PV)S
zinc (activated carbon)xanthate	zinc (AC)xanthate	zinc (AC)sulfide Zn(AC)S
zinc (ion exchange resin)xanthate	zinc (resin)xanthate	zinc (resin)sulfide Zn(res)S

In the case of zinc (resin)xanthate, the extractant holds the spherical shape of the parent resin. Figure 10.1 shows images of the resin-based extractant at various stages of synthesis. The matrix of the resin was poly(styrene-divinylbenzene) and the –OH bearing functional group was benzyldimethyl(2-hydroxyethyl)ammonium chloride.

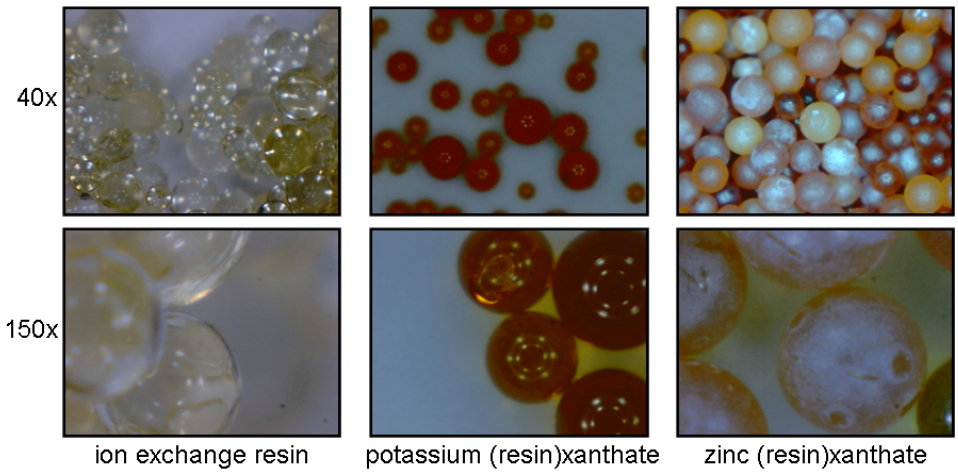

Figure 10.1: Microscope images of the parent ion exchange resin, potassium xanthate-functionalized resin, and zinc xanthate-funtionalized resin. Visually, there is no apparent difference between zinc (resin)xanthate and zinc (resin)sulfide, so no picture of Zn(Res)S is included.

For Zn(AC)S, the material looked like activated carbon at all stages of the chemical modification and remained in powder form. However, the shape and texture of Zn(PV)S could be varied. The most success was achieved by forming long tubes of zinc vinylxanthate. This was accomplished by forcing wet zinc vinylxanthate through a syringe with a 10 cm long nozzle that had a diameter of 3/16". The moist tubes were freeze dried to maximize surface area and finally fired at 150 °C. The tubes of Zn(PV)S were cut into small pellets, and the pellets were washed with water before being used to treat contaminated water.

Characterization. For infrared spectroscopic measurements, roughly 10 mg of the precursor or sulfide was mixed with approximately 100 mg FTIR-grade potassium bromide and the blend was finely ground. Spectra in the 4000-400 cm^{-1} region were collected by diffuse reflectance of the ground powder with a Nicolet Magna-IR 750

spectrometer. Usually, 128 scans were recorded and averaged for each sample (4.0 cm^{-1} resolution) and the background was automatically subtracted.

Raman spectroscopy was also used to characterize some of the xanthates and sulfides. A Nicolet NXR 9610 Raman Spectrometer was used for the analysis and a neat pressed pellet was used for each measurement. Typically, 32 scans were averaged in the 4500-50 cm^{-1} range at a resolution of 4.0 cm^{-1}.

Powder X-ray diffraction (XRD) measurements were obtained on a Bruker AXS D8 Advance diffractometer using Cu Kα radiation with an acceleration voltage of 40 kV and current flux of 30 mA. The diffractograms were recorded for a 2θ range of 17-70° with a step size of 0.02° and a counting time of 18 seconds per step. All the XRD patterns where collected at ambient temperature, and the phases were identified using the ICDD database. The peaks were profiled with a Pearson 7 model using Topas P version 1.01 software. The profiles of the standard and the sample were put into the Win-Crysize program version 3.05, which uses the Warren-Averbach evaluation method to determine crystallite size.

Low arsenic concentrations were determined using a Quick™ (481396) rapid arsenic test kit. An organic acid and zinc dust are reacted with the arsenic sample of interest. The important oxidation/reduction reactions in the detection are:

$$As_4O_6 + 12\ Zn + 24\ H^+ \rightarrow 4\ AsH_3 + 12\ Zn^{2+} + 6\ H_2O$$

$$Zn + 2\ H^+ \rightarrow Zn^{2+} + H_2$$

The arsine gas generated is allowed to react with a mercuric bromide test strip. The color change on the strip is matched to a scale, and the corresponding arsenic concentration is determined. The detection range is from 3 ppb to 500 ppb.

X-ray fluorescence was used to measure higher concentrations (500 ppb to 200 ppm) of arsenic. The instrument was a QuanX EC from Thermo Electron Corporation. A thick palladium filter was used to monitor the arsenic k-line at 10.5 keV.

Lead concentrations at the parts per million scale were measured with a Varian Atomic Absorption Flame spectrometer, and with a Hach HSA-1000 Lead Scanning Analyzer at parts per billion concentrations.

The specific surface areas were obtained with a conventional Brunauer-Emmett-Teller (BET) multilayer nitrogen adsorption method using a Quantachrome Nova 1200 instrument.

Thermogravimetric analysis (TGA) was performed on each of the xanthate complexes at a rate of 2.0°/min from room temperature to 600 °C using a Seiko Instruments Exstar 6200. None of the xanthates melt congruently, but a well behaved decomposition curve was observed each.

A Hach DR/890 Colorimeter was used to monitor hexavalent chromium. The colorimetric method relies on the formation of a purple chromium(VI) diphenylcarbohydrazide complex (complexing agent is 1,5-diphenylcarbohydrazide). The detection of the colorimeter is 10 ppb.

RESULTS AND DISCUSSION

Remediation of lead. Four kinetic experiments were performed on the reaction of nanocrystalline ZnS with Pb^{2+}. The nanocrystalline ZnS was generated by decomposing zinc ethylxanthate at 140 °C. In each of the four experiments, a one-liter sample of a 100 ppm solution of Pb^{2+} was mixed with 0.625 g, 1.258 g, 1.875 g, and 2.503 g of ZnS

respectively. At regular intervals, a small sample was extracted from each of the four mixtures and the lead concentration was determined by atomic absorption spectroscopy. Four plots of lead concentration versus time were generated, each suggesting a pseudo-first order depletion process. Figure 10.2 shows one of those four plots in a natural logarithm versus time format. Each point on the curve represents the average of three measurements.

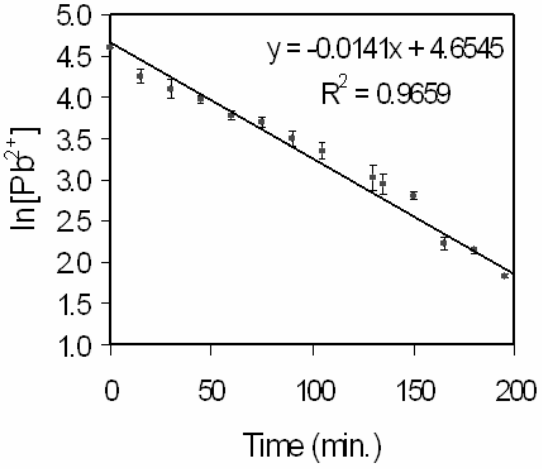

Figure 10.2: A plot that demonstrates the pseudo-first order removal of Pb^{2+} by ZnS. This plot corresponds to the experiment when 2.503 g of ZnS were used.

Three similar graphs were produced and the four slopes, which represent the individual rate constants, were plotted against the corresponding masses of ZnS that were used (Figure 10.3). The linear relationship shown in Figure 10.3 suggests that the reaction is first order in ZnS and first order in Pb^{2+} indicating an overall second-order rate law. The rate law can be represented by the equation

$$\text{Rate} = k[ZnS][Pb^{2+}]$$

The overall rate constant, k, can be determined from the slope of the line seen in Figure 10.3. The value of the rate constant is 6.3×10^{-3} $min^{-1}g^{-1}$, or if you factor in the initial surface area (320 m^2g^{-1}) of the ZnS, 2.0×10^{-5} $min^{-1}m^{-2}$.

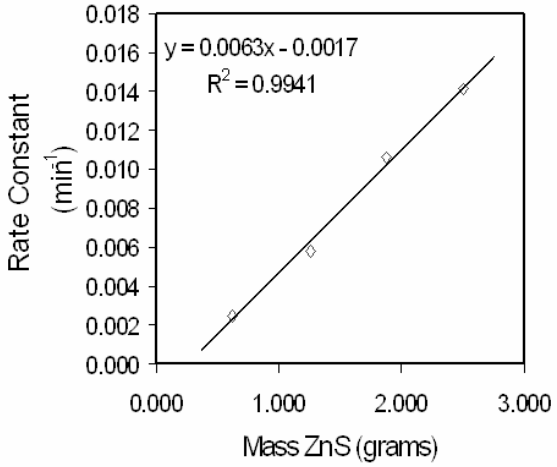

Figure 10.3: A plot of the pseudo-first order rate constants versus mass of ZnS.

Lead concentrations on the order of 100 ppm in drinking water are rare, so tests at lower concentrations were performed. Lead(II) solutions of 50 ppb, 200 ppb, and 1200 ppb were prepared, and ten milliliters of each solution was treated overnight with 0.05 g of ZnS. As determined by electrode stripping, the concentration of Pb^{2+} in each of the three samples was brought to lower than the 2 ppb detection limit. The 0.05 g amount of ZnS used was an arbitrary choice, and it seems likely that less extractant could achieve similar results.

The stoichiometric reaction between aqueous lead(II) nitrate and solid nanocrystalline zinc sulfide results in the formation of lead sulfide (galena) and zinc nitrate in near quantitative yields.

$$ZnS(s) + Pb(NO_3)_2(aq) \rightarrow PbS(s) + Zn(NO_3)_2(aq)$$

Powder X-ray diffraction was used to characterize the solid product formed from the reaction, and the pattern can be seen in Figure 10.4. The average crystallite size of the PbS was determined to be 4.5 nm by the Warren-Averbach method.

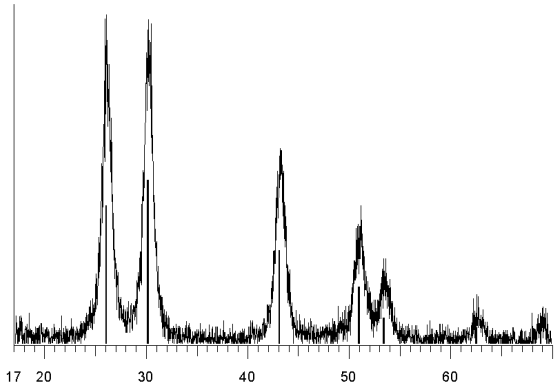

Figure 10.4: Powder X-ray diffraction pattern of the solid obtained from the reaction of lead(II) nitrate and zinc sulfide. The vertical bars represent the known diffraction signals for galena (ICDD 05-0592).

Zinc (AC)sulfide was briefly examined as a medium for lead uptake. Early indications revealed that the Zn(AC)S extractant had poor adsorption capacity and was abandoned. The only other extractant that was tested for lead remediation was zinc vinylsulfide. Kinetic data were not collected for the vinylsulfide composite. However, lead(II) solutions of 50 ppb, 200 ppb, and 1200 ppb were prepared, and ten milliliters of each solution was treated overnight with 0.10 g of Zn(PV)S. As with the free nanocrystals, ZnS embedded in a vinyl polymer was able to remove the lead in each of the three cases to below the detection limit of 2 ppb. Figure 10.5 shows the appearance of Zn(PV)S pellets before and after lead exposure. While the image shows a dramatic change in appearance, further investigation revealed that only the surface is black and the

bulk of the interior remains Zn(PV)S. If enough Pb^{2+} is present and enough time allowed, the lead will completely exchange with Zn^{2+}.

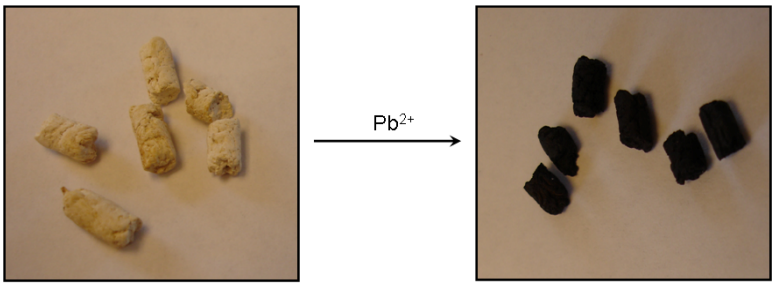

Figure 10.5: Zinc vinylsulfide pellets before (left) and after (right) lead exposure.

Chromate Reduction. Nanocrystalline ZnS powder was explored as a possible reducing agent for hexavalent chromium. One of the most important factors pertaining to the reduction was pH. In short, the reduction did not occur very readily at neutral or basic pH, but under acidic conditions, the reduction worked beautifully. The balanced redox reactions under acidic and basic conditions are:

$$3\ S^{2-} + 8\ CrO_4^{2-} + 40\ H^+ \rightarrow 3\ SO_4^{2-} + 8\ Cr^{3+} + 20\ H_2O \qquad \text{acidic}$$

$$3\ S^{2-} + 8\ CrO_4^{2-} + 20\ H_2O \rightarrow 3\ SO_4^{2-} + 8\ Cr^{3+} + 40\ OH^- \qquad \text{basic}$$

Two parallel reactions between ZnS and K_2CrO_4 were perfomed. One in acidic conditions (pH 5) and one in basic conditions (pH 8). The mole ratio of ZnS to K_2CrO_4 was 3:8 based on the above presumed reactions. The only insoluble substance in the reaction is ZnS, so its mass was monitored and used to determine the extent of each reaction. Under basic conditions, a loss of less than 10 % ZnS mass was observed. Under acidic conditions, however, only 9.6 % of the ZnS remained after the reaction. Also, under acidic conditions, over 99.9% of the Cr^{6+} was reduced to Cr^{3+}. To achieve a similar percentage under basic conditions, a larger ZnS-to-CrO_4^{2-} ratio is required.

It was determined that the maximum reduction capacity for neutral or basic conditions was roughly 8 mg/g. On the contrary, for acidic conditions, the maximum reduction capacity was determined to be approximately 1420 mg/g. At any pH, if enough ZnS is present, hexavalent chromium levels can be decreased to below 10 ppb, which is the detection limit of the colorimeter.

Well-water samples from Tinker Air Force Base in Oklahoma City were obtained due to the high chromium(VI) concentration. One sample had a concentration of 150 ppb while the other was much stronger at 13,000 ppb. Each sample was slightly basic (pH ~ 8). Kinetics information was gathered for the reduction of chromate from the lower concentration sample. The rate data is shown in Figure 10.6. The redox process appears to be first order, but it is important to say that the experiment conditions only warrant a claim of pseudo first order since ZnS was present in large excess. The half-life of the reduction process (based on first order kinetics) was calculated to be 260 minutes.

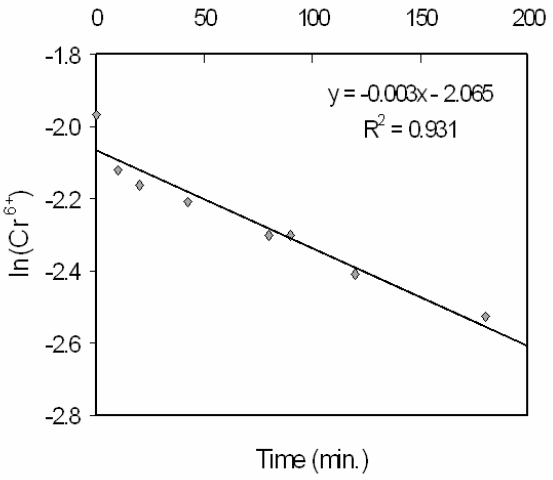

Figure 10.6: Hexavalent chromium reduction kinetic data for 150 ppb chromate well-water when treated with ZnS. Experimental conditions: 10.0 ml of well-water, 10.0 mg of ZnS.

Two experiments were conducted on the more concentrated well-water sample. Table 10.2 summarizes the data for those two experiments.

Table 10.2: Hexavalent chromium reduction data for ZnS and Tinker well-water.

	Mass ZnS (g)	Volume well-water sample (ml)	Initial Cr^{6+} concentration (ppb)	Final Cr^{6+} concentration (ppb)	**Specific reduction capacity (mg/g)**
Exp. 1	0.0243	20.80	13000	4200	**7.53**
Exp. 2	0.0870	19.92	13000	120	**2.96**

Arsenic remediation: free ZnS nanoparticles. When either As^{5+} or As^{3+} - in the form of arsenate and arsenite respectively - are reacted with the high surface area ZnS, the arsenate/arsenite species adsorb on the surface rather than replace zinc ions. The adsorption process of both forms of arsenic cannot be successfully modeled by Langmuir or Freundlich isotherms over the entire test range. Both the Freundlich and Langmuir isotherms suggest that the arsenate species adsorbs on two non-equivalent sites. Similar behavior has been reported elsewhere for arsenic uptake.[34] Table 10.3 contains the averaged data collected from several arsenate uptake experiments. The reaction time for each experiment was sixteen hours. As can be seen, the capacity value stabilizes at just over 25 mg/g.

Table 10.3: Uptake capacity data for arsenate removal by ZnS.

$[As^{5+}]_i$ (ppb)	$[As^{5+}]_f$ (ppb)	$[As^{5+}]_f - [As^{5+}]_i$ (ppb)	Mass ZnS (g)	Uptake Capacity (mg/g)
100	<5	~100	0.010	1.0
250	<5	~250	0.011	2.3
500	5	495	0.010	5.0
750	20	730	0.011	6.6
1000	80	920	0.010	9.2
2000	150	1850	0.011	16.8
3000	200	2800	0.011	25.5
4000	1500	2500	0.010	25.0
5000	1600	3400	0.013	26.2

The ability of ZnS to remove arsenite from water was tested in a fashion similar to that of the arsenate test. Roughly 0.01 g of ZnS was reacted with different concentrations of As^{3+} solutions overnight. Resembling the As^{5+} case, the uptake of arsenite continued to increase as the starting concentration increased until a maximum was reached. The highest arsenite capacity measured is 17.0 mg/g. The two plots in Figure 10.7 show the uptake capacities of ZnS for arsenate and arsenite versus initial testing concentration. Both plots show definite plateaus indicating the maximum uptake capacities. Both uptake capacities are very respectable. In fact they are over five times more efficient than most activated carbons.[14] It is also significant that the arsenite does not require pre-oxidation to arsenate for adsorption, and that both arsenite and arsenate can be removed to below the EPA limit of 10 ppb.

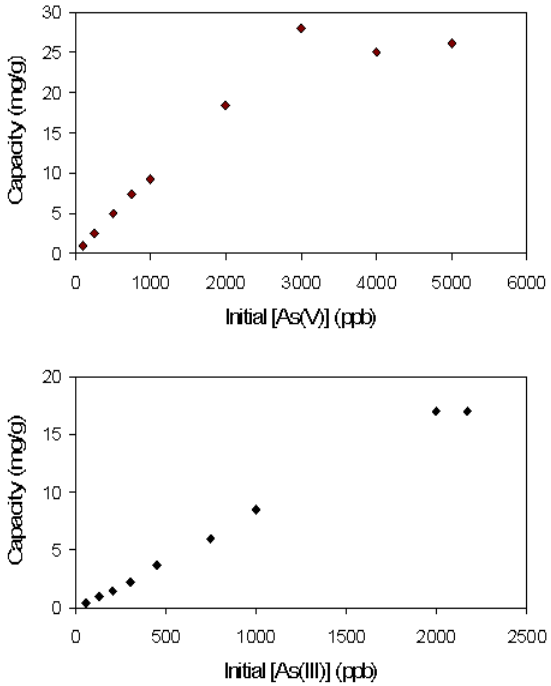

Figure 10.7: ZnS uptake capacities versus initial As^{5+} (top) and As^{3+} (bottom) concentrations.

Data pertaining to water analyzed for an Oilsands wastewater pond owned by Suncor Energy Inc. was used to prepare a mimic of the actual composition. The composition of the Suncor pond water and the lab mimic is shown in Table 10.4. ZnS (1.00 g) was reacted with 500 ml of the simulated pond water for 48 hours. Arsenic and lead levels were measured after treatment. It was determined that for both pollutants, their concentrations were lowered to below 5 ppb, which is well within EPA limits.

Table 10.4: Suncor pond water composition and pollutant remediation.

	Initial Concentration	Post-treatment Concentation
Sodium	540 ppm	--
Calcium	25 ppm	--
Magnesium	12 ppm	--
Chloride	90 ppm	--
Bicarbonate	950 ppm	--
Sulfate	290 ppm	--
Ammonia	14 ppm	--
Copper	660 ppb	--
Arsenic	15 ppb	< 3 ppb
Lead	190 ppb	4 ppb

Arsenic remediation: immobilized ZnS. ZnS-loaded ion exchange resin and ZnS-loaded polyvinyl were synthesized for the sole purpose of holding the sulfide nanocrystals in place. Introducing free nanoparticles into natural water or even in a treatment plant is generally a bad idea. The ultra small particles either pass through typical filters, and become pollutants themselves, or if they don't pass through filters, they often clog them. It was thought that immobilizing the high surface area particles on a plastic substrate would be the best compromise. The compromise being that of losing a percentage of active surface area, but providing a way of keeping the nanocrystals from passing through or clogging filters.

Various loadings of ZnS were incorporated into ion exchange beads. The highest loading achieved came about from mixing the parent resin, KOH, and CS_2 in a 1:1:1 mass ratio. After the resin was xanthated, it was reacted in a 1:1 (mass/mass) ratio with $ZnSO_4 \cdot 7H_2O$. Finally, zinc (resin)xanthate was fired to 150 °C to form Zn(res)S. Solutions of sodium arsenate (1.00, 2.00, 3.00, 4.00, 5.00, 6.00, and 7.00 ppm) were individually mixed with 1.00 g Zn(Res)S and allowed to react overnight. The treated water was examined for As^{5+} concentration. Figure 10.8 is a plot of uptake capacity versus initial arsenic concentration. The plateau feature occurs at a capacity of approximately 0.45 mg/g. The same data were used o generate a Langmuir isotherm, and the result is displayed in Figure 10.9. The Langmuir model fits the data exceptionally well. The maximum As^{5+} uptake capacity based on the isotherm is 0.48 mg/g.

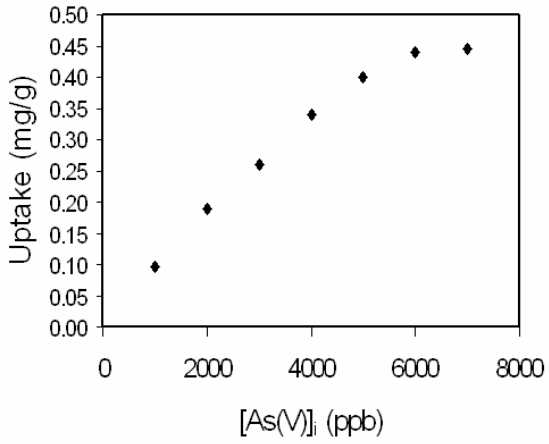

Figure 10.8: Zn(Res)S uptake capacity versus initial arsenic(VI) concentration.

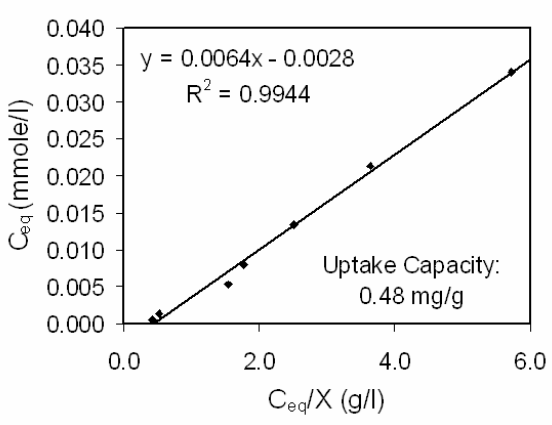

Figure 10.9: Langmuir adsorption isotherm for Zn(Res)S and As^{5+}.

The chemistry associated with the resin-based extractant is fairly clean and straightforward. A small amount of ZnS leaches out of the resins if prolonged contact with water is allowed. It is unknown if there would be any leaching in a continuous flow system. This extractant allows for the easy separation of arsenate from water, and columns could be easily prepared since resin beads are the substrate. However, the relatively low capacity would need to be improved before this technology finds a place in the water purification market.

It was not indicated in the experimental section, but free ZnS nanocrystals were "co-polymerized" with the Zn(PV)xanthate. It is not a true co-polymerization because the ZnS is just physically trapped in the xanthate polymer. In reality, there are two sources of ZnS in Zn(PV)S: 1) ZnS that was premixed with the potassium vinylxanthate, and 2) ZnS from the decomposition of Zn(PV)xanthate. It was possible to get more ZnS immobilized this way than from the xanthate functionalities themselves. The kinetics of arsenate adsorption onto Zn(PV)S were monitored. A sample experiment is included. A specified ratio of Zn(PV)S (150 mg) to 200 ppm As^{5+} (10.0 g) was used for this sample.

A 20 % weight loading of free ZnS nanoparticles was used for this specific experiment. At regular intervals, the arsenic concentration was measured, and the plot shown in Figure 10.10 resulted. For the given reaction conditions, the half-life was determined to be 3.75 hours based on a first order process. The data do not fit first order perfectly. In fact, the R^2-value for a plot of ln[As^{5+}] versus time is less than 0.9. It is clearly not a zero order uptake, and second order seems unlikely. Future work and more data will provide a clearer picture of the uptake kinetics.

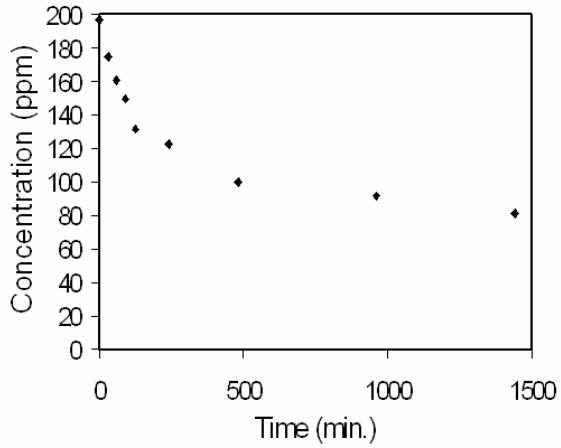

Figure 10.10: Arsenic(VI) concentration versus time for Zn(PV)S (150 mg) to 200 ppm As^{5+} (10.0 g) at room temperature.

The maximum uptake of arsenate by Zn(PV)S was estimated by creating a Langmuir isotherm. Various concentrations of As^{5+} (10.0 g of 100, 150, 200, 250, 300 ppm) were treated with 150 mg Zn(PV)S. The maximum uptake capacity calculated from the slope of the isotherm shown in Figure 10.11 suggests a value of 9.7 mg/g. This value is 20 times that of the resin-based adsorbant and superior to that of many commercial extractants.[14,35]

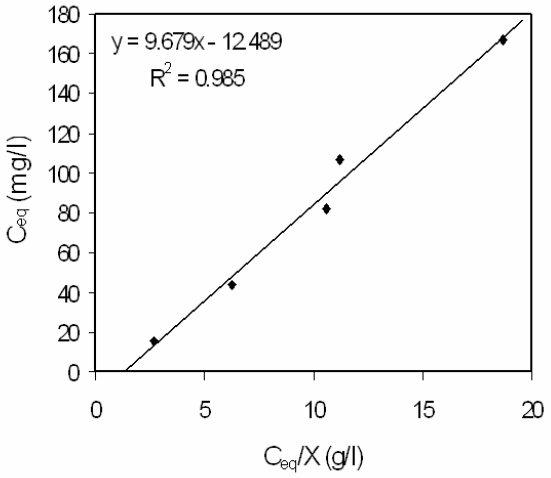

Figure 10.11: Langmuir adsorption isotherm for Zn(PV)S and As^{5+}.

Arsenic remediation: free CoS nanoparticles. Nanocrystalline CoS, prepared from the thermally induced decomposition of $Co(S_2COCH_2CH_3)_2$, was another extractant considered. Kinetic data for arsenate adsorption was collected and the half-life for a specific experiment – 20.0 mg CoS, 10.0 g 200 ppm As^{5+}, room temperature – was calculated . The value for $t_{1/2}$ was 50 minutes. The maximum uptake capacity was determined to be 100 mg/g. These preliminary results are very encouraging. The capacity is on the same order of magnitude with the best arsenate capacities ever reported.[14,34]

Arsenic remediation: iron(III) fumarate. The final extractant that will be discussed in this dissertation is iron(III) fumarate. As with many of the other adsorbants, kinetic and maximum uptake data were obtained. In this case, both arsenate and arsenite remediation were considered. The results of two kinetic experiments are shown in Figure 10.12. For arsenic(III), the uptake by iron(III) fumarate is rapid until a certain concentration is

reached, and then no more pollutant is removed after that point. For arsenic(V), the data do not fit zero, first, or second order models very well. The closest fit is a first order fit, so that is the assumed order with respect to arsenic. The half-life in the arsenate system is 1.6 hours. Using more iron(III) fumarate would remove more As^{3+}. For the specified conditions the half-life of the arsenite system is 9.8 minutes based on initial rates.

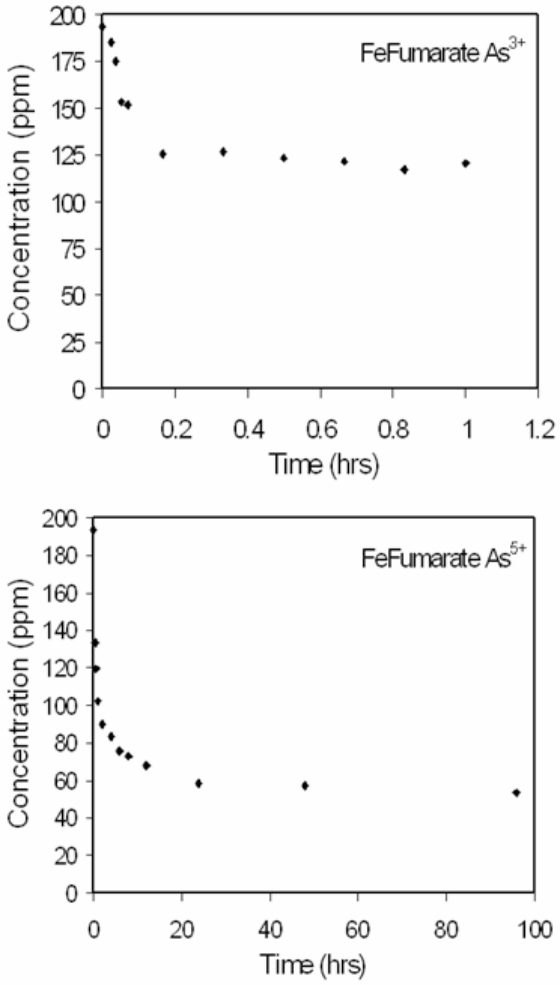

Figure 10.12: (Top): As^{3+} concentration versus time for 20 mg iron(III) fumarate, 10.0 g 200 ppm As^{3+}, room temperature. (Botton): As^{5+} concentration versus time for 20 mg iron(III) fumarate, 10.0 g 200 ppm As^{5+}, room temperature.

The maximum uptake of arsenic(III), based on the kinetic data, is 31 mg/g. The timescale in the arsenite kinetic graph only goes to roughly one hour, but the As^{3+} concentration never drops below about 120 ppm even after 24 hours. A Langmuir adsorption isotherm was easily fitted to some experiments performed on the arsenate system. The adsorption isotherm for iron(III) fumarate and arsenate is depicted in Figure 10.13. The maximum capacity is 150 mg/g.

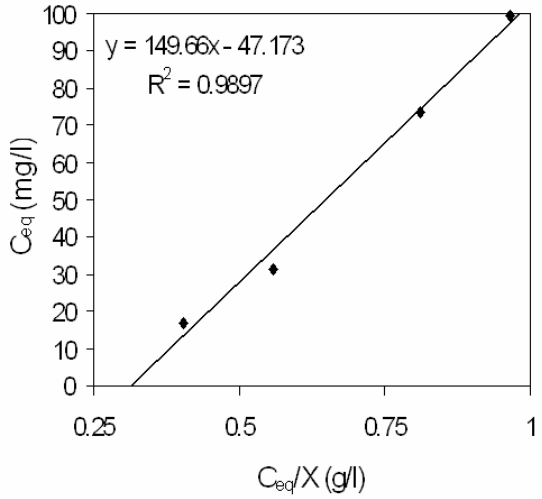

Figure 10.13: Langmuir adsorption isotherm for iron(III) fumarate and As^{5+}.

Arsenic remediation: a summary. Numerous extractants were investigated to determine their use as arsenic adsorbants. Table 10.5 summarizes the important results obtained for each.

Table 10.5: Summary of arsenic extractants. The pH for each solution is 6 to 7.

	Surface Area (m^2/g)	Reaction Order (As)	Capacity (mg/g)	
			As^{3+}	As^{5+}
ZnS	320	1st	17	26
CoS	17	1st	91	102
Zn(res)S	< 5	1st	NA	< 1
Zn(PV)S	15	1st	NA	10
Iron(III) fumarate	13	1st	37	150

CONCLUSIONS

High surface area ZnS proved to be a versatile tool for the remediation of inorganic pollutants from water. The nanocrystals can remove one lead ion for every zinc ion which corresponds to an uptake capacity of 2126 mg/g, and the equilibrium allows removal to less than 2 ppb. Lead removal proceeds via substitution rather than adsorption. In preliminary experiments, Zn(PV)S was shown to effectively remove lead from aqueous systems as well.

Under acidic conditions, ZnS nanopowder can quantitatively reduce hexavalent chromium to the less toxic trivalent species. In other words, the reduction capacity of high surface area ZnS under acidic conditions is 1420 mg/g. At neutral or basic pH, the

reduction does not occur as easily. In fact, at pH 7-8 the reduction capacity is only 8 mg/g.

ZnS nanopowder was also able to effectively remove arsenite and arsenate from water. However, to prevent the ZnS nanocrystals from escaping or clogging the filter apparatus, they were immobilized in various matrices. The best matrix proved to be a polyvinyl substrate. A reduction of uptake capacity of over 50% compared to the free particles occurred upon immobilization in polyvinyl, but the capacity is still 10 mg/g, which is still quite respectable. The drop in capacity is a necessary compromise.

Other extractants such as CoS and iron(III) fumarate demonstrated extraordinary uptake capacities for both arsenic(III) and arsenic(V). Not only does 150 mg/g put iron(III) fumarate on a very short list of substances that can adsorb over 100 mg/g As^{5+}, but it is non-toxic since the human body can tolerate high levels of both iron and fumaric acid/fumarate. It is a very promising material for future remediation technologies.

REFERENCES

[1] Chen, S.-L.; Dzeng, S. R.; Yang, M.-H.; Chiu, K.-H.; Shieh, G.-M.; Wai, C. M. *Environmental Science and Technology* **1994**, *28*, 877-81.

[2] Burkel, R. S.; Stoll, R. C. *Ground Water Monitoring and Remediation* **1999**, *19*, 114-121.

[3] Koch, I.; Feldmann, J.; Wang, L.; Andrewes, P.; Reimer, K. J.; Cullen, W. R. *Science of the Total Environment* **1999**, *236*, 101-117.

[4] Meranger, J. C.; Subramanian, K. S.; McCurdy, R. F. *Science of the Total Environment* **1984**, *39*, 49-55.

[5] Cebrian, M. E.; Albores, A.; Aguilar, M.; Blakely, E. *Hum Toxicol FIELD Full Journal Title:Human toxicology* **1983**, *2*, 121-33.

[6] Dhar, R. K.; Biswas, B. K.; Samanta, G.; Mandal, B. K.; Chakraborti, D.; Roy, S.; Jafar, A.; Islam, A.; Ara, G.; Kabir, S.; Khan, A. W.; Ahmed, S. A.; Hadi, S. A. *Current Science* **1997**, *73*, 48-59.

[7] Smith, A. H.; Lingas, E. O.; Rahman, M. *Bulletin of the World Health Organization* **2000**, *78*, 1093-1103.

[8] Mandal, B. K.; Suzuki, K. T. *Talanta* **2002**, *58*, 201-235.

[9] Woolson, E. A.; Editor *ACS Symposium Series, Vol. 7: Arsenical Pesticides*, 1975.

[10] Wedepohl, K. H.; Editor *Handbook of Geochemistry, Vol. 2*, 1969.

[11] Wedepohl, K. H.; Editor *Handbook of Geochemistry, Vol. 1*, 1969.

[12] Thirunavukkarasu, O. S.; Viraraghavan, T.; Subramanian, K. S.; Tanjore, S. *Urban Water* **2002**, *4*, 415-421.

[13] Oremland, R. S.; Stolz, J. F. *Science (Washington, DC, United States)* **2003**, *300*, 939-944.

[14] Mohan, D.; Pittman, C. U. *Journal of Hazardous Materials* **2007**, *142*, 1-53.

[15] Leist, M.; Casey, R. J.; Caridi, D. *Journal of Hazardous Materials* **2000**, *76*, 125-138.

[16] Chen, S. L.; Yeh, S. J.; Yang, M. H.; Lin, T. H. *Biological Trace Element Research* **1995**, *48*, 263-74.

[17] Korte, N. E.; Fernando, Q. *Critical Reviews in Environmental Control* **1991**, *21*, 1-39.

[18] McNeill, L. S.; Edwards, M. *Journal - American Water Works Association* **1997**, *89*, 75-86.

[19] Galal-Gorchev, H. *Water Supply* **1993**, *11*, 1-16.

[20] USEPA *Federal Register* **2001**, *66*, 6975-7066.

[21] Borho, M.; Wilderer, P. *Water Science and Technology* **1996**, *34*, 25-31.

[22] Leupin, O. X.; Hug, S. J. *Water Research* **2005**, *39*, 1729-1740.

[23] Lee, H.; Choi, W. *Environmental Science and Technology* **2002**, *36*, 3872-3878.

[24] Hansen, H. K.; Nunez, P.; Grandon, R. *Minerals Engineering* **2006**, *19*, 521-524.

[25] Apblett, A. W.; Kuriyavar, S. I.; Kiran, B. P. *Journal of Materials Chemistry* **2003**, *13*, 983-985.

[26] Baciocchi, R.; Chiavola, A.; Gavasci, R. *Water Science & Technology: Water Supply* **2005**, *5*, 67-74.

[27] de Lourdes Ballinas, M.; Rodriguez de San Miguel, E.; de Jesus Rodriguez, M. T.; Silva, O.; Munoz, M.; de Gyves, J. *Environmental Science and Technology* **2004**, *38*, 886-891.

[28] Kang, M.; Kawasaki, M.; Tamada, S.; Kamei, T.; Magara, Y. *Desalination* **2000**, *131*, 293-298.

[29] Ning, R. Y. *Desalination* **2002**, *143*, 237-241.

[30] Zhao, Y.; Zouboulis, A. I.; Matis, K. A. *Separation Science and Technology* **1996**, *31*, 769-85.

[31] Iberhan, L.; Wisniewski, M. *Journal of Chemical Technology and Biotechnology* **2003**, *78*, 659-665.

[32] Katsoyiannis, I.; Zouboulis, A.; Althoff, H.; Bartel, H. *Chemosphere* **2002**, *47*, 325-332.

[33] Moeser, G. D.; Roach, K. A.; Green, W. H.; Laibinis, P. E.; Hatton, T. A. *Industrial & Engineering Chemistry Research* **2002**, *41*, 4739-4749.

[34] Yean, S.; Cong, L.; Yavuz, C. T.; Mayo, J. T.; Yu, W. W.; Kan, A. T.; Colvin, V. L.; Tomson, M. B. *Journal of Materials Research* **2005**, *20*, 3255-3264.

[35] Mondal, P.; Majumder, C. B.; Mohanty, B. *Journal of Hazardous Materials* **2006**, *137*, 464-479.

VITA

Alan Piquette

Candidate for the Degree of

Doctor of Philosophy

Thesis: THE FABRICATION OF NANOMETRIC METAL SULFIDES FROM XANTHATE PRECURSORS

Major Field: Chemistry

Biographical:

Personal Data: Born in Florence, Colorado on December 23, 1979

Education:

Bachelors of Arts Degrees:

Chemistry, Western State College of Colorado, May, 2002

Physics, Western State College of Colorado, May, 2002

Doctor of Philosophy Degree:

Chemistry, Oklahoma State University, December, 2007.

Publications:

The author published and presented papers at numerous sectional, regional, national, and international conferences.

Professional Membership:

American Chemical Society (ACS).

American Ceramic Society (ACerS), NETD Division

Phi Lambda Upsilon (PLU): National Honorary Chemical Society.

Name: Alan Piquette Date of Degree: December, 2007

Institution: Oklahoma State University, Stillwater, Oklahoma

Title of Study: **THE FABRICATION OF NANOMETRIC METAL SULFIDES FROM XANTHATE PRECURSORS**

Pages in Study: 263 Candidate for the Degree of Doctor of Philosophy

Major Field: Chemistry

Scope and Method of Study: The objective of this research was the development of new chemical routes for the synthesis of nanoscale metal sulfides and metal oxides. This was accomplished by investigating a family of materials known as xanthates. It was determined that metal xanthates were ideal single-source precursors for both target products. A wide variety of metal centers and alkyl substituents were easily incorporated into xanthate species yielding new precursors with tunable properties. A systematic characterization of the various precursors by means of thermogravimetric analysis indicated that the decomposition temperatures required to convert the xanthates into nanometric sulfides is lower than that of any other known single precursor. Detailed analyses were performed on both the precursors and the sulfides/oxides using such tools as powder X-ray diffraction, electron microscopy, and nitrogen adsorption surface area analysis along with infrared, Raman, ultraviolet-visible, fluorescence, X-ray fluorescence, and atomic absorption spectroscopies. Two major goals were envisioned: develop metal sulfide and metal oxide materials with enhanced, tunable electrical and optical properties, and fabricate high surface area metal sulfide and/or metal oxide adsorbents for remediation of harmful contaminants in drinking water.

Findings and Conclusions: Metal sulfide and metal oxide nanoparticles were obtained from different xanthate-based precursors possessing distinctive properties such as ultra high surface area and intense emissivity. For example, zinc sulfide, with the largest specific surface area reported to date ($> 350\ m^2g^{-1}$), can be synthesized in a solvent-free, additive-free environment simply by heating zinc ethylxanthate to 125 °C. Cadmium, copper, silver, nickel, zinc, and other metal sulfide quantum dots were easily prepared in aqueous solution with little or no external stabilizing agents required since the thermal decomposition byproducts of the xanthates act as capping agents. The xanthate precursors can also be used to prepare ternary sulfides such as $CuInS_2$ and $CuIn_{1-x}Ga_xS_2$. A number of other beneficial materials such as mirror-like thin-films of metallic NiS, conductive polymers, and efficient water purification adsorbents were successfully synthesized. Succinctly, metal xanthate complexes are versatile compounds that can generate a wide array of useful metal sulfide and metal oxide semiconductor nanoparticles.

ADVISOR'S APPROVAL:_____ Allen Apblett_____